Synthetic Channels in Lipid Membranes and Solid State Substrates

Martin Andreas Langecker

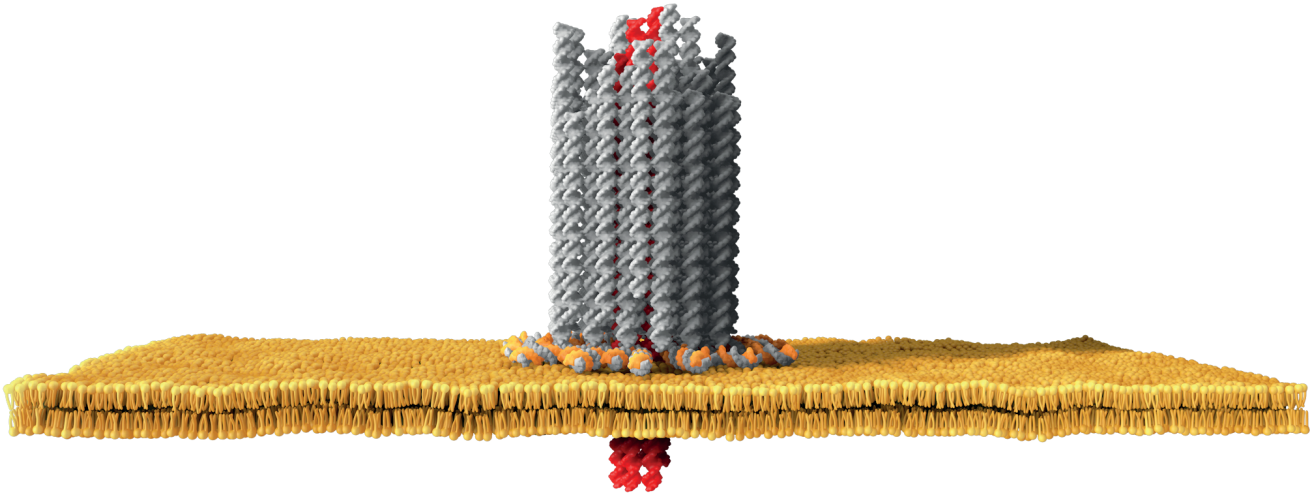

Technische Universität München
Physik Department
Physik synthetischer Biosysteme E14

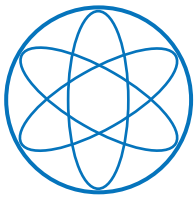

Physik Department
der Technischen Universität München

Physik synthetischer Biosysteme E14

Synthetic Channels in Lipid Membranes and Solid State Substrates

Martin Andreas Langecker

Vollständiger Abdruck der von der Fakultät für Physik der Technischen Universität München zur Erlangung des akademischen Grades eines Doktors der Naturwissenschaften (Dr. rer. nat.) genehmigten Dissertation.

Vorsitzender: Prof. Dr. Martin Zacharias
Prüfer der Dissertation:

1. Prof. Dr. Friedrich C. Simmel
2. Prof. Dr. Hendrik Dietz

Die Dissertation wurde am 21.11.2018
bei der Technischen Universität München eingereicht
und durch die Fakultät für Physik am 25.02.2019 angenommen.

Publication Record

Langecker, M., Ivankin, A., Carson, S., Kinney, S. R. M., Simmel, F. C. & Wanunu, M. Nanopores suggest a negligible influence of CpG methylation on nucleosome packaging and stability. *Nano Letters* **15**, 783-790 (2015).

Langecker, M., Arnaut, V., List, J. & Simmel, F. C. DNA nanostructures interacting with lipid bilayer membranes. *Accounts of Chemical Research* **47**, 1807-1815 (2014).

Arnaut, V., Langecker, M. & Simmel, F. C. Nanopore force spectroscopy of aptamer-ligand complexes. *Biophysical Journal* **105**, 1199-1207 (2013).

Langecker, M., Arnaut, V., Martin, T. G., List, J., Renner, S., Mayer, M., Dietz, H. & Simmel, F. C. Synthetic lipid membrane channels formed by designed DNA nanostructures. *Science* **338**, 932-936 (2012).

Langecker, M., Pedone, D., Simmel, F. C. & Rant, U. Electrophoretic time-of-flight measurements of single DNA molecules with two stacked nanopores. *Nano Letters* **11**, 5002-5007 (2011).

Pedone, D., Langecker, M., Abstreiter, G. & Rant, U. A pore-cavity-pore device to trap and investigate single nanoparticles and DNA molecules in a femtoliter compartment: Confined diffusion and narrow escape. *Nano Letters* **11**, 1561-1567 (2011).

Pedone, D., Langecker, M., Münzer, A. M., Wei, R., Nagel, R. D. & Rant, U. Fabrication and electrical characterization of a pore-cavity-pore device. *Journal of Physics: Condensed Matter* **22**, 454115 (2010).

Contents

Abstract

Synthetic membrane channels or pores offer great potential for applications in medicine, synthetic biology and single molecule sensing. The focus of this work lies on the development of such channels and their use in single molecule sensing experiments, including customized experimental methodology and instrumentation. We report on a novel synthetic membrane channel that is made entirely from DNA and anchored to a lipid bilayer via cholesterol side chains. It is created by means of molecular self-assembly reactions using scaffolded DNA origami, allowing structural precision and simple tailoring to specific applications. In single-channel electrophysiological current recordings, we characterized the channel's transport properties and demonstrated its application as single molecule biosensor. Moreover, we report on a novel solid state nanopore force spectroscopy platform we used to study the force-induced unraveling of individual nucleosome particles. As nucleosomes package the genome in eukaryotic chromatin, interactions between the ~ 146 basepairs long stretch of nucleosomal DNA and the disc-shaped histone octamer it is wrapped around affect gene accessibility and expression levels. We studied the sequence dependence of the DNA-histone interaction and quantified its free energy landscape. With CpG methylation, we examined the impact of an epigenetic factor on nucleosome-modulated gene accessibility. At last, we describe a solid state nanodevice consisting of two serially arranged nanopores which are separated by a femtoliter cavity. We use the signals of the two nanopore sensors to determine the time-of-flight of single DNA molecules and obtain their electrophoretic mobility. Moreover, we analyze the molecules' recoiling dynamics by correlating the current pulses obtained from both sensors.

Zusammenfassung

Synthetische Membrankanäle besitzen großes Potenzial für Anwendungen in der Medizin, in künstlichen biologischen Systemen und als Einzelmolekül-Sensoren. Die vorliegende Arbeit behandelt die Entwicklung synthetischer Membrankanäle und deren Anwendung in der Einzelmolekül-Messtechnik. Dabei wird im Besonderen auch auf die Entwicklung angepasster Messtechnik eingegangen. Im Folgenden wird ein neuartiger künstlicher Membrankanal vorgestellt, der vollständig aus DNS besteht und mithilfe von 26 angebrachten Cholesterinmolekülen in Lipiddoppelschichten verankert wird. Nach der DNA-Origami-Methode wurden die Sequenzen einzelner DNS-Stränge so gewählt, dass sie durch Hybridisierung selbstständig die vorgesehene Kanalstruktur bilden. Diese Technik ermöglicht die Herstellung exakt definierter Strukturen, die leicht an spezielle Anforderungen angepasst werden können. Mithilfe von elektrophysiologischen Methoden wurden die Transporteigenschaften des Kanals charakterisiert und erste Einzelmolekülmessungen durchgeführt. Des Weiteren wird der Aufbau einer neuen, auf Festkörper-Nanoporen basierenden Kraftspektroskopieplattform erläutert, mit deren Hilfe einzelne Nukleosomen durch Krafteinwirkung aufgetrennt wurden. Die Wechselwirkung von DNS und Histonen in Nukleosomen hat direkte Auswirkungen auf die Exprimierung einzelner Gene und stellt damit einen Mechanismus zur Genregulation dar. Im Rahmen dieser Arbeit wurde die Abhängigkeit der Wechelwirkungsstärke von der DNS-Sequenz bestimmt und es wurden erste quantitative Aussagen über den zugrundeliegenden Verlauf der freien Energie der Wechselwirkung getroffen. Zudem wurde anhand der Methylierung von CpG-Dinukleotiden der Einfluss eines wichtigen epigenetischen Faktors untersucht. Im letzten Teil der Arbeit wird ein System zweier seriell angeordneter Nanoporen vorgestellt, die durch eine Kammer mit einem Volumen im Femtoliterbereich miteinander verbunden sind. Durch Analyse der Stromsignale beider Nanoporen-Sensoren wurde die Laufzeit einzelner DNA-Moleküle durch die Kammer gemessen und damit deren elektrophoretische Mobilität bestimmt. Zudem konnte durch Korrelation beider Sensorsignale der zeitliche Verlauf der Relaxation einzelner DNS-Stränge beobachtet werden.

1 Introduction

Due to the compartmentalized nature of biological systems, transport of molecules and ions across separating membranes is vital to their function. While active membrane transporters move small molecules or ions against concentration gradients and build up electrochemical potentials, membrane channels regulate concentration levels and electrochemical potentials by controlling diffusion through their hydrophilic central pores. Among other membrane channels – such as aquaporins or the outer membrane porins of bacteria, mitochondria and chloroplasts – ion channels exhibit a particularly rich functional diversity. They play a major role in many biological processes such as neuronal signaling, sensory perception or muscle contraction [1]. Consequently, ion channels are also associated with a wide range of diseases [2]. Most of what we know today about their function has been discovered in electrophysiological experiments such as patch clamp recordings [3]. Using similar recording techniques, larger membrane channels such as bacterial outer membrane porins or pore-forming toxins have been converted to single molecule sensing devices [4, 5] in which the translocation of single macromolecules such as DNA is detected by a transient reduction of the transmembrane current. Among applications in DNA sequencing [6] and stochastic sensing [7], such nanopore sensors can be used for single molecule force spectroscopy experiments [8]. By providing insights into the free energy landscape of molecular bonds, force spectroscopy experiments contributed notably to our understanding of biological processes [9–11]. Compared to established techniques such as optical tweezers [12] – which has been awarded the Nobel Prize in physics 2018 – nanopore force spectroscopy experiments offer higher throughput and do not require labeling.

Inspired by the structural and functional diversity of membrane channels, efforts have been made to create synthetic analogues that could serve as drugs, components for synthetic biological systems or as analyte-tailored single molecule sensors. Researchers used nanostructuring tools to form nanoscale apertures in solid state membranes [13] and created amphiphiles from metal-organic scaffolds forming channels in lipid bilayers [14]. Moreover, first protein channels were designed *de novo* [15]. In this work, we describe the design, fabrication and characterization of a novel synthetic membrane channel based on DNA. Furthermore, we present two specific applications for synthetic pores in solid state membranes. Beforehand, we describe the customized instrumentation and methodology used in these experiments.

2 Measuring Current Signals Across Single Channels or Pores

The availability of methodology and instrumentation for measuring the ionic current passing through single membrane channels marked a leap forward in understanding the function of ion channels in cells and in drug development for ion channel related diseases such as diabetes or heart disease [2]. In this chapter, we review the experimental techniques used to characterize membrane channels by their ionic conductance. The discussed principles also apply for sensing applications based on membrane channels or solid state nanopores, which will be covered in Chapter 3. Finally, we describe and characterize the experimental setups used for the current measurements on membrane channels and solid state nanopores discussed in this work.

2.1 The Patch Clamp Technique

The first current measurements of individual ion channels became possible with development of the patch-clamp technique [16, 17], for which Erwin Neher and Bert Sakmann received the Nobel Prize in Physiology or Medicine in 1991. Its principle is depicted schematically in Figure 2.1a. The blunt tip of a fire-polished micropipette is brought into physical contact with the cell membrane, isolating a membrane patch from the bath solution. Via two electrodes, one inside the pipette and the other one inside the bath solution, the ionic current across ion channels inside the membrane

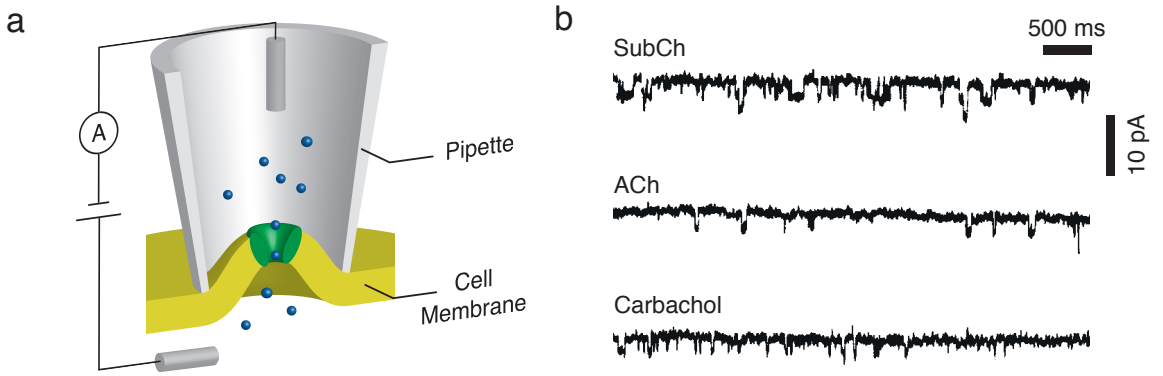

Figure 2.1: Patch Clamp Recordings. a) Schematic of an ion channel current recording in a cell-attached patch-clamp configuration. b) Early current recordings of the acetylcholine receptor in frog muscle cells in presence of suberyldicholine (SubCh), acetylcholine (Ach) and carbachol. Adapted with permission from [16]

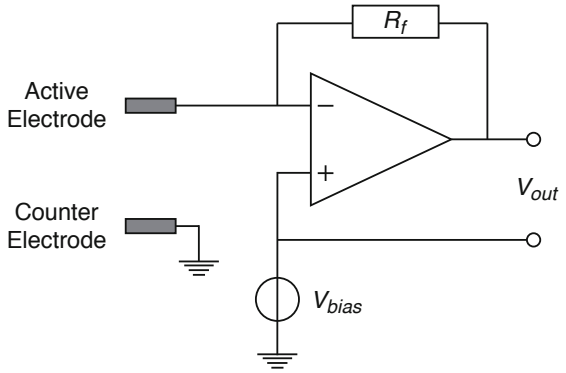

Figure 2.2: Circuit Diagram of a Patch Clamp Amplifier. Simplified circuit schematic of a patch clamp amplifier, consisting of a voltage source V_{bias}, an operational amplifier and a feedback resistor R_f. Ag/AgCl electrodes are depicted in gray.

patch can be measured (see Figure 2.1b). By applying gentle suction to the pipette, the leakage current across the pipette-membrane interface can be greatly reduced (i.e. a GΩ seal is established), so that high quality recordings with sub-pA resolution can be obtained [18]. Apart from this "cell-attached" configuration, several more recording configurations can be obtained [19]. For example, the patch may be ruptured intentionally by applying a stronger suction pulse. Strikingly, the membrane remains sealed to the pipette after the rupture, so that recordings of the entire cell membrane can be performed in this "whole-cell" configuration. Apart from fundamental research on ion channels and excitable cells, the patch-clamp technique has emerged as an important tool for screening ion channel related drugs [20]. *In vivo* patch-clamp recordings of neuronal action potentials are essential for many neuroscience studies [21]. However, promising optical electrophysiology techniques have been shown recently [22, 23].

2.2 Instrumentation Used in Single Channel Recordings

In the following, we describe the fundamental components used for current sensing in single channel recordings. Initially developed for patch clamp experiments, this instrumentation today is also commonly used for planar lipid bilayer recordings and solid state nanopore experiments as described in this work.

The Patch Clamp Amplifier. To detect single channel currents in the pA range, good electromagnetic shielding, e.g. a Faraday cage around the patch-clamp setup, and a sensitive current amplifier are needed. Most patch clamp amplifiers are current-voltage-converters [17, 19]. A simplified circuit diagram is shown in Figure 2.2. The active electrode (i.e. the electrode inside the pipette) is connected to the inverting input of an operational amplifier. Due to the amplifier's high gain and the feedback coupling via R_f, there is virtually no potential difference between the amplifier inputs, i.e. the voltage at the active electrode follows the bias voltage V_{bias}. This configuration is referred to as voltage-clamp, as the electrode is "clamped" to the bias voltage.

Because of the amplifier's high input resistance, all electrode current flows across the feedback resistor R_f. Therefore, the output voltage V_{out} is proportional to the electrode current. Commercial patch clamp amplifiers integrate a tunable analog low-pass filter to prevent aliasing when the signal is digitized. Furthermore, it can be used to achieve higher current resolution by reducing the measurement bandwidth (cf. Section 2.5).

Another common configuration is current-clamping. Here, the electrode current is held at a constant level while the corresponding potential is recorded. In most commercial patch clamp amplifiers, this is realized by an additional feedback circuit [24]. Whole cell current clamping is used to record action potentials of excitable cells such as neurons or cardiomyocytes [25].

Electrodes. Typically, silver/silver chloride (Ag/AgCl) electrodes are used to transduce ionic current into electric current and vice versa. At the anode surface, silver oxidation results in a release of an electron into the circuit. Subsequently, Ag^+ reacts with a chloride ion to form silver chloride (AgCl). At the cathode, the back reactions take place. Ag/AgCl electrodes are preferable due to their low junction potential and small polarizability [26]. They may be prepared either chemically by dipping a silver wire into sodium hypochlorite solution or electrochemically by driving current across a silver anode in potassium chloride solution.

2.3 Lipid Bilayer Recordings

In many cases, reducing the complexity of a system is necessary to understand the function of its constituents. For membrane channels, such a reduction can be achieved by channel reconstitution *in vitro* into planar lipid bilayers. In contrast to cell membranes, which are made from phospholipid bilayers with locally varying lipid composition and a huge amount of embedded proteins ($\approx 50\,\%$ wt.) [1], these model membranes are phospholipid bilayers made from a defined lipid mixture, which separate two aqueous compartments (*cis* and *trans*) with defined electrolyte composition. By placing an Ag/AgCl electrode in each compartment, the current across the bilayer may be recorded with a patch clamp amplifier. Planar lipid bilayer experiments enable detailed studies of channel properties such as ion conduction and selectivity [27, 28] or studies of the impact of lipid composition on channel function [29]. Furthermore, channels may be investigated that are not directly accessible via patch clamp experiments, such as outer membrane porins of gram-negative bacteria [30] or mitochondrial channels [31]. It is noteworthy that porins such as α-hemolysin [32] or mutated forms of MspA [33] are remarkably well-suited for channel-based sensing applications when reconstituted into lipid bilayers (cf. Chapter 3) [4, 5].

2.3.1 Methods for Bilayer Formation.

One of the most commonly used techniques to form planar lipid bilayers is the "painting" method developed by Mueller et al. [34] (see Figure 2.3a). A small aperture

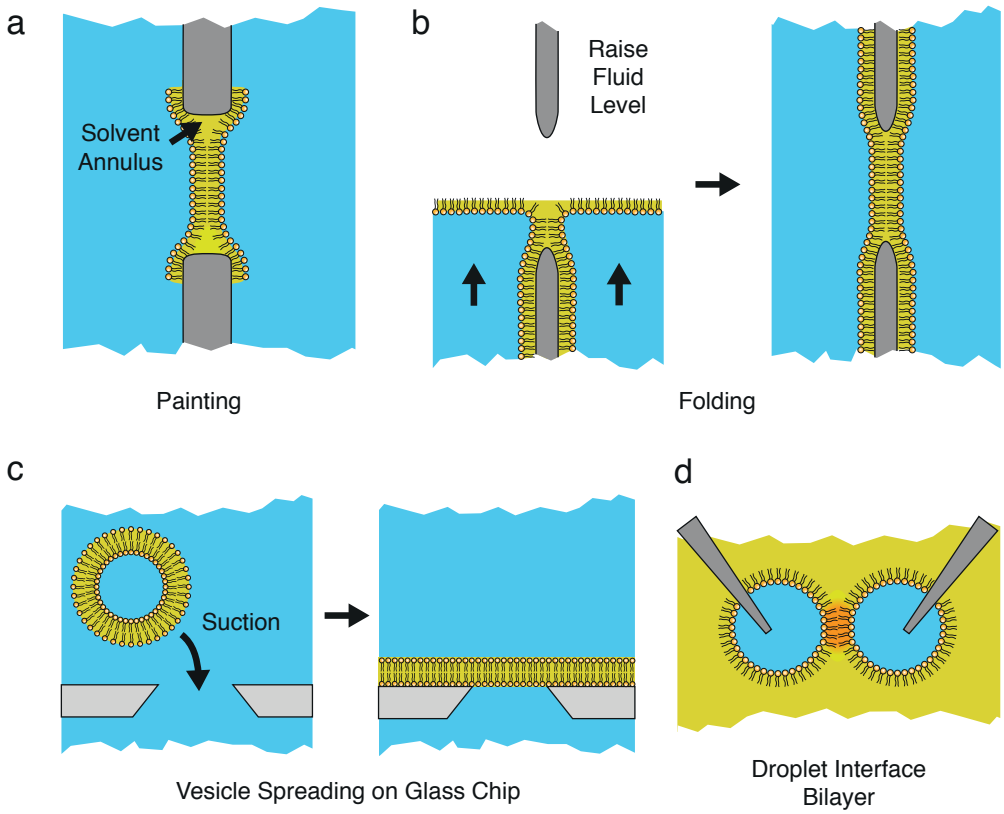

Figure 2.3: Methods for Bilayer Formation. a) Painting method. A lipid-solvent mixture is spread across an aperture, where it thins out spontaneously and forms a lipid bilayer. b) Folding method. Two monolayers at the air-fluid interface are folded across an aperture by raising the fluid level. c) Vesicle Spreading. Bilayers are formed by spreading of a giant unilamellar vesicle (GUV) across the aperture of a glass chip. d) Droplet interface bilayer. When two aqueous droplets are formed in an oil-lipid mixture, lipids arrange in a monolayer at the oil-lipid boundary. Bringing the droplets into contact, a bilayer forms at the interface.

(typically with a diameter of 50 µm to 1 mm) inside a thin septum made of polytetrafluoroethylene (PTFE), polycarbonate or similar, is pretreated with a mixture of phospholipids dissolved in a nonpolar solvent. After air-drying, the septum is assembled into a measurement cell, where it separates two compartments filled with electrolyte solution. Subsequently, the solvent-lipid mixture is "painted" across the aperture using a small spatula or hair, where it thins out spontaneously and forms a lipid bilayer. Thinning of the lipid film, which initially has a thickness of several µm, is driven by two mechanisms. First, there is solvent flow towards the rim of the aperture (Plateau-Gibbs-border suction), where a solvent annulus forms [35]. The second contribution is compression due to Van-der-Waals forces between the two adjacent fluid phases [36].

Another way to form planar lipid bilayers is the "folding"-method described by Montal et al. [37] (Figure 2.3b). As for the painting-method, a septum made from a hydrophobic material such as PTFE or Parafilm with a pretreated aperture is assembled into a measurement cell. By raising the fluid level in both compartments simultaneously, two lipid monolayers created at the air-liquid interface are folded across the aperture, where a lipid bilayer forms. Furthermore, lipid bilayers may be created by applying suction to spread giant unilamellar vesicles (GUVs) across a hole in a glass chip [38] (Figure 2.3c) or bringing microemulsion droplets with monolayers at their boundaries into physical contact [39] (Figure 2.3d). Such droplet interface bilayers (DIB) are not considered planar, although they are used for the same applications.

The methods described above differ strongly by the amount of solvent present in the bilayer, which effects the reconstitution of membrane channels (see Section 2.3.3). While bilayers created with the painting and the droplet-interface technique contain high amounts of solvent, folded bilayers contain significantly less [40] and bilayers formed by the GUV spreading technique are virtually solvent-free.

Another criterion is the size of the lipid membrane, which has implications on its stability, measurement noise (see Section 2.5) and channel incorporation efficiency [41]. Traditional painting and folding setups feature rather large apertures (typically 50 µm to 2 mm) and therefore large membrane sizes, whereas droplet bilayer membranes or membranes formed by vesicle spreading are significantly smaller (typically 1 - 4 µm).

2.3.2 Chip-Based 16 Channel Bilayer Recordings.

For the studies on synthetic DNA-based ion channels presented in Chapter 4 of this work, we created planar lipid bilayers on microelectrode-cavity arrays (MECA[1]) [42]. These arrays are fabricated on a borosilicate glass substrate using standard microfabrication techniques combined with galvanic electrodeposition. 16 individual wells are

[1]The MECA chips used in this work were kindly provided by Gerhard Baaken, member of the Behrends lab (Universität Freiburg, Germany). Prototypes for the actuation of the bilayer-forming magnetic stirrer and the relais board were provided by Nanion Technologies GmbH, Germany. By now, these chips are commercially available (Ionera Technologies GmbH, Freiburg, Germany) as is a recording setup with automated bilayer formation and switchable single channel/multichannel acquisition (Nanion Orbit 16).

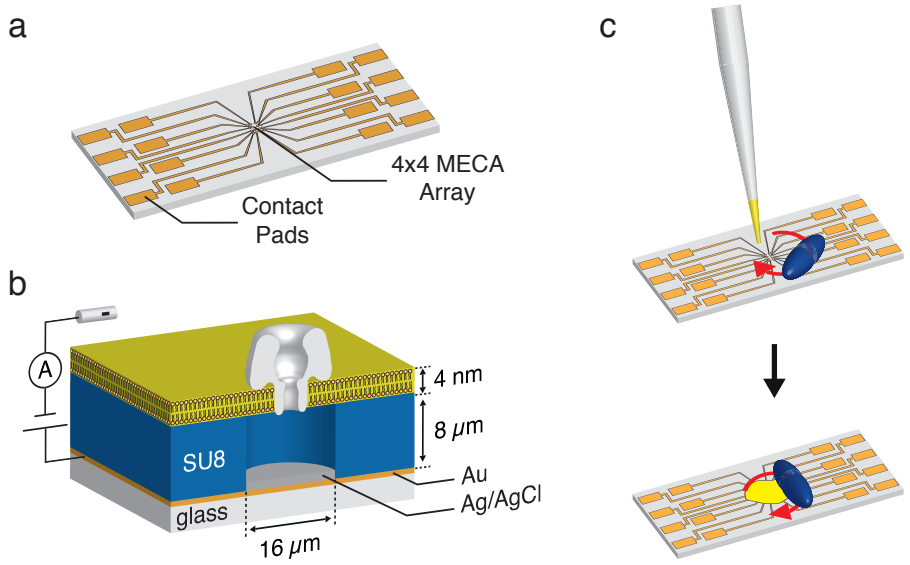

Figure 2.4: Microelectrode Cavity Arrays (MECA). a) Top view of a 4 x 4 MECA chip. b) Schematic of a single microelectrode-cavity recording configuration. A lipid bilayer is formed across the cavity, in which ion channels can be incorporated. Items not drawn to scale. c) Automated bilayer formation. After pipetting a drop of lipid solution next to the MECA array, it is spread by a PTFE coated magnetic stir bar and thins out to a bilayer. Broken bilayers can be reformed automatically.

structured into SU-8 photoresist, each featuring a diameter of 16 µm, a height of 8 µm and an Ag/AgCl microelectrode at its bottom, which is connected to a gold contact pad by a strip line (see Figure 2.4a and b). By sealing each of these wells with a lipid bilayer, we obtain 16 recording setups with individual *trans* compartments and a common *cis* compartment with a traditional Ag/AgCl electrode.

Bilayers are formed using a modified version of the painting technique [43]. At first a drop of lipid solution is pipetted next to the array. Then a PTFE-coated magnetic stirrer on top of the chip is actuated by a motorized counter magnet to perform a tumbling motion, by which it spreads the lipid solution across the wells (see Figure 2.4c). As for the traditional painting technique, spreading is followed by spontaneous thinning and bilayer formation. Broken bilayers may be reformed by rotating the stir bar again. Further addition of lipids usually is not required.

Acquisition Hardware. For parallel current recordings on all 16 wells, we use a 16 channel patch clamp amplifier board with integrated digitizer (Triton$^+$, Tecella LLC., USA). The recording bandwidth of this system is limited by the slow frequency response of the amplifier, i.e. current transitions at constant voltage exhibit transients with time constants of $\approx 300\,\mu s$. By fitting single exponentials to the signal edges as done by Baaken et al. [44], we manage to resolve signals with durations down to 1 ms, yielding an effective bandwidth of 1 kHz. For higher bandwidth recordings on single wells, we use a EPC 9 single channel amplifier (HEKA Elektronik, Germany) in combination with a NI PCI-6251 DAQ card (National Instruments, Germany). Each well can be switched electronically between the multichannel amplifier and the single

channel amplifier via a relay board. To minimize AC coupling due to ground loops, the board is battery powered and connected to the measurement computer via a custom-made optical isolator circuit. For a detailed wiring schematic of the setup, please see Appendix A.1.

Temperature Control. To control the measurement temperature, we machined a custom mount for the MECA chip made of aluminum, which serves as heat exchanger and integrates a Pt-100 temperature sensor. The sensor is connected to a thermostatic circulator (F30-C, Julabo GmbH, Germany) which pumps water through the heat exchanger. We account for thermal losses between the chip mount and the electrolyte compartment by multiplying the measured temperature value with a temperature-dependent correction factor, which was obtained experimentally.

Acquisition Software. For data acquisition and a unified control over all components of the measurement setup, we developed a custom measurement software in LabVIEW[2]. It integrates parallel acquisition and display of all 16 microwells, application of freely designable stimuli such as voltage step protocols or voltage ramps and control over all relevant amplifier functions, e.g. switching between amplifiers, configuration of the low-pass filter, gain setting, holding potential and capacitance compensation. If the single cannel amplifier is selected, the software switches to sequential acquisition of all selected recording channels. The data is efficiently saved into compressed MATLAB binaries including all relevant acquisition parameters (channel number, voltage protocol, filter frequency, sampling rate, temperature, date).

Automated Channel Incorporation. Apart from the standard acquisition and control functions described above, we implemented several experiment-specific extensions. As spontaneous incorporation of membrane channels often is a function of membrane voltage [45], we added an automatized incorporation protocol. A brief incorporation pulse (typically 250 - 350 mV for 10 ms) is applied repeatedly, e.g. every 150 ms. After each pulse, the membrane voltage is measured. When it exceeds a predefined threshold current, the well is being disconnected in order to prevent additional incorporations. The command potential output of the multichannel amplifier is limited to 250 mV. However, the MECA setup features very stable bilayers and higher voltages can be beneficial for efficient channel incorporation. Therefore, we integrated the "zap" function of the amplifier into the incorporation protocol, as it is realized by a separate voltage source and provides voltages of up to 1000 mV.

Conditional Measurements. Nanopore force spectroscopy applications using an anchor/fishing technique (cf. Section 3.4.1) require capture of a molecule or a complex before the actual measurement can be performed. As the capture can be detected by a current transition, we implemented an option for conditional measurements. Here, a

[2]LabVIEW drivers for the Tecella Triton$^+$ amplifier were kindly provided by Timo Stengel (Nanion Technologies GmbH, Germany).

capture protocol is applied repeatedly to a single recording channel. After each cycle, the pore current is measured and compared to predefined threshold values. If the capture is considered successful, the actual measurement protocol is started. Subsequently, the capture protocol is initiated on the next recording channel.

2.3.3 Channel Reconstitution

Although the planar lipid bilayer technique is a powerful tool to characterize membrane channels, it is only applicable for channels that may be reconstituted *in vitro*. Some peptide channels such as alamethicin [46] or gramicidin [47] and few protein channels such as the bacterial porins OmpF [30] and MspA [5] or the bacterial toxin α-hemolysin [48] incorporate sponanteously into lipid bilayers after adding the channel protein or peptide dissolved in detergent to one of the electrolyte compartments. Often, protein channels that do not incorporate spontaneously may be reconstituted into proteoliposomes which are subsequently fused with the planar lipid bilayer [41].

The probability of channel incorporation or vesicle fusion is typically higher for solvent-containing bilayers, which is attributed to larger variations in membrane thickness providing a better match to the hydrophobic patches of membrane channels [49]. Furthermore, the probability of incorporation or fusion increases with membrane size [41]. Since the measurement noise increases and stability decreases with membrane size (cf. Section 2.5), usually a tradeoff is required between incorporation probability and recording quality. The 16 channel MECA setup described in the previous section provides the best of both worlds. Individual microwells feature small membrane sizes with high stability and low noise, whereas all 16 wells together have a membrane area large enough for channels with low incorporation probability.

2.4 Solid State Nanopore Recordings

The term solid state nanopore typically refers to a single nanoscale aperture created in a solid state membrane by means of top-down nanostructuring techniques (see Figure 2.5a) [13]. Compared to lipid bilayers, solid state membranes offer superior mechanical and chemical robustness. While protein channels such as α-hemolysin or MspA offer atomic precision, solid state nanopores can be created with tunable sizes, which has made them indispensable tools for single molecule sensing. In Chapter 5 of this work, we describe the fabrication of two different solid state nanopore devices and their use for different single molecule sensing applications. Here, we describe the measurement setups used for these experiments.

The thin membranes of the solid state nanopore devices used in this work are stabilized by a chip-like silicon substrate. To drive ionic current across such a pore, the corresponding chip is mounted between two electrolyte compartments. Therefore, the nanopore chip is treated with piranha acid or oxygen plasma to render the surface hydrophilic [50, 51] before it is mounted into one out of two custom measurement cell designs (see Figure 2.5b and c).

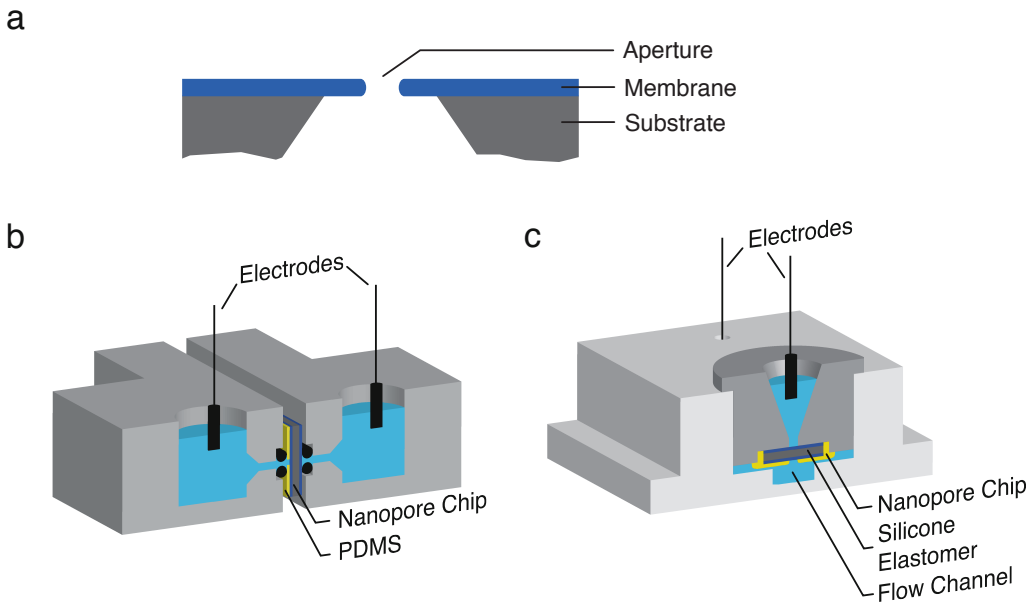

Figure 2.5: Solid State Nanopore Recordings. a) Schematic of a solid state nanopore device. b) Horizontal measurement cell design (cross-section). The 6 x 6 mm nanopore chip is mounted between two electrolyte compartments made from polycarbonate and sealed with o-rings. c) Vertical measurement cell design (cross-section). The measurement cell (PTFE) features a flow channel at its bottom. The chip is glued to the bottom of an insert (dark gray) with a silicone elastomer (Ecoflex 5 Smooth-On Inc., USA) before it is assembled into the cell.

The first design consists of two identical pieces made from polycarbonate with the nanopore chip sandwiched in between. Each piece features an electrolyte compartment which is sealed to the nanopore chip by a silicone o-ring (0.7 mm inner diameter). This limits the area of the chip-electrolyte surface in order to minimize measurement noise (cf. Section 2.5). Prior to mounting the nanopore chip into the cell, we apply a thin passivation layer of PDMS (polydimethylsiloxane) using a single hair brush attached to a micromanipulator. That way, only a small area around the pore location in the order of $\sim 10^{-2}$ mm^2 is left untreated. For assembly, we bring one of the polycarbonate pieces into upright position with one o-ring attached. Then we carefully place the nanopore chip on top of the o-ring, followed by the second o-ring and polycarbonate piece. The sandwich structure is stabilized by two screws connecting both polycarbonate pieces, which we tighten gently. At last, we fill both compartments with electrolyte solution and insert two Ag/AgCl electrodes.

The second cell design consists of a PTFE base with a flow channel and a polycarbonate inset. Here, we glue the nanopore chip by hand to the bottom of the inset with a fast-curing silicone elastomer (Ecoflex 5, Smooth-On Inc., USA), which serves both as sealing and as passivation layer. The uncoated membrane area around the pore is larger as for the first measurement cell design, since no micromanipulator is used for application. Then, we press the inset into the base of the cell and fill it with electrolyte solution. At last, we flush the flow channel below the chip with electrolyte and insert the Ag/AgCl electrodes.

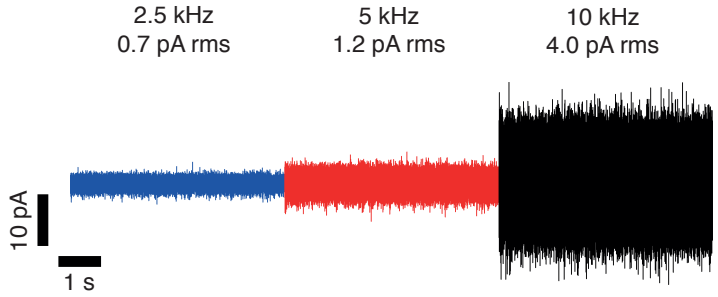

Figure 2.6: Noise in Ionic Current Recordings. Current trace of a planar lipid bilayer recording at different bandwidths, obtained using the MECA setup. The rms current noise is indicated.

The current is measured via a patch clamp amplifier (Axopatch 200B, Molecular Devices, USA) and digitized with a NI DAQ card (NI USB-6229 or NI PCIe-6351). To minimize AC pickup noise, the measurement cell is placed in a Faraday cage. As for the bilayer setup, we use custom LabVIEW-based software, which integrates high speed current acquisition and voltage control. Furthermore, it controls a hardware-based trigger circuit for active voltage control (see 3.3.1). The current traces are saved as MATLAB binaries, including all relevant measurement parameters.

2.5 Noise in Ionic Current Recordings

In Figure 2.6, a typical current trace from a bilayer recording is shown. Its noise level can be characterized by the root-mean-square (rms) current noise I_{rms}, which is given by the standard deviation of the current signal from its mean value [26]. As apparent in Figure 2.6, the rms noise is an increasing function of the measurement bandwidth. This relationship has important implications for ion channel and nanopore recordings. As the current signals studied in these recordings are typically weak (they range from a few pA to several nA), the temporal resolution of a recording often is not limited by the frequency response of the amplifier, but by the signal-to-noise ratio $\Delta I/I_{rms}$ of the setup [52]. The noise characteristics of a measurement setup therefore determine both its ability to detect small current changes and its temporal resolution. This chapter covers the fundamentals of noise analysis in ion channel and nanopore recordings. These considerations share many aspects with traditional patch clamp experiments [53]. We give an overview on the relevant noise sources and their origin in bilayer and solid state nanopore experiments where we take into account previous noise studies on lipid bilayer [54] and solid state nanopore systems [51, 55, 56]. Finally, we discuss the noise performance of the measurement setups used in this work.

2.5.1 Electrical Circuit Schematic of a Bilayer Recording Setup

For the discussion of noise sources in the following section, we consider an equivalent circuit model for the recording setup (see Figure 2.7). It is based on previous noise studies [51, 54, 56, 57] and on electrochemical impedance spectroscopy data [58, 59].

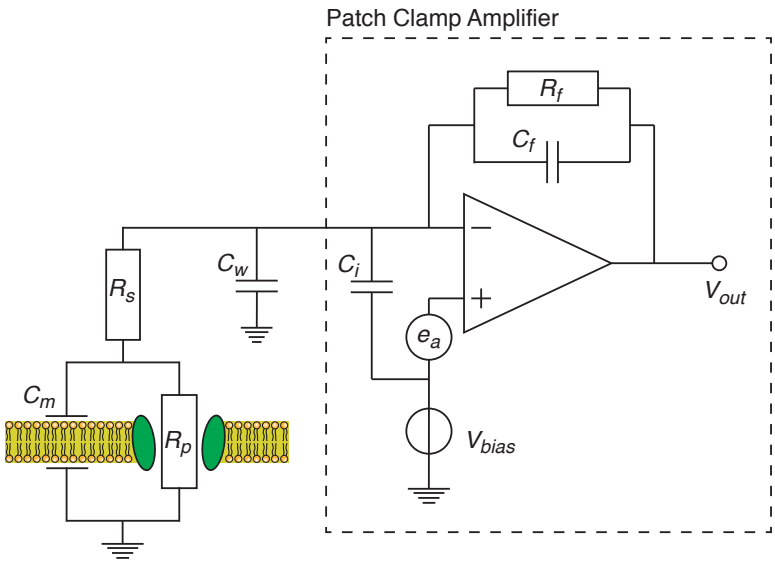

Figure 2.7: Equivalent Circuit Model of a Lipid Bilayer Recording Setup. The channel is represented by its resistance R_p in parallel to the membrane capacitance C_m and in series to the resistance R_s of wiring, electrodes and electrolyte compartments. Stray capacitances of the wiring (C_w), the feedback circuit (C_f) and the amplifier input (C_i) are indicated, as is the voltage noise e_a of the amplifier.

The lipid membrane itself can be considered a dielectric with capacitance C_m, which depends on the lipid type and membrane size. DPhPC bilayers as used for the bilayer experiments in this work have a specific capacitance of $0.5\,\mu F/cm^2$ [60]. Eventual capacitance contributions of the membrane support are subsumed into C_m as well. The equivalent circuit element of a membrane channel in its simplest form constitutes an electrical conductor with resistance R_p, which is in parallel to the membrane capacitance. This parallel combination of resistance and capacitance may also be used to describe solid state nanopores. Here C_m accounts for the dielectric properties of the solid-state membrane and the chip support, whereas R_p characterizes the resistance of the solid-state pore. In both cases, a second resistor R_s in series accounts for the resistance of wirings, electrodes and electrolyte compartments. Potential stray capacitances of the measurement cell or wirings are described by C_w. The model also includes a simplified circuit schematic of the voltage clamp amplifier. C_i is the capacitance of the input FET of the amplifier, whereas R_f and C_f are the resistance and capacitance of the feedback element, respectively.

2.5.2 Noise Sources

The noise level in a current recording is usually determined by a combination of several individual noise sources. If these sources are uncorrelated, their rms contributions add up in quadratic fashion [53]. Therefore, the largest individual noise contribution will dominate the overall current noise. In order to identify individual noise sources, we consider the current noise power spectral density (PSD) $\bar{S}^2$. It describes the noise

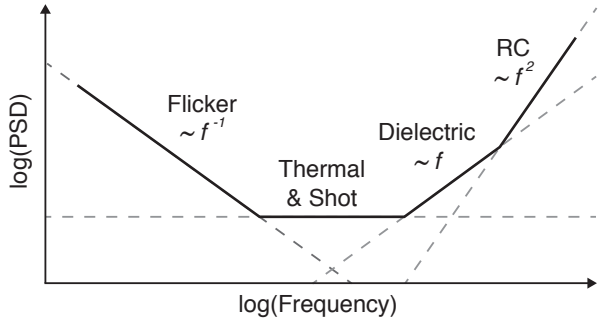

Figure 2.8: Noise Sources. Schematic power spectral density of an ion channel or nanopore recording. Individual noise sources and their frequency dependence are indicated.

power as a function of frequency and is obtained from current traces via a Fast-Fourier transform. Uncorrelated noise sources contribute linearly to the spectrum and often can be distinguished by their frequency dependence. In Figure 2.8, a schematic illustration of the relevant noise sources and their frequency dependence is given. In the following, we will discuss the individual contributions in detail.

Thermal Noise Thermal noise (often also Johnson- or Nyquist-noise) is created by the thermally induced movement of charge carriers such as electrons or ions [61]. The voltage noise spectral density e_{Th}^2 of an electrical conductor with resistance R is given by

$$e_{Th}^2 = 4k_bTR \tag{2.1}$$

It is proportional to the resistance and independent of the applied potential. Eq. 2.1 can also be used to calculate the thermal noise spectral density of electrical circuits containing more elements than a single resistor. In this case, R is replaced by the real part of the circuit impedance. To obtain an expression for the current noise spectral density $\bar{S}_{Th}^2$, the voltage spectral density is divided by the squared transfer impedance Z from the terminals of the circuit element in which the noise is generated to the output of the circuit [62]:

$$\bar{S}_{Th}^2 = \frac{e_{Th}^2}{|Z|^2} \tag{2.2}$$

For a single resistor with resistance R, this yields:

$$\bar{S}_{Th}^2 = \frac{4k_bT}{R} \tag{2.3}$$

The thermal noise contribution of a single resistive element is considered white noise, as it does not scale with frequency. The same is true for a resistor in parallel to a capacitor, as in the equivalent circuit of a membrane channel or a solid-state nanopore described above (see Figure 2.7). Eq. 2.3 serves well to describe the thermal noise inside an ion channel or a nanopore. It represents the theoretical noise limit for such current recordings. The amplifier exhibits thermal noise as well. However, due to a more complex transfer impedance, it exhibits frequency dependency (see considerations below).

RC Noise RC noise is the thermal noise generated by a resistor in series with a capacitor. For the transfer impedance of such a series connection, Eq. 2.2 becomes frequency dependent:

$$\bar{S}_{RC}^2 = 4k_bT \cdot \frac{(2\pi f)^2 C^2}{1 + (2\pi f)^2 C^2 R_s^2} \tag{2.4}$$

Here, R_s is the resistance in series to the capacitance C. Initially, $\bar{S}_{RC}^2$ scales quadratically with frequency. A first-order Taylor expansion yields:

$$\bar{S}_{RC}^2 \approx 4k_bTR_s \cdot (2\pi f)^2 C^2 \tag{2.5}$$

At high frequencies, the RC-circuit acts as a low pass filter and $\bar{S}_{RC}^2$ saturates:

$$\lim_{f\to\infty} \bar{S}_{RC}^2(f) = \frac{4k_bT}{R_s} \tag{2.6}$$

In most cases, just the initial increase $\propto f^2$ is observed in the PSD distribution, which is dominant at high frequencies (cf. Figure 2.8). The saturation level typically isn't observed due to bandwidth limitations of the amplifier [55]. In bilayer or solid-state nanopore recordings, RC noise may be caused by the combined resistance R_s of the electrodes and electrolyte compartments in conjunction with the membrane capacitance C_m. This contribution becomes important if the measurement cell has a high series resistance R_s, e.g. at low salt concentrations, if microfluidics or micropipettes are used to interface with the membrane, or if Ag/AgCl microelectrodes with a small electrode surface are used [42]. Another source of RC noise is the thermal voltage noise e_a of the amplifier in conjunction with the combined capacitance of the measurement setup (i.e. membrane capacitance C_m, wiring capacitance C_w, feedback capacitance C_f and amplifier input capacitance C_i, see Figure 2.7). As it scales with $\sim C^2$, RC noise can be minimized most effectively by reducing parasitic capacitances. For lipid bilayer experiments this can be achieved by reducing the membrane size and choosing a low dielectric constant support material such as PTFE [54]. To lower C_m in solid state nanopore experiments, dielectric passivation layers such as PDMS or SiO_2 may be applied [55, 63]. The capacitance contributions of the amplifier can be reduced by switching to integrated designs [55].

Dielectric Noise Dielectric noise is the thermal noise generated by the loss conductance of a non-ideal dielectric. Its current spectral density can be obtained by extending the admittance of an ideal capacitor $Y_C = i \cdot 2\pi fC$ with a real part $Y_D = 2\pi fCD$ [53]. Here, D is the dielectric loss of the dielectric. The impedance of a lossy capacitor is then

$$Z_{CD} = \frac{1}{Y_C + Y_D} = \frac{D - i}{2\pi fC(1 + D^2)} \tag{2.7}$$

By inserting its real part and absolute value into Eq. 2.1 and Eq. 2.2, respectively, we obtain an expression for the dielectric noise spectral density:

$$\bar{S}_D^2 = 8\pi k_bTDCf \tag{2.8}$$

Dielectric noise shows a linear frequency dependence and is important from intermediate to high frequency ranges (cf. Figure 2.8). In lipid bilayer recordings, dielectric noise is attributed to the lipid membrane and support capacitance C_m, whereas the major loss contribution is attributed to the support [54]. In solid-state nanopore devices as used in this work (see Chapter 5), dielectric noise arises from the capacitance and dielectric loss of the silicon nitride membrane and the electrochemical double layer forming at its interface to the electrolyte solution [51]. Although stoichiometric silicon nitride can have excellent loss properties with loss factors as low as $\sim 10^{-5}$, considerably higher losses may occur in the Si-rich low-stress silicon nitride membranes used for nanopore fabrication [55]. In fact, values up to 0.27 have been reported for silicon nitride based solid state nanopores [51]. As for RC noise, dielectric noise can be minimized by reduction of the membrane capacitance. Therefore, the corresponding considerations apply here as well. Passivation layers like PDMS or SiO_2 are particularly effective to minimize dielectric noise in solid state pores, as they reduce the dielectric loss of the silicon nitride membrane as well [63]. However, recent findings suggest that RC noise may easily be interpreted falsely as dielectric noise due to poor fits to the bandwidth-limited spectra [55].

Flicker Noise Flicker noise is characterized by its inverse frequency dependence. Therefore, its influence is largest in the low frequency regime (cf. Figure 2.8). In contrast to the noise contributions described above, the physical origin of flicker noise is not fully understood. In biological membrane channels, it is attributed to conductance fluctuations due to the conformational dynamics of the channel protein subunits [64]. Furthermore, flicker noise is observed in the presence of molecules interacting with the channel and can be used to characterize these interactions [65]. Despite the fact that solid state nanopores usually do not contain any "moving parts", they often exhibit flicker noise, whose strength varies from device to device [51]. Its power spectral density is described well by Hooge's phenomenological expression [66]:

$$\bar{S}_F^2 = \frac{AI^2}{f} \tag{2.9}$$

Here I is the ionic current and A is a proportionality constant characterizing the noise power. It was found to depend on the membrane material [67] and can be reduced by chemical treatment of pores, e.g. with piranha solution [63]. Therefore, surface charge fluctuations [67] or hydrophobic patches on the pore surface [68] have been suggested as possible origins of flicker noise. However, the origin of flicker noise in solid state pores is controversial and a consistent model is missing [69].

Other Noise Sources The noise sources described above are the most relevant ones in lipid bilayer and solid state nanopore recordings. Some additional noise sources have minor influence or are important in specific systems only. These include surface charge fluctuations inside some ion channels [70] or the shot noise contribution of the amplifier input FET [56]. Furthermore, AC signal pickup by ground loops or due to

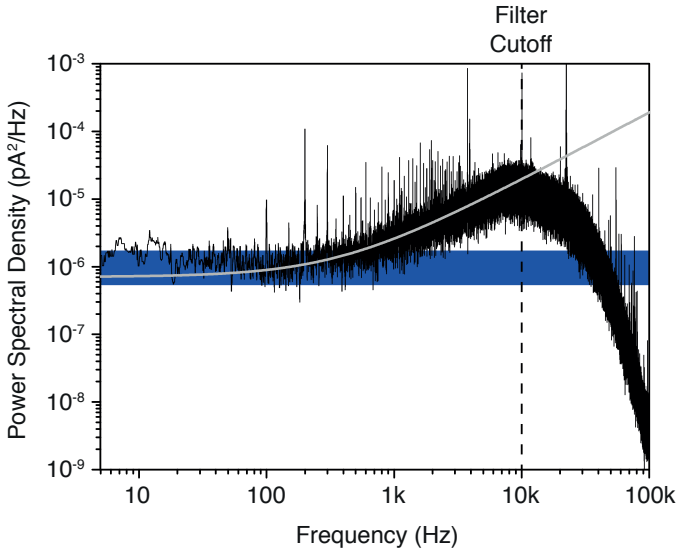

Figure 2.9: Power Spectral Density of the MECA system. Acquired at 10 kHz and 100 mV bias on a microcavity sealed with a lipid bilayer. The expected thermal noise spectral density of the seal resistance is indicated in blue. Gray line indicates a fit to Eq. 2.3 + Eq. 2.8.

improper shielding manifests itself by distinctive peaks in the noise PSD distribution. The latter contribution is usually small if proper shielding is applied and ground loops are avoided.

2.5.3 Noise Analysis

After elucidating the characteristics of individual noise sources, we now evaluate the noise performance of the experimental setups used in this work. Therefore, we analyze the power spectral density and identify individual noise contributions.

16 Channel MECA Setup In Figure 2.9, the power spectral density of a single microcavity is shown. It was obtained with the EPC 9 single channel amplifier at a bias voltage of 100 mV and a bessel filter setting of 10 kHz after forming bilayers from DPhPC lipids on top of all cavities. As electrolyte, 1 M KCl solution buffered at pH 8 was used. We observed a rms noise of 4 pA for the corresponding current trace. Due to the Bessel filter, the frequency components above the cutoff frequency (here 10 kHz) are damped, which manifests itself in a strong decrease of the spectral density. As we did not incorporate a membrane channel, we investigate the noise contributions of the lipid membrane and the measurement electronics only. A typical bilayer seal resistance of 10 - 40 GΩ was found for the MECA system [42]. The low frequency part of the spectral density matches with the predicted thermal noise arising from this resistance. At higher frequencies, we observe a linear increase of the PSD with frequency, which is an indication for dielectric noise. Fitting the spectral density with the sum of Eq. 2.3 and Eq. 2.8, we obtain a value of $1.85 \cdot 10^{-2}$ pF for the product of capacitance and dielectric loss CD.

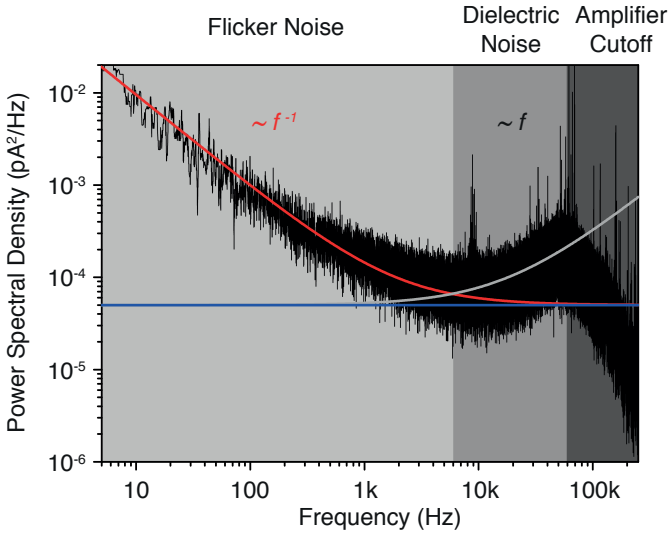

Figure 2.10: Power Spectral Density of a Solid State Nanopore Current Recording. Acquired at 100 kHz and a bias of 400 mV. Blue line indicates the thermal noise contribution corresponding to the pore resistance. Red line and gray lines represent fits to Eq. 2.9 and Eq. 2.8, respectively. The thermal noise contribution of the pore is accounted by an additional constant. Background shading indicates regions with different noise contributions dominating the spectrum.

Due to the small membrane dimensions of the MECA system, its capacitance contribution is small. In fact, 0.9 pF were measured for this configuration, which includes the capacitance of the gold strip line connecting the cavity [42]. However, the relay board used for acquisition (cf. Section 2.3.2) adds a more significant amount of capacitance. It incorporates a total of 32 reed relais (HI05-1A66, Meder Electronics, Germany), each contributing 0.2 pF in open state. During acquisition from a microcavity with the single channel amplifier, a single relay is in the closed state, while 31 relays in parallel to the first one are open. Therefore, we estimate the total capacitance contribution of the relays board to ~ 6 pF. Neglecting other capacitance contributions, we obtain a dielectric loss factor of $3.1 \cdot 10^{-3}$ from the fit to the PSD. This value matches well with typical dissipation factors of glass materials used for the fabrication of reed relays [71]. Therefore, we infer that dielectric noise caused by the combined capacitance of the relay board is the dominant noise source at high frequencies. Furthermore, we observe spikes in the PSD across a frequency range of 100 Hz to 100 kHz. This indicates AC signal pickup due to ground loops or insufficient shielding that is a result of the complex wiring scheme of the dual amplifier relay board system.

We conclude that the noise performance of the MECA setup is limited by the use of the relay board to switch between individual channels. In fact, for a single channel recording with the amplifier directly connected to a single microwell, noise levels below 250 fA at 10 kHz bandwidth were measured [42]. This limitation may be overcome by combining the MECA system with a high quality multichannel amplifier, ideally with an integrated design [55, 72].

Solid State Nanopore Setup In Figure 2.10, the noise PSD of a solid state nanopore recording is shown. It was obtained with the Axopatch 200B amplifier (Molecular Devices, USA) at a bias of 400 mV and a filter setting of 100 kHz. The nanopore was fabricated by the TEM drilling method (see Section 5.1.1) and has a diameter of 2.8 nm. It features a SiO_2 passivation layer and was pretreated with piranha acid prior to assembly into the vertical measurement cell using 0.4 M KCl electrolyte buffered at pH 8. The pore showed a rms noise of 33 pA and a resistance of 328 MΩ. The latter corresponds to a thermal noise spectral density of $5.0 \cdot 10^{-5}$ pA^2/Hz (see blue line in Figure 2.10).

In the low frequency regime, flicker noise dominates the spectral density. From a fit to Eq. 2.9, we obtain a flicker noise power A of $6.4 \cdot 10^{-8}$. This value is comparable to the lower limit for A observed in previous studies [51]. At higher frequencies we observe a linear increase in the spectral density, which is attributed to dielectric noise. From a fit to Eq. 2.8, we obtain a value of $2.7 \cdot 10^{-2}$ pF for the product of dielectric loss and capacitance. With a membrane capacitance of ~ 30 pF, this yields a dielectric loss factor D of $9 \cdot 10^{-4}$, which is reasonable for a high quality silicon nitride membrane with SiO_2 coating [55]. At frequencies above ≈ 60 kHz, we observe a decrease in the spectral density due to the limited frequency response of the amplifier. The spikes observed in the noise PSD at high frequencies arise from AC pickup, which is in part caused by the amplifier's switching power supply [73].

We conclude that for the present nanopore recording setup, flicker noise is the dominant noise source, followed by dielectric noise at higher frequencies. Although there is no known measure to further reduce the flicker noise contribution, dielectric noise may be further reduced by minimizing the uncoated membrane surface when applying the silicone elastomer passivation (cf. Section 2.4). For devices with lower capacitance due to better passivation, RC noise often dominates the PSD spectrum in the high frequency range [55].

2.6 Conclusion

In this chapter, we covered the materials and methods used for the current recordings of single channels and pores presented in this work. We chose patch clamp recordings as an example to describe the fundamental instrumentation for high bandwidth recordings of ionic currents in the pA range. After a brief introduction of planar lipid bilayer recordings, we described an integrated and highly automatized MECA setup that enables recordings of 16 individual lipid bilayers in parallel. Moreover, we illustrated the measurement setups used for solid state nanopore recordings. Finally, we elucidated the basics of noise analysis in ionic current recordings and characterized the measurement setups according to their noise performance. For the MECA planar lipid bilayer setup, we identified the relay board as the major source of noise, whereas for the solid-state nanopore system, flicker noise was dominant.

3 Nanopores as Single Molecule Sensors

Inspired by the rich functionality of membrane channels in biological systems, several biotechnological applications based on membrane channels or pores were investigated in the past decades, including applications for cancer treatment [74] and neuronal silencing [75]. An *in vitro* application of membrane channels receiving great attention is single molecule sensing. In 1996, Kasianowicz et al. demonstrated that α-hemolysin porins reconstituted into planar lipid bilayers can be used to detect single-stranded DNA or RNA molecules by monitoring changes in the transmembrane current [4]. It was a follow-up to this publication which termed the word nanopore analysis or nanopore sensing [76]. Since then, many different molecules such as DNA, RNA, proteins, peptides or small molecules were subject of such investigations using protein pores such as α-hemolysin or MspA and solid state nanopores [77]. As a matter of fact, an entire field of research emerged from these efforts, generating as many as 750 publications a year[1] by now. This may be explained by the benefits of nanopore sensing compared to other single molecule techniques such as low detection limits in the femtomolar range [78], no requirement for labeling of analyte molecules and high temporal resolution due to the electrical detection concept [55]. An important stimulus for development of the field were the prospects of nanopore-based sequencing [52], as marked by the NHGRI 1000 $ genome project of 2004. However, nanopore sensing is not limited to detection or sizing of molecules. In fact, nanopores may also be used to study molecular interactions [8], intramolecular dynamics [79] or the physics of molecular transport [80]. In this chapter, we will introduce the principles of nanopore based sensing, which are fundamental for the experiments discussed later in this work. We specifically cover feedback-controlled sensing approaches and nanopore force spectroscopy (NFS).

3.1 Resistive Sensing

Most nanopore sensing approaches rely on an electrical detection concept commonly referred to as resistive-pulse sensing [81]. Using a setup as described in Chapter 2, in which a nanopore provides the only connection between two electrolyte compartments, ionic current is driven across the pore and recorded, simultaneously. When an analyte molecule of appropriate size traverses the pore, a fraction of its volume becomes

[1] ISI Web of Science publication count for the topic "nanopore" in the year 2017

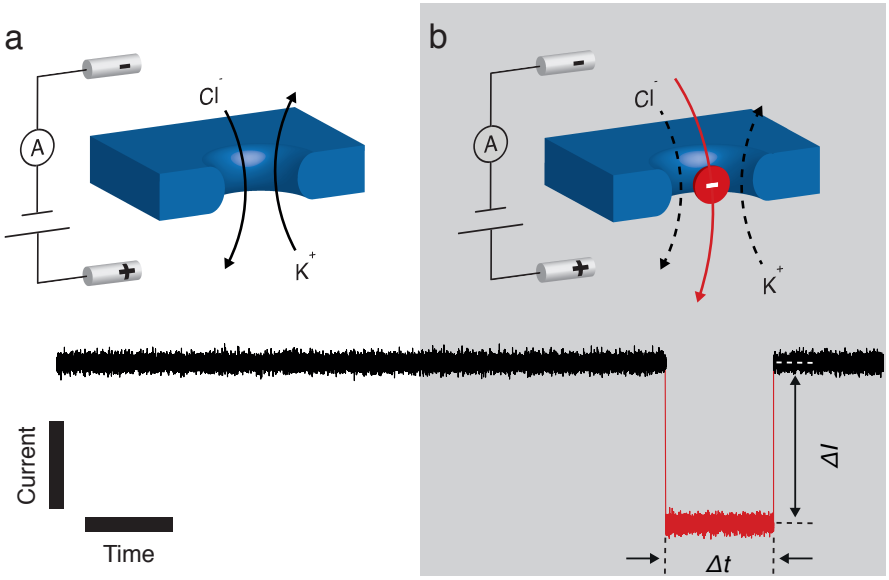

Figure 3.1: Resistive Sensing. a) An electric bias is applied across a nanoscale aperture. The corresponding ionic current is recorded. b) Upon passage of an analyte molecule, a fraction of the pore volume is blocked for ions, which leads to a transient reduction of the ionic current. Amplitude and duration of this resistive pulse characterize the molecule and its transport properties.

temporarily inaccessible for ions, which manifests itself in a transient reduction of the ionic current (see Figure 3.1), a resistive pulse. Its amplitude ΔI and duration Δt are both characteristic for the traversing molecule. As ΔI scales with the volume the molecule occupies inside the pore, it can be used to distinguish individual bases of a DNA molecule [82] or proteins of different molecular mass [83]. However, for highly charged analytes such as DNA, the volume exclusion effect described above is accompanied by a conductance increase effect, caused by the strip-off of counterions upon translocation [84]. While this effect is negligible at high ionic strength, it can dominate the experiment at low ionic strength conditions and can lead to the observation of transient conductance enhancements upon analyte translocation. At intermediate ionic strength, i.e. at the crossover between both regimes, it may outbalance the volume exclusion effect and render analyte detection impossible. In the following, we will discuss a simple model for the blockade amplitude in order to illustrate demands on the nanopore design for a high sensing performance. In doing so, we limit our discussion to the high ionic strength regime, where the volume exclusion effect clearly dominates. The interpretation of the blockade duration Δt will be covered separately in Section 3.2.

Modeling the Blockade Amplitude. For high ionic strength, Ohm's law limits the current flow across the pore [85] and surface contributions to the conductance may be neglected [84]. Assuming a cylindrical pore geometry, the pore resistance is given by [85]:

$$R_p(\rho, d, h) = R_c + R_a = \frac{4\rho}{\pi d^2}\left(h + \frac{\pi d}{4}\right) \tag{3.1}$$

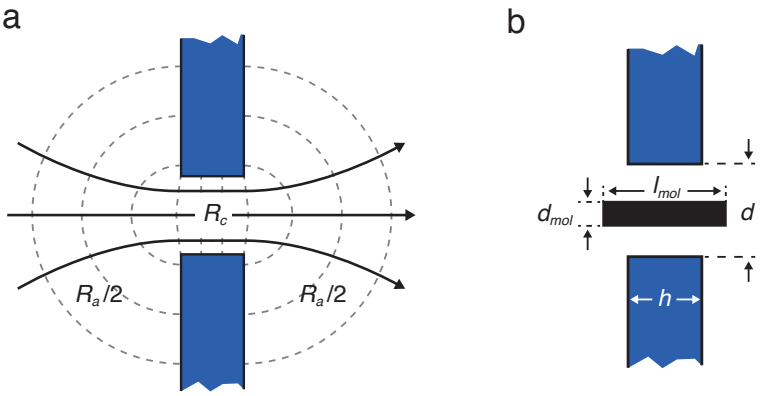

Figure 3.2: Modeling the Blockade Amplitude. a) Contribution of access resistance R_a and channel resistance R_c to the total pore resistance R_p. Field lines and equipotential regions are indicated. b) Schematic for the current blockade model. Pore and analyte molecule are approximated as cylinders. Dimensions are indicated.

Here, R_c is the resistance of the channel itself and R_a is the pore's access resistance, which is obtained by integrating the electrolyte resistance from infinity to the disc-like pore mouth (see Figure 3.2a) [85]. ρ, d and h represent the specific resistance of the electrolyte solution, the pore diameter and pore length, respectively. The access resistance contribution to the open pore resistance corresponds to an effective increase in pore length by $\pi d/4$. Therefore, it is particularly important for short pores, where the pore length is comparable to its diameter. As DNA is the primary analyte in the resistive sensing experiments described in this work, we assume a cylindrical analyte shape with a diameter d_{mol} and a length $l_{mol} > h$ for our calculations (see Figure 3.2b). For spherical analyte molecules such as proteins, a similar calculation may be pursued [86]. To describe the pore resistance in its blocked state R_b, we replace the pore diameter d in Eq. 3.1 by an effective diameter $d_{eff} = \sqrt{d^2 - d_{mol}^2}$ of the occupied pore [78]. The blockade amplitude ΔI then is given by:

$$\Delta I = V \left(\frac{1}{R_p(\rho, d, h)} - \frac{1}{R_p(\rho, d_{eff}, h)} \right) \tag{3.2}$$

Here, V is the applied membrane voltage. Using 3.1 and Eq. 3.2, open pore current and blockade amplitude can be calculated as functions of electrolyte conductivity and pore dimensions. This model may also be used to characterize solid state nanopores electrically. As most solid state pores clearly deviate from a cylindrical shape, an effective pore length h_{eff} is determined from the current blockade ΔI, corresponding to the length of a cylindrical pore with equivalent sensing properties [78, 87].

Pore Design Considerations for Resistive Sensing Performance. From the blockade model described in the previous section, we may infer nanopore design criteria for high current signals in specific sensing applications. To obtain a measure for the blockade amplitude which is independent of the membrane potential, we consider the amplitude of the conductance change $\Delta G = \Delta I/V$. In Figure 3.3, the absolute and

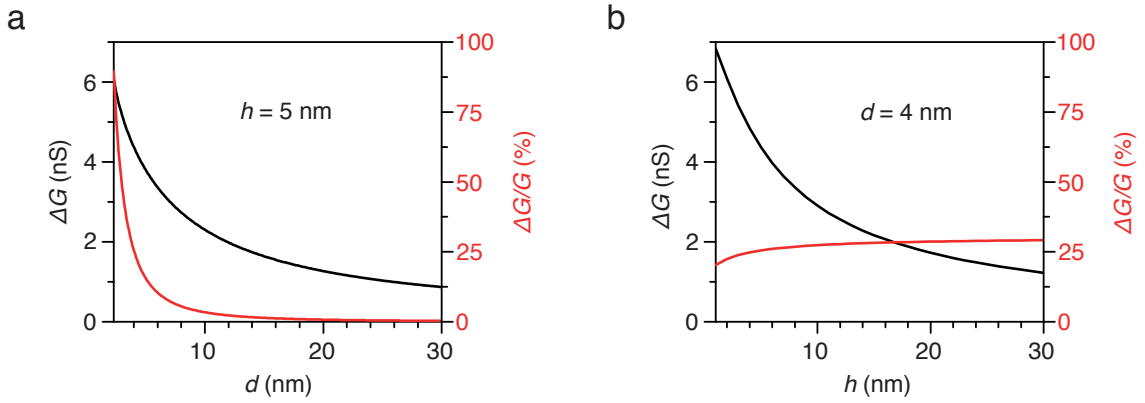

Figure 3.3: Impact of Pore Design on dsDNA Detection. Absolute and relative conductance blockade amplitude ΔG and $\Delta G/G$ as a function of a) pore diameter d and b) pore length h. Curves were calculated from Eq. 3.1 and Eq. 3.2, using a dsDNA diameter $d_{mol} = 2.2\,\text{nm}$ and a specific electrolyte resistance of $\rho = 9\,\Omega\text{cm}$ (for 1 M KCl solution at 23° C).

relative conductance change ΔG and $\Delta G/G$ upon translocation of double stranded DNA are shown as a function of pore diameter d. We observe that ΔG increases for smaller pore diameters. Although this relation is somewhat intuitive, it actually is a consequence of considering the access resistance in Eq. 3.1. Neglecting it would render ΔG independent of the pore diameter. Reducing d therefore is most effective for short pores, where the access resistance becomes important. For the relative conductance change, the situation is slightly different: Even when neglecting the access resistance, a decrease in pore diameter causes an increase of $\Delta G/G$, as the open pore conductance G is decreased. The sensing performance of a pore therefore is best, if its diameter is just slightly larger than the analyte molecule. However, in some cases a tradeoff is necessary, as analyte interactions with the pore walls may increase drastically if the pore diameter gets close to the analyte size [88, 89]. In Figure 3.3b, the influence of the pore length h on the conductance change is shown. As in the previous case, we observe an increase of ΔG for decreasing length. It is caused by the increase in pore conductance, which increases the ion density inside the occluded pore volume as well. Neglecting the access resistance, ΔG and G would increase equally, leading to a constant $\Delta G/G$. However, by accounting for R_a, we observe a slight decrease in $\Delta G/G$ for decreasing pore length. Although the absolute conductance change suggests a better sensing performance for shorter pores, it should be noted that the measurement noise may increase with the pore conductance, as it is the case for thermal noise ($I_{rms} \propto \sqrt{G}$) and flicker noise ($I_{rms} \propto G$) (cf. Section 2.5). Hence, a tradeoff might be necessary for pores with a strong flicker noise contribution. Short pores are also desirable if molecular substructures shall be detected, e.g. individual nucleotides in nanopore-based sequencing approaches [52].

An example for a well-suited pore geometry for sensing is given by the MspA porin [90]. It features a $\sim 1\,\text{nm}$ long constriction zone with a diameter of 1.3 nm, which is just wide enough for single stranded DNA. A mutated variant with eliminated charge in the constriction region is used for nanopore-based sequencing applications [6, 33].

3.2 Molecular Transport Across Nanopores

In this chapter, we discuss the transport of analyte molecules in nanopore sensing experiments. Following a brief review of transport mechanisms, we discuss the physics of polymer capture and elucidate a theoretical framework to interpret translocation time distributions.

3.2.1 Transport Mechanisms

As for analyte detection, analyte transport across the pore often is accomplished electrically, allowing active control of the transport process, i.e. the translocation rate, speed and direction. This is possible, as many molecules and solids become charged in contact with aqueous solution, e.g. by ionization of surface groups, rendering them susceptible to electric fields [91]. This includes biopolymers such as DNA, RNA, proteins or peptides, as well as solids such as silicon nitride or silicon dioxide. Their surface charge in solution may be positive or negative, depending on the ratio of basic and acid groups and on solution pH. To maintain overall charge neutrality, the surface charge is screened by a layer of more or less mobile counterions, the electrical double layer (EDL). In this chapter, we describe the response of charged analyte molecules and their counterions to electric fields and the influence of diffusion on analyte transport. Along the way, we will point out the specifics of transport across channels compared to bulk transport. We limit ourselves to passive transport, skipping enzyme-controlled translocation as used for DNA sequencing approaches [92–94].

Electrophoresis. In the presence of an electric field, charged molecules in solution are subject to electrophoretic migration [95]. As the electric field acts on the molecular charges as well as on the mobile fraction of counterions surrounding it, the resulting electrophoretic force $\vec{F}_{ep}$ is a combination of electrostatic forces $\vec{F}_{el}$ acting on the molecule and drag forces $\vec{F}_{drag}$ due to electrophoretic movement of counterions in the opposite direction. While the molecule is in motion, these forces are outbalanced by Stokes drag $\vec{F}_{Stokes}$

$$\underbrace{\vec{F}_{el} - \vec{F}_{drag}}_{\vec{F}_{ep}} - \vec{F}_{Stokes} = 0 \tag{3.3}$$

and the molecule moves with an electrophoretic drift velocity that scales with the electric field $\vec{E}$:

$$\vec{v}_{ep} = \mu_{ep}\vec{E} \tag{3.4}$$

The proportionality constant μ_{ep} is defined as the electrophoretic mobility of the molecule. In contrast to free solution electrophoresis, the electrophoretic force inside a nanopore may depend on the pore geometry due to hydrodynamic coupling of the counterion movement to the pore walls [96].

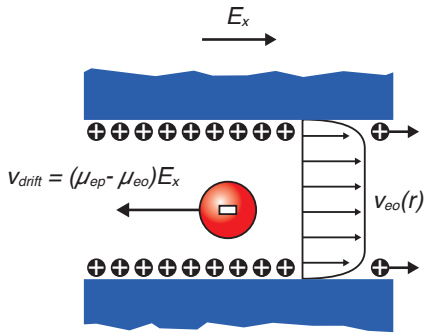

Figure 3.4: Molecular Transport Under the Influence of Electrophoretic and Electroosmotic Forces. Electrophoretic migration of the electric double layer at the pore surface causes hydrodynamic flow across a nanopore (electroosmosis). Apart from electrophoretic force and Stokes drag, the analyte molecule (red) is subject to an additional drag force due to the electroosmotic flow. It may coact or counteract the electrophoretic transport, depending on the nanopore surface charge.

Electroosmosis. Another contribution to drift is given for pores with charged sidewalls [97]. If a voltage is applied across the pore, the mobile fraction of counterions in the electrical double layer at the pore surface is subject to electrophoretic motion. Due to viscous interaction, the counterions drag along the fluid and cause a net flow across the pore. If the electrical double layer's extension (i.e. the Debye length) is small compared to the pore diameter, this electroosmotic flow (EOF) features a plug-like velocity profile (see Figure 3.4) with a velocity

$$v_{eo} = \mu_{eo} E_x \tag{3.5}$$

Here E_x is the field component in direction of the pore axis and μ_{eo} is the electroosmotic mobility. The latter is a function of the pore surface charge and may be obtained by streaming potential measurements [98].

The net velocity of an analyte molecule which is subject to both electrophoretic and electroosmotic forces then can be written as:

$$v_{drift} = (\mu_{ep} - \mu_{eo}) E_x \tag{3.6}$$

The electroosmotic mobility μ_{eo} may be positive or negative, depending on the polarity of the surface charge. Therefore, electroosmosis may coact or counteract electrophoretic analyte transport if pore surface and analyte have opposite or equal polarity, respectively. In the latter case, the electroosmotic contribution may outbalance the electrophoretic one, causing a situation where transport is governed by diffusion only. Electroosmosis has been shown to strongly influence protein translocation experiments in solid state pores [98]. By varying both surface charge and protein charge with variation of the solution pH, regimes of transport dominated by electrophoresis, electroosmosis or diffusion were observed for the translocation of avidin through silicon nitride pores. In contrast to proteins, DNA is highly negatively charged across a wide pH range due to its phosphate backbone [99]. Therefore, electrophoretic transport is the dominant mechanism for DNA translocation experiments [100]. Nevertheless,

electroosmotic flow in negatively charged solid state pores was shown to reduce the net force acting on a DNA molecule stalled inside the pore and therefore reducing the expected net translocation speed [101]. This effect was also predicted by molecular dynamics simulations [102]. For the α-hemolysin porin, electroosmotic flow was found to enhance the capture of small molecules [103], while its influence on polymer translocation was found to be insignificant [104].

Diffusion. Macromolecules such as DNA or proteins in solution undergo random motion due to collisions with thermally agitated solvent molecules. For an ensemble of macromolecules, the molecular flux $\vec{J}$ is given by Fick's first law of diffusion:

$$\vec{J} = -D\vec{\nabla}c \tag{3.7}$$

Here, D is the diffusion coefficient of the macromolecule and c is its number concentration. Diffusive flux may be utilized to transport uncharged analytes across nanopores such as polyethylene glycol [105]. If the analyte transport is governed by drift due to electrophoresis or electroosmosis, the concurrent diffusive motion causes deviations from a straight pathway, leading to a biased random walk and a scatter in the observed transport times (see Section 3.2.3).

Other Mechanisms Apart from the aforementioned transport mechanisms, other electrokinetic mechanisms such as dielectrophoresis [106] or electrothermal effects [107] may affect analyte transport in nanopore experiments. Furthermore, interactions with the pore walls may slow down transport [89]. Here, we only consider the mechanisms discussed above, which are sufficient to describe the experimental phenomenology of this work.

3.2.2 Analyte Capture

An important aspect of analyte transport across nanopores is the delivery of analyte molecules to the pore entrance, which determines the event rate in resistive sensing experiments. Here, we give a basic analytical description of the capture process, where we discuss the contributions of diffusion, drift and entropic effects (see Figure 3.5). Our discussion follows previous studies on the capture process of polymers [108–110]. We consider the flux of molecules

$$\vec{J}(\vec{r},t) = -D\vec{\nabla}c(\vec{r},t) + c(\vec{r},t)\mu\vec{E} + c(\vec{r},t)\frac{D}{k_bT}\vec{\nabla}F(\vec{r}) \tag{3.8}$$

Here, D, μ and c represent the diffusion coefficient, electrophoretic mobility and number concentration of analyte molecules, respectively. The first term of Eq. 3.8 describes the diffusive part of the flux and is given by Fick's first law (Eq. 3.7). The second and third term describe the convective part of the flux, which is given by $\vec{J}(\vec{r},t) = c(\vec{r},t)v(\vec{r},t)$. Replacing v by the electrophoretic velocity $\vec{v}_{ep} = \mu_{ep}\vec{E}$, we account for the drift motion of analyte molecules in the electric field surrounding the

pore opening. The last term describes the convective contribution of an additional free energy barrier $F(\vec{r})$ for analyte capture. The electroosmotic contribution to the flux may be considered by adding one more term $c(\vec{r},t)v_{eo}$ to Eq. 3.8. However, as the electroosmotic velocity near the pore cannot be obtained as easily as inside a channel and as studies suggest a rather small electroosmotic contribution to the capture of DNA [111], we neglect it here. The total flux given by 3.8 must obey the continuity equation:

$$\frac{\partial c(\vec{r},t)}{\partial t} = -\vec{\nabla}\cdot\vec{J}(\vec{r},t) \tag{3.9}$$

The experimental event rate or capture rate is given by the flux in steady state, for which both sides of Eq. 3.9 equal 0. In the following, we consider the regimes of diffusive capture, capture by drift and barrier-dominated capture individually and obtain expressions for the dependence of the capture rate on experimental parameters in each case.

Diffusive Regime. For the diffusive regime, we neglect the second and third term in Eq. 3.8. If we consider spherical symmetry for the molecular flux from the bulk to the pore mouth, Eq. 3.9 yields

$$\frac{\partial c(r,t)}{\partial t} = D\frac{1}{r^2}\frac{\partial}{\partial r}\left[r^2\frac{\partial c(r,t)}{\partial r}\right]. \tag{3.10}$$

For the steady state case, this equation may be solved by integration and $c(r) = c_0(1-R/r)$ is obtained for the boundary conditions $c(R)=0$ and $c(r\to\infty)=c_0$. Here, c_0 is the bulk number concentration of molecules and R is the pore radius. The steady state flux through a half-sphere with radius R around the pore entrance is then given by

$$\bar{J}_{diffusion} = 2\pi DRc_0. \tag{3.11}$$

The flux (and therefore the capture rate) does not exhibit a dependence on membrane voltage. However, it scales linearly with the pore size, bulk concentration and diffusion coefficient of the analyte molecule. For long polymers, which adapt a coil-like conformation in solution, the diffusion coefficient scales with $D\sim N^{-\nu}$, where N is the chain length of the polymer and $\nu\simeq 0.6$ in the high ionic strength regime [112]. The capture rate in the diffusion-dominated regime therefore scales with the polymer length by $\bar{J}_{diffusion}\sim N^{-0.6}$.

Drift Regime. For the regime dominated by electrophoretic drift of the analyte molecule, we consider the second term in Eq. 3.8 only. Assuming again spherical symmetry, we may use Ohm's law to obtain an expression for the electric field outside the pore:

$$E(r) = \frac{\rho I}{2\pi r^2} \tag{3.12}$$

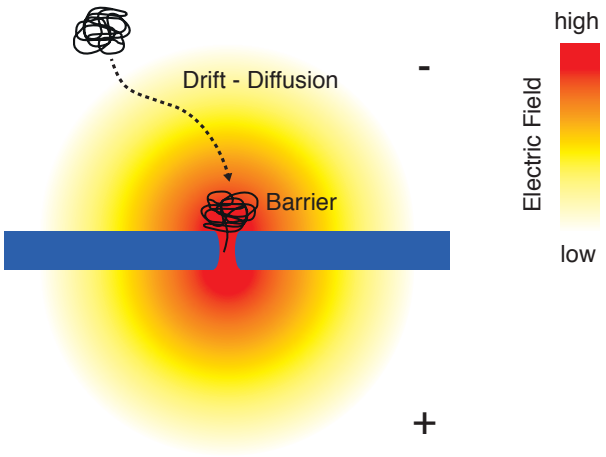

Figure 3.5: Electrophoretic Capture of DNA Molecules. The capture process can be divided into two stages. In the first stage, diffusion and electrophoretic drift govern the molecule's motion towards the pore entrance. As a consequence of the radial field distribution around the pore entrance, diffusive motion is dominant at large distances and drift increases the closer the molecule approaches the pore. This leads to a funneling effect, which directs molecules effectively to the pore mouth. The second stage involves overcoming of the free energy barrier associated with localizing a chain end at the pore entrance und reducing the molecule's conformational degrees of freedom upon threading.

Here, I is the current across the pore and ρ is the resistivity of the electrolyte solution. The continuity equation in spherical coordinates is then given by

$$\frac{\partial c(r,t)}{\partial t} = \frac{1}{r^2}\frac{\partial}{\partial r}\left[r^2 \mu \frac{\rho I}{2\pi r^2} c(r,t)\right]. \tag{3.13}$$

For the steady state, we obtain $c(r) = const. = c_0$. The steady state flux is then

$$\bar{J}_{drift} = c_0 \mu V_m \frac{\rho}{R_{pore}}, \tag{3.14}$$

where V_m is the membrane potential and R_{pore} is the pore resistance. To illustrate the influence of the pore geometry on the capture rate, we use the expression for the pore resistance obtained in Section 3.1 (Eq. 3.1), where we neglect the access resistance for simplicity. The capture rate then gets

$$\bar{J}_{drift} = c_0 \mu V_m \frac{R^2 \pi}{h}. \tag{3.15}$$

It follows a linear dependence on membrane voltage, as it is observed for protein translocations [83] and translocations of dsDNA through solid state pores in some cases [113]. Its quadratic scaling with pore size makes higher analyte concentrations and membrane voltages necessary to realize acceptable capture rates with very small pores. Remarkably, the capture rate in the drift regime does not depend on the chain length for long DNA molecules, which is due to their free-draining property ($\mu \sim N^0$) [95].

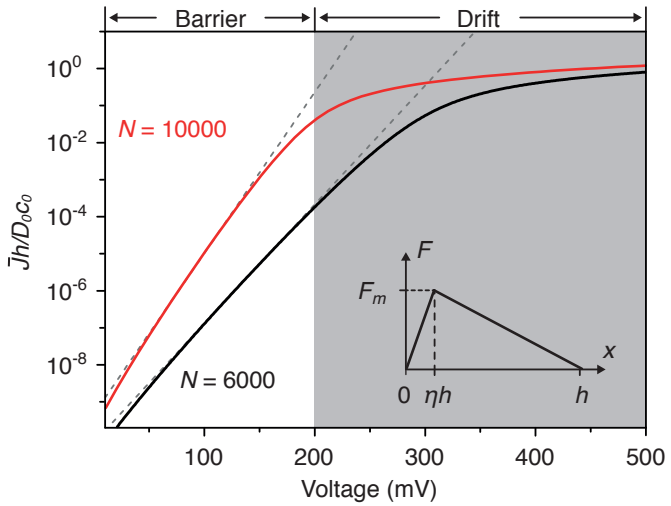

Figure 3.6: Entropic Barrier Regime. Normalized polymer capture rate as a function of applied voltage. Curves were calculated from Eq. 3.16 for a chain length of 10000 (red) and 6000 (black). Parameters $F_0 = 126\, k_bT$,$\eta = 0.1$ and $\mu/D_0 = 4{\cdot}10^{-3}$ were used. For $N = 10000$, this corresponds to a barrier height of $20\, k_bT$ and $\mu/D = 1$ (for $N = 6000$, the corresponding barrier height is $22\, k_bT$). Gray dashed lines indicate exponential scaling in the barrier-limited regime. Barrier and drift regimes are indicated for $N = 10000$. Inset: Free energy profile used for calculations.

Barrier Regime. Describing the capture rate in the barrier-dominated regime is more challenging than for the drift and diffusion regimes as all three terms in Eq. 3.8 have to be considered and knowledge of the free energy profile $F(x)$ describing the barrier is necessary. Muthukumar et al. discuss two major contributions to the barrier for polymer capture into nanopores [108]. The first contribution is the reduction in translational entropy due to localization of one end of the polymer chain at the pore entrance. For a sufficiently long polymer with a volume fraction > 0.1 that is jammed at the pore entrance due to the electric field, a dependence $F_l \sim N^{-\alpha}$ ($\alpha = 0.2 \pm 0.1$) of the localization barrier height F_l on the chain length was obtained from numerical calculations [114, 115]. The second contribution is the reduction of conformational degrees of freedom associated with threading a part of the polymer chain into the pore. Its impact on the free energy profile depends strongly on polymer properties and pore geometry. It can give rise to multiple barriers, as it is the case for DNA translocation through the α-hemolysin porin due to its trap-like vestibule [110].

By assuming that pore dimensions are sufficiently small compared to the radius of gyration of the polymer, this nucleation contribution to the barrier may be neglected. Using further simplifications such as a ramp-like model free energy profile, a homogeneous electric field distribution and an absorbing boundary at the opposite end of the pore ($c(L) = 0$), an analytical expression can be obtained for the one-dimensional case [108]:

$$\bar{J} = \frac{Dc_0}{h}\left[\frac{\eta\left(e^{\frac{F_m}{k_bT}-\frac{\eta}{D}|\mu V_m|}-1\right)}{\frac{F_m}{k_bT}-\frac{\eta}{D}\mid \mu V_m \mid} + \frac{(1-\eta)\left(e^{\frac{F_m}{k_bT}-\frac{\eta}{D}|\mu V_m|}-e^{-\frac{|\mu V_m|}{D}}\right)}{\frac{F_m}{k_bT}-(\eta-1)\frac{|\mu V_m|}{D}}\right] \tag{3.16}$$

Here, F_m is the maximum of the free energy profile at the position $x = \eta h$ (see inset of Figure 3.6). To account for the chain length dependence of the barrier height and the diffusion coefficient, we define $F_m = F_0 N^{-\alpha}$ and $D = D_0 N^{-\nu}$, respectively. Using Eq. 3.16, we illustrated the voltage dependence of the capture rate for two different chain lengths (see Figure 3.6). At low voltages, an approximately exponential increase with $\bar{J} \sim e^{VN^{\nu}\mu/D_0}$ is observed. As the barrier decreases with increasing chain length, the rate at a given voltage is higher for the longer polymer. At a voltage of $V_c \approx F_m D/(\mu\eta k_b T) = F_0 D_0/(\mu\eta k_b T N^{\nu+\alpha})$, a transition to the drift dominated regime occurs, which exhibits linear voltage scaling and no dependence on chain length. For the illustrated case, the transition takes place at $\approx 200\,\mathrm{mV}$ and $\approx 300\,\mathrm{mV}$ for $\mathrm{N} = 10000$ and $\mathrm{N} = 6000$, respectively. For sufficiently long polymers, Eq. 3.16 implies that the barrier regime disappears and only the drift regime is observed. Wanunu et al. observed this behavior experimentally in a 3.5 nm solid state pore [116]. While a transition from exponential to linear voltage scaling at $\approx 425\,\mathrm{mV}$ was observed for the translocation of 3.5 kbp DNA, only a linear regime could be observed for 48 kbp at voltages $> 225\,\mathrm{mV}$. The barrier height has strong implications on a system's sensing performance, limiting the capture rate and thereby the minimum measurement voltage. An example is given by the α-hemolysin porin, where the pore geometry gives rise to different energy barriers for capture from the *cis* or *trans* side, respectively [117].

3.2.3 Modeling Translocation Time Distributions

In contrast to a molecule's capture, which can be characterized only indirectly via the capture rate, its transport across the pore can be timed directly by measuring the duration of the observed resistive pulse. For an analytical description of experimentally obtained translocation time distributions, we consider the continuity equation (Eq. 3.9). In the limit of high dilution, the concentration $c(\vec{r}, t)$ can be identified with the probability $P(\vec{r}, t)$ of finding an analyte particle at the position $\vec{r}$ at time t [108]. Eq. 3.9 then represents the Fokker-Planck-Equation. Considering diffusive flux and drift along the pore axis (1D), we obtain

$$\frac{\partial P(x,t)}{\partial t} = D\frac{\partial^2 P(x,t)}{\partial x^2} - v\frac{\partial P(x,t)}{\partial x}, \tag{3.17}$$

where D is the diffusion coefficient and v is the drift velocity of the analyte particle. For a polymer molecule such as DNA, v corresponds to the drift velocity of the segment inside the pore and may contain electrophoretic as well as electroosmotic contributions. Hereby, we assume that internal relaxation of the DNA molecule is fast, i.e. each segment is in equilibrium during translocation [104]. If analyte capture is considered via the boundary condition $P(x, 0) = \delta(x)$ and escape into the trans compartment is described by $P(L, t) = 0$, Eq. 3.17 can be solved analytically. Here, L corresponds to the contour length for polymeric analytes and to the pore length h, otherwise. The corresponding probability density of dwell times is then [118]:

$$F(t) = \frac{L}{\sqrt{4\pi D t^3}} e^{-\frac{(L-vt)^2}{4Dt}} \tag{3.18}$$

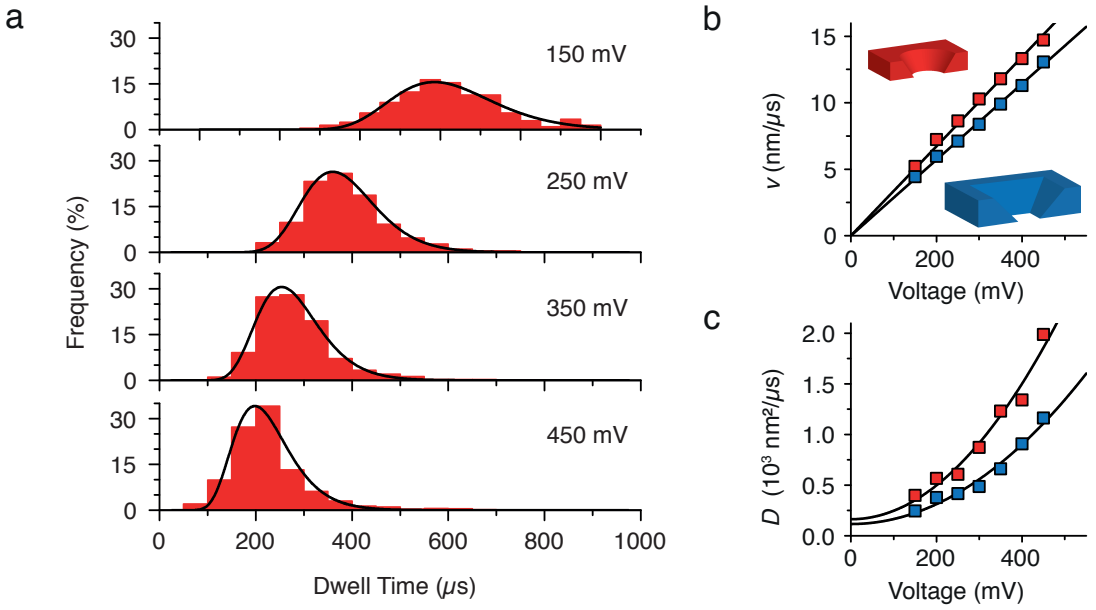

Figure 3.7: Modeling Translocation Time Distributions. a) Dwell time distributions for the translocation of 10 kbp DNA fragments through the 28 nm silicon nitride (SiN) pore of a PCP device (cf. Section 5.1.2) at different voltages. Black lines are fits to the drift-diffusion model described in the text (Eq. 3.18), using a contour length of 3.4 µm. The electrolyte buffer was 1 M KCl, 10 mM Tris and 1 mM EDTA at pH 8. b) Drift velocity obtained from fits to dwell time histograms as a function of bias voltage for translocation through the SiN pore (red) and the 23 x 23 nm silicon (Si) pore (blue) of the PCP device. Inset illustrates pore geometries. c) Diffusion coefficient obtained from fits to dwell time histograms as a function of bias voltage for the SiN pore (red) and Si pore (blue).

The distribution described by Eq. 3.18 features a mean $\langle t \rangle = L/v$ and a variance $\sigma^2 = 2D\langle t \rangle^3/L^2$. If diffusion is slow compared to drift, ie. $D \ll vL$ or $D \ll L^2/\langle t \rangle$, Eq. 3.18 is closely approximated by a Gaussian distribution with above characteristics.

In Figure 3.7a, dwell time distributions for the single-file (fully linearized) translocation of 10 kbp DNA through a 28 nm solid state pore are shown. The pore is part of a solid state nanodevice featuring two pores in series with a cavity in between (PCP device, cf. Chapter 5). The distributions show a single population, which shifts towards faster timescales for higher voltages. For all voltages, the dwell time populations are well-described by fits to Eq. 3.18. The obtained drift velocities and diffusion coefficients are shown as a function of voltage in Figure 3.7b and c, respectively. Here, also results for the second pore of the PCP device are shown, which has a quadratic-pyramidal geometry (see inset of Figure 3.7b) and a size of 23 nm x 23 nm. With values of several nm/µs, the drift velocities compare well to previous studies on similar-sized pores [118] and show a linear voltage dependence as expected for an electrophoretically driven translocation process. The quadratic pore shows slightly slower transport (29 nm µs^{-1} V^{-1} versus 34 nm µs^{-1} V^{-1}), which can be attributed to a lower potential drop across it (see Section 5.3.6). For the diffusion coefficient, quadratic voltage scaling is observed, which has been attributed to a Taylor dispersion effect caused by a inhomogeneous electroosmotic flow profile [118]. The extrapolated diffusion coefficients at

zero voltage of $1.2 \cdot 10^2\,\mathrm{nm}^2/\mu\mathrm{s}$ and $1.6 \cdot 10^2\,\mathrm{nm}^2/\mu\mathrm{s}$ compare reasonably well to a diffusion coefficient of $0.7 \cdot 10^2\,\mathrm{nm}^2/\mu\mathrm{s}$ for a cylindrical rod with a length h of half of the pore length and diameter $d_{DNA} = 2.2\,\mathrm{nm}$, obtained from the Stokes-Einstein relation $D_0 = k_b T/\zeta$ with a drag coefficient $\zeta = 2\pi\eta h/ln(h/d_{DNA})$, as suggested by Ling et al. [118].

So far, Eq. 3.18 has been used to describe transport for a wide range of pore sizes for proteins as well as for unstructured DNA [83, 89, 118]. For DNA translocation in smaller solid state pores with diameters below $\approx 3\,\mathrm{nm}$, diffusion coefficients are obtained, which are significantly smaller than expected from simple calculations and do not exhibit a significant voltage dependence [89]. This is attributed to confinement effects and DNA-pore interactions, which become important for pore diameters close to the dimensions of the DNA strand. The formalism discussed here does not account for time-dependent drift velocities, which can arise from barrier effects or drag forces caused by the remaining DNA coil during translocation [119]. Such influences are subsumed into an effective drift velocity for the whole translocation process.

3.3 Active Voltage Control

Measurement voltage is an important control parameter in resistive sensing experiments, by which analyte transport speed and capture rate can be adjusted. However, often a tradeoff between a high capture rate and low transport speed is necessary, which narrows down the effective voltage range for translocation experiments. This limitation may be overcome by active control of the transmembrane voltage during the measurement, which is triggered by changes in the transmembrane current. Such active control setups have been realized previously, allowing for rapid reduction of the transmembrane voltage upon analyte capture and triggering of time-dependent voltage protocols [120, 121]. Moreover, the voltage may be inverted after a given delay time in order to recapture translocated molecules and perform multiple measurements on the same molecule [79, 122]. Here, we describe the experimental realization of an active voltage control setup for nanopore sensing experiments. After illustrating the experimental setup, we demonstrate its potential in DNA recapture experiments with small solid state pores.

3.3.1 Setup

We implemented active control by combining two commercially available data acquisition boards (National Instruments, Germany). The analog input of a NI PCIe-6351 card is connected to the signal output of an Axopatch 200B patch clamp amplifier. Via a custom LabVIEW routine, the card's onboard comparator circuitry is programmed to generate a trigger signal on rising or falling edges of the measurement signal. It offers 16 bit resolution, which theoretically allows triggering on current blockades with amplitudes as low as 3 pA or 300 fA at an amplifier gain of 0.1 mV/pA or 1 mV/pA, respectively. In practice, measurement noise limits the ability to trigger on very small

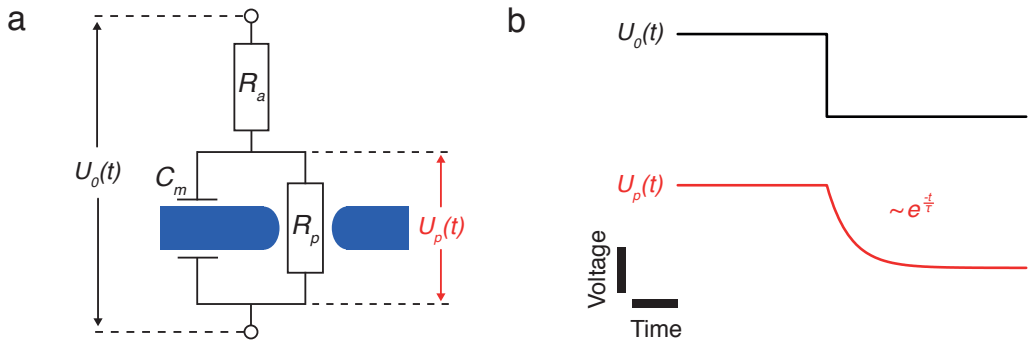

Figure 3.8: Voltage Steps. a) Equivalent circuit of a nanopore setup, consisting of the membrane capacitance C_m in parallel to the pore resistance R_p and the series resistance R_s. b) When a rectangular voltage step $V_0(t)$ is applied to the circuit terminals, the membrane voltage $V_p(t)$ follows an exponential time course due to charging of the membrane capacitance.

current changes. The trigger signal is routed to a NI PCI-6230 card, where it is used to trigger the measurement voltage output. The card features electrically isolated outputs to prevent ground loops in the measurement circuitry, thereby ensuring low measurement noise at high bandwidth. Current acquisition, trigger control and voltage output are unified in a custom-built LabVIEW program, similar to the one discussed in Section 2.3.2.

Response Time. The response time of our active control setup is governed by several contributions. Without external load, we determine a switching response of $\approx 1\,\mu s$ directly at the respective in- and outputs of the two data acquisition boards. Upon triggering on a resistive pulse, additional delay is introduced by the amplifier's finite slew rate[2], which is $\approx 10\text{-}15\,\mu s/nA$ in our experiments. Moreover, upon trigger firing, the combined RC response of nanopore chip, measurement cell, amplifier, and wiring determines the time necessary to induce a change of the measurement voltage. As discussed earlier (cf. Section 2.5.1), we consider an equivalent circuit of a resistor and a capacitor in parallel and another resistor in series to account for the pore resistance R_p, the membrane capacitance C_m and the series resistance R_a, respectively (see Figure 3.8a). In response to a voltage step, a transient charging current across the membrane capacitance leads to a voltage drop at the cell's series resistance (see Figure 3.8b). The voltage applied to the pore therefore follows an exponential time course with a time constant of

$$\tau = \frac{C_m R_a R_p}{R_a + R_p}. \tag{3.19}$$

To quantify the RC response of our active control setup, we mounted a 2.8 nm solid state pore (see Section 5.1.1 for details on fabrication) into the vertical measurement cell (cf. Section 2.4) with 0.4 M KCl electrolyte buffered at pH 8. Considering a pore resistance of 320 MΩ, a typical membrane capacitance in the order of $\sim 30\,pF$ and a

[2]The Axopatch 200B's maximum internal bandwidth is specified as 70 kHz in resistive feedback mode.

combined series resistance in the kΩ-range, we expect a time constant $\tau < 1\,\mu s$. To test our considerations, we analyzed the system's current response to predefined voltage steps, where we determined a time constant of $\tau \approx 4\,\mu s$. Considering the amplifier's limited internal bandwidth of 70 kHz, this finding meets our expectations. In addition, we obtained estimates for membrane capacitance C_m and series resistance R_s by integrating the current transients (determining the accumulated charge) [123], finding $\sim 50\,pF$ and $\sim 30\,k\Omega$, respectively. Considering Eq. 3.19, these values correspond to a time constant of $\sim 1.5\,\mu s$.

From the sum of the contributions discussed above, we expect a switching response in the order of $\sim 10\,\mu s$ for our active control setup. However, the actual switching speed is further degraded by the current limit of the amplifier's feedback resistor. The Axopatch 200B's feedback headstage is supplied by 15 V, which corresponds to a maximum current of 30 nA for the 500 MΩ feedback resistor. For large voltage steps with high charging currents, this slows down the time response considerably. This issue may be solved by using capacitance compensation circuitry as built into the patch clamp amplifier, which supplies the charging current via a dedicated capacitor that can deliver larger currents [26]. However, the Axopatch 200B amplifier provides only a 5 pF injection capacitor for the 500 MΩ feedback stage, which cannot supply a large enough charging current for our solid state nanopore setup. While for the 50 MΩ stage the current limit is 300 nA and a 50 pF capacitor is available, it offers a considerably worse signal-to-noise ratio. Therefore, we chose not to utilize capacitance compensation for the experiments described in this work. Future experiments may benefit from a recording system that offers a larger injection capacitor.

Output Glitches. A problem common to fast analog signal generation is output glitches that occur at code transitions of the digital-to-analog (DA) converter [124]. The DA converter on the NI PCI-6230 board is subject to glitches of up to 100 mV for $\approx 3\,\mu s$ when switching the output polarity, i.e. when the most significant bit (MSB) changes. By scaling down the voltage at the amplifier input, the maximum glitch amplitude is reduced to a value of 10 mV, which is further damped by the low pass effect of the measurement circuit. Moreover, at transitions that do not involve a polarity change, considerably smaller glitches are observed. As we do not expect a significant influence of these glitches on our experiments, we did not attempt to remove them from the voltage output, e.g. by using an adapted track-and-hold circuit [124]. In the case of voltage ramps, where glitches in the current response impede data analysis, we apply a median filter after acquisition (cf. Section 5.2).

3.3.2 Recapture of 500 bp DNA Fragments

To characterize our active control setup, we performed DNA recapture experiments as initially demonstrated by Gershow et al. [122]. By applying a transmembrane voltage, double-stranded DNA molecules are electrophoretically captured into a solid state nanopore. When a DNA molecule translocates the nanopore from *cis* to *trans*, the rising edge of the associated current blockade is used to trigger reversal of the

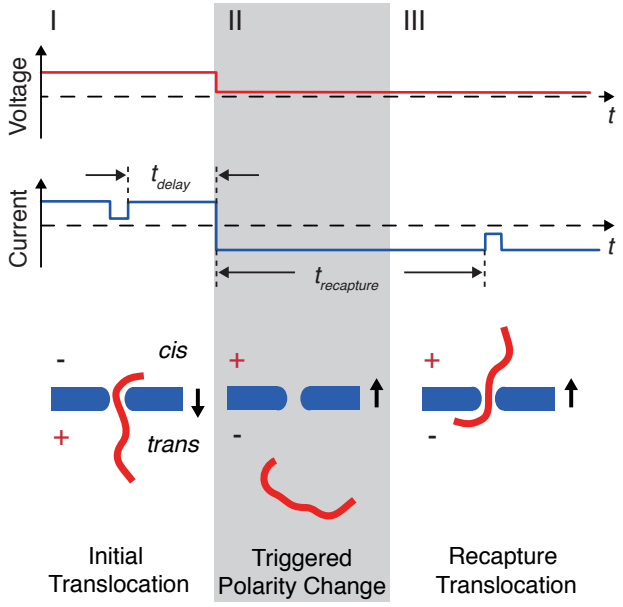

Figure 3.9: Recapture Experiments. I) After addition of dsDNA fragments to one of the electrolyte compartments, positive bias is applied to facilitate DNA translocation. II) Upon translocation, a characteristic current blockade is observed. The bias is reversed a defined time span t_{delay} after the rising edge of the blockade has been detected. III) When the molecule is recaptured by the electric field outside the pore, another current blockade is observed. The corresponding recapture time trecapture is recorded.

Table 3.1: Transport Parameters. Obtained from recapture experiments shown in Figure 3.10. Uncertainties are fit errors.

	Initial Translocation	Recapture Translocation
v(nm/µs)	0.62 ± 0.01	0.44 ± 0.01
D (nm^2)/µs)	3.0 ± 0.3	3.8 ± 0.5

measurement voltage (see Figure 3.9) after a defined delay time t_{delay}. As no DNA was added to the *trans* side, a subsequent current blockade at negative bias is attributed to the recapture of the initial DNA fragment. The corresponding recapture time $t_{recapture}$ depends on the diffusion coefficient and the electrophoretic mobility of the DNA molecule. Moreover, it depends on pore geometry and ionic strength.

In our experiments, we used 500 bp dsDNA fragments that are translocated through a 2.8 nm solid state nanopore under conditions as described in Section 3.3.1. In Figure 3.10a, a typical current trace at a voltage of ±275 mV is shown. Here, the voltage was reversed 200 µs after detecting the rising edge of the initial current blockade. The corresponding recapture event is observed 8.8 ms after reversal. A scatter plot of blockade amplitude vs. dwell time for initial translocation events and corresponding recapture events is shown in Figure 3.10b. Although both event populations overlap strongly and have similar blockade amplitudes (0.46 nA and 0.47 nA), we observe a notable difference in the dwell time distribution. To quantify this difference, we obtained

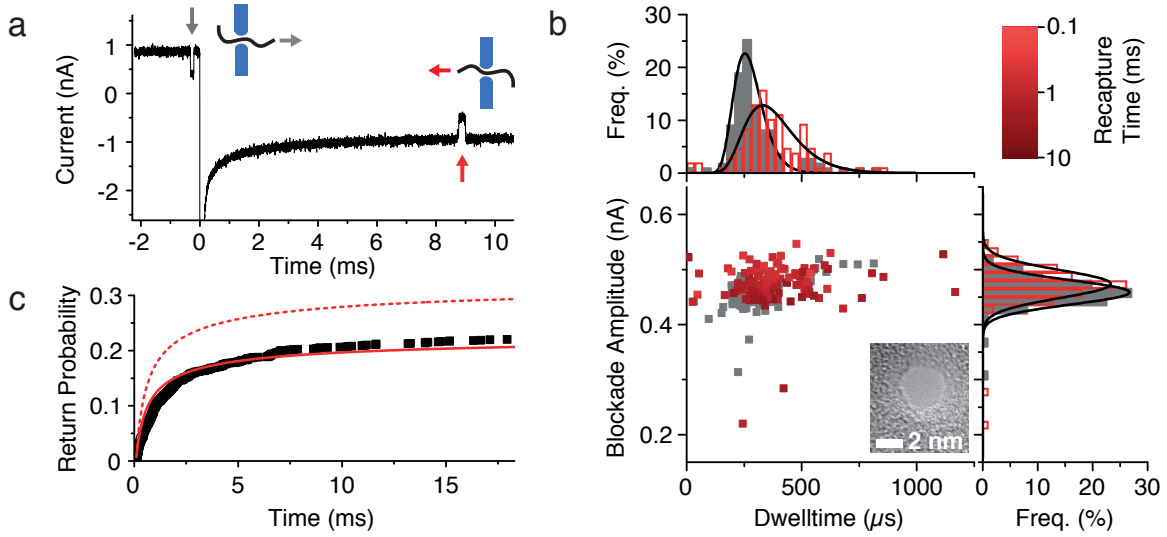

Figure 3.10: Recapture of 500 bp DNA. a) Current trace of a recapture experiment with a 2.8 nm pore at a bias of ±275 mV and a delay time of 200 µs. Capture and recapture event are indicated by gray and red arrow, respectively. Experiments were performed at 400 mM KCl buffered to pH 8 b) Scatter plot of blockade amplitude vs. event duration for the initial blockade (gray) and the recapture blockade (red). Color coding indicates corresponding recapture time before the event. Corresponding histograms are shown on top and right of the plot. Black lines correspond to fits to Eq. 3.18 (top) and to Gaussian fits (right). Inset: TEM micrograph of a 2.8 nm Si_3N_4 nanopore as used in the experiment. c) Return probability as a function of elapsed time since the polarity change. Dashed red line: Prediction of the drift diffusion model discussed in the text. Solid red line: Drift diffusion model scaled by a factor of 0.70 ± 0.05 (determined from fit to the data).

drift velocities and diffusion coefficients for both populations by fitting the dwell time histograms to Eq. 3.18. The results are summarized in Table 3.1 and compare well to previous studies on similar sized pores [89]. For recapture, we observe slower drift paired with stronger diffusion compared to the initial translocation, which we attribute to details of the nanopore geometry.

In Figure 3.10c, the recapture probability is shown as a function of elapsed time after the voltage switch. Only events with recapture times $t_{recapture} > 100\,\mu s$ could be considered due to the current transient upon switching. Analogous to Gershow et al. [122], we model our findings with the time-dependent radial drift-diffusion equation (cf. Eq. 3.8, Eq. 3.9 and Eq. 3.12):

$$\frac{\partial c(r,t)}{\partial t} = \frac{1}{r^2}\frac{\partial}{\partial r} r^2 \left(\frac{\mp \rho \mid \mu I \mid}{2\pi r^2} c(r,t) + D \frac{\partial c(r,t)}{\partial r} \right) \tag{3.20}$$

Here, the negative sign accounts for movement away from pore and the positive sign for coming back. A free energy barrier for capture is not taken into account. We solved Eq. 3.20 numerically for appropriate boundary conditions using free solution values for the electrophoretic mobility and the diffusion coefficient of 500 bp DNA (see Appendix A.2 for details). The obtained return probability is shown in Figure 3.10c. We took into account return times $> 100\,\mu s$ only for better comparability with our

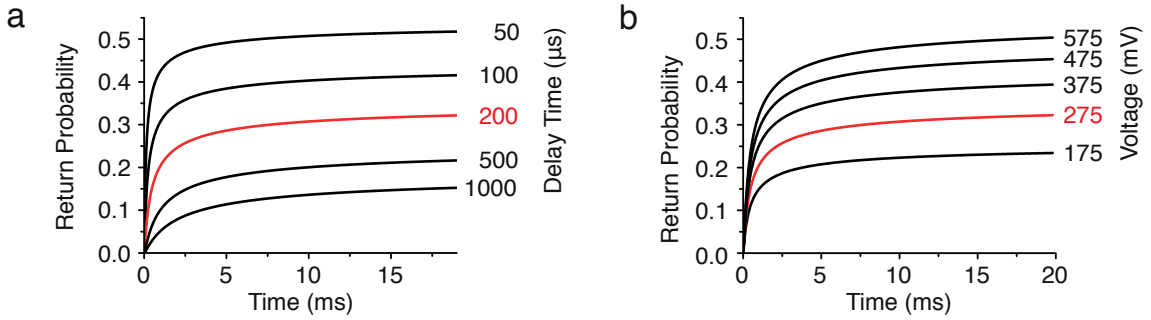

Figure 3.11: Recapture Simulations. Calculated return probabilities for various delay times (a) and bias voltages (b). Values marked in red correspond to the experiments shown in Figure 3.10. All remaining parameters were chosen accordingly. In contrast to Figure 3.10c, here events with return times $< 100\,\mu s$ were considered.

experimental findings. The calculated return probability is higher than our findings, saturating at 29 % compared to $\approx 22\,\%$ for the experiment. However, in contrast to the absolute values, the time dependence follows the data quite well. Scaling the simulated model probability with a factor b, we fitted it to our measurement data and found good agreement for $b = 0.70 \pm 0.05$. Gershow et al. found an identical scaling factor, attributing the missing events to nonspecific binding of DNA molecules to the membrane [122]. However, the reduced switching response due to the amplifier's current limit may also contribute to it. There is no indication for an additional free energy barrier for translocation, although we assume full recoiling of the translocated strand before the voltage is reversed. This is supported by a Zimm relaxation time $\tau_Z = \eta R^3/(\sqrt{12\pi} k_b T) \approx 70\,\mu s$ for 500 bp DNA, where R is the mean end-to-end distance of the polymer [112] and η is the viscosity of the solution. For a detailed study of the possible influence of an energy barrier, voltage dependent studies are necessary.

Compared to previous studies, we observe considerably lower recapture efficiencies. This is a consequence of the smaller pore dimensions (2.8 nm versus 5 x 7 nm [122] and 20 nm [79]) and shorter DNA (500 bp versus 4 kbp [122] and 48.5 kbp [79]), which give rise to a more localized electric field and faster diffusion. However, such small pores offer a significantly higher signal-to-noise ratio and allow shorter molecules to be studied [78]. They can be used to actively manipulate the analyte, e.g. by stripping off DNA-binding proteins [125] or triggering conformational changes upon translocation. Furthermore, recapture experiments with such small pores provide a method to probe association rate constants of DNA-protein complexes: Following its initial translocation, the DNA molecule may interact with DNA-binding proteins added to the *trans* compartment. By recording the corresponding recapture event, both interaction time and bound/unbound state of the molecule may be determined. The efficiency of recapture in experiments with small pores can be improved by increasing the measurement potential or by reducing the delay time (see Figure 3.11). Moreover, the lower detection limit may be improved by using a patch clamp amplifier that is able to supply larger charging currents for the high gain stage.

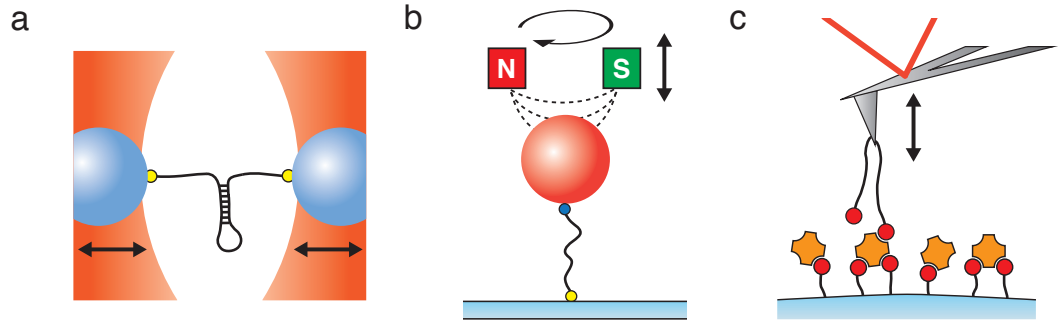

Figure 3.12: Common Force Spectroscopy Techniques. a) Optical tweezers (dumbbell assay). A molecule or complex (here a DNA or RNA hairpin) is attached to two dielectric beads (blue) via linker molecules. Each bead is controlled individually by the laser beam of an optical trap. A force clamp can be realized by steering the beads into a region with low trap stiffness and adjusting the laser power accordingly [126]. Force-extension curves can be obtained by moving the traps apart [127]. In both cases, the force is measured by monitoring bead displacement. b) Magnetic tweezers. The analyte molecule (here a dsRNA strand) is tethered to a glass slide on one end and linked to a paramagnetic bead on the other [128]. Force in vertical direction is applied by the permanent magnets above it. By varying their z-position, the field gradient at the bead position is changed and the force applied to the bead can be adjusted. Rotation of the magnet assembly can be used to apply torque to the molecule. The extension is measured by tracking the bead's z-position. c) Atomic force microscopy (interaction assay). The surface of an agarose bead is covered with streptavidin using biotinylated linkers [129]. The tip of an AFM cantilever is functionalized with biotin. When the tip approaches the bead, one or more streptavidin-biotin bonds can form. During the cantilever's retraction motion, an increasing load is applied to the bond, leading to its rupture, which is detected by a sudden change in beam deflection.

3.4 Nanopore Force Spectroscopy

In the preceding sections, we discussed how resistive sensing with nanopores can be used to detect and discriminate analyte molecules by their size, conformation and transport characteristics. Furthermore, we introduced the concept of active recapture, which may be used to probe the kinetics of internal molecular relaxation [79] or association rate constants of bimolecular complexes. Apart from facilitating analyte transport, the highly localized electrical field inside a nanopore may also be used to exert force on molecular bonds. Such force studies – or force spectroscopy experiments – probe details of molecular interactions that cannot be assessed with bulk experiments. They greatly enhanced our understanding of fundamental biological processes such as cellular motility [9, 130], genome packaging [10], transcription [131] or protein folding [11, 132]. In contrast to established force spectroscopy techniques such as optical tweezers [12], magnetic tweezers [133] and atomic force microscopy [129] (see Figure 3.12), nanopore-based force spectroscopy (NFS) requires no labeling and offers high throughput. In this section, we illustrate the working principle of nanopore-based force spectroscopy (NFS). We specifically discuss dynamic NFS and present DNA hairpin unzipping data obtained from parallel NFS experiments. Moreover, we cover the basics of analysis and interpretation of force spectroscopy data before we compare NFS to other single molecule force spectroscopy techniques.

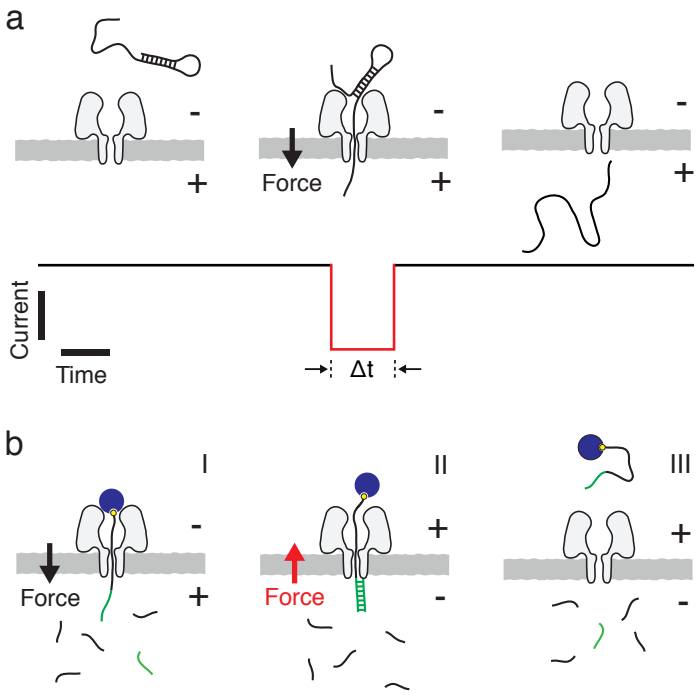

Figure 3.13: Nanopore Force Spectroscopy. a) Force-induced unzipping of a DNA hairpin structure. The structure is captured into the channel by a single stranded tail. As the duplex region cannot pass the pore constriction, the electrophoretic force acting on the thread is converted to a drag force acting on the duplex region and promoting its unzipping. The observed duration of the current blockade Δt corresponds to the hairpin lifetime at the applied voltage. b) Anchor/fishing technique used in [134]. I: A stable anchor (blue) prevents full translocation of a single stranded DNA probe. II: Following the hybridization of a complementary strand to the translocated region of the probe, the voltage is reversed and III: the duplex is unzipped again.

3.4.1 Principle

The functional principle of NFS is illustrated in Figure 3.13, where it is exemplified for the forced dissociation of a DNA hairpin structure. The hairpin is electrophoretically captured into an α-hemolysin porin using a short single stranded thread. The α-hemolysin porin features a 1.4 nm wide constriction zone [32], which is too narrow for the double stranded stem region of the hairpin. Therefore, the electrophoretic force exerted on the thread section inside the pore does not facilitate its immediate translocation, but pulls the stem against the vestibule, promoting its unfolding. After a certain time, the stem region unfolds and the DNA molecule exits the pore at the *trans* side. The observed dwell time Δt is the sum of the unfolding time t_{unzip} and the translocation time $t_{translok}$. For sufficiently strong interactions, the translocation time may be neglected ($\Delta t \approx t_{unzip}$). In that case, the observed dwell time is a direct measure for the bond lifetime under force. This concept of a force-dependent study of DNA duplex stability with α-hemolysin was introduced by Sauer-Budge et al. in 2003 [8]. They observed an exponential dwell time distribution for a 50 bp duplex region, which is reasonable if duplex dissociation can be modeled as a two-state process

that is described by a first-order rate equation:

$$\dot{S}(t) = -k(t)S(t) \tag{3.21}$$

Here, $S(t)$ is the probability that unfolding has not yet occurred at time t and $k(t)$ is the unfolding rate. For experiments performed at constant voltage, the unfolding rate is a constant. The distribution of unfolding times $\dot{S}(t)$ then follows a single exponential time course $\dot{S}(t) \propto e^{-kt}$, where k is the characteristic dissociation rate constant at the voltage used in the experiment.

A great improvement compared to Sauer-Budge's initial studies was made by Mathé et al. [121], who implemented active voltage control for the NFS setup, thereby enhancing the voltage range considerably and allowing the study of less stable structures such as hairpins with a 7 bp duplex region or less. A similar improvement was made by Nakane et al. [134], who implemented an anchor/fishing strategy (see Figure 3.13b): The 3' end of a single-stranded DNA probe is captured into the pore from its vestibule side. While a stable biotin-avidin modification at the 5' end prevents full translocation of the probe strand, complementary DNA strands hybridize to the translocated part and are subsequently unzipped upon voltage reversal. This approach also excludes any influence of the vestibule on the unzipping process, while still providing the enhanced DNA capture rates of the vestibule side [117]. Apart from the study of DNA-DNA interactions, NFS has been utilized to study DNA-protein complexes [125] and protein-protein interactions [135]. The basic requirement for an interaction pair to be studied with NFS is that one of its parts needs to include a charged thread and must be small enough to traverse the pore, while the other part needs to be larger than the pore opening. Synthetic channels are appealing for NFS applications, as their tunable geometry might considerably enhance the range of systems to be studied with NFS.

3.4.2 Dynamic Nanopore Force Spectroscopy

Dynamic NFS is an alternative measurement mode to the NFS studies under constant force discussed in the previous section. It requires separation of analyte capture from the actual dissociation process by implementing either active voltage control or an anchor technique. The principle of dynamic NFS is illustrated in Figure 3.14 for force-induced hairpin unzipping. Following analyte capture, the force acting on the hairpin is increased gradually by ramping up the voltage at a constant loading rate. As for constant force experiments, hairpin unzipping is detected by monitoring the opening transition in the current signal when the DNA strand is leaving the pore. The corresponding voltage at which hairpin dissociation occurs is recorded. In contrast to constant force NFS, here a whole range of forces/voltages is probed in a single experiment. Dynamic force spectroscopy techniques are used in interaction assays with AFM [136], optical tweezers [127] and the biomembrane force probe [137] technique. Dynamic NFS studies so far have been carried out to study DNA hairpin unzipping [121], aptamer-target interactions [138] and the dissociation of a ssDNA-exonuclease I complex [139]. In contrast to constant force experiments, dynamic force

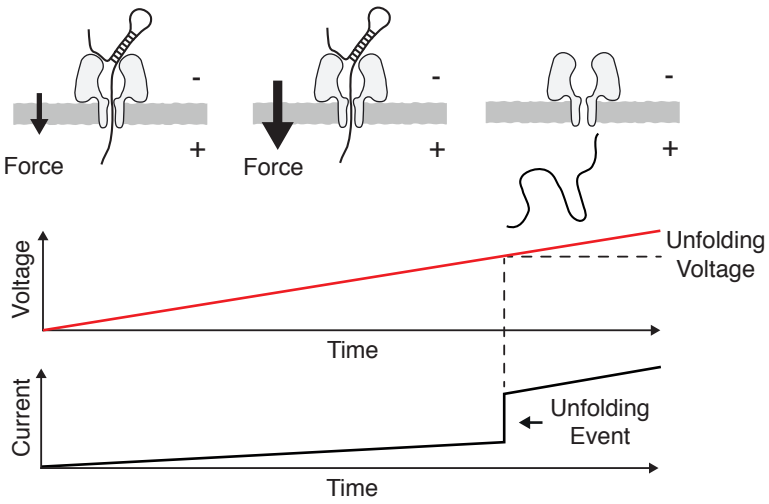

Figure 3.14: Dynamic Nanopore Force Spectroscopy. Hairpin unzipping. After successful capture of a hairpin structure, the voltage is ramped up linearly. The unfolding voltage corresponding to the current transition upon DNA traversal is recorded.

spectroscopy data cannot be interpreted in a straightforward manner. Instead, analytical concepts are needed to obtain kinetic information from dissociation force/voltage distributions (see Section 3.4.4).

3.4.3 Parallel Dynamic Nanopore Force Spectroscopy on DNA Hairpins

Due to the heterogeneity of biological assemblies, NFS experiments are subject to substantial experimental scatter, even under identical conditions. Quantitative studies therefore require several independent NFS experiments to be performed. By multiplexing such experiments, a substantial increase in throughput would be possible. So far, parallel NFS experiments only have been realized using ensemble detection schemes [140]. We investigated the potential of parallelizing NFS experiments on a bilayer platform using the 16 channel MECA setup introduced in Section 2.3.2. Therefore, we formed bilayers from DPhPC lipids in 1 M KCl electrolyte buffered at pH 8. As a model system, we studied the force-induced dissociation of a DNA hairpin with an 8 bp stem region in the α-hemolysin porin. We chose a passive anchor technique to capture the hairpin structure (see Figure 3.15a). The DNA construct consists of the hairpin under study, a 50 base polythymidine spacer and a very stable 12 GC anchor hairpin (see Figure 3.15b). At a capture voltage of 120 mV, the 8 bp hairpin dissociates and traverses the pore, while the anchor hairpin prevents full translocation. After allowing the hairpin to refold at a voltage of 50 mV, the ramp experiment is started and the hairpin is unzipped again. In Figure 3.15c, data obtained from two parallel NFS acquisitions are shown. The experiment was initially started with three parallel acquisitions, but one pore clogged soon after. For one of the two remaining pores, 40 typical current traces with unzipping transitions are shown. Below, unzipping voltage

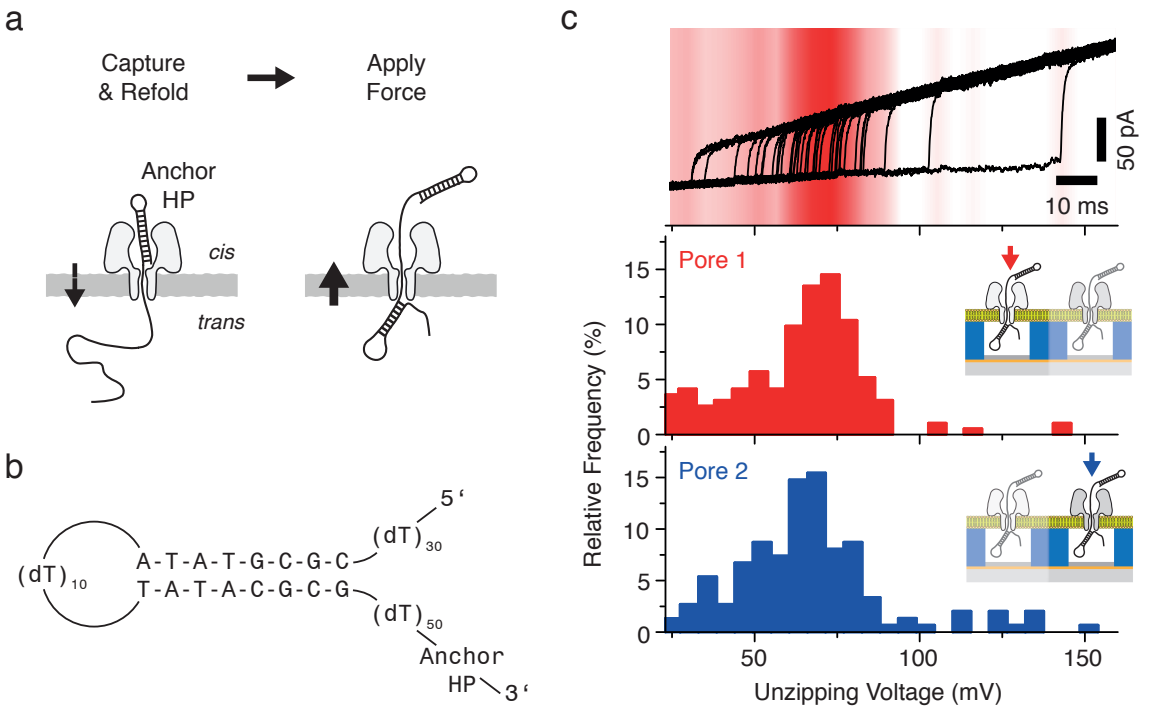

Figure 3.15: Parallel Nanopore Force Spectroscopy. a) DNA hairpins are unzipped at the *trans* side of α-hemolysin by applying voltage ramps. To enable parallel recordings on two separate channels, hairpin capture is realized with a stable anchor hairpin. b) Sequence of the hairpin under study. The stem region consists of 4 AT base pairs followed by 4 GC base pairs. The anchor hairpin features a stem region with 12 GC base pairs. c) Top: 40 representative current traces recorded at a ramp speed of 1.25 V/s. Only traces featuring an unzipping transition are shown. Color coding indicates transition voltage distribution for the complete dataset (193 events). Bottom: Unzipping voltage distribution corresponding to top (red) and for a second pore recorded in parallel (blue).

histograms for both acquisitions are presented. The most probable unfolding voltage is comparable (69 mV and 73 mV) and matches results obtained on a droplet interface bilayer setup [141]. The measurements shown in Figure 3.15 represent a proof of principle for parallel NFS recordings. However, the use of this parallelization approach is limited so far: The success rate for capture with the aforementioned anchor technique is low (here 4 %). In single NFS experiments, the capture success can be greatly improved by using a conditional capture protocol (cf. Section 2.3.2), where the voltage ramp is only started upon detection of successful capture. However, due to hardware limitations of the 16 channel patch clamp amplifier used in our studies, only one stimulus can be applied to one or more cavities at a time, whereas individual stimuli for each channel would be required to realize a parallel version of the conditional capture protocol. Such an improvement would be particularly important, as the typical pore lifetime on the MECA setup was observed to be shorter than in droplet interface bilayer experiments. Together with an improvement of the incorporation protocol, the throughput of bilayer-based NFS measurements may be greatly enhanced. For NFS with solid-state nanopores, an all-optical detection scheme may be a more promising candidate for highly parallelized experiments [142, 143].

3.4.4 Analysis of Dynamic Force Spectroscopy Experiments

The interpretation of unfolding voltage distributions obtained in dynamic force spectroscopy experiments is not as straightforward as for constant voltage experiments. Typically, the most probable unzipping voltage is determined for different loading rates. Logarithmic regimes in the loading rate dependence are interpreted as distinct molecular interactions, which are characterized by the crossing of a single energy barrier [137, 144]. Characteristics of the barrier then may be obtained by fitting models to the experimentally obtained loading rate dependence (see Section 3.4.5). Alternatively, unzipping voltage distributions can be analytically converted to voltage dependent lifetime data. We assume that the unfolding or rupture process can be described as the irreversible crossing of a single energy barrier, which is not influenced by preceding barriers [145]. Furthermore, unfolding times need to be longer than the diffusional relaxation times of the system, i.e. the measurement is performed in "quasi-adiabatic" or "quasi-equilibrium" conditions [146, 147]. If above criteria are met, the system obeys the first order rate equation given by Eq. 3.21. A solution for a time-dependent dissociation rate $k(t)$ can be found by separation of variables:

$$S(t) = exp\left(-\int_0^t k(t')dt'\right) \tag{3.22}$$

The distribution of unfolding voltages $p(V)$ is given by:

$$p(V) = \frac{d}{dV}(1 - S) \tag{3.23}$$

This can be transformed into $p(V)dV = -\dot{S}dt$ and substituted into Eq. 3.21 and Eq. 3.22, and we obtain:

$$p(V) = \frac{k(V)}{\dot{V}} exp\left(-\int_0^V \frac{k(V')}{\dot{V}} dV'\right) \tag{3.24}$$

Here, $\dot{V} = dV/dt$ is the loading rate of the experiment. For conventional force spectroscopy experiments, a similar expression is obtained using $p(F)dF = -\dot{S}dt$ for the above transformation. Eq. 3.24 can be inverted to obtain an expression for the voltage-dependent unfolding rate $k(V)$ or lifetime $\tau(V)$:

$$k(V) = \tau^{-1}(V) = \frac{p\left(V|\dot{V}\right)\dot{V}}{\int_V^\infty p\left(V'|\dot{V}\right)dV'} \tag{3.25}$$

This equation was derived by Dudko et al. [146] and allows direct mapping of unfolding voltage distributions to voltage-dependent dissociation rates $k(V)$ or complex lifetimes $\tau(V)$ as obtained from constant voltage experiments. In Figure 3.16, the result of this transformation is shown for the hairpin unzipping data presented in Section 3.4.3. It does not rely on a specific assumption for the voltage dependence of the unfolding process, i.e. the shape of the underlying energy landscape. Its applicability to a specific unfolding experiment can be tested by obtaining data at different loading rates, as it predicts that these data all collapse onto a single master curve. Furthermore, constant voltage experiments can be performed to confirm its validity.

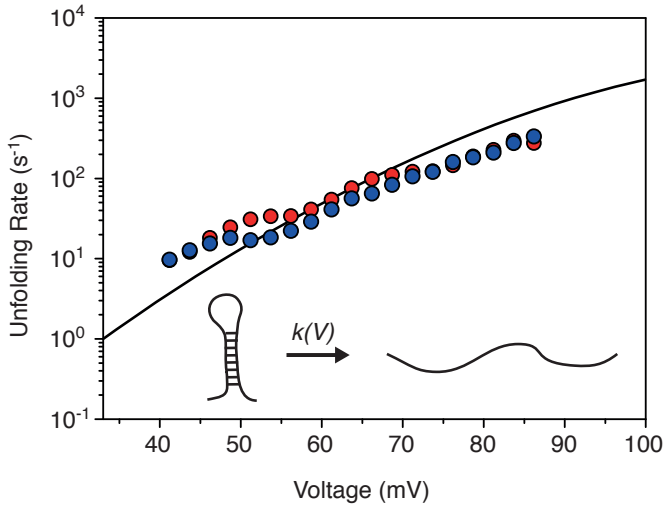

Figure 3.16: Rate Transformation. Hairpin unfolding rate as a function of voltage for the experiments discussed in Section 3.4.3 (red: pore 1, blue: pore 2). Rates were obtained from unzipping voltage distributions using Eq. 3.25. Black line corresponds to a mesoscopic model for hairpin unzipping described by Schink et al. [141].

3.4.5 Interpretation of Force Spectroscopy Data

To extract kinetic and thermodynamic parameters from force spectroscopy experiments, a theoretical model is necessary, which relates the obtained rates under force to microscopic characteristics of the interaction. Ideally, a specific model for the system under study is developed which accounts for the underlying free energy surface and kinetics [141]. However, often knowledge about the system under study is limited and a more general theoretical framework is needed. Dudko et al. presented an analytical approach to extract thermodynamic properties and rate constants from force spectroscopy data based on Kramers diffusion theory [148]. Dissociation is described as barrier crossing in the one-dimensional free energy landscape along the pulling coordinate. The latter is assumed to be a "good" reaction coordinate, i.e. dynamics are slower than along any other coordinate. The free energy profile along the pulling coordinate $U(x)$ is given as the sum of the equilibrium profile $U_0(x)$ and a term $U_F(x)$ which describes the influence of an external pulling force. The dissociation rate under constant voltage is then [148]:

$$k(V) = k_0 \frac{\int_{well} e^{-\beta U_0(x)} dx \int_{barrier} e^{\beta U_0(x)} dx}{\int_{well} e^{-\beta [U_0(x)+U_F(x)]} dx \int_{barrier} e^{\beta [U_0(x)+U_F(x)]} dx} \tag{3.26}$$

Here, $\beta = (k_b T)^{-1}$ is the inverse thermal energy. The integrals are performed across the well and barrier regions of the free energy profile, respectively. Due to its electrophoretic and electroosmotic origin, the force in NFS experiments can safely be assumed to depend linearly on the applied voltage V. Furthermore, we take the force to be independent of the section of the thread DNA inside the pore, i.e. the force does not depend on extension. The potential is then given by $U_F(x,t) = -aV(t)x$,

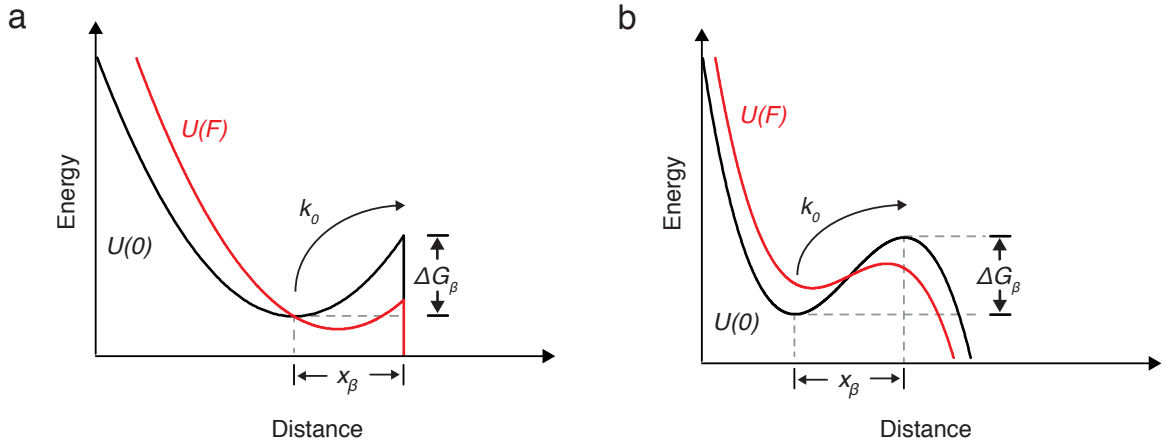

Figure 3.17: Model Free Energy Profiles. Schematics of the energy landscapes used for calculation of Eq. 3.27 in equilibrium (black) and under force (red). a) harmonic well with cusp-like barrier. b) linear-cubic energy profile.

where a is a proportionality constant that depends on experimental conditions such as pore geometry, thread type and buffer conditions. It has the dimensions of an electric charge per length unit. Dudko et al. [149] and Hummer et al. [150] evaluated Eq. 3.26 analytically for two model energy profiles: one with a harmonic well and a cusp-like barrier ($U_0(x) = \Delta G_\beta (x/x_\beta)^2$ for $x < x_\beta$ and $U_0(x) = -\infty$ for $x \geq x_\beta$) and one with a cubic-linear surface ($U_0(x) = (3/2)\Delta G_\beta (x/x_\beta) - 2\Delta G_\beta (x/x_\beta)^3$). Their results are described by [148]:

$$k(V) = k_0 \left(1 - \frac{\nu V}{\beta \Delta G_\beta V_\beta}\right)^{1/\nu - 1} e^{\beta \Delta G_\beta \left[1 - \left(1 - \frac{\nu V}{\beta \Delta G_\beta V_\beta}\right)^{1/\nu}\right]} \tag{3.27}$$

For $\nu = 1/2$ and $\nu = 2/3$, this equation corresponds to the cusp-like barrier and the linear-cubic case, respectively (see Figure 3.17). For $\nu = 1$, Eq. 3.27 corresponds to the phenomenological Bell formula $k(V) = k_0 e^{V/V_\beta}$ [151]. By fitting Eq. 3.27 to experimental data, the parameters ΔG_β, k_0 and V_β can be obtained. The first two describe the activation energy and the dissociation rate in absence of external force, respectively. V_β is the voltage that corresponds to a free energy reduction of $k_b T$ and is given by $V_\beta = k_b T/(a x_\beta)$. It scales inversely with the barrier position x_β, which can be calculated from V_β if the factor a is known from calibration measurements (see Section 3.4.6). As 3.26 only holds for sufficiently high barriers $> k_b T$, Eq. 3.27 is valid for voltages $V_c < \beta V_\beta \Delta G_\beta \nu^{-1}$ only. To improve the model for voltages near V_c and beyond, more involved calculations are necessary [152].

The solution obtained by Dudko et al. may also be applied to describe unfolding voltage distributions obtained in dynamic force spectroscopy experiments. Therefore, Eq. 3.27 is substituted into Eq. 3.24. For a linear voltage ramp, i.e. $\dot{V} = const.$, the integral in Eq. 3.24 can be evaluated analytically and we obtain [148]:

$$p(V) = \frac{k(V)}{\dot{V}} exp\left\{\frac{V_\beta}{\dot{V}}\left[k_0 - k(V)\left(1 - \frac{\nu V}{\beta \Delta G_\beta V_\beta}\right)^{1-1/\nu}\right]\right\} \tag{3.28}$$

This expression may be fitted directly to sets of unfolding voltage distributions at different loading rates, e.g. by using a global maximum-likelihood approach [153]. An approximation for the loading rate dependence of the most probable dissociation voltage V^* is given by

$$V^*(\dot{V}) \sim 1 - \left[\frac{1}{\beta\Delta G_\beta} ln\left(k_0 e^{\beta\Delta G_\beta} V_\beta/\dot{V}\right)\right]^\nu . \tag{3.29}$$

V^* is a nonlinear function of the loading rate, which exhibits logarithmical scaling in the limit of Bell's description (for $\nu = 1$). Although the model described here is based on specific assumptions on the shape of the underlying free energy profile, the obtained parameter values may be interpreted in a more general way if they are insensitive to changes in ν [146]. Alternatively, the shape of the energy landscape along the pulling direction may also be recovered directly by evaluating Eq. 3.26 numerically and optimizing the energy profile $U_0(x)$ to reproduce the data [154].

Multiple Barriers. So far, we assumed that the unfolding process can be described by the crossing of a single barrier. If multiple barriers govern the dissociation process, crossing of the highest barrier is expected to be rate-determining and regimes with different slopes in the logarithmic loading rate dependence of the most probable transition force/voltage are typically interpreted as a change of the rate-determining barrier with increasing force [144]. However, preceding barriers may influence the escape rates even when they are not rate determining [145]. In this case, the rate transformation derived above (Eq. 3.25) is not applicable, as the system does not obey a simple first order rate equation anymore. Although there are methods to account for multiple barriers [145], they usually involve separate analysis of individual dissociation steps, which is not possible for NFS experiments. An effective rate may be obtained from constant voltage experiments in that case, although this requires an exponential dwell time distribution, which may not be given in the case of multiple barriers.

3.4.6 Comparison with Other Force Spectroscopy Techniques

Due to conceptual differences, each force spectroscopy technique has its specific benefits and limitations, which makes it more or less useful for a certain application. A comprehensive review of the most common force spectroscopy techniques is given in [155]. Based on this review, we compare the potential of NFS with more established methods. In Table 3.2, an overview is given. At first sight, the NFS specifications are rather unimpressive: While its negligible[3] stiffness (strength of the extension-dependent restoring force) makes NFS well-suited for force clamp experiments and its high temporal resolution in principle allows the study of fast processes, its force range is small compared to other techniques and no spatial information may be obtained so far[4], which severely limits the information that can be gathered. Another drawback

[3] Not considering dielectrophoretic effects

[4] In future, this could be realized by discriminating individual nucleotides via their current blockade [156].

Table 3.2: Comparison of Single Molecule Force Spectroscopy Techniques. Adapted from [155].

	Optical tweezers	Magnetic tweezers	AFM	NFS
Force range (pN)	0.1 - 100	10^{-3} - 10^{4}	10 - 10^{4}	10^{0} - 10^{2} [100]
Spatial Resolution (nm)	0.1 - 2	2 - 10	0.5 - 1	-
Temporal Resolution (s)	10^{-4}	10^{-4}	10^{-3}	10^{-6} [55][5]
Stiffness (pN/nm)	0.005 - 1	10^{-3}-10^{-6}	10 - 10^{5}	≈ 0
Typical Applications	3D manipulation Tethered assay Interaction assay	Tethered assay 3D manipulation	Pulling & Interaction assay	Interaction assay
Features	Low noise & drift Dumbbell geometry	Torque studies Parallel expts. In-cell expts.	Imaging	Label-free High throughput No effect of linkers Unique force geometry
Limitations	Photodamage Sample heating Nonspecific	Low spatial resolution	Large probe High stiffness High min. force Nonspecific	No spatial resolution Difficult calibration Small force range

is that obtaining absolute force values is considerably more involved than for other force spectroscopy techniques. As the electrophoretic force on a stalled DNA thread inside a nanopore depends on the pore geometry and differs from the force on a freely translocating molecule [96], sophisticated experimental studies are necessary to obtain a calibration for the force-voltage relationship [100]. To obtain this relationship from translocation speeds of unstructured DNA, differences between static and dynamic cases such as electroosmotic flow, pore-DNA interactions and DNA stretching need to be considered.

However, NFS may also have clear benefits for specific systems. It offers a unique force geometry by pulling the analyte molecule or complex against a constriction, which is similar to the way proteins are unfolded by membrane voltage when imported into mitochondria [90]. A real strength of NFS is given where common force spectroscopy techniques share drawbacks: For each analyte type or variant, laborious labeling and purification steps are necessary to create bead, tip or surface conjugates. Often reloading is also time-consuming. Systematic screening of analyte libraries therefore is not feasible with these approaches. With NFS however, no linker molecules or probes are

[5] In NFS, the temporal resolution is limited by the transport time of the unfolded analyte molecule.

necessary, the analyte assemblies are essentially label-free. Moreover, fast reloading of molecules due to electrophoretic capture allows for high throughput experiments ideally suited for screening purposes. This benefit may be enhanced even further by parallelizing NFS experiments as shown in Section 3.4.3. Nanopores may also be tailored to specific ligand-receptor interactions by functionalizing the pore with appropriate receptor molecules [7, 157, 158]. That way, association rates may be obtained from NFS experiments as well.

3.5 Conclusion

In this chapter, we covered the fundamental aspects of nanopore sensing. Based on a simple geometrical model for the pore resistance, we related pore geometry and current signal and discussed pore design criteria for a high sensing performance. After recapitulating the mechanisms of analyte transport, we presented an active control setup that extends resistive sensing studies beyond the voltage limits imposed by the principles of analyte capture and enables experiments with time-dependent voltage protocols. To benchmark the setup, we performed DNA recapture studies with small solid state pores, where we find reasonable agreement with theoretical predictions. Compared to previous studies, pore and DNA are downsized considerably, which opens up new experimental prospects, e.g. to study association rates of dsDNA-protein complexes. Finally, we discussed nanopore force spectroscopy (NFS) as a label-free, high throughput alternative to conventional force spectroscopy techniques. We illustrated its working principle, presented our efforts to parallelize NFS studies and recapitulated the theoretical framework for analysis and interpretation of NFS data.

4 DNA-Based Synthetic Membrane Channels

Ever since direct observation of individual transmembrane channels became possible through single channel recordings in the 1970's, researchers have made efforts to study their transport characteristics and relate them to the structure of their constituents. Today, a great deal is known about the functional properties of transmembrane channels such as voltage-gating, ligand gating or selective transport [85] and in many cases, structural features have been identified which give rise to these properties [159–161]. However, as expressed by Richard Feynman's quote "What I cannot create, I do not understand", true understanding of a system includes the ability to rationally design and create synthetic analogues *de-novo* with definable structural and functional properties. Apart from providing a means to test and enhance our knowledge, such custom-made membrane channels are also desirable as components for synthetic biological systems such as compartmental networks [162] or artificial cells [163], as drugs for treatment of channel-related diseases [2] and as analyte-tailored nanopore sensors for stochastic sensing [7] or nanopore sequencing [6].

Via organic synthesis a variety of synthetic channels based on cyclodextrin, crown ethers, cholates and other organic or metal-organic compounds have been created over the last decades [14, 164], demonstrating large structural diversity and replicating basic channel functions such as voltage gating [165], ion selectivity [166] or ligand gating [167]. Unfortunately, limitations imposed by the organic scaffolds used as well as the laborious nature of preparation (mostly linear multistep synthesis) make it hard to fine-tune channel properties and to quickly implement changes.

Compared to that, amino acid scaffolds are much more versatile, as evident from the large structural and functional diversity of naturally occurring protein channels or enzymes and other molecular machines. With synthetic protein design, channel properties may be programmed by adapting the genetic code and fabrication is possible with high yield for both *in-vivo* and *in-vitro* applications using well-established biotechnological methods [168]. Moreover, desired functional properties may be enhanced via directed evolution [169]. However, *de novo* design of protein channels [170] is still at an early stage with limited potential for rational design, as predicting structural and functional properties from the amino acid sequence is complicated due to the high level of complexity present in amino acid interactions (van der Waals forces, hydrogen bonding, hydrophobic packing, disulphide bridges, electrostatics and different side chain interactions [171]). Although tremendous progress has been made over the last years [15], most efforts in synthetic protein channel design are spent on redesigning natural channels for specific purposes [33, 75, 172–174], leaving most of their structural features untouched.

Over the last decades, structural DNA nanotechnology emerged as a viable alternative, allowing structures of up to several MDa to be created with high yield and precision in a very predictable and tunable manner [175]. In this chapter, we present a DNA-based synthetic membrane channel designed *de-novo* and fabricated via molecular self-assembly that is anchored to a lipid membrane with cholesterol side chains. After a brief introduction to the methods applied for design and fabrication, we illustrate the channel's structural specifics and study its interaction with lipid membranes by means of transmission electron microscopy (TEM). The channel's transport properties are characterized with planar lipid bilayer recordings and its potential for single molecule sensing applications is evaluated. The results shown in sections 4.2 to 4.5 of this chapter were published in [176]. Channel design, assembly and the TEM studies presented were carried out by Thomas G. Martin.

4.1 DNA as Building Block for Synthetic Membrane Channels

Before DNA was identified as the actual carrier of genetic information in the mid-1940s [177], it was considered only a structural element packing the more important chromosomal proteins [178]. Even though DNA's actual role in nature is not a structural one, researchers discovered DNA to be a very versatile and simple to use material for artificial nanostructures [179]. DNA's inherent simplicity, which kept researchers from recognizing it as the genomic material for decades, bears considerable advantages for designing artificial structures: Compared to amino acid interactions in proteins, nucleic acid interactions are far less complex and well-predictable [180, 181]. Furthermore, DNA synthesis is cheap and DNA ligation chemistry is highly advanced, making it simple and cost-effective to modify DNA with hydrophobic molecules, dyes or similar [182]. In this section, we briefly review the fundamental concepts of structural DNA nanotechnology and the DNA origami technique in particular. Afterwards, we give an overview of lipid-DNA interactions with regard to designing a synthetic membrane channel.

4.1.1 Structural DNA Nanotechnology

Structural Properties of DNA. Under physiological conditions, DNA adopts a right-handed double-helical conformation known as B-form [184]. An outline of its structural characteristics is given in Figure 4.1. It consists of two single-stranded nucleic acids, each a polymer chain of covalently linked nucleotides with a common sugar-phosphate backbone from which individual base portions (adenine (A), thymine (T), guanine (G) and cytosine (C)) extend. Their sequence on the strand encodes the genetic information. The backbone is formed by phosphodiester bonds that join the 3'-hydroxyl group of one nucleotide's sugar with the 5'-hydroxyl group of the next one, giving each single DNA strand a distinct directionality. In duplex DNA, two antiparallel strands are joined via hydrogen bonds forming between their base portions.

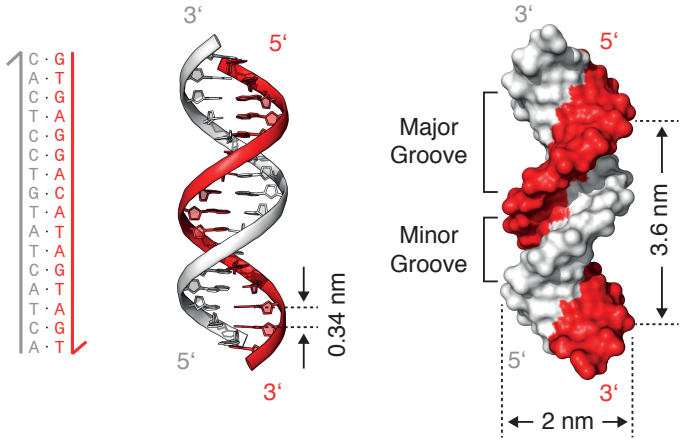

Figure 4.1: Structural Properties of B-Form DNA. Structure of a hexadecameric duplex. Left: Schematic representation indicating nucleobase sequence (A for adenine, T for thymine, G for guanine and C for cytosine) and 3' end (half arrows) for each strand. Middle: Cartoon representation, showing base and ribose rings. Ribbons represent backbone phosphates. B-form DNA features an average base-to-base distance of 0.34 nm [183]. Right: Rendering of the solvent-accessible surface. Dimensions are indicated.

This interaction is referred to as Watson-Crick base-pairing and is efficient only for specific, complementary pairs of nucleobases (A-T and G-C). The duplex is further stabilized by base-stacking interactions [185], which together with Watson-Crick base-pairing counteract the electrostatic repulsion between the negatively charged backbone phosphates. Under physiological conditions, a width of 20 Å, an average base-to-base distance of 3.4 Å and a helix rise of 10.5 base pairs per turn have been determined for the resulting right-handed double-helical structure [183]. It features a major groove and a minor groove, which may both be targeted by DNA binding proteins or other molecules such as intercalating dyes. Stronger sequence specificity is typically observed for interactions with the major groove, where the base regions are more exposed [186].

Double stranded DNA is considered a semi-flexible polymer whose mechanical and statistical behavior for the most part can be described by the worm-like chain (WLC) model [112]. Below its persistence length $l_p \approx 50\,\text{nm}$ which describes the range of orientational correlation between individual chain segments, dsDNA is well-described as an elastic rod with defined stiffness, whereas on length scales considerably larger than the persistence length, molecules are treated statistically.

DNA Junctions and Other Motifs. Due to the aforementioned sequence-specific nature of Watson-Crick base pairing, a large number of specific interactions between individual DNA strands may be "programmed" deliberately by sequence design, a prerequisite for creating complex structures via molecular self-assembly reactions. However, duplex DNA seems not to qualify very well for a building block in terms of connectivity, since connections are possible only along a linear (not necessarily straight) axis. To provide connectivity in three or more directions, branched structures are necessary. Such structures exist as intermediates during processes such as

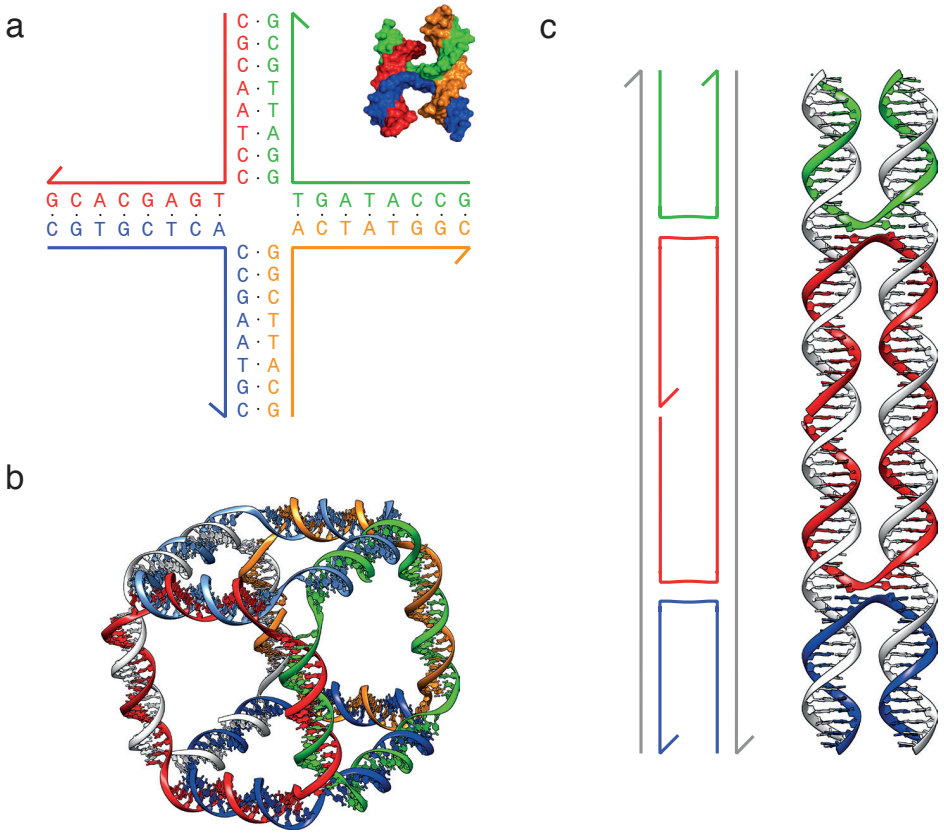

Figure 4.2: DNA Nanotechnology. a) Immobile Holliday junction structure proposed by N. Seeman [187], composed of four hexadecameric DNA strands with sequences optimized to prevent branch migration. Inset: Representative surface rendering of a Holliday junction in its X-stacked conformation [188]. Coordinates were taken from PDB code 2WJ0. b) DNA cube design by J. Chen & N. Seeman [189] (actual structure may differ greatly due to torsional strain and electrostatic repulsion). c) Double crossover (DAE) motif [190], schematic (left) and cartoon representation (right). Two immobilized four-way junctions interconnect two antiparallel domains of B-form DNA.

replication or recombination. However, they are unstable and resolve into separate double-helical domains via branch migration [188]. Key to the development of structural DNA nanotechnology was Ned Seeman's proposal to create stable versions of these intermediates by careful sequence design, particularly by avoiding their inherent sequence symmetry [187]. His design of a migrationally immobile analog to the Holliday junction [188] is depicted in Figure 4.2a. Providing connectivity in four directions, Seeman envisioned assembling it into large three-dimensional lattices, serving as protein positioning templates for X-ray crystallography. In the presence of divalent ions, the immobilized Holliday junction adopts an X-stacked conformation with two roughly parallel arms [188] (see inset of Figure 4.2a). Therefore, by using pairs of Holliday junctions, two double-helical domains may be arranged in parallel fashion (see Figure 4.2b). Known as the double crossover motif [190], this concept allows rigid linkage between multiple duplexes with defined relative position and is fundamental to scaffolded DNA origami [191] (see below) and related assembly techniques such as DNA bricks [192]. An early example of a discrete DNA nanostructure is the cube

design shown in Figure 4.2c [189]. In its assembled state, it consists of six circular 80-mer DNA strands forming duplexes along the edges and three-way junctions at the corners of a cubic frame. For its assembly, ten individual strands were ligated and hybridized in multiple steps. Since torsional strain and electrostatic repulsion effects were not specifically accounted for, the object's actual shape may deviate considerably from its design.

4.1.2 The DNA Origami Technique

In 2006, a novel method termed DNA origami was published. Similar to the Japanese art of paper folding it was named after, a long circular single strand of DNA derived from the M13p18 phage genome was folded into predefined shapes of about 5 MDa in size in a single molecular self-assembly reaction [191]. While initially limited to flat objects, the technique was soon to be extended to three-dimensional assemblies [193] and amended with structural features such as global bends and twist [194]. One of the greatest achievements, however, is a highly developed computer-aided design and evaluation workflow [195, 196] that considerably shortened prototyping cycles and lowered the initial barrier for adopting this method for different areas of research. Here, we describe the basic concepts of DNA origami design and fabrication. A comprehensive review can be found elsewhere [197].

In Figure 4.3, the design of a short hexagonal DNA tube is illustrated, which bears structural similarities to the membrane-penetrating stem of the synthetic channel discussed in the following sections. The initial tube layout is created by arranging six cylindrical domains that define the duplex positions of the final structure on a honeycomb lattice (see Figure 4.3a). The circular scaffold strand is then routed to form a closed path across all six domains. Often, the M13p18 phage genome is used, which consists of 7249 bases. However, several longer and shorter derivatives have been realized so far (e.g. 2800, 3200, 7560 and 8064 bases [193, 198]). Since the scaffold length usually is not tailored to a specific target shape, the size of the target structure either has to be adjusted to exactly incorporate the scaffold of choice or it is chosen smaller and one or more loops of unpaired scaffold DNA extend from the final structure, as indicated in Figure 4.3a. This limitation is absent for DNA bricks [192], where no scaffold strand is used. Another constraint is defined by DNA's double-helical geometry: The scaffold strand may cross over from one domain to another only at positions where the backbones of the corresponding duplexes face each other. The terminal positions of individual duplex regions may have to be further adjusted to prevent inter-structural interactions due to blunt-end stacking (not considered here) [199]. The resulting scaffold layout forms the basis of the structure design. In the next design step, short "staple" strands with a typical length of 18 to 50 nucleotides are added to the layout in order to hybridize to the scaffold and cross-link the domains (see Figure 4.3b). As for the scaffold-layout, staple crossover positions have to obey the constraints imposed by duplex geometry. On a hexagonal lattice, each domain has three nearest neighbors with an angle of 120° in between. With a natural helix rise of 10.5 bp/turn, this three-fold symmetry can be fulfilled by placing staple crossovers in intervals of

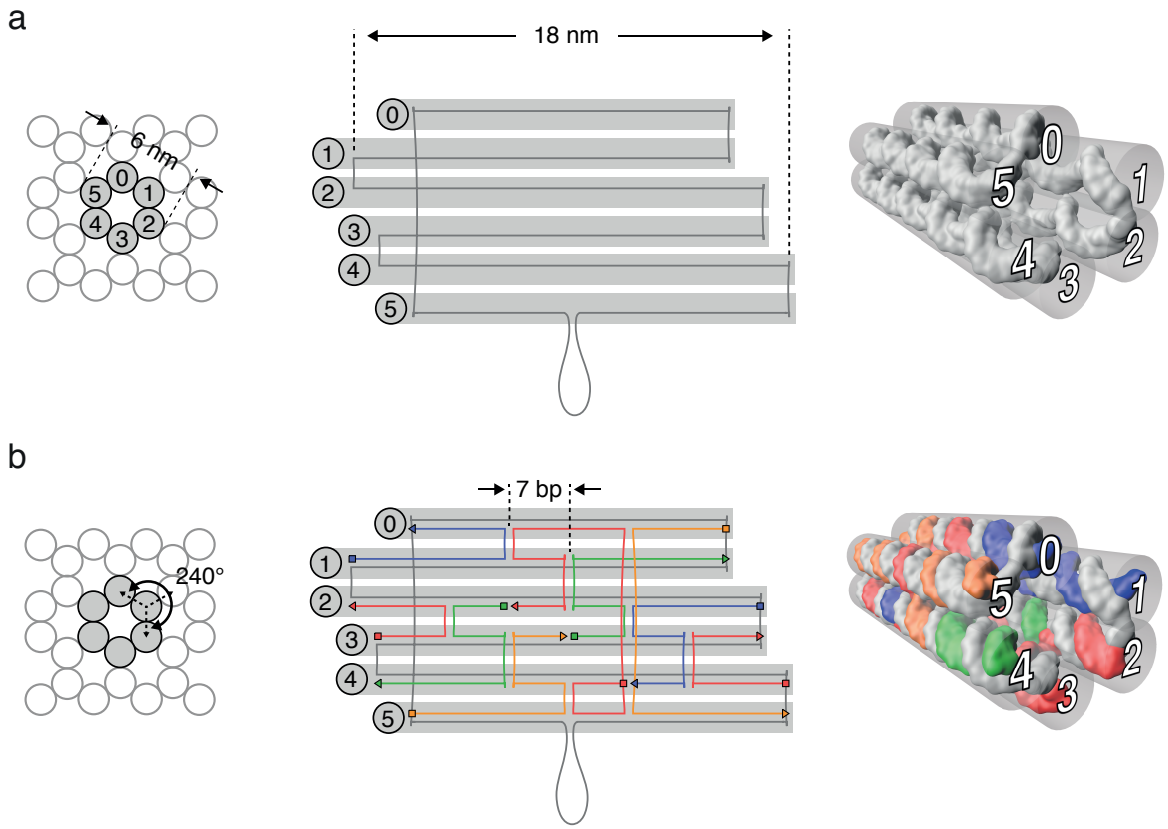

Figure 4.3: DNA Origami Design. Design principle, exemplified for a hexagonal tube with a length of 18 nm and a diameter of 6 nm. Left & Middle: schematic representation of lattice arrangement and spread view as used in caDNAno [195]; Right: surface rendering. a) Six cylindrical domains serving as placeholders for duplex DNA are arranged on a hexagonal lattice. The circular scaffold strand (gray, typically M13mp18 genomic DNA or a derivative) is then routed through the domains in such manner that a closed path filling the entire structure is obtained. The loop indicates unpaired scaffold DNA. b) Staple strands are added to cross-link the scaffold and to form duplex DNA. On a hexagonal lattice, staple crossovers may be placed in intervals of 7 bp, corresponding to a helix turn of 240°.

7 bp, which corresponds to a helix turn of 240°. Deviations from the rule are possible. However, if not carefully outbalanced, they cause torsional as well as axial strain in the structure [194]. An important part of the design process is therefore structure prediction with numerical tools such as CanDo [196]. After a scaffold-staple layout has been determined, staple sequences may be computed. Since the scaffold strand is circular, different sets of staple sequences may be created for a given layout and scaffold sequence by cyclic permutation, which can be used to optimize the folding pathway and stability of the final structure [200]. To avoid stacking interactions, the staple strands at the duplex termini are often extended beyond the scaffold layout, typically with a low affinity sequence such as poly-thymidine. Such staple extensions are possible virtually at any position in the scaffold-staple layout where staple breaks are located and may also be used to functionalize the DNA origami structure with molecules ligated to fitting adaptor strands.

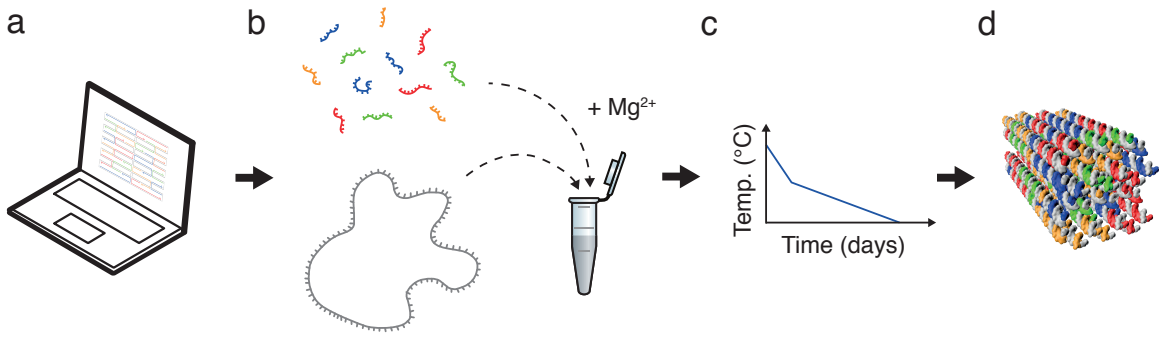

Figure 4.4: Fabrication Workflow. a) Using design software such as caDNAno [195] in combination with structure prediction tools such as CanDo [196], a scaffold-staple layout is generated for a desired target shape and staple sequences are computed. b) The pool of staple strands (red, green, orange and blue) is mixed with scaffold strand (gray) under addition of divalent ions to screen inter-helical repulsion and to stabilize the stacked crossover conformation [201]. c) The mixture is subjected to a temperature protocol to facilitate the hybridization process. d) The structure is purified from the reaction mix using gel electrophoresis, filter- or PEG- purification.

The fabrication steps following structure design are outlined in Figure 4.4. For a structure that incorporates the entire M13 scaffold, typically a set of ≈ 180 staple strands is needed. They are usually generated via chemical synthesis and are commercially available, although biotechnological mass production of staple strands has been shown recently [198]. The scaffold is produced biotechnologically and may either be obtained commercially or fabricated in-house. As exemplified by the cube design in the preceding section, early attempts to create discrete objects from DNA usually involved a sophisticated workflow including multi-step assembly reactions with low overall yield. In contrast, the assembly of DNA origami structures takes place in a simple and robust single-pot reaction. Scaffold and staple strands are mixed in the presence of divalent ions in order to screen the repulsion between helices and to stabilize the stacked form of the crossover four-way junctions (see Figure 4.4b) [201]. In cases where divalent ions such as magnesium are not desirable, they may be substituted with elevated concentrations of monovalent ions [202]. Staple strands typically are added in excess to reduce errors and improve the folding yield. To facilitate the self-assembly reaction, the mixture is heated and thermally annealed for a few hours up to several days (see Figure 4.4c). The actual self-assembly or folding reaction was found to take place in a narrow temperature range that depends on details of the structure design and scaffold sequence [200]. The resulting structures are purified from the reaction mix via gel extraction, filter- or PEG purification (see Figure 4.4d). The folding success is assessed with nanoscale imaging techniques such as atomic force microscopy or transmission electron microscopy (TEM).

4.1.3 DNA-Lipid Interactions

A major challenge in realizing an artificial membrane penetrating pore from DNA is its insertion and anchoring within the lipid membrane. While protein channels contain

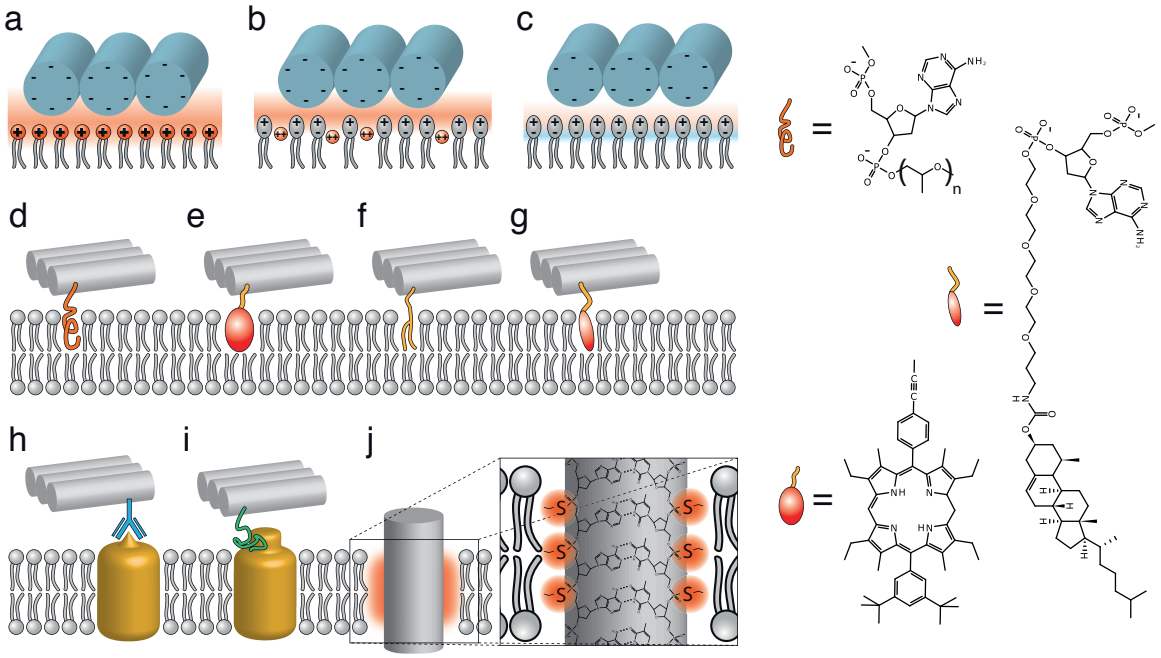

Figure 4.5: DNA-Lipid Interactions. a-c): Electrostatic binding to a) cationic lipids, b) zwitterionic lipids in the presence and c) in the absence divalent cations. d-g): Amphiphilic DNA conjugates with d) PPO, e) porphyrin, f) lipid, g) cholesterol. h-i): Interactions involving membrane-associated proteins. h) DNA-antibody conjugates, i) aptamer-protein interaction. j) Hydrophobic ethyl-thiophosphate backbone modification.

hydrophobic patches that interact with the hydrophobic core of the lipid membrane, a DNA origami structure is highly hydrophilic and strong interactions are needed to compensate for the energetic cost of inserting a part of it into the membrane core. Moreover, the interaction must be localized to facilitate association in the right orientation. In the following, we review different ways to bind DNA to lipid membranes and discuss their dependence on buffer conditions as well as their preference for specific lipid phases. The bigger part of this discussion is also published in [203].

Electrostatic Interactions. As a negatively charged polyelectrolyte, DNA strongly interacts electrostatically with cationic lipids such as DOTAP[1] or DOTMA[2] (see Figure 4.5a). In their presence, DNA is compacted and forms spherical "lipoplexes" [204]. The interaction is strongest for low salt concentrations, when electrostatic screening effects are small [205].

In the presence of divalent cations such as Mg^{2+} or Ca^{2+}, DNA also binds strongly to zwitterionic lipids [206, 207], but the mechanism of the interaction is not fully understood. While for anionic lipids divalent cations are assumed to bridge negatively charged lipid headgroups and the DNA backbone, for zwitterionic lipids the cations are thought to insert between the phosphates of neighboring lipid molecules. This

[1] 1,2-dioleoyl-3-trimethylammonium-propane
[2] 1,2-di-O-octadecenyl-3-trimethylammonium propane

neutralizes the negative charge on each lipid, resulting in a net positive charge (see Figure 4.5) [206, 207]. However, some studies report weak binding to zwitterionic lipids also in the absence of divalent cations (Figure 4.5c) [208, 209], potentially mediated by ion-dipole interactions [210]. Electrostatic binding is also affected by lipid composition and phase behavior. dsDNA was observed to preferentially bind to the liquid-ordered (L_o) phase [209, 211], which may be explained by the closer packing and thus higher surface charge density of the lipids. For the design of a DNA-based channel that attaches to the lipid membrane in a defined orientation, electrostatic interactions may be not desirable. Using low concentrations of divalent ions in combination with large concentrations of monovalent ions, electrostatic interactions between DNA origami structures and lipid bilayers can be suppressed effectively [203].

Hydrophobic Functionalization. DNA-based nanostructures can also be attached to lipid membranes using DNA conjugates with lipids or other hydrophobic molecules (see Figure 4.5d-g). Such DNA-lipid conjugates are commonly used for gene transfection. Moreover, they can be used to induce vesicle fusion [212, 213] or to specifically crosslink vesicles or even cells [214–216]. Lipid-DNA conjugates can be generated by incorporation of lipids during DNA synthesis using phosphoramidite coupling, or post-synthetically by conjugation to thiol- or amino-modified DNA oligonucleotides. The conjugation step can be performed directly on a lipid membrane containing a small fraction of reactive lipids [217].

Cholesterol is probably the most commonly used lipid for DNA conjugation, although its association with membranes is weak compared to other lipid-DNA conjugates. This can be compensated by the use of multiple cholesterol modifications, however, and already a combination of two cholesterols was observed to lead to almost irreversible binding to membranes [218]. DNA origami structures can easily be modified with several cholesterol moieties. By varying the number of modifications, the strength of the interaction may be fine-tuned to provide good membrane association at an acceptable level of aggregation. For cholesterol-modified DNA origami structures, strong attachment to lipid bilayers can be achieved even at high monovalent salt concentrations [203]. Even binding to bilayers with negative DOPS[3] is observed under such conditions [219].

The binding properties of cholesterol are strongly affected by the nature of the linker through which it is attached to DNA. Cholesterol alone influences lipid membrane packing and increases its order [220]. In contrast, cholesterol linked to tetraethylene glycol (TEG) was not observed to alter membrane structure. In DLPC[4]:DPPC[5]:chol mixtures with coexistent solid and fluid phases, chol(-TEG)-DNA conjugates were observed to partition into the liquid disordered phase (L_α) only [221]. In mixtures containing two fluid phases such as DOPC[6]:DPPC:chol, chol(-TEG)-DNA conjugates

[3] 1,2-di-O-octadecenyl-3-trimethylammonium propane
[4] 1,2-dilauroyl-sn-glycero-3-phosphocholine
[5] 1,2-dipalmitoyl-sn-glycero-3-phosphocholine
[6] 1,2-dioleoyl-sn-glycero-3-phosphocholine

distributed evenly into both phases, while cholesterol alone is known to strongly prefer the L_o-phase. Bivalent conjugates were observed to prefer the L_o over the L_α phase for this lipid mixture. A similar behavior was observed for DNA origami structures in presence of Mg^{2+}. Both chol- and chol(-TEG)- modified structures were observed to prefer the ordered (L_o) phase of phase separated GUVs (giant unilamellar vesicles) [203, 219]. In absence of Mg^{2+}, the chol(-TEG)- modified structures were predominantly found in the disordered (L_α) phase.

Apart from lipids, other hydrophobic molecules can be attached to DNA. For example, DNA has been conjugated to α-tocopherol [222], polypropyleneoxide (PPO) [223], or porphyrin [224, 225] (see Figure 4.5f), and conjugates were shown to incorporate into lipid membranes. Finally, the DNA backbone itself may be alkylated to become hydrophobic [226] (see Figure 4.5g).

Interactions Involving Membrane-Bound Proteins. DNA may also be coupled to membranes via membrane-associated molecules. These can be highly specific for a certain cell type, or even for the disease state of a cell, and thus can be utilized for targeting biological membranes more specifically. Binding to membrane proteins has been achieved using aptamer-target interactions [227, 228], DNA-antibody conjugates [229, 230], or by direct covalent coupling [231]. Such interactions do not, however, necessarily involve a direct interaction with the lipid membrane itself.

4.2 Channel Design and Assembly

The shape of our synthetic channel[7] is inspired by the natural channel protein α-hemolysin [32], but it differs from it in its physical properties such as charge, hydrophobicity, and size. It was constructed via molecular self-assembly with scaffolded DNA origami (cf. Section 4.1.2) using the 7249 base M13mp18 scaffold (for a detailed assembly and purification protocol as well as for caDNAno maps and staple sequences, see [232]). The channel's structure is illustrated in Figure 4.6a. It consists of two modules: a stem that penetrates and spans a lipid membrane, and a barrel-shaped cap that adheres to the *cis*-side of the membrane. Adhesion to the lipid bilayer is mediated by 26 cholesterol moieties that are attached to the *cis*-facing surface of the barrel (Figure 4.6a, see below). The stem protrudes centrally from the barrel and consists of six double-helical DNA domains that form a hollow tube. The interior of this tube acts as a transmembrane channel with a diameter of $\approx 2\,\text{nm}$ and a length of $\approx 42\,\text{nm}$ and runs through both stem and barrel (Figure 4.6b and c). Transmission electron microscopy (TEM) images taken from purified structures (Figure 4.6d) confirmed that the intended shape is realized (see [232] for details on TEM imaging).

Scaffold Loops. The channel's duplex domains incorporate only 4865 bases of the M13mp18 scaffold. The remaining 2384 bases are distributed among loops of unpaired

[7] Channel design, assembly and TEM imaging were conducted by Thomas G. Martin

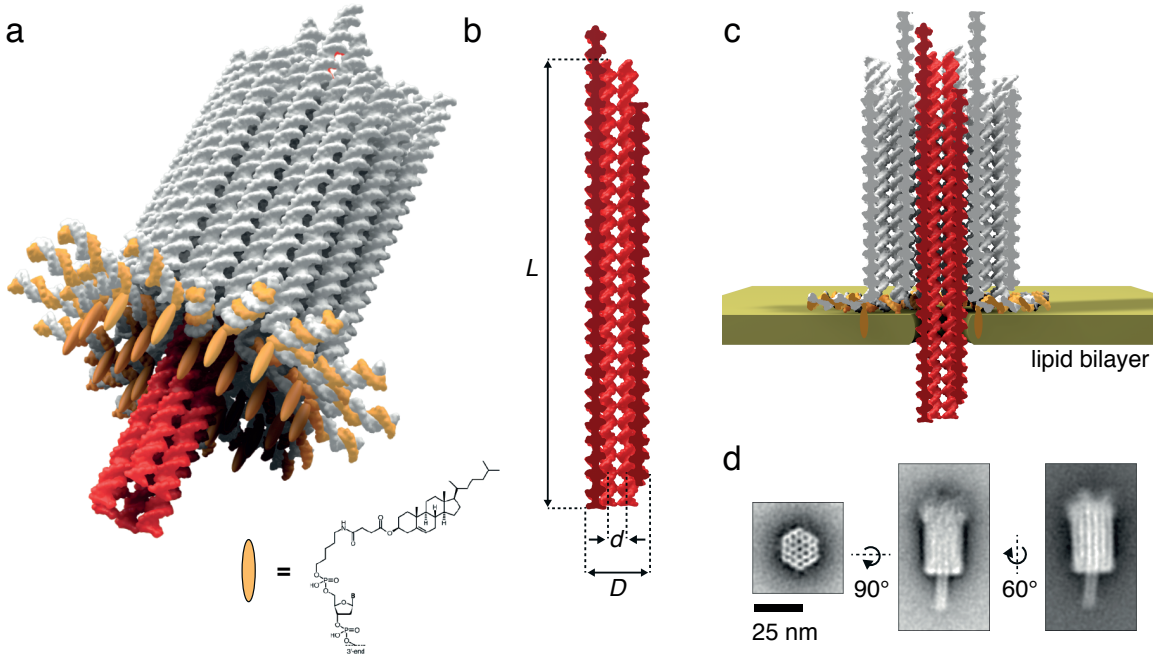

Figure 4.6: Synthetic DNA Membrane Channels. a) Illustration of the channel formed by 54 double-helical DNA domains packed on a honeycomb lattice. Red: transmembrane stem. Orange strands with orange ellipsoids indicate cholesterol-modified oligonucleotides that hybridize to single-stranded DNA adaptor strands. b) Geometric specifications of the transmembrane channel. Length $L = 47\,\text{nm}$, tube diameter $D = 6\,\text{nm}$, inner diameter $d = 2\,\text{nm}$. The length of the central channel fully surrounded by DNA helices is 42 nm. c) Cross-sectional view through the channel when incorporated in a lipid bilayer. d) Averaged negative-stain TEM images obtained from purified DNA channel structures (class averages, for raw images please see [232]), fuzzy regions indicate scaffold loops).

DNA extending from the duplex termini. The end of the stem features a 44 base loop and two 30 base loops while from the opposing surface of the barrel several loops with lengths from 24 to 238 bases extend (cf. Figure 4.6d, see caDNAno maps in [232]). On the *cis*-facing surface of the barrel, several short 4 base loops are present.

Cholesterol Modifications. To promote binding of the DNA channel to lipid bilayer membranes in an orientation that facilitated penetration of the stem through the lipid membrane, cholesterol-modified DNA oligonucleotides were hybridized to single-stranded adaptor strands protruding at 26 positions from the *cis*-facing surface of the 'barrel' domain (cf. Figure 4.6, staple sequences and design diagrams in [232]). The cholesterol-modified DNA oligomers had the sequence 5'-CCTCGCTCTGCTAATCC-TGTTA-3'. Depending on the position of the modification (5' or 3') on the adaptor strand, the cholesterol moiety can either be placed in close vicinity of the channel structure or within a distance of 22 bases from the cap. Both versions were investigated in our studies and showed electrically detectable interactions with the lipid membrane. The proximal modification version was found to lead to more stable insertions into the membrane, whereas the distal version mainly caused transient current fluctuations that were not stable upon voltage reversal. We thus used the proximal modification for the experiments presented here.

4.3 Interactions with Lipid Membranes

4.3.1 TEM Studies on SUVs

To study the binding of our channel to lipid membranes, we incubated DNA channels with small unilamellar vesicles (SUVs)[8] created from POPC[9]. POPC is a phospholipid with an unsaturated fatty acid chain that adopts the liquid disordered (L_α) state under our experimental conditions. Following incubation, we stained the mixture with uranyl formate and imaged the samples with transmission electron microscopy[10] (see [232] for a detailed protocol). DNA channels with cholesterol modification were predominantly found attached to lipid membranes. Most frequently, we observed vesicles with one or two channels attached and a size comparable to the channel itself (Figure 4.7a), while more rarely we observed larger SUVs with multiple channels attached (Figure 4.7b). DNA channels without the cholesterol modification did not show any appreciable interaction with the membranes (see [232] for additional image data for modified and unmodified channels). As apparent in Figure 4.7a and b, the cholesterol modifications at the stem-face of the barrel promote binding of the DNA channel to lipid membranes in the desired orientation in which the cholesterol-modified face of the barrel forms tight contact with the membrane and the stem appears to protrude into the lipid bilayer. Accordingly, on membrane patches formed from burst vesicles (Figure 4.7c) a considerable fraction of channels is found in an otherwise less probable 'upright' position. A detailed statistical analysis of channel binding as a function of projected vesicle diameter (from the TEM image it cannot be judged whether the vesicles burst and restructured or collapsed on the TEM grid) and number of cholesterol modifications is shown in Figure 4.7d and e. The fraction of vesicles with at least one DNA channel increased with the number of cholesterols, with good binding starting above ≈ 10 cholesterols per channel. We considered only channels bound in an orientation supporting stem insertion for this analysis. Considering the mechanism of contrast in negative-stain TEM imaging, the notion of membrane-insertion of the stem domain of the DNA channel is further supported by differences in stem visibility for channels attached to small vesicles with high contrast as shown in Figure 4.7a compared to channels attached to larger, low-contrast vesicles (Figure 4.7b). A detailed discussion on TEM evidence for membrane insertion of the stem domain is given in [232].

4.3.2 Discussion

Lipid Arrangement and Energetics. The results of our TEM experiments shown above suggest that the synthetic DNA channels could form membrane pores as designed. As the energetic cost for insertion of the charged DNA structure into the hydrophobic core of the lipid membrane would be prohibitively high, membrane penetration is thought to involve reorganization of the lipid bilayer around the charged

[8] SUVs were provided by Jonathan List
[9] 1-palmitoyl-2-oleoyl-sn-glycero-3-phosphocholine
[10] TEM imaging was performed by Thomas G. Martin

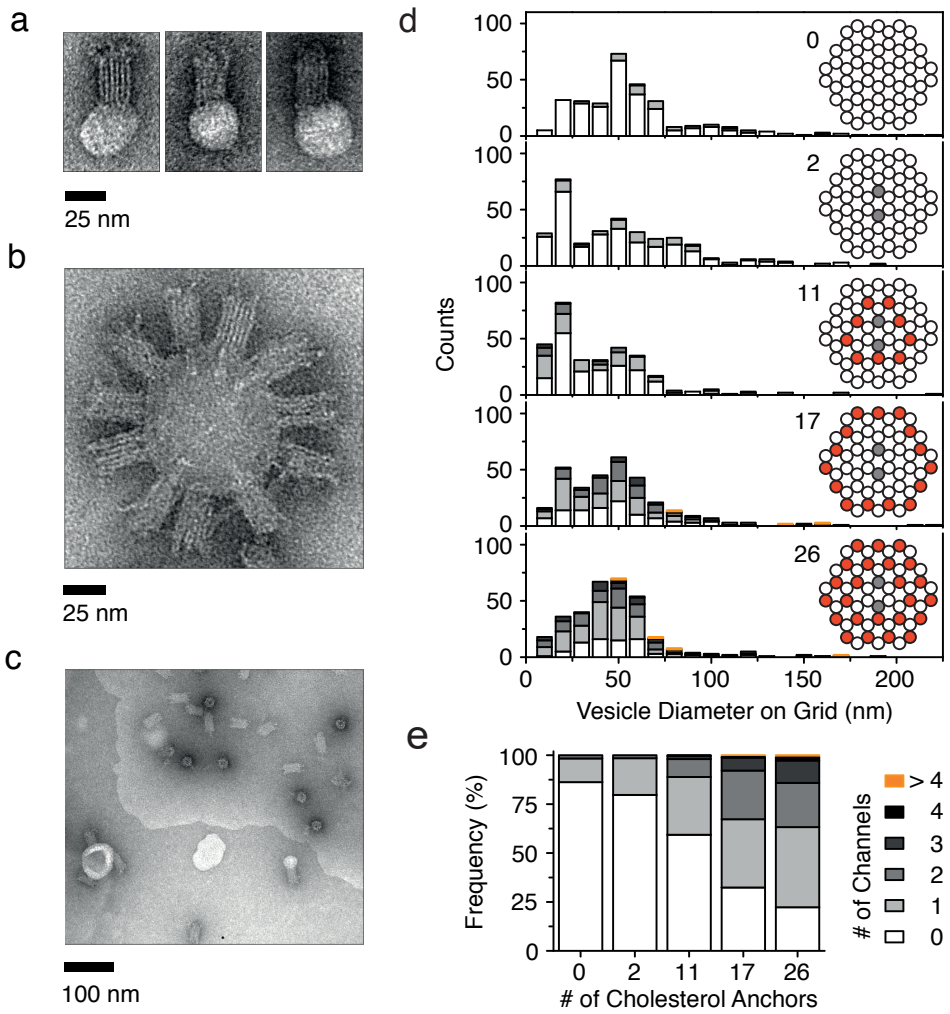

Figure 4.7: Interaction with Lipid Membranes. a), b) Examples for TEM images of DNA channels adhering to small unilamellar vesicles (SUVs) made from POPC lipids. Samples were stained with uranyl formate. (see [232] for protocol and more images). c) TEM image of DNA channels binding to an extended lipid bilayer in the upper right part of the image. DNA channels are found predominantly on lipid covered areas or sticking to SUVs. d) Statistical analysis of channel interaction with SUVs. Histograms showing the SUV size distribution (apparent diameter upon adsorption to the TEM grid) and the number of bound channels for five different cholesterol modification patterns (see inset; red: barrel modification, gray: stem modification, number of modifications is indicated). For color-coding, see panel e). Only channels adhering to SUVs in an orientation conformable with insertion of the stem into the membrane were considered. e) Combined channel binding efficiency for all vesicle sizes shown in d).

stem, with the hydrophilic lipid headgroups oriented towards the DNA structure. This orientation not only is energetically favorable in terms of hydrophobicity, but also allows the zwitterionic lipid headgroups to interact electrostatically with the stem as described in Section 4.1.3. The energy gain due to insertion of the 26 cholesterol modifications at the bottom face of the barrel-section into the lipid membrane is expected to readily outbalance the cost of forming such a toroidal lipid arrangement (for a quantitative discussion, see [232]). Four years after initial publication of our results, molecular dynamics and coarse-grained simulations were published confirming above assumptions concerning lipid arrangement and energetics [233].

Mechanism of Stem Insertion. On the actual process of membrane insertion, no studies have been carried out so far. We surmise that the channels initially adsorb to the lipid bilayer through some of their cholesterol modifications. Due to their concentric arrangement around the stem domain, the latter needs to orientate more and more perpendicular to the membrane with increasing number of cholesterol insertions while the barrel is remaining in close contact. The stepwise energy gain associated with subsequent insertion of cholesterols may therefore facilitate crossing the energy barrier associated with hole formation. This barrier is expected to be strongly dependent on lipid type and composition, as well as on membrane curvature and presence of phase boundaries or defects [234, 235]. As described above, the POPC membranes of our SUVs are in the highly fluctuating L_α state, in which the mobility of individual lipids is high compared to bilayers in one of the more ordered states. This not only is expected to lower the barrier associated with hole formation, but also may enhance the rate of defect formation, which are thought to nucleate insertion of membrane proteins [236, 237]. Moreover, SUVs feature a higher membrane curvature than larger vesicles or suspended lipid bilayers, which is known to enhance insertion of pore forming proteins [238], possibly due to a larger separation of lipid headgroups. We suppose that under these conditions, the energetic barrier for penetration of the stem domain of our channel through the lipid membrane is low enough to allow for spontaneous insertion, whereas under different conditions such as for the very stable planar lipid bilayers formed from DPhPC[11] for our electrophysiology experiments, additional stimulus may be required for insertion (see Section 4.4.1).

4.4 Electrophysiological Characterization

To characterize the electrical conductivity of the membrane pores formed by our DNA channel, we performed single-channel electrophysiological experiments on planar lipid bilayers using the integrated chip-based setup described in Section 2.3.2. 100 µl of electrolyte solution containing 1 M KCl, 10 mM Tris and 1 mM EDTA at pH 8 were added to the measurement chamber. 1 - 2 µl of lipid solution prepared from DPhPC and dissolved in octane at a concentration of 10 mg/ml were pipetted in the vicinity

[11] diphytanoylphosphatidylcholine

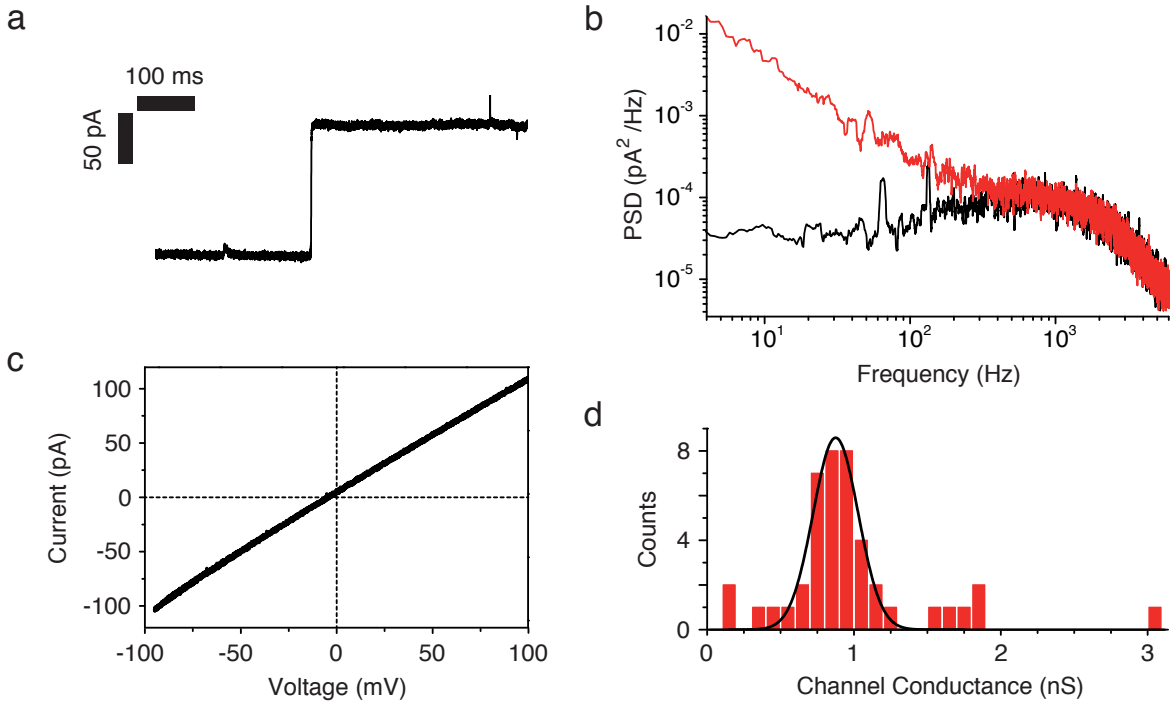

Figure 4.8: Electrical Characterization. Performed on painted DPhPC bilayers on a chip-based electrophysiology setup. a) Stepwise increase in ionic current during an incorporation event at $V = 200\,\text{mV}$. b) Noise power spectra before (black line) and after the incorporation of a single origami pore (red line). Current traces were recorded at 100 mV at a filter frequency of 3 kHz. c) Current-voltage dependence of the channel after incorporation. d) Histogram of channel conductances obtained from 43 incorporation events. The black line depicts a Gaussian fit. We obtain a mean channel conductance of $0.87 \pm 0.15\,\text{nS}$.

of the cavities followed by painting the lipid bilayer. Current recordings were either acquired on up to 16 wells in parallel using the Triton$^+$ amplifier board or a single well was switched to the EPC 9 single channel amplifier. All data were analyzed using custom MATLAB routines (see Appendix A.3 for details).

4.4.1 Channel Incorporation into Planar Lipid Bilayers

We added synthetic DNA channels at low concentrations ($\approx 200\,\text{pM}$) to the *cis* side of the MECA chip setup and applied voltage pulses as described in Section 2.3.2 to facilitate incorporation into the membrane [45, 239]. As with biological channels, successful membrane incorporation of individual synthetic DNA channels manifested itself in a stepwise increase in transmembrane current (Figure 4.8a) along with an increase in low frequency noise (see Figure 4.8b, cf. 2.5). In control experiments with a modified channel structure lacking the central stem, no such incorporation events were observed (see Appendix A.3). The synthetic DNA channels displayed an average Ohmic conductance of $G = 0.87 \pm 0.15\,\text{nS}$ ($I = 174\,\text{pA}$ at $200\,\text{mV}$) per channel in a solution containing 1 M KCl and 2 mM $MgCl_2$ (Figure 4.8c and d).

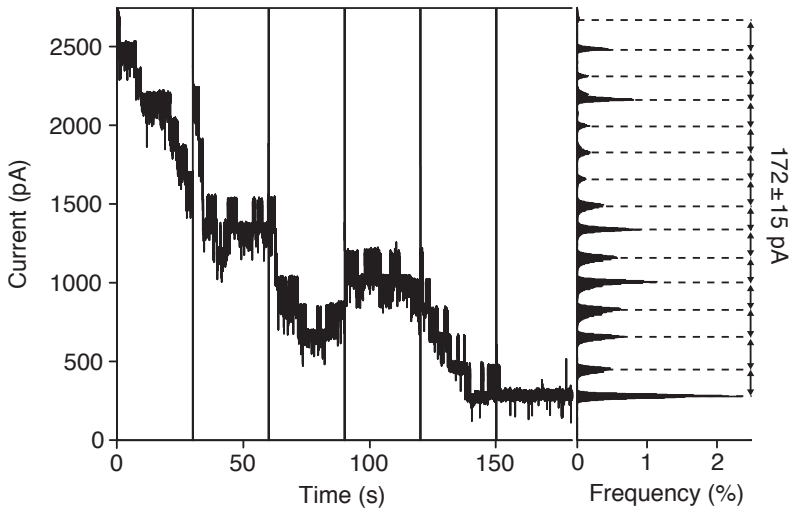

Figure 4.9: Multiple Insertions. Time course of the ionic current across the lipid bilayer with multiple origami channels incorporated at 200 mV bias voltage. The DNA channel structures used here had a 7 nt modification at site M2 (see Section 4.4.2). Vertical lines mark limits of continuous recording. The recording was suspended at these positions with no applied bias for a few ms. Right: Corresponding all-point current histogram, showing a mean peak-to-peak distance of 172 ± 15 pA This corresponds to a mean conductance change of 0.86 ± 0.08 nS.

Multiple Insertions. In experiments with elevated membrane voltages (e.g., constant $V = 200$ mV), occasionally large conductances/currents were observed that corresponded to the presence of several channels in parallel (see Figure 4.9). We assume that in such cases, cholesterol-mediated aggregates of DNA channels initially adsorbed to the membrane inserted into the membrane in concert. In these cases, we observed stepwise closing of single channels over time. Partial recovery of the channel conductance is observed after setting the bias temporarily to 0 mV. A detailed study of transient closing events at moderate membrane voltages around 100 mV can be found in the following section. As shown in Figure 4.9, current histograms display the quantized conductance of the DNA channels.

Discussion. The simple geometrical model for channel conductance described in Chapter 3 (see Eq. 3.1) predicts $G = 0.79$ nS for a channel with diameter 2 nm and length 42 nm. While this prediction fits our experimental findings surprisingly well, a simple resistor approximation may not be adequate for a quantitative description of the channel conductance. As observed previously [240], ionic current through the cap and stem of our structure may contribute significantly to the channel conductivity. On the other hand, it is expectable that the stem is being compressed by the surrounding lipid membrane, leading to a smaller effective channel cross-section in the bilayer region.

Three years after initial publication of our results, first molecular dynamics simulations on a DNA channel became available [241], confirming the aforementioned leak conductivity and channel compression. Moreover, a strong electroosmotic contribution

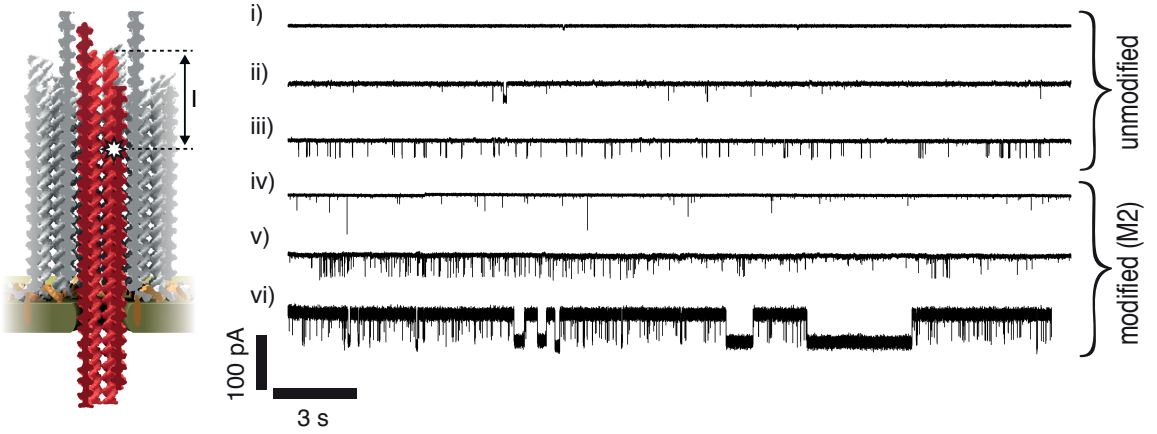

Figure 4.10: Channel Gating. Left: Channel cross-section indicating the position of a 7 base strand extension acting as a 'defect' in channel 'mutants' (star symbol; $l = 15\,\text{nm}$ for mutant M1 and $l = 14\,\text{nm}$ for mutant M2). Right: Typical current traces obtained from unmodified 'wildtype' channels (i-iii), and 'mutants' with modification M2 (iv-vi).

to the channel conductance was observed. Designed as a six-helix bundle following the DNA origami principle, the simulated structure is similar to the stem region of our channel (cf. Figure 4.17c, Section 4.6). Its reduced length ($\approx 14\,\text{nm}$) and the absence of a cap allow for fewer crossovers, potentially resulting in a more flexible structure that is more susceptible to mechanical tension. As a major difference, it features hydrophobic DNA backbone modifications in the membrane spanning region of the channel, reducing the solute-accessible pore diameter and causing a very different lipid arrangement around it. Since Mg^{2+} ions were not included in the simulations, the negative charge of the DNA's phosphate backbone is not screened, potentially leading to a less compact channel conformation and more pronounced surface effects such as electroosmotic flow. Due to the listed differences between the simulated structure and our channel, a quantitative comparison of our channel's electrical properties with theory remains elusive.

4.4.2 Channel Gating

The majority of natural ion channels are more than just small holes, i.e. their conductance switches between multiple distinct states caused by conformational transitions [85]. In single channel recordings of synthetic DNA channels we observed similar behavior, i.e. the channels exhibited fast transitions between different conductance levels. While for high bias voltages the channels underwent full closure as seen, e.g., in Figure 4.9, at lower voltages we typically observed current reduction amplitudes ΔI corresponding to fractions of a single channel conductance (see Figure 4.10, trace i-iii). The characteristics of these transitions varied considerably between individual channels. While some channels were subject to frequent current transitions (Figure 4.10, Trace iii), others displayed no transitions at all (Figure 4.10, Trace i).

We hypothesized that thermal fluctuations of the channel structure may be the

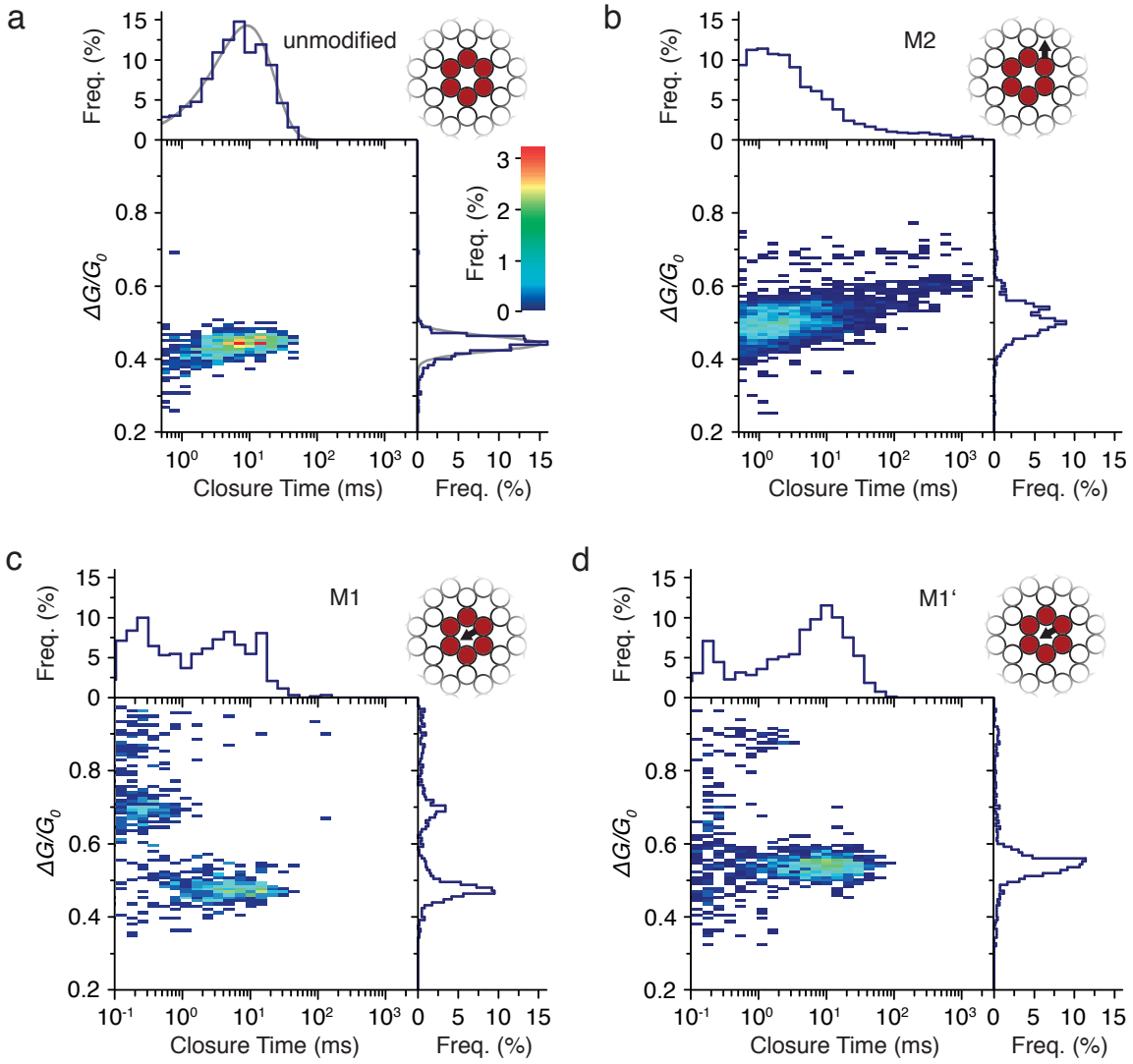

Figure 4.11: Gating Characteristics. Heat maps of the relative conductance change versus dwell time for the closure states of a) a 'wildtype' channel, b) a channel with modification (sequence TTTC-CGG) on site M2, c) with modification (sequence TTTCCGG) on site M1, d) with a modification on site M1 but with sequence $(dA)_7$ at 100 mV bias voltage (see inset for orientation of the modification sequence). Event frequencies were calculated from a total of 697 events (wildtype), 2532 events (M2), 623 events (M1) and 931 events (M1') recorded. On the right and on the top the corresponding histograms are shown. Gray lines correspond to mono-exponential (top) and Gaussian fits (right).

cause for this gating behavior and that stochastic unzipping and rezipping of short double-helical DNA domains in the channel may contribute to it. To test this idea, we designed three channel 'mutants' that differed from the 'wild type' channel only by a single-stranded heptanucleotide protruding from the central transmembrane tube (see Figure 4.10, for caDNAno maps please refer to [232]). This modification potentially could fluctuate, block the channel, or act as a 'handle' for the electric field and lead to partial unzipping of a DNA staple strand. We studied three channel mutants – for modification M1 the heptanucleotide pointed into the central channel, for modification M2 the staple extension was oriented away from the central stem (pointing into one of the "other" holes of the cap, see insets of Figure 4.11 and caDNAno schemes in [232]). Modification M1' is located at the same site than modification M1, but with sequence $(\mathrm{dA})_7$. The mutant channels showed more pronounced gating than wildtype channels (Figure 4.10, trace iv-vi). In particular, we found that both modifications increased the frequency of gating events. While we never observed a current signal without gating for the mutants, many of the unmodified DNA channels did not display gating events (such as current trace i in Figure 4.10).

Gating Characteristics. We analyzed the closed state kinetics and associated conductance changes of four exemplary channels, i.e. an unmodified channel and one for each modification (M2, M1 and M1') at moderate bias voltage (100 mV). Our findings are shown in Figure 4.11. For the unmodified channel, we observe a sharp single-peaked population with a mean conductance drop $\Delta G/G$ of $45 \pm 2\,\%$ and a dwell time distribution that follows a single exponential with time constant of 9.0 ± 0.3 ms (see Figure 4.11a). The characteristics of channel mutants M1 and M1' (cf. Figure 4.11c and d) resemble each other. Both feature a peak comparable to the unmodified channel, accompanied by additional subpopulations with faster kinetics. A weak population with conductance reduction $> 80\,\%$ is observable in both cases. However, while for the channel with modification M1 a sharp subpopulation with a mean conductance drop of $70 \pm 2\,\%$ is apparent, only a few sparsely distributed events in this region may indicate its presence for modification M1'. For the latter a cluster of events with a conductance change close to the unmodified channel but considerably faster kinetics is observed, which cannot be discerned for modification M1. For the channel with modification M2 (Figure 4.11b, heptanucleotide pointing away from the stem), a broad distribution of gating events is observed with closure kinetics covering the entire detection range. While for modifications M1 and M1' event durations were typically below 100 ms, here some events feature closure times of up to several seconds. In contrast, only a small fraction of events (approx. 2 %) features conductance drops in the range of 60 % to 80 % and no conductance drops larger than 80 % are observed. As indicated by the skewed form of the distribution in the heat map and the multimodal nature of the conductance change histogram, the distribution presumably consists of multiple overlapping subpopulations that cannot be clearly resolved.

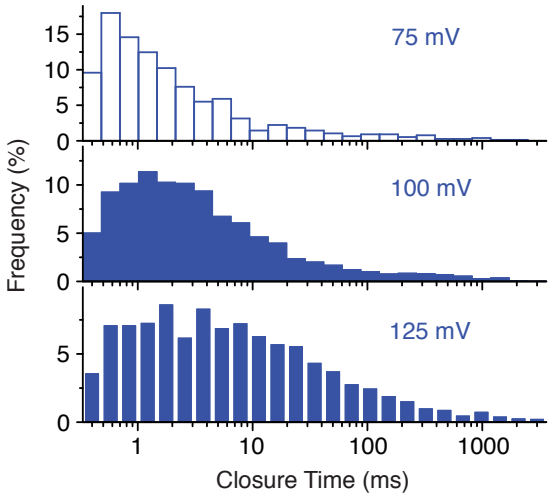

Figure 4.12: Gating Voltage Dependence. Closure time for a mutant channel with modification M2 obtained from current recordings at 75 mV (top), 100 mV (middle) and 125 mV (bottom) membrane voltage.

Voltage Dependence. In Figure 4.12, channel closure kinetics for modification M2 are shown for three different membrane voltages. Although the distributions' aforementioned multimodal nature impedes a quantitative analysis, we observe a clear tendency towards longer timescales with increasing membrane voltage.

Discussion. In our gating studies on synthetic membrane channels with different modifications, we observe a common population for the unmodified channel and for two different mutants. For the third mutant, its presence is also indicated. We attribute this population to the channel structure's inherent gating behavior. The mutant channels give rise to additional subpopulations, mostly with faster kinetics. For the modifications M1 and M1' with the heptanucleotide modification protruding into the central channel, most subpopulations feature considerably larger conductance drops with single events reaching up to 97 %, while for modification M2 with the heptanucleotide pointing away from the central channel comparable events were rarely recorded and never exceeded 80 %. From this observation we conclude that in fact the central channel constitutes the primary current path across the channel structure, even inside the barrel region ≈ 17 nm away from the lipid membrane, where the heptanucleotide modification is located. Moreover, our findings show that the presence of unpaired oligonucleotides inside the channel may give rise to conductance changes similar to those observed for the unmodified channel. For modification M2 we observe events with slow kinetics in the order of seconds, implying structural changes that go beyond transient unzipping and rezipping of a single staple strand. These findings show that the transmembrane current is in fact dependent on fine structural details of the synthetic DNA channel. The gating kinetics slow down with increasing voltage (Figure 4.12), indicating coupling of the closure events to electrostatic forces. Although the kinetics of the channel's inherent gating behavior suggest a simple two-

state process with a first order rate transition in between, a detailed analysis including the kinetics of the open state would be necessary to confirm this notion. For the channel mutants, a more sophisticated model e.g. based on a Hidden-Markov chain would be necessary [242].

4.5 Single Molecule Sensing

The central pore of the DNA channel features a diameter of $\approx 2\,\mathrm{nm}$, which is expected to be wide enough not only to allow for ionic transport across the membrane as demonstrated in the previous section, but also to permit translocation of considerably larger molecules such as single stranded DNA. Provided that a single stranded DNA tail can be electrophoretically captured and threaded into the channel, its presence may be detected by a transient reduction of the transmembrane current as in resistive sensing applications with α-hemolysin (cf. Chapter 3). As for α-hemolysin, larger DNA secondary structures such as hairpins or guanine quadruplexes [243] are not expected to fit through the channel. In order to translocate, the structures need to unzip or unfold, thus providing a characteristic time delay in the current blockades that reveals the kinetics of structural transitions (cf. Section 3.4.1). Here, we performed planar bilayer recordings as described in the previous section to study the unfolding of single DNA hairpins and guanine quadruplexes using the synthetic membrane channel.

4.5.1 Hairpin Unzipping

For the first set of experiments, we used a DNA hairpin with a 9 base pair long stem with sequence ATCTACATA flanked by 50 thymidines on the 3' end and 6 thymidines on the 5' end dissolved in 10 mM Tris, 1 mM EDTA solution at pH 8. The hairpin molecules were initially added to the *cis* side of a lipid membrane containing a single synthetic DNA channel that displayed a stable current baseline without gating and a conductance of 0.3 nS, corresponding to the lower end of the distribution shown in Figure 4.8d. Application of a positive voltage bias leads to transient current blockades we attribute to capture, unzipping, and translocation of the hairpin structures (4.13a and b). Reversal of the bias after approximately ≈ 30 minutes again led to transient current blockades with decaying event rate, which we attribute to molecules that had accumulated in the 1.6 pl *trans* compartment by previous translocation through the DNA channel. It is reasonable to expect an accumulated analyte concentration in the *trans* compartment in the range of $\sim 0.1\,\mu\mathrm{M}$ from the observed event rate and measurement time. The blockade amplitudes for both translocation directions were $\Delta I_{cis-trans} = 11.9 \pm 2.7\,\mathrm{pA}$ and $\Delta I_{trans-cis} = 20.3 \pm 4.2\,\mathrm{pA}$. The blockade dwell times were distributed exponentially with a characteristic lifetime of $\tau_{cis-trans} = 1.5 \pm 0.1\,\mathrm{ms}$ and $\tau_{trans-cis} = 1.0 \pm 0.1\,\mathrm{ms}$, respectively (Figure 4.13c). Additional experiments in forward direction yielded a reduced time constant of $0.9 \pm 0.1\,\mathrm{ms}$ at elevated membrane voltage (250 mV) and increased dwell times in the range of several milliseconds

at reduced membrane voltage (100 mV, for measurement data see Figure A.4 in Appendix A.3).

4.5.2 Quadruplex Unfolding

In another set of experiments, we added quadruplex-forming oligonucleotides with a 60 thymidine long single-stranded tail (Q-T60) to the *cis* side of a membrane containing a single synthetic DNA channel with a conductance of 0.7 nS (Figure 4.13d and e). Again, we observed transient current blockades, which we attribute to the capture and threading of quadruplex DNA molecules into the channel, followed by unfolding and subsequent translocation through the pore. Removal of the analyte from the *cis* compartment restored a stable baseline current without blockades. Subsequent addition of quadruplex DNA with a longer $(dT)_{125}$ tail (Q-T125) led to larger current blockades. The average current blockades were $\Delta I_{Q-T60} = 5.6 \pm 1.0$ pA and $\Delta I_{Q-T125} = 15.3 \pm 2.3$ pA, respectively (Figure 4.13f). The blockade dwell times are distributed exponentially with characteristic lifetimes of $\tau_{Q-T60} = 9.7 \pm 0.5$ ms and $\tau_{Q-T125} = 8.2 \pm 0.9$ ms. While τ_{Q-T60} was obtained from a single-parameter fit, an additional area scaling parameter was necessary to obtain a satisfying fit for the Q-T125 dwell time distribution. This is a consequence of the excess of long-lived blockade events with dwell times > 40 ms (see top histogram in Figure 4.13f), which are not covered by the mono-exponential model. As the distribution had to be rescaled by a factor of 0.87, these outliers correspond to 13 % of the total event count. We found these long-lived blockade events to increase strongly for prolonged measurement times (see Appendix A.3), indicating an accumulation effect. A comparable effect was not observed for the Q-T60 measurement or for the Q-T125 backward translocation measurement (see below).

Experiments in Backward Direction As for the hairpin unzipping experiments shown in the previous section, we also recorded backward translocation events (from *trans* to *cis*) of Q-T125 DNA at negative bias potential. The corresponding scatter plot is shown in Figure 4.14. The scatter plot histograms yield a blockade amplitude that is 27 % lower (11.2 pA) and a characteristic dwell time that is 2.3 times shorter (3.5 ms) than for the forward direction.

4.5.3 Discussion

Both the hairpin and the quadruplex structures used in this study trigger a characteristic transient reduction of the ionic current across the DNA channel as detected by their current blockades. Upon analyte addition, blockades were only observed at positive membrane voltage as expected for the electrophoretic transport of a negatively charged molecule such as DNA across the membrane. For the hairpin structures we observe a decrease of the blockade duration with increasing transmembrane voltage (by a factor of 0.6 ± 0.1 for a voltage increase of 50 mV) as expected for the voltage-assisted unfolding of a DNA secondary structure. In the following, we will make attempts to

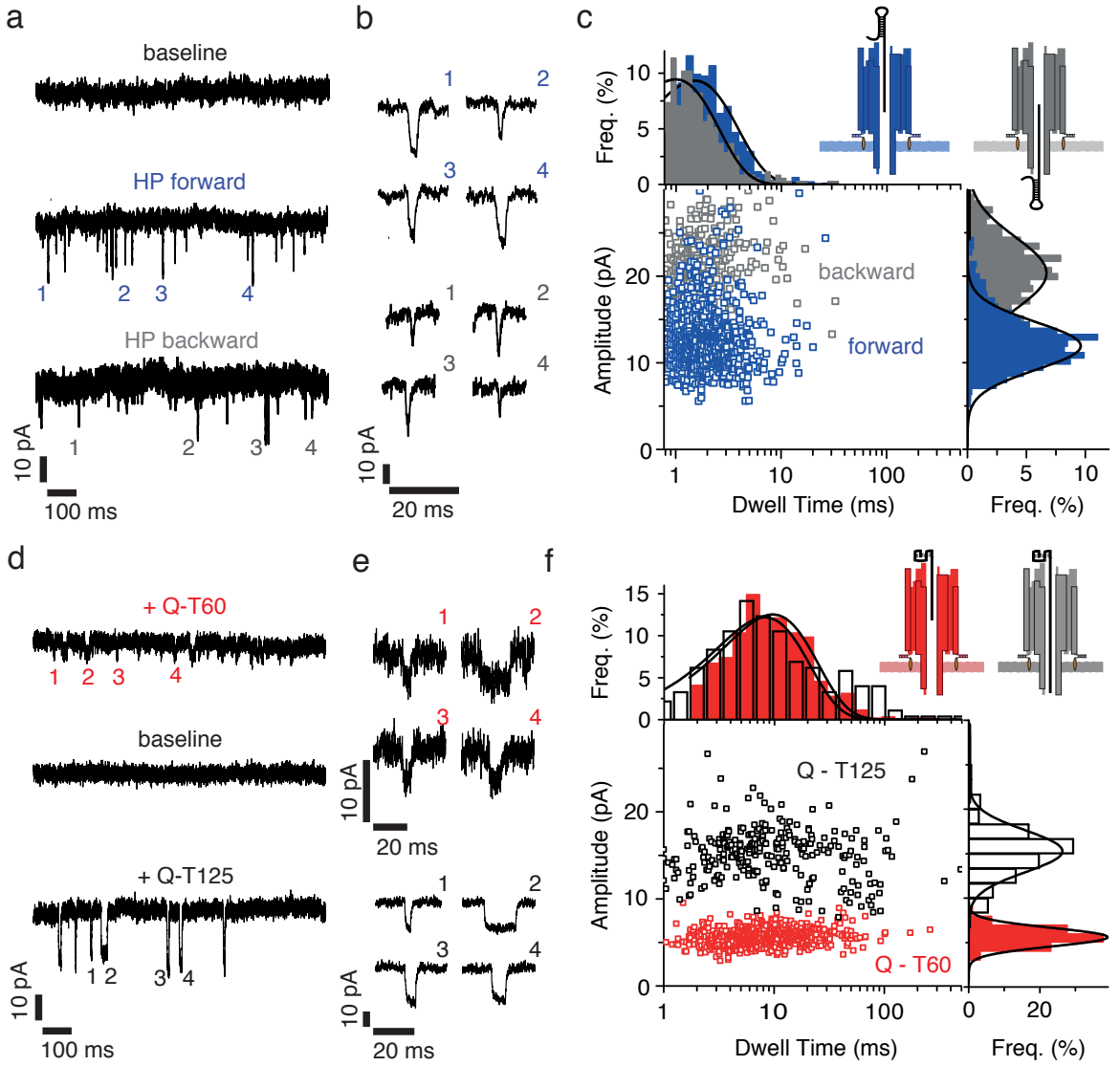

Figure 4.13: Hairpin Unzipping and Quadruplex Unfolding. a) Addition of DNA hairpins (T5-HP-T50) to a DNA channel at $V = 200\,\text{mV}$ results in the appearance of current blockades, indicating unzipping and translocation of hairpin molecules from *cis* to *trans*. Hairpins accumulated on the *trans* side can also be transferred back from *trans* to *cis* by a reversal of the transmembrane voltage. b) Representative blockade events for forward (top) and backward (bottom) translocation of DNA hairpins. c) Scatter plot for the translocation of T5-HP-T50 DNA through a DNA channel from *cis* to *trans* (blue) and from *trans* to *cis* side (gray) at V = 200 mV, and corresponding histograms. The lines correspond to single exponential (top) and Gaussian fits (right). Each data point corresponds to a single translocation event. In total, 777 (forward) and 379 (backward) events were analyzed. d) Top: Typical current trace at $V = 200\,\text{mV}$ after addition of 10 µM of Q-T60 DNA. Middle: Current trace after rinsing with buffer solution. Bottom: Current trace after subsequent addition of 10 µM of Q-T125 DNA to the same channel. e) Representative blockade events for Q-T60 (top) and Q-T125 DNA (bottom). f) Scatter plot of the current blockade versus dwell time for the translocation of Q-T60 (red) and Q-T125 DNA (black) through the DNA channel. In total 631 (Q-T60) and 279 (Q-T125) events were analyzed. On the right and on the top corresponding histograms are shown. The lines correspond to single exponential (top) and Gaussian fits (right).

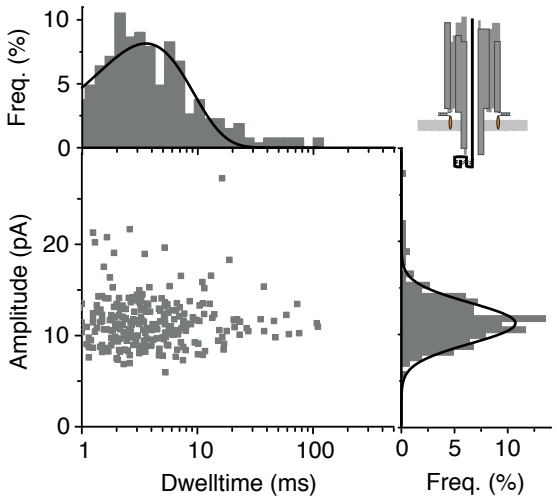

Figure 4.14: Quadruplex Unfolding in Backward Direction. Scatter plot of the current amplitude vs. dwell time for the *trans-cis* translocation of Q-T125 through the artificial ion channel at negative bias voltage (-200 mV), accompanied by the corresponding histograms. 266 Events were detected. The solid line corresponds to single exponential (top) and Gaussian (right) fits to the histograms, yielding a time constant of 3.5 ms and a blockade amplitude of 11.2 pA, respectively.

relate the observed blockade amplitudes and time constants to the channel's structural details. Since the open channel conductance of the two DNA channels used in the hairpin and quadruplex experiments differed considerably, we limit ourselves to comparisons between experiments performed on the same channel.

Dependence of the Blockade Amplitude on Analyte Tail Length. In the experiments described above, molecules with polythymidine tails of different lengths (60 and 125 nt for the quadruplex structures, 50 nt for the hairpin) were investigated. A 125 thymidine tail fully stretched to its contour length has a length of $L_{DNA} \approx 50\,\text{nm}$ (assuming a base-to-base distance of 0.4 nm), i.e., it spans the whole length of the DNA channel (see [232] for considerations about the conformation of ssDNA inside the channel). In comparison, a 60 nt long tail corresponds to a length of $L_{DNA} \approx 24\,\text{nm}$, which occupies roughly half of the channel length. In the simple resistor pore picture discussed in Chapter 3, this would correspond to half the amount of blocked ions. Hence, for the ratio of blockade amplitudes ΔG_{125} of the quadruplex structure with 125 nt tail and ΔG_{60} of the corresponding structure with 60 nt tail one would expect a factor of ≈ 2. Experimentally, we observe a ratio $\Delta G_{125}/\Delta G_{60}$ of 2.7. For the hairpin unzipping experiments, where no dependence of blockade amplitudes on the translocation direction is expectable from the simple pore picture, we observe a 1.7-fold increase. However, as discussed in Section 4.4.1, it is reasonable to assume a partially conductive DNA channel structure, which would result in a more complicated electric field distribution. Since quantitative predictions for the electric field inside our channel are not at hand, we performed FEM calculations for a simplified geometry using COMSOL Multiphysics and its *Electric Currents* module. We modeled the duplex regions

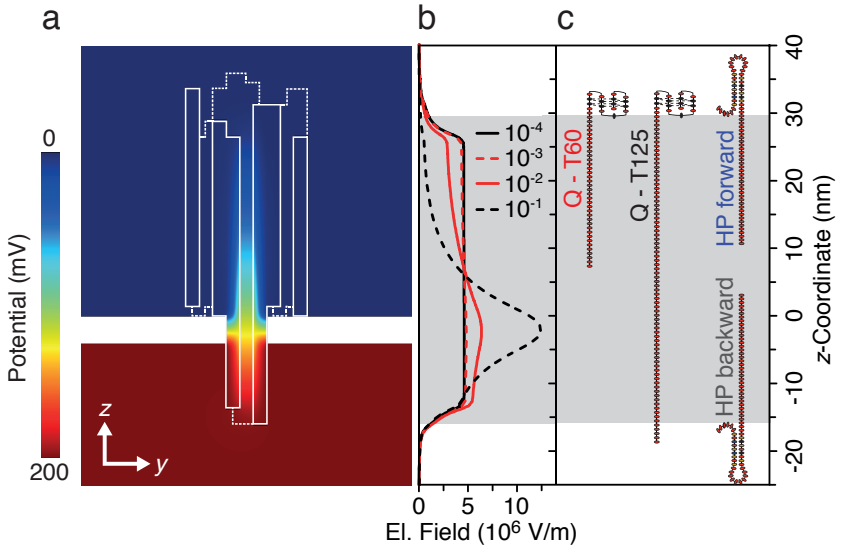

Figure 4.15: FEM Simulations. Simulated electric field and potential distribution of the DNA channel obtained by solving Poisson's equation numerically for a simplified channel geometry using COMSOL Multiphysics (see text). a) Color map of the electrical potential distribution at the cross-sectional y-z plane containing the channel's axis of symmetry calculated for a conductivity of 10^{-2} S/m of the DNA origami structure (white lines mark structure boundaries), 11 S/m bulk conductivity and an insulating bilayer (white). b) Electric field along the channel's axis of symmetry (z-axis) for conductivity values of 10^{-4} S/m (solid black line), 10^{-3} S/m (dashed red line) 10^{-2} S/m (solid red line) and 10^{-1} S/m (dashed black line) of the origami structure. c) Schematic illustration of the penetration depth of the structures used in translocation experiments before unzipping (cf. Figure 4.13).

of our DNA channel as cylinders ($d = 2$ nm) with conductivity σ_{DNA} and the bilayer as an insulating layer with thickness 4 nm. The channel inside and the solution compartments were modeled with KCl bulk conductivity (11 S/m [244]). Notably, this calculation can by no means serve as substitute for a detailed MD simulation, as it does not consider ion accumulation effects caused by the negatively charged phosphate backbone of the channel structure although the Debye screening length (≈ 0.3 nm) is comparable to the channel's dimensions. Moreover, we did not model the specifics of ion transport and fluid flow, neglecting effects such as electroosmosis, which may have a considerable influence due to the highly charged DNA backbone [241]. In fact, our calculations shall be considered an extension of the simple resistor approximation for channel conductance discussed in Section 4.4.1 and in Chapter 3, taking into account the channel's hexagonal structure and leak currents through it. In Figure 4.15a, the electric potential distribution along a cross-sectional plane through the channels axis of symmetry is depicted for $\sigma_{DNA} = 10^{-2}$ S/m. For zero leak conductivity, we obtain a channel conductance of 1.0 nS, which is 26 % larger than the value obtained from the simple pore picture above. This is a result of the channel cross-section of our simulation model, featuring a 30 % larger area than a circle with 2 nm diameter. For a leak conductivity of 10^{-2} S/m as illustrated in Figure 4.15a, we obtain a conductivity of 1.4 nS.

The corresponding electric field along the central axis of the channel is plotted in

Table 4.1: Simulation Results. Channel conductance and blockade ratios calculated for different leak conductivity values along with experimental results.

σ_{DNA} (S/m)	10^{-4}	10^{-3}	10^{-2}	10^{-1}	experimental
G_{sim} (nS)	1.0	1.0	1.4	2.9	0.87 ± 0.15
$\Delta G_{125}/\Delta G_{60}$	1.7	1.8	3.5	35	2.7
$\Delta G_{50fwd}/\Delta G_{50bwd}$	1.1	1.3	3.7	98	1.7

Figure 4.15b for four different values of σ_{DNA}. While we observe a homogeneous field distribution inside the channel for the insulating case ($\sigma_{DNA} = 10^{-4}$ S/m or less), for $\sigma_{DNA} \geq 10^{-3}$ S/m a considerable inhomogeneity of the electric field is apparent, which peaks at the bilayer position. As illustrated in Figure 4.15c, the quadruplex structures with 125 nt tail and the hairpin structures in backward direction extend into the bilayer region while the other structures do not. To obtain an estimate for the effect of leak conductance on the blockade amplitudes from our FEM calculations, we modeled the polythymidine tails as insulating cylinders with an effective diameter of 1 nm for ssDNA as described above and placed them inside the central channel according to the scheme in Figure 4.15c. The calculated ratios of blockade amplitudes for different tail length and translocation direction are summarized in Table 4.1 along with calculated channel conductance values and experimental results. For both ratios the experimentally obtained values lie between our calculations for a leak conductivity of 10^{-3} S/m and 10^{-2} S/m, respectively. Based on this qualitative agreement, we rationalize that the observed dependence of current reduction on tail length not only is another clear indication of translocation through the central channel of our DNA structures, but also supports the notion of a partially conductive channel structure that gives rise to an inhomogeneous electric field distribution inside the channel with its peak at the bilayer position. It has to be noted, however, that our considerations do not explain the lower blockade amplitude observed for the *trans-cis* translocation of the quadruplex structures with T125 tail, since it should span the whole length of the channel. With $\Delta G_{trans}/\Delta G_{cis} = 1.36$, the change is weaker than the difference between forward and backward translocation for the hairpin structure and in opposite direction. Should it affect our hairpin studies as well, the field-related conductance difference between forward and backward direction would have been underestimated from our measurements.

Dependence of Unfolding Kinetics on Tail length and Translocation Direction. As discussed above, we expect that due to leak conductance, molecules with tails that extend into the bilayer region are subject to stronger electric fields and therefore larger forces than molecules with tails not extending into this region. For our hairpin structures with short tails, this implies direction-dependent translocation kinetics, which is in agreement with our results. As expected for an increase in electrical force, we observe a reduced time constant for the backward direction (see Figure 4.13c). Accordingly, we expect a reduced dwelltime for the unfolding of quadruplex structures with 125 nt tail, which extends into the bilayer region, compared to the ones with 60 nt

tail. Although this trend is apparent in our experiments, here the shift ($18 \pm 12\,\%$ or $1.5 \pm 1.0\,\mathrm{ms}$) is considerably smaller. This is in accordance to unfolding experiments with α-hemolysin, where a considerably weaker voltage scaling is observed for G-quadruplex unfolding than for DNA hairpin unzipping (see [232]). The kinetics discussed above are all consistent with our simplified electric field considerations assuming leak conductance through the channel structure. However, this is not the case for our observations for quadruplex unfolding in backward direction. As the 125 nt tail is expected to extend along the entire channel length, the integrated electrophoretic force along the DNA channel should be independent of the direction of translocation.

Influence of Scaffold Loops. The differences in blockade amplitude and unfolding kinetics for the Q-T125 unfolding experiments discussed above indicates a directionality of the translocation process itself, which may be caused by steric or binding interactions at the entrance of the asymmetrically designed origami structure. A potential source for such interactions is given by the scaffold loops present at the duplex termini on both sides of the channel (cf. Section 4.2). Such binding interactions may also lead to the agglomeration of analyte molecules at the channel entrance over the course of a measurement run, potentially causing the time dependent increase of long-lived blockade events in forward direction. In fact, after addition of quadruplex DNA the event rate continuously increased, indicating that the DNA concentration at the pore entrance rises over time, however, this could as well have been caused by insufficient mixing upon analyte addition (we mixed very gently to avoid destruction of the membrane). Transient interactions of analyte molecules with scaffold loops may even mediate their capture into the channel. While molecular dynamics simulations on a related structure [241] (cf. Section 4.4.1) confirm electrophoretic transport of ssDNA across the channel, the authors question the possibility of electrophoretic capture. However, as no divalent ions were considered, the simulation conditions differ considerably from the present case.

4.6 Alternative Channel Designs

Based on DNA nanotechnology, the geometry of our synthetic membrane channels may easily be tuned to suit specific applications, e.g. for single molecule sensing. While the channel design described in Section 4.2 features a barrel-shaped cap and a hexagonally arranged transmembrane stem with an inner diameter of $\approx 2\,\mathrm{nm}$ that facilitates transport of ssDNA, we developed another channel structure[12] that consists of a flat top plate and a transmembrane stem with quadratic cross-section and an inner diameter of $\approx 4\,\mathrm{nm}$ (see Figure 4.16a and b). This channel features 57 cholesterol moieties and is large enough to allow transport of double stranded DNA [249]. A planar lipid bilayer recording with several incorporated channels exhibiting strong gating behavior is presented in Figure 4.16c.

[12]Design and TEM characterization were performed by Thomas G. Martin.

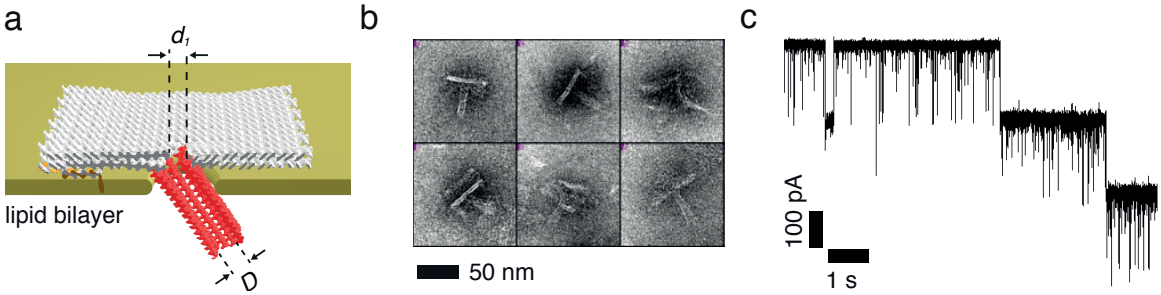

Figure 4.16: A Larger DNA Channel. a) Design of a DNA-based membrane channel (cross-sectional view) that features a quadratic transmembrane domain (red, $D = 4.2\,\text{nm}$) and a flat support (white) with a rectangular aperture (side length $d_1 = 3.7\,\text{nm}$ and $d_2 = 8.4\,\text{nm}$) b) Transmission electron micrographs of channel structures stained with uranyl formate. c) Current trace of multiple channels incorporated into a DPhPC bilayer using the MECA setup and 1 M KCl electrolyte at pH 8. Obtained at 150 mV bias.

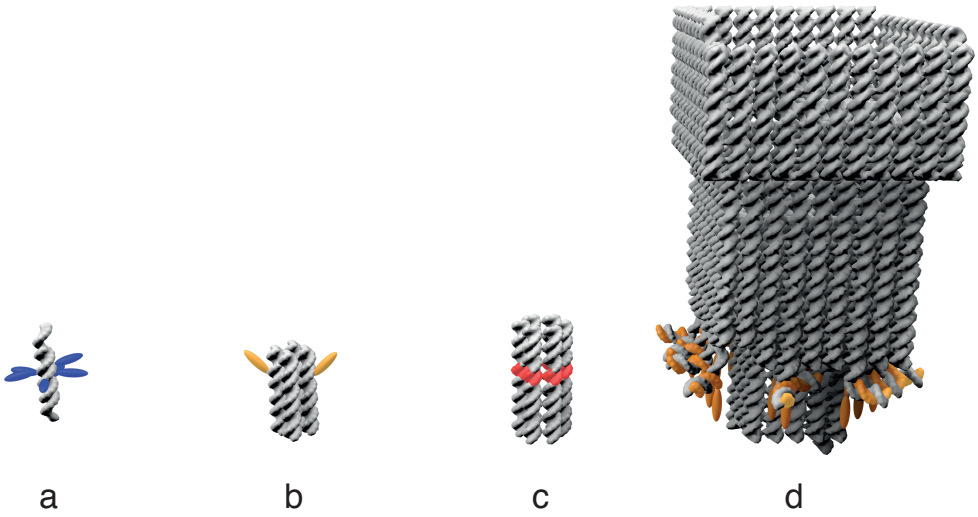

Figure 4.17: DNA Channels Created by Other Research Groups. a) Membrane-spanning duplex with six prophyrin anchors [245]. b) Four-helix DNA tile design with two cholesterol anchors [246]. c) Six-helix bundle with selectively alkylated DNA backbone [247]. A similar design featuring porphyrin anchors has been published as well [248]. d) Large conductance channel design with 19 cholesterol moieties and a $\approx 6 \times 6\,\text{nm}$ channel cross-section [233].

Since initial publication of our results, several DNA-based channels with different geometries have been developed by other research groups [233, 245–248] (see Figure 4.17), ranging from a channel formed by a single DNA duplex [245] to a large structure featuring a transmembrane stem with a $\approx 6 \times 6$ nm inner cross-section [233]. Several different concepts have been devised to anchor these channels into a lipid membrane, including selective alkylation of the DNA backbone [247] (cf. Figure 4.17c and Section 4.1.3) and functionalization with porphyrin anchors [245, 248] (see Figure 4.6). Independently, solid state nanopores have been combined with DNA origami structures to create hybrid sensing devices [240, 250].

4.7 Conclusion

In this chapter, we described the *de novo* design and assembly of a synthetic DNA-based membrane channel. We briefly introduced the concepts of structural DNA nanotechnology, where immobilized junction motifs are used to assemble multiple DNA strands into extended objects. We exemplified the basics of scaffolded DNA origami by the design of a short hexagonal tube and gave an overview of the different interactions between DNA and lipid membranes.

Thereafter, we illustrated the channel's design in detail. It features a barrel-shaped cap modified with 26 cholesterol moieties from which a membrane-penetrating stem extends. Using negative stain TEM, we confirmed its adhesion to lipid membranes in the intended orientation and found first evidence for the formation of a transmembrane pore by insertion of the channel's stem into the lipid membrane. We discussed the energetics of channel insertion and proposed a toroidal lipid arrangement around it with the headgroups facing the stem. Moreover, we speculated that subsequent membrane incorporation of cholesterol modifications may drive spontaneous channel insertion into SUVs.

Further evidence for formation of an electrically conductive transmembrane pore was provided by planar lipid bilayer recordings. Facilitated by voltage pulses, we observed the incorporation of single DNA channels with a conductance of 0.87 ± 0.15 nS and Ohmic behavior across the measurement range of -200 mV to +200 mV. Similar to biological channels, we observed voltage dependent gating transitions which we could relate to the channel's structural specifics.

Moreover, we confirmed that our synthetic DNA channels can be used as sensing devices to discriminate analyte molecules by studying their translocation characteristics. Specifically, we investigated the force-induced unfolding of DNA hairpin structures and G-quadruplexes. Our findings indicate additional current pathways through the channel's sidewalls, causing an inhomogeneous electric field distribution inside the channel which peaks at the bilayer position.

Finally, we demonstrated the versatility of DNA-based membrane channels by presenting an alternative channel design featuring a quadratic stem with $\approx 4 \times 4$ nm cross-section.

5 Solid State Nanopore Sensors

Since their initial demonstration by Li et al. in 2001 [251], an increasing number of studies has utilized solid-state nanopores [13] for single molecule sensing applications. Compared to lipid-embedded channels like α-hemolysin [32], MspA [5] or the DNA-based channels presented in Chapter 4, solid-state nanopore devices have clear limitations in their range of application. Their geometric properties are less defined and are subject to pore-to-pore variations. Functional groups may only be introduced into the pore lumen in an unspecific fashion [157] and often unwanted analyte interactions with the pore sidewalls are observed [252, 253]. However, solid state nanopore devices also do have clear advantages to their biological counterparts: Based on solid state membranes, they offer superior mechanical and chemical stability, allowing considerably higher voltages to be applied. Their sizes can be tuned easily to suit specific applications such as sensing of proteins [83, 98, 252–259] or dsDNA-protein complexes [135, 260–264]. Lastly, solid-state fabrication methods enable more complex nanodevices that combine multiple nanopores [58] or equip them with electronic sensing capabilities [265–267] and some of their drawbacks may be overcome by the use of hybrid devices [240, 250, 268, 269].

In this chapter, we report two specific applications for solid-state nanopore sensors. Following a brief outline of the fabrication procedures, we present a novel solid-state nanopore force spectroscopy platform, which we use to study DNA-histone interactions in individual nucleosomes (cf. Figure 5.1a). Moreover, we describe a method to obtain the electrophoretic mobility of DNA in a single molecule experiment by electrophoretic time-of-flight measurements with a pore-cavity-pore nanodevice (cf. Figure 5.1b).

5.1 Fabrication

Solid-state nanopores have been realized in various material systems, including silicon-based materials [251, 254, 255, 270–275], polymers [252, 276], glass [277, 278], graphene [279–281] and (transition) metal oxides [282, 283]. Likewise, a broad range of techniques was utilized to fabricate pores, including "drilling" methods using highly focused electron [273, 279–282] or ion beams [251, 272], electron beam lithography [254, 255, 275] and ion track etching [252, 274, 276].

In the experiments presented in this chapter, silicon nitride membranes on silicon substrate were used. This material system offers high mechanical stability and can be processed using standard semiconductor tools. Depending on the nature of an experimental task, specific combinations of material and fabrication methods are better suited than others. As the experiments shown in this chapter differ greatly in their

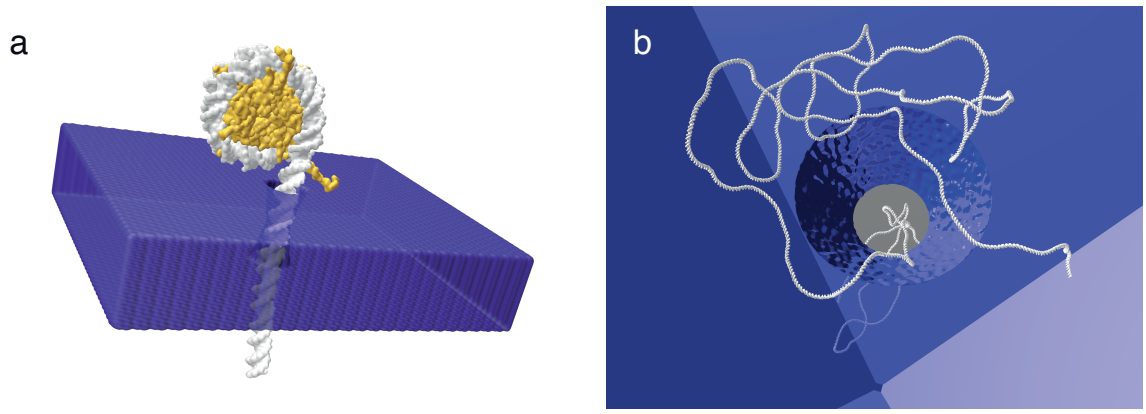

Figure 5.1: Solid State Nanopore Experiments Presented in This Work. a) Nucleosome unraveling with small solid state pores (see Section 5.2). b) DNA time-of-flight experiments with a pore-cavity-pore nanodevice (see Section 5.3).

requirements, we used two different fabrication methods, each suited particularly well for the specific experimental task.

5.1.1 TEM Drilling of Locally Thinned Silicon Nitride Membranes

Among solid state pore fabrication techniques, TEM-drilling is one of the most established ones [13]. Pores can be created and characterized in a single fabrication step and diameters down to 1 nm can be realized. Moreover, visually assisted tuning of the pore geometry is possible after initial pore formation. In this section, the fabrication of TEM-drilled pores in locally thinned silicon nitride membranes is outlined[1]. A more detailed description can be found in Wanunu et al. [78].

The fabrication procedure (see Figure 5.2a) can be divided into three parts. In the first part, devices with freestanding membranes are created from ⟨100⟩ silicon wafers with a nominal thickness of 500 µm, which are coated with a 2.5 µm thick SiO_2 passivation layer and a 40 nm thick LPCVD[2]-grown silicon nitride layer (Si_3N_4) on each side. Optical lithography and reactive ion etching (RIE) with carbon tetrafluoride (CF_4) are used to process a quadratic window into the bottom SiN layer. The membrane is then released in the upper silicon nitride layer and individual devices are separated via wet chemical etching. Buffered oxide etch (BOE) is used to remove the SiO_2 passivation layers and the silicon substrate is etched anisotropically with KOH. The silicon nitride layers serve as masking layers for these steps. In the second part, electron beam lithography and reactive ion etching are used to thin a $\sim$50 µm square on the silicon nitride membrane to a final thickness of $\sim$15 - 20 nm. In the third part, a nanopore is drilled in the thinned membrane region by exposing it to the highly focused beam of a transmission electron microscope (JEOL 2010FEG).

[1]The TEM-drilled nanopores used for the experiments described in Section 5.2 were fabricated by Spencer Carson and other members of the Wanunu lab (Northeastern University, Boston, MA, USA).

[2]low pressure chemical vapor deposition

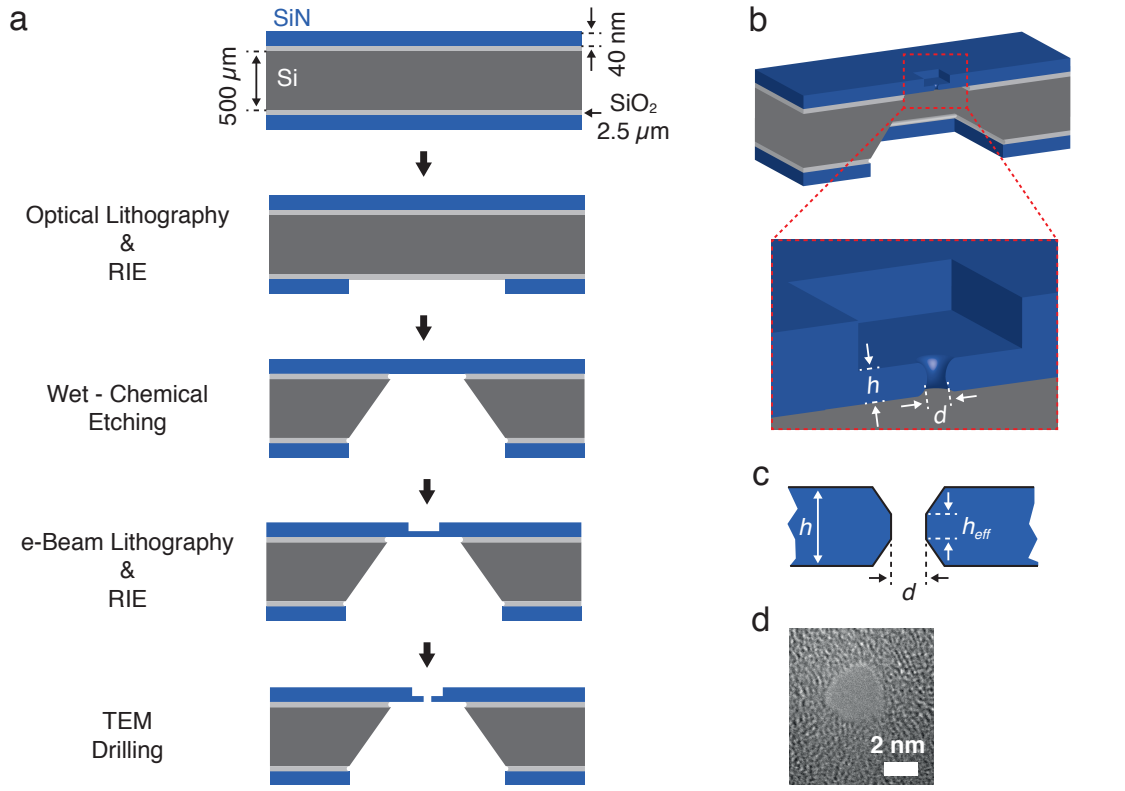

Figure 5.2: TEM Drilling of Nanopores in Ultrathin Membranes. a) Schematic outline of the fabrication procedure. Devices are created from silicon wafers passivated with a SiO_2 layer and coated with a Si_3N_4 layer on each side. Freestanding silicon nitride membranes are released in each device using optical lithography and reactive ion etching (RIE), followed by wet chemical etching. Membranes are thinned locally using e-beam lithography and reactive ion etching. Nanopores are drilled by exposing the membrane to the highly focused beam of a transmission electron microscope. b) Schematic of the final nanopore device with a magnified view of the thinned region containing the nanopore. Dimensions are not drawn to scale. c) Cross-sectional view with dimensions. d) TEM micrograph of a pore with a diameter of 2.8 nm.

A schematic of the final nanopore device is shown in Figure 5.2b. Pores created by TEM-drilling feature an 'hour-glass' shape, with a narrow 'waist' region at the center [284]. We classify our pores by their diameter d and effective length h_{eff} (see Figure 5.2c). The latter corresponds to the length of an equivalent cylinder with equal diameter and conductance, and is obtained from ionic current measurements [78, 87] (see Section 3.1). A representative TEM image of a nanopore with a diameter of 2.8 nm is shown in Figure 5.2d. The method described here allows tuning of the pore diameter with 0.1 nm precision and effective lengths down to 2 nm can be realized. These two parameters quantitatively describe the sensing performance of a nanopore device, i.e. their ionic conductance and blockade ratio upon DNA translocation (cf. Figure 3.3). Another important factor is the parasitic device capacitance, as it contributes to the device's current noise (cf. Section 2.5) and limits its voltage switching performance (cf. Section 3.3.1). The SiO_2 layers in between the silicon nitride layers and the silicon substrate help to greatly reduce this capacitance. In combination with silicone

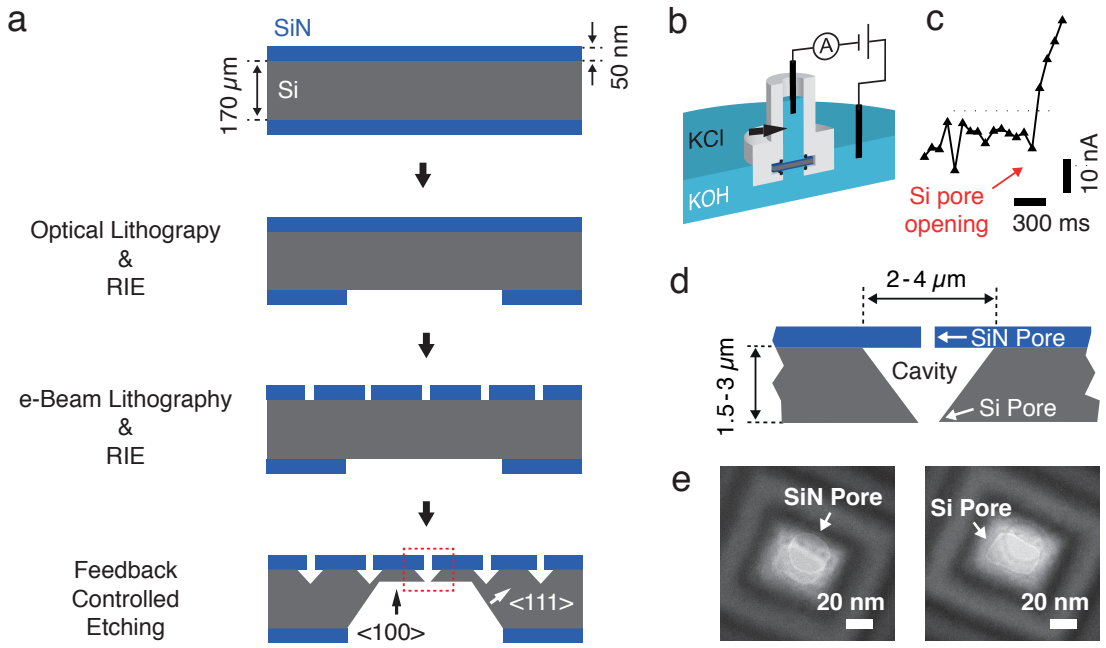

Figure 5.3: Pore-Cavity-Pore Device Fabrication. a) Schematic outline of the fabrication procedure. Devices are created from silicon wafers coated with a silicon nitride (SiN) layer on each side. A quadratic window is released in the bottom layer by optical lithography and reactive ion etching (RIE). An array of nanopores is created in the top layer by e-beam lithography and RIE. In an anisotropic etching step with KOH solution, pyramidal cavities form in the silicon substrate below the pore positions and a large etch pit forms at the bottom side. b) Schematic of the setup used for feedback-controlled etching. The PCP chip is mounted into a PTFE chamber which separates the etchant (KOH) from the electrolyte solution (KCl) c) Representative current trace during pore formation. When one of the cavities is being truncated, a pore forms at its apex and a sharp increase in ionic current is detected (see red arrow). d) Magnified view of the PCP device (see red box in (a)), illustrating pore locations and cavity dimensions. e) TEM micrographs of a PCP device with focus on the SiN pore (left) and on the Si pore (right), respectively.

elastomer passivation upon mounting (see Section 2.4), values of 6 pF are possible [55]. Typically, we observe capacitance values of ~ 30 pF in our experiments.

5.1.2 Pore-Cavity-Pore Device Fabrication

We developed a solid state nanodevice featuring two nanopore sensors separated by a femtoliter-sized cavity [58]. Referring to its geometry, we named it pore-cavity-pore (PCP) device. It is created by combining two different pore fabrication techniques: electron beam lithography [254, 255, 275] and feedback-controlled wet chemical etching [271]. In this section, its fabrication is described briefly. For more details refer to Pedone et al. [58].

The PCP fabrication procedure is shown in Figure 5.3a. We use a 170 µm thick silicon substrate with ⟨100⟩ orientation, which is coated with 50 nm of silicon nitride on each side. As for the TEM-drilled nanopore devices described in the previous section, a square window is opened in the bottom silicon nitride layer at first, using

optical lithography and reactive ion etching (RIE). In the second step, an array of nanopores is defined by electron beam lithography and transferred into the top silicon nitride layer by another reactive ion etching step. In the following wet chemical etching step with KOH solution, cavities form in the silicon substrate underneath the pores and a large etch pit develops at the bottom window. This process is highly anisotropic, i.e. it depends on the crystallographic orientation of the silicon substrate. Due to a difference in activation energies, etching of the ⟨111⟩ crystal direction is suppressed by a factor of 30 - 100 compared to the ⟨100⟩ direction [285]. The cavities therefore feature an inverted pyramidal geometry with sidewalls that are defined by the (111) crystal planes. These are oriented in an angle of 54.7° to the base, which corresponds to a (100) plane. For the final stage of the etching process, the PCP chip is mounted into a PTFE chamber which only exposes the bottom side of the chip to the etchant, while the top side is exposed to KCl solution (see Figure 5.3b). With this configuration, a voltage can be applied across the device while the ionic current is monitored (see Figure 5.3c). As soon as the growing etch pit truncates one of the cavities, a pore forms at its apex and ionic current can flow across the device. This increase in ionic current is detected and triggers instantaneous termination of the etching process.

A schematic of the final device geometry is shown in Figure 5.3d. The size of the pyramidal cavity can be tuned by varying the duration of the initial KOH etch step. Until now, we created devices with cavity heights ranging from 1.5 to 3 µm. The individual pores of the device can be imaged via transmission electron microscopy (TEM, see Figure 5.3e). The pore created in the top silicon nitride membrane (SiN pore) features a conical shape with an aperture angle of ∼71° [275]. By varying the e-beam exposure dose, pore sizes of 13 - 70 nm can be realized. The pore at the cavity apex (Si pore) features a more quadratic shape and sizes down to 7 x 11 nm were achieved so far. Its aperture angle of 38° is given by the crystal structure. A feature common to TEM micrographs from PCP devices are the alternating bright and dark regions surrounding the Si pore. These originate from Bragg diffraction of electrons at the silicon lattice and reflect the pyramidal cavity geometry.

5.2 Probing DNA-Histone Interaction with Nanopore Force Spectroscopy

The nucleosome provides the fundamental level of organization in eukaryotic chromatin. Its high resolution structure was obtained from X-ray crystallography studies in 1997 [286]. Promoted by a common structural motif, the so-called 'histone-fold', the histone proteins H2A, H2B, H3 and H4 assemble – two copies of each – into a disc-shaped octamer core. Around this core, ∼146 basepairs dsDNA are wound 1.7 times (see Figure 5.4). This assembly has an axis of pseudo-symmetry, the dyad axis. An extensive list of interactions between nucleosomal DNA and histones was identified, which can be categorized in the interaction of helix dipoles with backbone phosphates, hydrogen bonds, salt bridges, nonpolar contacts with the backbone sugar groups and

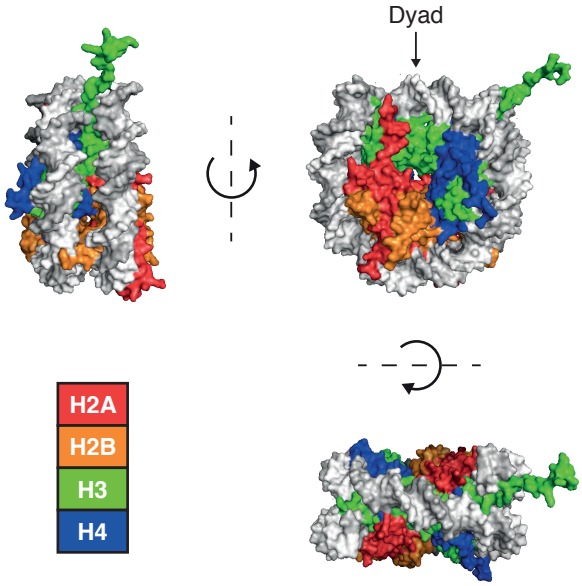

Figure 5.4: The Nucleosome. Structure of the nucleosome core particle as published in [286] (PDB ID: 1AOI). A 147 bp long stretch of dsDNA (gray) is wrapped around the histone octamer. Histones are color coded. The dyad axis is indicated.

insertions of arginine side chains into the minor groove. With exception of the last category, all of these interactions happen between histones and the DNA backbone, which suggests a rather unspecific interaction. However, side chain insertions prefer certain sequence motifs [287]. Another important contribution to the sequence-specificity of the DNA-histone association derives from the fact that the DNA has to bend sharply in order to adopt the tightly wrapped conformation observed in nucleosomes, as the local deformability of DNA is strongly sequence dependent [288]. While nucleosomes were observed to assemble on virtually any sequence, competitive reconstitution assays confirmed sequence dependent affinities [289, 290] and synthetic sequences with particularly high affinities were generated [291] using the SELEX (Systematic Evolution of Ligands by EXponential Enrichment) technique [292, 293].

However, it is highly controversial to what extent intrinsic nucleosome interactions determine their positioning *in vivo*. This question is of particular importance, as nucleosomes sterically hinder the accessibility of specific genomic regions to proteins that effect molecular processes such as transcription regulation and DNA repair [294–296]. While some studies suggest that positioning is governed by statistical packing principles [297–300], others indicate genomically encoded nucleosome positioning [301, 302].

Moreover, nucleosomes are highly dynamic structures, which undergo spontaneous 'breathing' transitions, where a stretch of DNA transiently unwraps from the histone core [303]. This mechanism provides access to nucleosomal DNA for DNA-binding proteins and is important for the invasion of nucleosomes by DNA polymerase. The accessibility of nucleosomal regions may also be altered dynamically via ATP-dependent remodelers [304, 305] or by epigenetic modifications to DNA and

histone proteins [306]. The latter are of particular relevance, as they can be related to cancer development [307, 308]. However, the mechanisms by which epigenetic factors influence the accessibility of nucleosomal regions are not fully understood. Despite evidence that some epigenetic modifications modulate the intrinsic nucleosome stability [309], our knowledge of the impact of various histone and DNA modifications on nucleosome stability is limited.

Nucleosomal interactions have been studied using a variety of bulk and single-molecule techniques, the latter of which can provide information on both stability and dynamics. Single-molecule techniques include equilibrium measurements such as Förster resonance energy transfer (FRET), which probes stability over time using a distance-dependent fluorescence pair [310], as well as optical tweezers [10, 311–313] and atomic force microscopy [314, 315], which apply force to end-tethered DNA molecules (cf. Section 3.4.6). These single-molecule experiments rely on chemically modifying the DNA and/or histone proteins for photo-labeling or surface tethering. This requirement makes single-molecule measurements more complicated to perform, often resulting in experiment-specific outcomes. For example, while DNA methylation is a well-recognized epigenetic mark involved in gene expression, its effect on the stability and dynamics of nucleosomes is highly controversial: FRET and other fluorescence-based studies have reported increases in the rigidity and compaction of nucleosomes upon CpG methylation [316, 317], while other studies have reported a looser, more open conformation for the methylated state [318, 319].

Single molecule force spectroscopy experiments are appealing in this context, as they can provide insights into the energy landscape of the interaction. The response towards external forces is supposed to give the most valuable information on how intrinsic nucleosome interactions affect their mechanical invasion. However, the nature of force application in such experiments may impact the measurement. In fact, in conventional single molecule stretching experiments the rotation of the spool geometry of the nucleosome is supposed to influence the force signatures [320]. Geometry can also present a limitation on the type of interactions that can be probed. For example, DNA-histone interactions at the axis of symmetry, the so-called dyad axis, are difficult to study in stretching experiments because the histone octamer may not completely unbind upon DNA stretching [321]. This problem was recently tackled by pulling apart the nucleosomal DNA (i.e., the duplex is unzipped) to remove it from the histone core [313, 322]. However, an unraveling pathway that involves unzipping of the double-stranded DNA (dsDNA) helix wound around the core octamer is not necessarily comparable to a pathway where the DNA helix remains intact. Presumably due to their high level of complexity, single-molecule force spectroscopy studies that probe the influence of epigenetic modifications on intranucleosomal interactions have yet to be reported. Nanopore force spectroscopy (NFS) is a promising alternative for this task. Using lipid-embedded protein channels such as α-hemolysin, NFS has been used for studying the stability of DNA secondary structures like hairpins [120, 121, 134, 140, 323] or aptamers [138], as well as an exonuclease I-ssDNA complex [139]. However, biological channels that translocate dsDNA are not as well established and simple to use [174, 324] and the bias that can be applied without rup-

turing the supporting lipid membrane is limited. Solid-state nanopores, on the other hand, show great potential for studying nucleic acid-protein interactions [325, 326]. The reduced membrane fragility allows a wider range of forces to be applied, and the pore geometry can be fine-tuned using advanced nanofabrication techniques to suit the application.

In a previous study, nanopore-based unraveling of nucleosomes at constant force was reported [125]. In this study nucleosomes were only detected at moderately high voltages, which presumably is due to the large entropic barrier associated with threading of the nucleosomal dsDNA tail into the pore. This limitation of constant voltage experiments to the large-force regime has prompted us to develop the first solid-state NFS apparatus to our knowledge, which we use here for probing the stability of individual nucleosomes. The results shown in this chapter were published in [327]. The TEM-drilled nanopores used for the experiments were fabricated by Spencer Carson and other members of the Wanunu lab (Northeastern University, Boston, MA, USA). Nucleosome assembly and DNA methylation was performed by Shannon R. M. Kinney (Western New England University, Springfield, MA, USA).

5.2.1 Measurement Setup

All experiments were performed at room temperature ($23 \pm 1°$ C). After cleaning a nanopore chip with hot piranha solution and a copious water rinse, it was mounted into the upright measurement cell (cf. Section 2.4). Each compartment was filled with buffer (265 mM KCl, 83 mM NaCl, 1 mM EDTA 10 mM Tris, pH 8) and an Ag/AgCl electrode. The assembled cell then was connected to a patch clamp amplifier (Axopatch 200B) and a DAQ interface for active voltage control (see Section 3.3.1). Due to the amplifier's current limit, we typically observed a time constant of ~ 300 µs for the systems current response. At the end of each ramp, a reverse bias pulse was applied (-400 mV for 20 - 40 ms) to prevent long-lived pore blocks. Current recordings were filtered at 100 kHz using the amplifier's built-in Bessel filter and digitized at sampling rates of at least 250 kHz.

Data Analysis All data were analyzed using custom MATLAB scripts. The raw current traces were median-filtered using a 40 - 80 µs time window, and a derivative-based step detection algorithm was used to identify the transition voltages. Traces corresponding to clogged states of the pore, as indicated by a reduced open pore current prior to capture were removed automatically beforehand.

Principle The measurement principle is depicted schematically in Figure 5.5a. Initially, a capturing voltage of 350 - 550 mV is applied until threading of a ~ 20 - 50 bp-long nucleosomal dsDNA tail into a 2.6 - 2.8 nm diameter pore is detected (I). The current drop that marks DNA threading signals a hardware trigger (see Section 5.2.2) to reduce the voltage and then ramp it upwards at a constant loading rate (2.5 V/s - 40 V/s) (II). Since the nucleosome dimensions (~ 11 nm) are larger than the pore

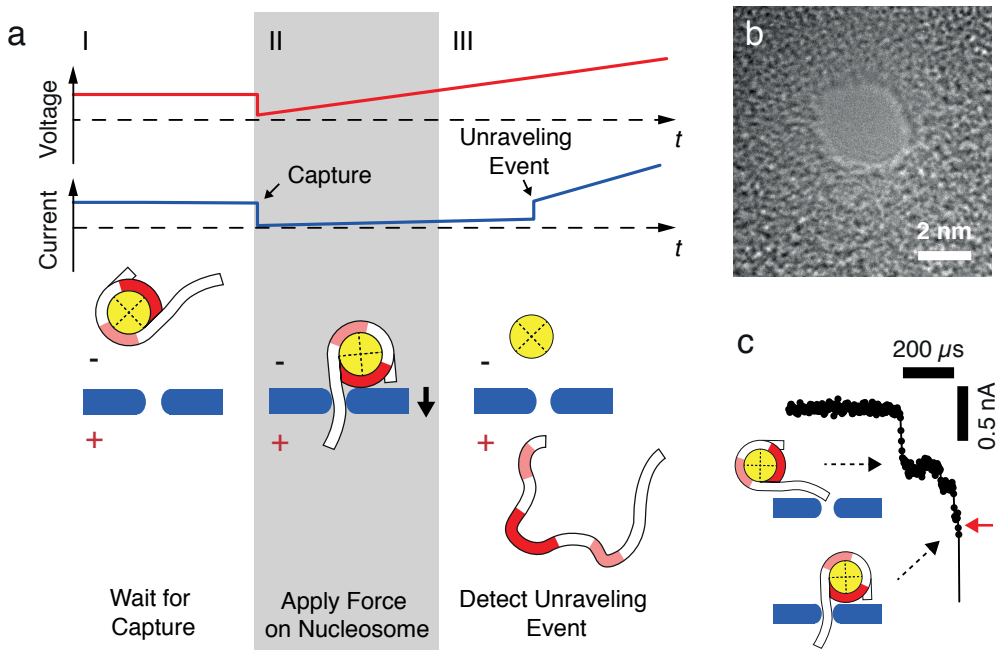

Figure 5.5: Nanopore Force Spectroscopy on Nucleosomes. a) Schematic depiction of the measurement principle. I: A constant voltage is applied to capture a mononucleosome. II: A potential ramp is triggered, applying increasing force on the nucleosome. III: When the nucleosome unravels, the DNA molecule escapes from the pore and a stepwise increase in the current signal at a specific transition voltage is observed. Light and bold red shaded areas on the nucleosomal DNA represent off-dyad and on-dyad areas of interaction, respectively (see text). b) Transmission electron microscope (TEM) image of one of the ∼2.8 nm silicon nitride nanopores used in our experiments. c) Representative current trace of a capture event at 400 mV voltage; red arrow indicates trigger level.

dimensions, the electrophoretically pulled dsDNA tail gradually strains the complex until the nucleosome is ruptured, after which DNA is rapidly (10 - 50 µs) released from the pore (III). The release event, which signals nucleosome rupture, is detected as a fast opening transition in the ionic current. In all of our experiments we have used a narrow range of pore dimensions (diameters of 2.6 - 2.8 nm, effective pore lengths of 5 - 8 nm), as determined via the ionic current traces (cf. Section 3.1).

5.2.2 Nucleosome Capture

A representative transmission-electron microscopy (TEM) image of one of the pores that was used in our experiments is shown in Figure 5.5b. In the geometry of our study the pore diameter (2.8 nm) is only slightly larger than the cross-sectional diameter of a DNA molecule (∼2.2 nm), and the rigid nucleosome and one of its DNA tails must be oriented towards the pore mouth in order for DNA threading to occur. In Figure 5.5c, a representative nucleosome capture event is shown (For a more extensive display of capture events, see Figure A.6a in Appendix A.4). As observed in constant voltage nanopore experiments [125], nucleosome-associated current blockades feature a multilevel structure with one or more shallow current blockade levels that precede a

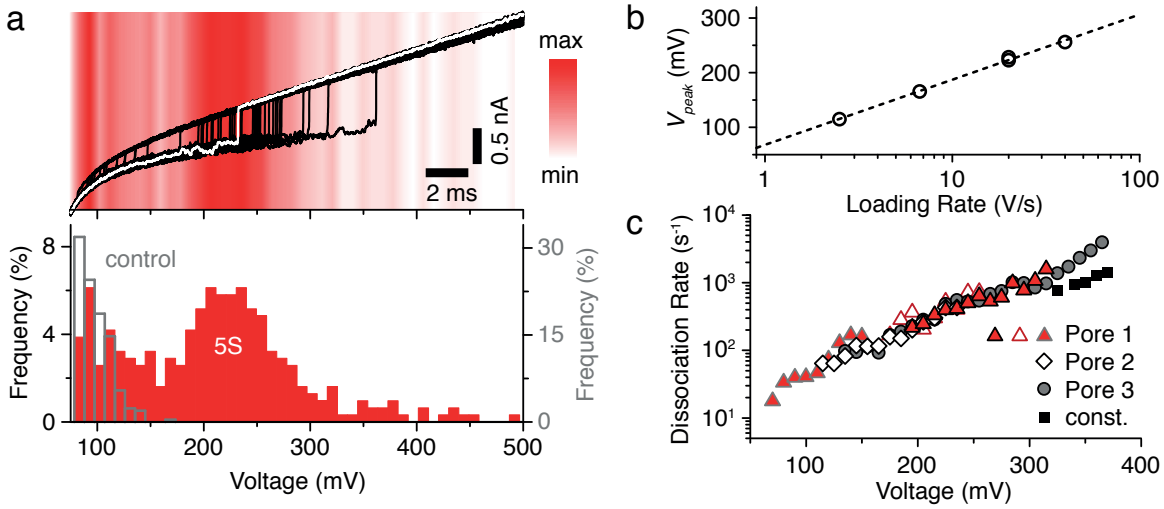

Figure 5.6: Nucleosome Unraveling Experiments. a) Top: Current traces acquired during triggered potential ramps in presence of nucleosomes assembled from the sea urchin 5S sequence (subset of 50 representative traces with an opening transition, 20 V/s loading rate, typical trace highlighted in white). Red color shading: Distribution of opening transitions for the complete dataset (314 detected transitions). Bottom: Corresponding transition voltage histograms for the dataset (red) and for a 250 bp DNA control (gray). b) Peak position of the nucleosome-attributed population as a function of loading rate. Dashed line represents a logarithmic fit. For a loading rate of 20 V/s, the peak position is shown for two experiments with different capture voltages (400 mV and 550 mV). c) Voltage-dependent dissociation rate of 5S nucleosome structures determined from measurement data using Eq. 3.25. Data from 3 different pores (triangles, diamonds and circles) at loading rates of 2.5 V/s (red triangles with gray border), 6.7 V/s (diamonds), 20 V/s (red triangles with black border & open triangles) and 40 V/s (gray spheres) are shown. Data from constant voltage nanopore experiments [125] are shown for comparison (black squares). Pores with diameters d = 2.6 - 2.8 nm and effective length h_{eff} = 5 - 8 nm were used.

deep blockade level (see Figure A.6b). We attribute the shallow levels to nucleosome interactions with the pore before threading of the DNA tail into the pore lumen has occured, and the deep blockade level to capture of a DNA tail. Therefore, in our NFS acquisition protocol we set the trigger level for nucleosome capture to a value that suggests complete DNA threading, as shown by the red arrow in Figure 5.5 and Figure A.6a.

5.2.3 Nucleosome Unraveling

We first performed force spectroscopy studies on nucleosomes assembled from sea urchin 5S rDNA (for details on the nucleosome assembly and sequence details, please see [327]). This positioning sequence is known to form nucleosomes with a relative energy gain of 0.5 kcal/mol compared to a pool of random DNA sequences [291]. For each detected capture event, we recorded the ionic current before and during the triggered voltage ramp. A representative set of 50 overlaid current traces obtained in a 5S nucleosome unraveling experiment is shown in Figure 5.6a. For the sake of discussion we highlight a model trace in white. At the beginning of the voltage ramp the current

was in a low state that corresponds to an occupied pore. At some critical voltage ($\sim 235\,\mathrm{mV}$ for the model trace) an opening transition is observed, signaling nucleosome rupture. The red background in the image reflects the relative frequency of unraveling at each particular voltage range during the experiment ($n = 314$). In rare cases the pore remained in its blocked state throughout the voltage ramp; such events were not considered in our analysis. Apart from these long-lived events, the traces show two distinct regions in which events are frequently seen. Below the traces in Figure 5.6a we show the distribution of transition voltages, which reveals a dominant population centered at $\sim 230\,\mathrm{mV}$ that we attribute to nucleosome unraveling. In addition to this well-defined population, we observe the tail of a second minor population that vanishes as the voltage reaches 150 mV. By performing a control measurement using a 250 bp dsDNA fragment, we were able to assign the minor population to free dsDNA. Since our sample contains both free DNA and nucleosomes, we tuned our experimental conditions so that the relative capture frequency of nucleosomes to DNA is maximized. By performing this experiment using various loading rates (i.e., voltage ramp speeds), we found that the peak voltage (V_{peak}) of nucleosome unraveling scales with the logarithm of the loading rate in the range of 2.5 - 40 V/s (see Figure 5.6b).

In Figure 5.6c, we calculated the nucleosome dissociation rate as a function of bias using Eq. 3.25, where only events assigned to the nucleosome population in the transition voltage distribution were taken into account. All data obtained from three different pores at various loading rates collapse onto a single master curve, confirming the applicability of the transformation defined by Eq. 3.25 (see Section 3.4.4). We also evaluated the possible influence of capture voltage on the unraveling statistics by performing measurements at two different capture voltages (400 mV and 550 mV) for identical ramp parameters (20 V/s, 50 mV starting voltage). While we found the rate of nucleosome capture to increase at the higher voltage, in Figure 5.6b we show that the most probable nucleosome unraveling voltages for the 20 V/s ramps are independent of the capture voltage, implying that our capture conditions are not nucleosome-destructive. Finally, when comparing the obtained dissociation rates with previous constant voltage data [125], we find a systematic trend in which constant voltage rates are always lower than our NFS data (Figure 5.6c, black squares). These consistently slower rates obtained in constant voltage experiments arise from the way in which we performed our analysis: for constant voltage data the full duration of the event was measured, including the shallow current level at the beginning, whereas in NFS any pre-threading time is not taken into account.

Discussion Our findings give rise to the following interpretation: logarithmic regimes of the most probable transition voltages across a wide range of loading rates are associated with an irreversible crossing of a single energy barrier at a fixed location along the unbinding pathway [137, 144]. Likewise, the validity of the transformation used for the voltage-dependent dissociation rate representation of our data (3.25) is coupled to the assumption of an escape over a single barrier. As nanopore force spectroscopy experiments do not provide information on the unraveling coordinates, escape over in-

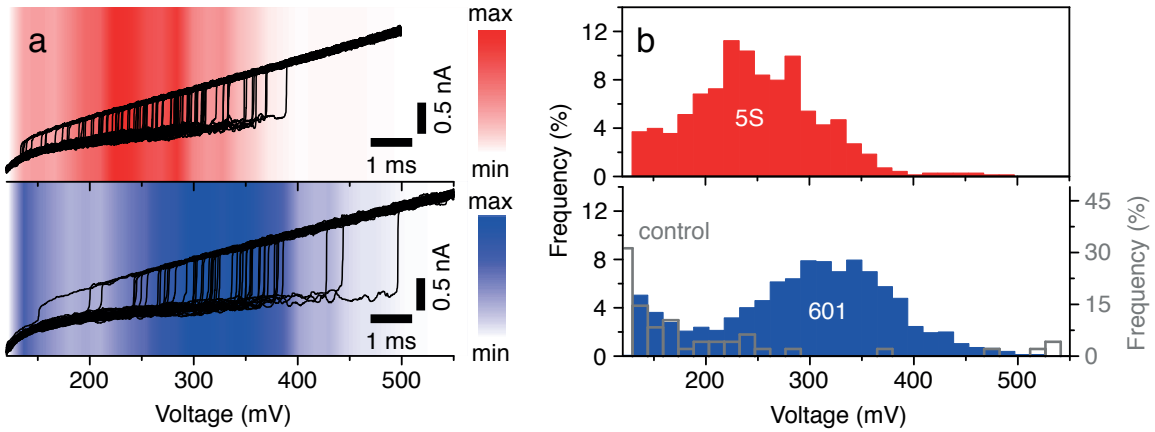

Figure 5.7: Impact of the Positioning Sequence on Unraveling Characteristics. a) Current traces acquired during triggered potential ramps in presence of nucleosomes assembled from the sea urchin 5S (red) and the Widom 601 sequence (blue) (subsets of 50 representative traces with an opening transition, 40 V/s loading rate). Color shading: Distribution of opening transitions for the complete datasets (703 and 1547 detected transitions for 5S and 601, respectively). b) Corresponding transition voltage histograms for 5S nucleosomes (red), 601 nucleosomes (blue) and a 250 bp DNA control (gray).

dividual energy barriers within a multi-barrier landscape cannot be separated. Thus, even for a multi-barrier energy landscape, our findings imply that one distinct energy barrier limits the transition across our experimental bias range. Should multiple barriers with comparable energy govern the transition, the rate transformation shown in Eq. 3.25 would not reflect dissociation rates at constant voltage. To explain our observation of a single barrier we turn to the prior literature: A study by Hall et al. [313] in which nucleosomal DNA was unzipped using optical tweezers has identified three major regions of interaction (cf. Figure 5.5a). Whereas the interaction region at the nucleosome dyad, where the nucleosomal DNA interacts with the H3-H4 tetramer was found to be the strongest, the other two regions, where the DNA interacts with the H2A & H2B dimers are significantly weaker. Further, single-molecule FRET studies have revealed a salt-induced decrease in the stability of the H2A/H2B interactions [310]. This salt dependence is presumably due to a shift in the balance of DNA bending and electrostatic interaction with the histone core, which is screened more efficiently at elevated salt concentrations. Given that our experiments were conducted at an ionic strength that is similar to that inside of a eukaryotic nucleus [328], we conclude that the interactions at the nucleosome dyad constitute the most energy-costly barrier of the unraveling process in our experiments.

5.2.4 Sequence Dependence

Next, we studied the sensitivity of our NFS technique to positioning sequence by comparing the 5S nucleosome to nucleosomes assembled from the Widom 601 clone [291]. Compared to 5S rDNA, a relative energy gain of 2.8 kcal/mol was determined for this SELEX-generated positioning sequence, which is known to form the most stable and

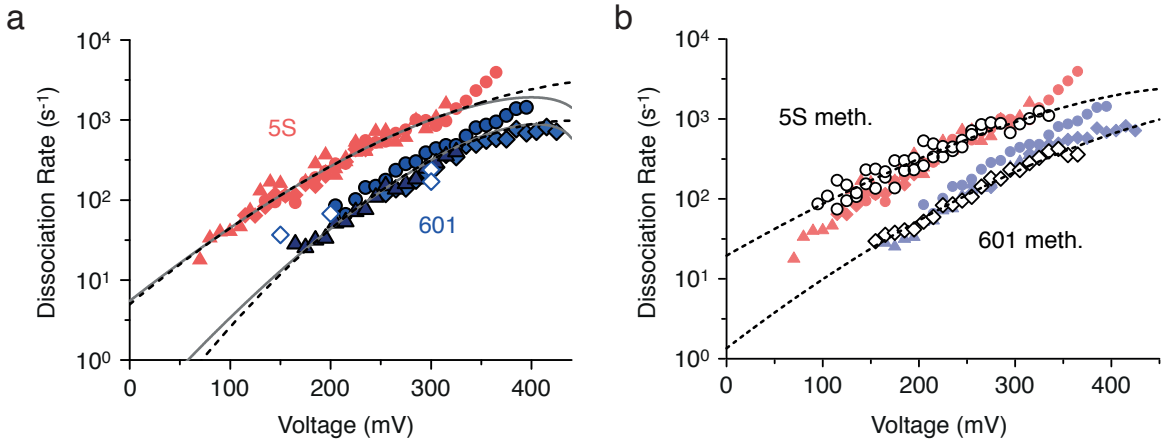

Figure 5.8: Analysis of Dissociation Rates. a) Voltage-dependent dissociation rate of nucleosomes assembled from the Widom 601 (blue symbols) and the 5S positioning sequence (red symbols, shown for comparison). 601 data was obtained from 3 different pores at loading rates of 10 V/s (triangles) and 40 V/s (diamonds and circles). Hollow diamonds: Dissociation rate for 601 nucleosomes obtained in triggered constant voltage experiments using 3 different pores. Lines indicate least-square fits to the Kramers diffusion model for a harmonic well with a cusp-like barrier (dashed black line) and for a linear-cubic energy surface (gray line) (Eq. 3.27, see text). b) Voltage-dependent dissociation rate of nucleosomes assembled from methylated DNA (mCpG) using the Widom 601 (open diamonds, single experiment) and the 5S positioning sequence (open circles, two experiments using the same pore). Data from (a) are shown for comparison. Dashed lines indicate least-square fits to the Kramers diffusion model for the cusp-like barrier.

most accurately positioned nucleosome assembly. As its selection was mainly driven by the interaction of its central ~ 70 bp with the H3-H4 tetramer [329], dyad interactions are particularly strong for this sequence. In Figure 5.7 we display raw NFS traces for 5S (red) and Widom 601 (blue) nucleosomes under identical conditions at a loading rate of 40 V/s. In agreement with its higher stability, we observe for 601 nucleosomes considerably higher transition voltages than for 5S nucleosomes: V_{peak} is 260 mV for the 5S sample, while it is 330 mV for the 601 sample.

In Figure 5.8a, voltage-dependent dissociation rates are analyzed for both positioning sequences by compiling data from experiments using multiple pores and different loading rates. Similarly to the 5S nucleosomes, unraveling rates for the Widom nucleosomes at different loading rates (10 V/s and 40 V/s) fall on the same master curve. Furthermore, triggered constant voltage experiments obtained from three different pores (see Figure 5.8a open symbols, see Appendix A.4 for the actual measurement data) reveal a good agreement of dissociation rates with transformed ramp data.

To extract quantitative information about the free energy landscape governing the interaction between nucleosomal DNA and the histone core, we used the Kramers diffusion model described in Section 3.4.5. We fitted Eq. 3.27 to our data (see Figure 5.8a) using the harmonic well free energy profile with a cusp-like barrier ($\nu = 1/2$) and the linear-cubic profile ($\nu = 2/3$). Our results are summarized in Table 5.1. For the 5S sequence we obtained comparable parameter values for both model profiles,

Table 5.1: Kramers Model. Parameters obtained from 5S and Widom 601 nucleosome samples by fits to the Kramers diffusion model (Eq. 3.27) for a cusp-like barrier ($\nu = 1/2$) and a linear-cubic profile ($\nu = 2/3$).

	5S		**601**		**5S meth.**		**601 meth.**	
ν	1/2	2/3	1/2	2/3	1/2	2/3	1/2	2/3
k_0 (s^{-1})	5.0	5.5	$6.7 \cdot 10^{-2}$	$16 \cdot 10^{-2}$	19	20	1.4	1.4
ΔG_β (k_bT)	8.4	7.3	11.7	10.1	7.4	6.2	9.3	7.8
V_β (mV)	39	42	24	30	58	60	44	46

indicating the generality of the result. Using Eq. 3.28 and Eq. 3.29, we were able to accurately predict the shapes of unraveling voltage distributions and the loading rate dependence for 5S nucleosomes from this set of parameters (see Appendix A.4). Our findings for the Widom sequence showed some dependence on the actual shape of the model energy profile. The obtained values for the scaling parameter V_β and the equilibrium dissociation rate k_0 differ by factors of 1.25 and 2.4, respectively. Here, measurement voltages approach the model's limit of validity for the linear-cubic profile ($V_c \approx 450\,\mathrm{mV}$ for the obtained parameters, cf. Section 3.4.5). For the cusp-like barrier, this limit is considerably higher ($V_c \approx 560\,\mathrm{mV}$), which makes it the better choice in this case. However, for all parameters the observed sequence dependence is considerably larger than model-dependent variability.

Discussion Despite various potential pitfalls from pore-to-pore variability and possible ionic strength fluctuations we are able to clearly resolve both positioning sequences, and we find that in the investigated voltage range, 5S rates are universally $\sim$5-fold faster than Widom 601 rates. Interpreting our data based on two different free energy profiles describing the shape of the rate-determining energy barrier, we relate the increase in stability to a general rise in barrier height of $\sim 3\,k_bT$. Even though our model does not provide absolute values for the barrier position $x_b = k_bT/V_\beta a$ due to lacking knowledge of the scaling parameter a (cf. Section 3.4.5), we obtain a relative position shift by a factor of ~ 1.4 - 1.6. This increase in barrier width for the Widom 601 nucleosomes may be related to the higher bending preference of this sequence [330].

5.2.5 Influence of DNA Methylation

Finally, given the controversy over the effect of epigenetic modifications on nucleosome stability we have decided to investigate the impact of DNA methylation using our method. First, we used a methyltransferase to partially methylate CpG sites in both positioning sequences (5S rDNA and Widom 601, for details on the methylation protocol, see [327]), and after confirming methylation we reconstituted nucleosomes and performed NFS experiments. In Figure 5.8b we present dissociation rate vs. voltage data for methylated (hollow markers) and unmethylated (solid markers) nucleosomes. In both cases, dissociation rates are very similar for the methylated and unmethylated samples across the range of voltages investigated. However, we observe

a tendency towards weaker voltage scaling for the methylated samples, specifically for the 5S nucleosomes.

As only data from one pore is available for 5S and Widom 601, respectively, we cannot estimate the pore-to-pore variance and the parameters from fits to the Kramers diffusion model (see Table 5.1) may be considerably less accurate. Qualitatively, we observe a similar tendency for both sequences: Compared to the unmethylated dataset, we obtain increased equilibrium dissociation rates, a reduced barrier width (V_β increases) and a slightly decreased barrier height.

Discussion While our findings suggest a minor influence of CpG methylation on nucleosome stability at first sight, analyzing the voltage-dependent scaling of dissociation rates using the Kramers diffusion model suggests higher equilibrium dissociation rates and a narrower barrier for the methylated samples. These findings indicate a more open nucleosome conformation in the methylated state, which is in accordance with previous fluorescence-based studies [318, 319]. As the barrier height is nearly unchanged (as are the absolute dissociation rates in the investigated voltage range), we conclude that the central H3-H4 tetramer interactions on the dyad region are hardly affected by DNA methylation. Since nucleosome positioning models accounting for the sequence-dependent bendability of DNA suggest that in the dyad region the DNA is less bent [331, 332], we expect that changes in DNA mechanical properties will influence this region of the nucleosome less strongly [333]. We emphasize that although our findings appear to be reasonable, we did not quantify the pore-to-pore variability for the methylated case. Moreover, the obtained parameters may not reflect equilibrium dynamics of the entire nucleosome. As discussed in Section 3.4.5, modeling a complex interaction consisting of many different interactions with a single barrier may not be sufficient for a full description.

5.3 Electrophoretic Time-of-Flight Measurements of Single DNA Molecules

In Section 5.1.2, we described the fabrication of a solid-state device that consists of two stacked nanopores separated by a micron-sized pyramidal compartment (a "pore-cavity-pore" (PCP) device, see Figure 5.9a) [80]. In contrast to single nanopore devices, the PCP architecture has extended sensing and manipulation capabilities, e.g., it can be used to electrophoretically trap single particles or macromolecules within the cavity, and controllably release them with a voltage pulse. Both nanopores act as resistive pulse sensors, and therefore the effective electrical information collected from each molecule is doubled. Furthermore, correlations between signals obtained from the two pores can be used to gain additional information about the dynamics of the translocating molecules. Here, we apply the PCP device to determine the free-solution electrophoretic mobility of double-stranded DNA (dsDNA) molecules in the length range from 6 kbp - 15 kbp. The mobility is derived from single molecule time-of-

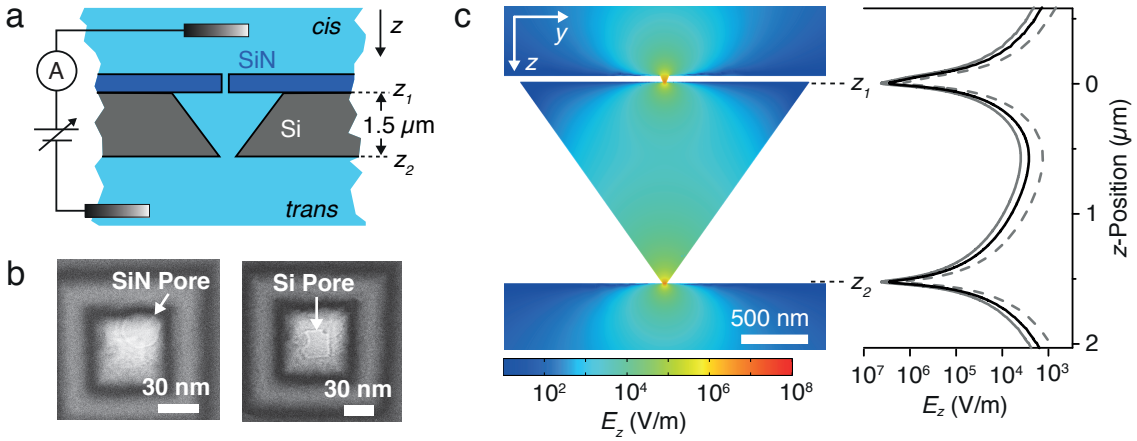

Figure 5.9: Pore-Cavity-Pore Device. a) Schematic depiction of the pore-cavity-pore (PCP) device separating two electrolyte compartments electrically contacted with Ag/AgCl electrodes. A pyramidal microcavity embedded in silicon is connected to the *cis* side via a nanoscale pore in a 50 nm thick silicon nitride layer (SiN Pore) and a second pore at its apex (Si Pore). b) Transmission electron micrographs showing the round SiN pore (left, diameter 28 nm) and the rectangular Si Pore (right, 23 x 23 nm). Arrows indicate pores. c) Simulated electric field distributions inside the PCP's cavity. Left: Cross-sectional view of the PCP device at 300 mV bias voltage; color coding shows the electric field distribution (z-component). Right: Simulated electric field distribution along the center axis versus z-position for different bias voltages. Solid black line: 300 mV, dashed gray line: 150 mV, solid gray line: 450 mV. $z_1 = 0$ µm corresponds to the inner constriction of the SiN pore. The Si pore is situated at $z_2 = 1.5$ µm.

flight (TOF) measurements obtained from the time the DNA molecules take to travel from pore to pore. By analyzing the resulting TOF distributions, we can identify the influence of drift, diffusion and barrier-dominated escape on the transport of DNA through the device. Our results were originally published in [334].

5.3.1 Measurement Setup

For the present work we fabricated a PCP device that features a SiN pore with a diameter of 28 nm, a Si pore with size 23 x 23 nm (cf. Figure 5.9b) and a pore-to-pore distance of 1.5 µm. For translocation measurements, we used a measurement setup as described in Section 2.4. The PCP chip was mounted into the horizontal measurement cell (cf. Figure 2.5b) and a bias potential was applied across the device via Ag/AgCl electrodes placed in either of the two electrolyte compartments separated by the chip (cf. Figure 5.9a). The current across the device was measured using a patch clamp amplifier (Axopatch 200B, see Section 2.4 for details). The buffer electrolyte was 1 M KCl, 10 mM Tris, 1 mM EDTA, pH 8, and all experiments were performed at room temperature. For these conditions, we simulated the electric field distribution inside the PCP device using COMSOL Multiphysics and its *Electric Currents* module as described previously [58]. Our results are summarized in Figure 5.9c.

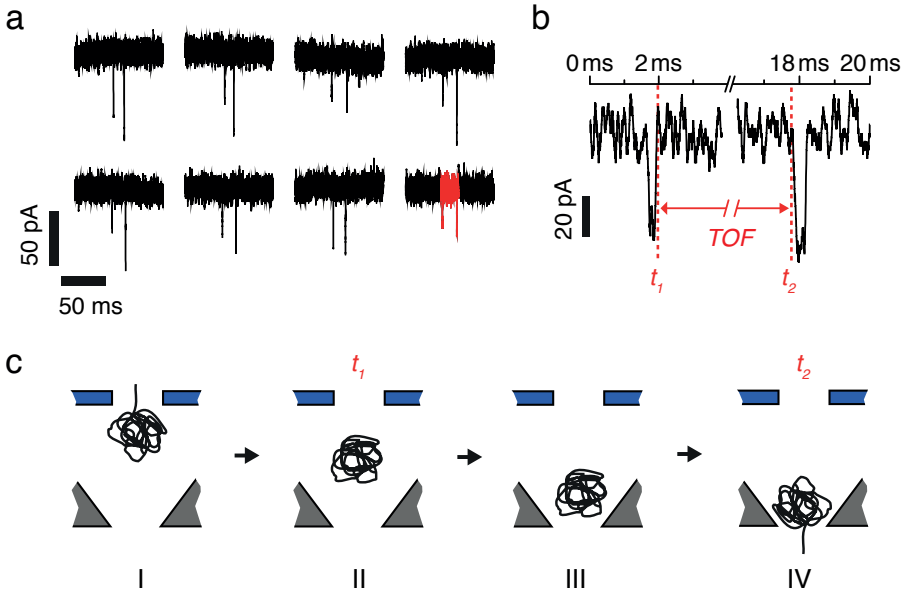

Figure 5.10: DNA Translocation. a) Eight current blockade pairs detected in a representative 4 s current-time trace after addition of 100 pM of 10 kbp dsDNA to the *cis* side of the PCP device at a bias voltage of 300 mV. Equally spaced current spikes indicate sequential DNA translocation through the two nanopores of the PCP device. b) Magnified view of the region marked in a). We define the time difference between the rising edge of the first blockade and the falling edge of the second as the time of flight (TOF) of the molecule traversing the cavity. c) Schematic depiction of the passage of a DNA molecule through the PCP device in four steps. I: Completed translocation through the first pore (t_1) accompanied by rapid recoiling. II: Electrophoretic transport towards the second pore. III: Jammed state at the entrance of the second pore. IV: Threading into the second pore after successful chain-end localization (t_2) (see below, Section 5.3.3).

5.3.2 Time-of-Flight Experiments

Upon addition of 10 kbp long dsDNA molecules ($c = 100$ pM) to the *cis* side of the device, typically a series of spikes in the current traces is observed. These temporary current blockades arise from single molecules translocating through either one of the two nanopores of the PCP device. Each nanopore hence works as a conventional resistive pulse sensor [81]. However, as the DNA molecules sequentially have to pass the two pores, the current spikes are correlated. As shown in Figure 5.10a, for sufficiently low analyte concentrations, resistive pulses are typically observed as isolated pairs. We assign the first pulse of each pair to the molecule's passage through the SiN pore, while the second pulse – under our experimental conditions delayed by 5 - 50 ms – is assigned to its subsequent translocation through the Si pore. Importantly, the presence of the second peak provides direct experimental evidence that the molecule causing the resistive pulses has actually translocated through the first pore, and has not left the pore region to the *cis* side again [4]. While for conventional nanopore devices such evidence is available via dedicated measurements like probing the dependence of translocation time on the length of the molecule [335] or utilizing optical tweezers [100, 336], the PCP device provides this proof "on the fly" for any single molecule measurement that

is performed. This could be especially valuable for analytes like proteins [337]. In our experiments, we were able to assign 94 % of all detected resistive pulses unambiguously to pairs. The remaining 6 % are mainly due to two or more pulse pairs that were close to each other and therefore no unambiguous correlation was possible.

Another important observation is that even for high voltages applied across the device the paired peaks did not merge into a single prolonged event, which would indicate that an elongated DNA molecule is present in both pores simultaneously. In principle, 10 kbp dsDNA with a contour length of 3.4 µm, could span the distance between the two pores (which is 1.5 µm). However, the presence of the two peaks shows that the DNA strands recoil during their passage between the pores. This is reasonable as simulations show that the electric field rapidly decreases within the cavity (see Figure 5.9c), and therefore also the electrophoretic velocity. Hence, after passing the pore, the leading segment of the DNA molecule slows down immediately while successive segments are still being accelerated. This leads to instantaneous recoiling of the molecule. Furthermore, the Zimm relaxation time $\tau_Z = \eta R^3 / \left(2\sqrt{3\pi} k_b T\right)$ (where η is the viscosity of water and R is the root-mean-square end-to-end distance of the polymer) [112] – as a measure for the maximum recoiling time – for 10 kbp DNA is $\approx$ 7 ms. For further analysis of the translocation process, we determined the interval between the end of a current blockade and the onset of the subsequent blockade for all pulses (see Figure 5.10b). The resulting distribution of time intervals exhibits a single peak in the range of 5 - 50 ms and represents the molecules' time-of-flight between the pores. By excluding times much longer than the peak of the distribution, we can identify all pairs of resistive pulses and assign each pulse to a translocation event through the first or the second pore (cf. Appendix A.5).

5.3.3 TOF Distribution as a Function of Voltage

In Figure 5.11a, representative TOF distributions are shown for four different bias voltages. The distributions are skewed, but their asymmetry decreases with increasing bias voltage. This asymmetry cannot be explained taking into account diffusive motion and drift only. For a passage time in the order of 5 - 50 ms and a diffusion coefficient of $1.93 \pm 0.12\,\mu m^2/s$ for 10 kbp DNA (determined via dynamic light scattering, see Appendix A.5), the solution to the Fokker-Planck equation in 1D given by Eq. 3.18 describes a nearly symmetric distribution closely approximated by a Gaussian function (cf. Section 3.2.3). As the DNA molecule is supposed to traverse the cavity of the PCP device in coiled conformation, we hypothesize that the free energy barrier associated with localizing one of the molecules' ends at the entrance of the second pore gives rise to the observed asymmetry. To obtain a description for time-of-flight distributions under the influence of drift, diffusion and a free energy barrier, as in Eq. 3.8, an additional term describing the barrier's contribution to the flux of molecules has to be considered when solving the continuity equation (Eq. 3.9, cf. Section 3.2.2). However, this requires knowledge of the free energy profile $F(x)$ describing the barrier and an analytical solution may only be found for special cases. Therefore, we follow a different approach: Skewed distributions are well-known from chromatography, and in fact the

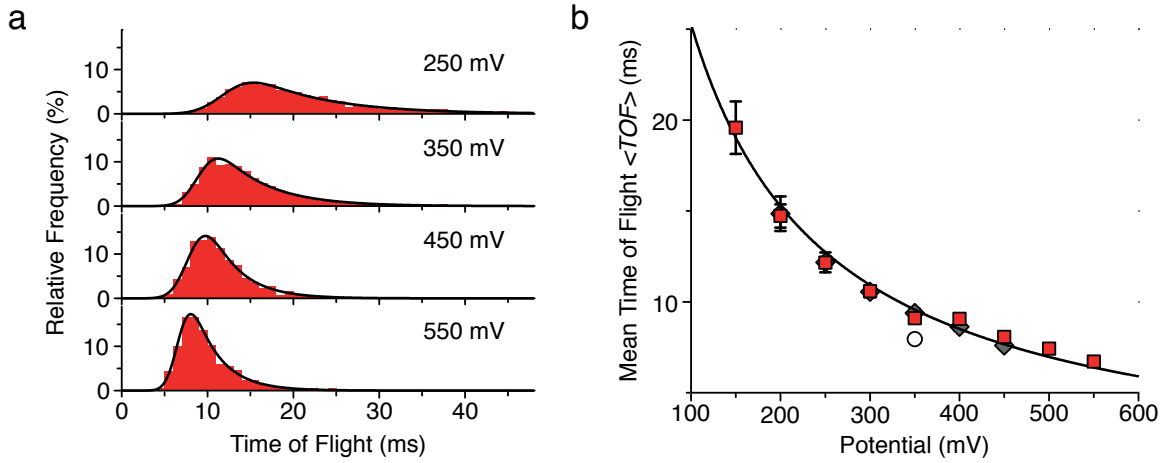

Figure 5.11: DNA Time of Flight. a) TOF distribution for 10 kbp DNA at different bias voltages. The solid lines represent numerical fits with an exponentially modified Gaussian (EMG) model, from which the mean times of flight (plotted in b)) are extracted. b) Mean time of flight versus bias potential V for 6 kbp (gray diamonds), 10 kbp (hollow squares) and 15 kbp (hollow circles) DNA molecules. The solid line represents a numerical fit with an inverse voltage-dependence ($\langle TOF \rangle \sim V^{-1}$) (see text).

"exponentially modified Gaussian" (EMG) used for chromatographic peak analysis fits our data remarkably well [338]. Processes that lead to symmetric broadening of the distribution around the mean value are accounted for by a Gaussian distribution. Asymmetric broadening caused by additional processes with slow (first order) kinetics is modeled by an exponential distribution. The EMG distribution is given by the convolution of these two contributions:

$$EMG(t) = \frac{A}{\sqrt{2\pi}\sigma} \int_0^t exp\left(-\frac{(t'-t_G)^2}{2\sigma^2}\right) exp\left(-\frac{t-t'}{\tau}\right) dt' \tag{5.1}$$

Fitting of this distribution to our data results in three fit parameters: the center of the Gaussian t_G, – which we identify with the mean time-of-flight $\langle TOF \rangle$ of the molecules – its width σ, characterizing the extent of diffusive broadening, and the kinetic rate constant $k = \tau^{-1}$. The latter can be interpreted as a Kramers rate for crossing of the free energy barrier associated with capture of the DNA molecule into the second pore, as will be discussed below.

5.3.4 Electrophoretic Mobility of DNA

In Figure 5.11b, the TOF values obtained from the EMG fits are shown as a function of bias voltage. These can be related to the electrophoretic mobility in the following manner. For a charged molecule in solution moving in an electric field E in direction z, the velocity is given by $v = dz/dt = \mu E$, where μ is the electrophoretic mobility. As the electric field inside the cavity of the device is not homogeneous, the TOF is

related to the electric field via the expression

$$\langle TOF \rangle = \int_{t_{in}}^{t_{out}} dt = \frac{1}{\mu} \int_{z_1}^{z_2} [E(z)]^{-1} \, dz \tag{5.2}$$

where the integral is performed from the cavity's entrance z_1 to its exit z_2 (see Figure 5.9c)[3]. The electric field scales linearly with the applied bias voltage V. We can therefore introduce a reduced electric field $\epsilon(z) = E(z)/V$, which depends only on the geometry of the cavity and has the dimension of a length. Hence, we expect an indirect proportionality between the $\langle TOF \rangle$ and V of the form $\langle TOF \rangle = \alpha/V$, which is very well fulfilled by our experimental data.

The proportionality factor is given by $\alpha = \mu^{-1} \int_{z_1}^{z_2} [\epsilon(z)]^{-1} \, dz$. This factor can be obtained from a fit to the data displayed in Figure 5.11a, which results in $\alpha = 0.4 \cdot 10^{-2}$ Vs. On the other hand, we can numerically calculate the integral $\int_{z_1}^{z_2} [E(z)]^{-1} \, dz$ using the electric field distribution within the cavity known from finite element calculations (see Figure 5.9c), which yields 77.6 µm^2. Hence, the electrophoretic mobility for 10 kbp long DNA is obtained as $\mu = 1.8 \cdot 10^4$ µm^2/(Vs), which agrees well with mobility measurements performed in bulk using Laser Doppler electrophoresis ($\mu = 2.2 \cdot 10^4$ µm^2/(Vs), see Appendix A.5).

From measurements performed on 6 kbp long DNA, we obtained essentially the same TOF data and hence the same mobilities as for 10 kbp DNA (Figure 5.11a). This reflects the well-known free-draining nature of long dsDNA, resulting in a free-solution electrophoretic mobility that is independent of molecular weight for DNA molecules longer than ≈400 bp [339]. For 15 kbp DNA, the $\langle TOF \rangle$ value is substantially lower, resulting in a higher mobility value of $2.8 \cdot 10^4$ µm^2/(Vs). This observation is consistent with an analysis of the molecule's conformational dynamics inside the device (see below), suggesting that the molecule does not relax completely before reaching the second pore.

In principle, the mobility values can also be used to determine the zeta potential of the translocating molecules. Using the Helmholtz-Smoluchowski equation $\zeta = -\frac{\mu\eta}{\epsilon_0 \epsilon_r}$ [340], where η and ϵ_r are the viscosity and permittivity of water, respectively, we obtain ζ = -22.6 mV for 10 kbp DNA at 1 M KCl, assuming a spherical conformation of the DNA molecule.

In contrast to bulk methods, with time-of-flight experiments mobility measurements can be performed at very low analyte concentrations. In particular, they can be performed well below the polymer overlap concentration and therefore molecular or hydrodynamic interactions between polymer coils can be excluded. Furthermore, mobilities can be determined for higher salt concentrations than utilized in conventional zetasizers. This technique works for any charged analyte which is detectable upon translocation through the device's nanopores and can be especially valuable for analytes with a very low light scattering efficiency and no option for labeling.

[3]The spatial extension of the molecule is not taken into account for the bounds of the integral. As $E(z)$ is large in the vicinity of the pores, choosing alternative bounds $z^*_{1,2} = z_{1,2} \pm R_g$ only has minor influence on the result (see Figure 5.9c).

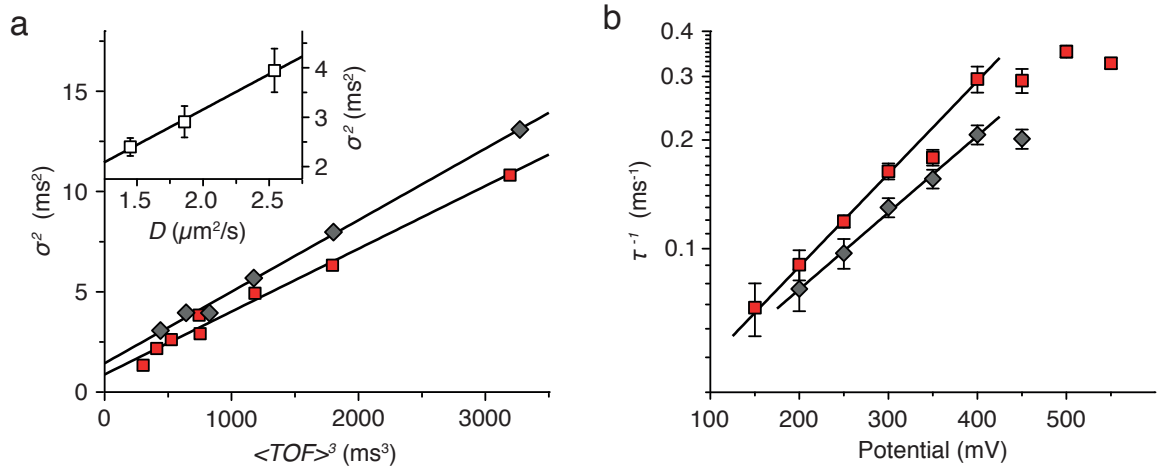

Figure 5.12: Broadening Mechanisms. a) Variance σ^2 of the Gaussian part of the EMG fit versus $\langle TOF\rangle^3$ for 10 kbp (hollow squares) and 6 kbp (gray diamonds) DNA. The solid lines represent linear fits to the data. Inset: Variance σ^2 versus diffusion coefficient at a bias voltage of 350 mV for 6 kbp, 10 kbp and 15 kbp molecules. The solid line represents a linear fit. b) Escape rate τ^{-1} as a function of the applied bias potential in a semi-logarithmic plot for 10 kbp (hollow squares) and 6 kbp DNA (gray diamonds). The solid lines represent exponential fits to the data.

5.3.5 Broadening Mechanisms

The symmetric broadening of the TOF distributions can be well explained by diffusion. The distribution of particle passage times t for a distance L under the influence of electrophoretic drift and diffusive motion along one dimension can be described by Eq. 3.18 (assuming a constant drift velocity, see Section 3.2.3). The variance of this distribution – which closely resembles a Gaussian distribution under present conditions – is given by $\sigma^2 = 2D\langle t\rangle^3/L^2$. Assuming that the inhomogeneous electric field distribution $E(z)$ along the molecules' pathway through the cavity can be subsumed into an effective drift velocity, we identify t with the mean time-of-flight and L with the pore-to-pore distance d. We obtain

$$\sigma^2 \approx \frac{2D}{d^2}\langle TOF\rangle^3. \tag{5.3}$$

This relationship may also be obtained by reasoning: The average velocity in z-direction of a molecule traversing the device is given by $\bar{v} = d/\langle TOF\rangle$. In the presence of diffusion, the variance of the distance traveled in time t is given by $(\Delta z)^2 = 2Dt$, where D is the diffusion coefficient of the molecule. The variance in arrival times at the second pore can then be estimated as $\sigma^2 = \langle(t - \langle TOF\rangle)^2\rangle \approx \frac{(\Delta z)^2}{\bar{v}^2}$ [341], or $\sigma^2 \approx 2D\langle TOF\rangle^3/d^2$. As shown in Figure 5.12a, the TOF variance obtained from the EMG fit for DNA molecules of length 6, 10, and 15 kbp follows the expected relationships $\sigma^2 \sim D$ and $\sigma^2 \sim \langle TOF\rangle^3$ remarkably well.

The asymmetric part of the EMG distribution, represented by the time constant τ, is analyzed in Figure 5.12b. The inverse time constant τ^{-1} increases exponentially with the potential over a wide range of voltages. At elevated voltages transition to a

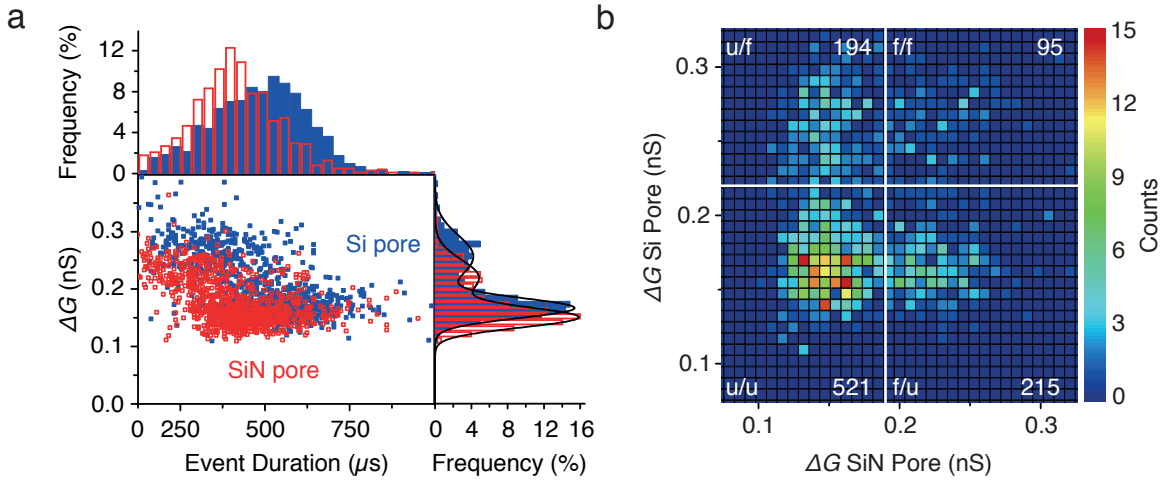

Figure 5.13: DNA Conformation. a) Scatter plot of the conductance blockade versus event duration for the translocation of 10 kbp DNA fragments through the SiN pore (red) and the Si pore (blue) of the PCP device at a bias voltage of 200 mV. Each data point corresponds to a single translocation event. On the right and the top the corresponding histograms are shown. The lines correspond to Gaussian fits. b) 2D histogram of the conductance change due to Si pore translocation vs. the corresponding conductance change due to subsequent Si pore translocation of 10 kbp DNA at 200 mV bias for a total of 1025 correlated event pairs. The color-coding indicates the number of molecules for the corresponding ΔG values. The white lines separate areas attributed to events in which DNA translocated in a folded state from areas attributed to unfolded events. The total event count of each quadrant is shown in the corners.

non-exponential regime is observed. This is in perfect agreement with the theoretical prediction for the activated crossing of the free energy barrier associated with localization of one of the molecules' ends close to the pore entrance (cf. Section 3.2.2), as is the observed increase with chain length.

In previous experiments, we studied the escape of nanoparticles from an unbiased PCP device [80]. In this case the escape process was governed by the confinement inside the cavity and the diffusive motion of the particle. By contrast, we here observe directed motion towards the second pore (due to the applied electric field) and a barrier-dominated escape (due to the DNA molecule's conformation and its large size compared to the small pore diameter).

By analyzing TOF distributions, the escape process can be investigated uncoupled from diffusion and independent from analyte concentration, while in conventional nanopore experiments the mechanism of pore entry can only be accessed experimentally via the capture rate, which represents a combination of diffusion, drift and barrier escape (cf. Section 3.2.2).

5.3.6 Influence of DNA Conformation

A unique feature of the PCP device is the possibility to correlate the translocation events detected by the two nanopores. In Figure 5.13a, a scatter plot of the maximum conductance change ΔG versus event duration is shown for 10 kbp DNA translocations

through the first and second pore, accompanied by the corresponding histograms. For both pores, the conductance change histograms exhibit a bimodal distribution, which can be fit by the sum of two Gaussian distributions.

We assign the lower conductance level to events, in which DNA translocates through the pores linearly, while the second conductance peak – mainly caused by multi-level events with a short-lived second level – is attributed to partially folded DNA. These types of translocation events have also been reported in previous publications on single nanopores of comparable size [113]. The different mean conductance changes and dwell times for the first and the second pore are easily explained by the differences in pore dimensions. We observe a mean conductance change of 0.15 ± 0.02 nS and 0.17 ± 0.02 nS for the first (SiN) pore and the second (Si) pore, respectively. For the PCP device used here, the Si pore's cross-sectional area is 14 % smaller compared to the SiN pore. As the conductance change is expected to scale inversely with this area (cf. Section 3.1), a 13 % higher value is reasonable. The pore geometry (round vs. quadratic, 38° vs. 71° aperture angle) seems to have negligible influence on the conductance change. For a detailed analysis of dwell time distributions, see Section 3.2.3. The Si pore shows slightly slower transport (29 nm µs^{-1} V^{-1}) compared to the SiN pore (34 nm µs^{-1} V^{-1}), which can be related to the different voltage drops across the two pores. In fact, the simulated potential drop within a 50 nm range around the pore mouth is 21 % lower for the Si pore. An important related question is whether the conformation of the DNA molecules arriving at the second pore is somehow affected by the first translocation event. To probe such an influence, we plotted a 2D histogram of the respective pore conductance changes (see Figure 5.13b) for 10 kbp DNA at 200 mV bias voltage and divided it into four quadrants corresponding to the four possible combinations of folding states in the first and second pore, respectively: u/u, u/f, f/u and f/f (f: folded, u: unfolded). In statistical terminology, this represents a 2 x 2 contingency table that can serve as the basis of a χ^2-test to probe the statistical independence of the events [342]. $\widehat{\chi^2}$ can be calculated as follows:

$$\widehat{\chi^2} = \frac{n_{total}(n_{uf}n_{fu} - n_{uu}n_{ff})^2}{(n_{uf} + n_{uu})(n_{ff} + n_{fu})(n_{uf} + n_{ff})(n_{uu} + n_{fu})} \tag{5.4}$$

where n_{ij} is the frequency of the respective quadrant and n_{total} is the total number of events. The test yields $\widehat{\chi^2} = 1.318$, which confirms their independence for a significance level of 0.05. We performed this test for all 10 kbp DNA measurements in a range from 200 mV to 550 mV bias voltage, resulting in a mean $\widehat{\chi^2}$ of 1.26 ± 0.98 with a maximum value of $\widehat{\chi^2}_{max} = 2.56$ for the 400 mV measurement. Hence, statistically the folding state of the DNA at the second pore is not significantly altered due to its passage through the first pore. By way of contrast, measurements performed on 15 kbp DNA yielded a $\widehat{\chi^2}$ value[4] of 15.06, indicating that in this case the molecule's conformation still "remembers" its first translocation when entering the second pore. This means for sufficiently long DNA molecules (for a given pore-to-pore distance) the previous assumption of instantaneous recoiling is not valid anymore. This could also explain

[4]For 15 kbp DNA, we obtained $n_{uu} = 583$, $n_{uf} = 614$, $n_{fu} = 203$ and $n_{ff} = 323$ at 350 mV.

the substantially lower TOF value for 15 kbp DNA. This type of correlation analysis is a unique feature of the PCP device. It may be also used, e.g., to detect modifications or conformational changes occurring during the traversal of the microcavity.

5.4 Conclusion

In this chapter, we presented two very different applications for solid-state-based nanopore sensors. In Section 5.1, we outlined the fabrication of small solid state pores in silicon nitride membranes by TEM drilling. Moreover, we described the fabrication of a "pore-cavity-pore" device comprised of a pyramidal microcavity connected to its environment via two nanopore openings. It is created by a combination of e-beam lithography, reactive ion etching, and a feedback-controlled wet chemical etching step.

Probing DNA-Histone Interaction with NFS. In Section 5.2, we demonstrated nanopore force spectroscopy experiments on nucleosomes by combining small solid-state nanopores and active voltage control. We adapted a dynamic voltage-ramp technique previously developed for biological channels to obtain nucleosome unraveling voltage distributions and voltage dependent lifetimes. By application of a bias voltage, individual nucleosomes are captured by their DNA tails into a nanopore, where their presence triggers a voltage ramp experiment. Unraveling of the nucleosome is then detected by an opening transition in the ionic current when the nucleosomal DNA leaves the pore. This technique does not require any labeling, offers high throughput, and is not compromised by the need for long linker molecules as in other single-molecule force spectroscopy techniques. Our results for the sea urchin 5S rDNA positioning sequence compare reasonably well to conventional nanopore experiments, while considerably extending their force range and eliminating the influence of the capture process. We observe a logarithmic loading rate dependence, which supports an interpretation in terms of the crossing of a single energy barrier given by the interaction of nucleosomal DNA with the H3-H4 tetramer in the dyad region. For the high-affinity Widom 601 positioning sequence, we obtain dissociation rates that are reduced by a factor of 5, demonstrating the sensitivity of the method towards changes in the positioning sequence. Based on Kramers diffusion theory, we related our findings to an increase in barrier height and extension for the Widom 601 nucleosomes. Due to its high throughput and simplicity, our technique is well suited to screen different epigenetic markers and assess their influence on nucleosome stability under external force. We demonstrated its use by first unraveling experiments on nucleosomes with methylated DNA sequences, where we find indications for a more open equilibrium conformation, while within the range of our experiment, the forces necessary for breaking the interaction at the central dyad region are nearly unaffected. Our findings are in accordance to previous studies and may contribute to develop and test more sophisticated models for DNA histone interactions.

Electrophoretic Time-of-Flight Experiments In Section 5.3, we have demonstrated that the pore-cavity-pore device can be used for electrophoretic time-of-flight measurements on single DNA molecules of 6 - 15 kbp length. The experiments indicate that upon translocation of the DNA through the first pore, it immediately relaxes and traverses the cavity as in free-solution electrophoresis. Exit of the DNA from the cavity through the second pore is found to occur over a free energy barrier that is reduced with elevated voltages. The statistical distribution of the duration of the overall process is well-described by an exponentially modified Gaussian function. As the electric field distribution within the pyramidal cavity can be calculated, TOF (and, hence, velocity) measurements can be used to determine the free-solution mobility of the molecules. This in turn can be used to determine their ζ potential. Our method works particularly well at low analyte concentrations not suitable for bulk experiments. Another important feature of the PCP device is the possibility to assign resistive pulses to translocations through either entry or exit pore of the cavity, enabling time-dependent studies of conformational changes.

6 Conclusion

In Chapter 2, we illustrated the methods and instrumentation for high bandwidth single channel ionic current recordings as used for the experiments described in this work, including a parallelized and automatized planar lipid bilayer setup. We characterized the latter in terms of noise performance and identified the relay board used for switching between amplifiers and channels to be responsible for the dominant dielectric noise contribution. For the solid state nanopore setup used in this work, flicker noise was found to dominate the noise spectra.

The principles of single molecule sensing with nanopores were covered in Chapter 3. Besides discussing the fundamental aspects of analyte transport and sensing performance, we introduced an active control setup that can trigger changes in measurement potential from detected current blockades. It was benchmarked in DNA recapture experiments using considerably shorter molecules and smaller pores as used in previous studies. This setup is ideally suited for force spectroscopy experiments, whose principles and interpretation were discussed afterwards. In this context, we described first efforts to parallelize nanopore force spectroscopy studies.

In Chapter 4, we presented a novel DNA-based membrane channel that was constructed via molecular self-assembly using scaffolded DNA origami. 26 cholesterol moieties attached to the channel's barrel-shaped cap mediate its adhesion to lipid bilayers. TEM studies on SUVs confirmed adhesion in the intended orientation and provided first evidence for the channel's stem spanning the lipid membrane. We assume a toroidal lipid arrangement around the stem with the headgroups oriented towards it. In planar lipid bilayer recordings, we determined a single channel conductance of 0.87 ± 0.15 nS and Ohmic behavior in the observed voltage range (-200 mV to +200 mV). The channels displayed voltage-dependent gating transition as observed for their biological counterparts. By designing three channel 'mutants', we verified that the channel's gating behavior depends on its structural details. In first DNA hairpin unzipping and G-quadruplex unfolding experiments we confirmed the channel's application as single molecule sensor. Our findings suggest that besides the main ionic current pathway along the stem's central channel, additional pathways through the channel's sidewalls contribute to the total transmembrane current. The versatility of DNA-based channels is exemplified by an alternative channel design featuring a stem with larger cross-section.

Chapter 5 covers two specific applications for solid-state nanopore sensing devices. We outlined the fabrication of solid state nanopores just slightly larger than the diameter of a DNA double helix that are drilled into silicon nitride membranes using the highly focused electron beam of a transmission electron microscope (TEM). Moreover, we present a pore-cavity-pore nanodevice that is created by subsequent e-beam

lithography, reactive ion etching and feedback-controlled wet chemical etching steps.

Combining the small TEM-drilled pores with the active voltage control setup described in Chapter 3, we established a solid-state NFS platform for probing biomolecular interactions, which was used here to explore DNA/histone interactions in mononucleosomes. Our method applies either a constant or a time-varying force to a nucleosomal dsDNA tail in order to overcome interactions between the DNA and histones. Compared to conventional nanopore experiments, our method covers a considerably wider range of unraveling voltages (i.e. forces) and is not influenced by the capture process. Our results are well-described by the escape over a single energy barrier – presumably given by the strong interaction of nucleosomal DNA with the H3-H4 tetramer in the dyad region – under quasi-adiabatic conditions. Our method offers great sensitivity for changes in the positioning sequence with a factor of 5 difference betweeen dissociation rates of a high affinity sequence (Widom 601) and the sea urchin 5S sequence. We related this shift in stability to an increase in barrier height and extension. With CpG methylation, we performed first force spectroscopy studies on an epigenetic marker. While the force-induced dissociation of nucleosomes assembled from methylated DNA was found to be nearly unaffected, a detailed analysis of its voltage scaling suggests a more open equilibrium conformation as suggested by previous studies.

In Section 5.3, we determined electrophoretic mobilities of 6 - 15 kbp dsDNA fragments by clocking their time-of-flight through the cavity of a pore-cavity-pore device. Our findings indicate fast relaxation of translocated molecules upon cavity entry and a barrier-dominated escape. Our method is ideal for electrophoretic mobility or zeta potential measurements at low analyte concentrations. Demonstrating a particular feature of our method, we probed the molecules' relaxation kinetics by correlating the current signals corresponding to cavity entry and exit, respectively.

7 Outlook

7.1 A Future Perspective on Synthetic Lipid Membrane Channels

In the following, we give a perspective on the further development of DNA-based membrane channels as described in Chapter 4 of this work. In this context, we discuss potential studies, possible modifications and improvements as well as future applications.

Relating Structure to Function. In Sections 4.4 and 4.5 we studied the transport characteristics of our DNA-based membrane channel and made first attempts to relate them to structural details. Potential applications for DNA-based channels would benefit from further investigations to obtain a deeper understanding of their structure-function relationship. This includes studies on ion selectivity and dependence on ionic strength which may help to characterize the influence of the DNA backbone charge on ion flow through the central channel and along other pathways. Temperature-dependent studies could reveal how Brownian dynamics of the DNA structure impact its conductance (cf. Figure 7.1[1]). Moreover, systematic studies of channel gating [242] could provide strategies on how to deliberately induce reversible conformational changes for applications in synthetic biology.

Tailoring Structure and Function. In Section 4.5, we demonstrated our DNA channels' use as single molecule sensing devices. While sensors based on naturally occurring membrane pores provide excellent electrical properties, altering the geometry of biological pores and introducing chemical functions through genetic engineering or chemical conjugation is challenging. In the last decade, huge efforts have been made to create mutants based on natural membrane pores such as α-hemolysin [343], MspA [92] or ClyA [173] in order to optimize them for DNA sequencing and other sensing tasks. By contrast, the geometry of synthetic DNA objects and their chemical properties can be tailored for custom nanopore sensing applications for which no suitable biological pore or solid state system exists. The channel designs described in this work feature diameters of $\approx 2\,\mathrm{nm}$ and $\approx 4\,\mathrm{x}\,4\,\mathrm{nm}$, allowing transport of single stranded and double stranded DNA, respectively. While the well-established protein pores α-hemolysin and MspA feature diameters perfectly suited for ssDNA and some protein pores have

[1] Design and TEM characterization of the channel shown in this figure were performed by Thomas G. Martin.

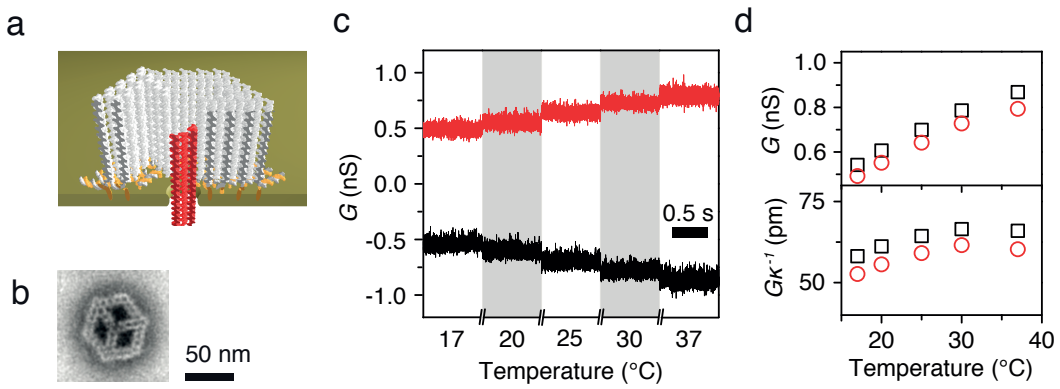

Figure 7.1: Temperature Dependence of Channel Conductance. a) Alternative DNA channel design used for temperature dependent conductance studies. Compared to the channel design presented in Chapter 4, it features a wheel-shaped support and a shorter stem (28 nm) with identical cross-section. b) TEM class average of the structure (top view) c) Current traces of a single DNA channel incorporated into a DPhPC bilayer using the MECA setup and 1 M KCl electrolyte buffered at pH 8. Red: Forward bias. Black: Reverse bias. d) Temperature dependence of channel conductance (top) and conductance divided by bulk conductivity (bottom) for forward (red) and reverse bias (black).

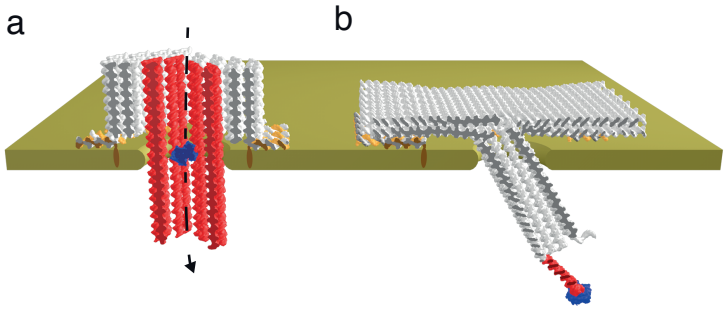

Figure 7.2: Tailoring Structure and Function of DNA-Based Membrane Channels. a) Proposed channel design featuring a 8 nm stem domain for protein translocation experiments b) Proposed modification of the channel described in Section 4.6, adding a flap with a ligand-gated locking mechanism.

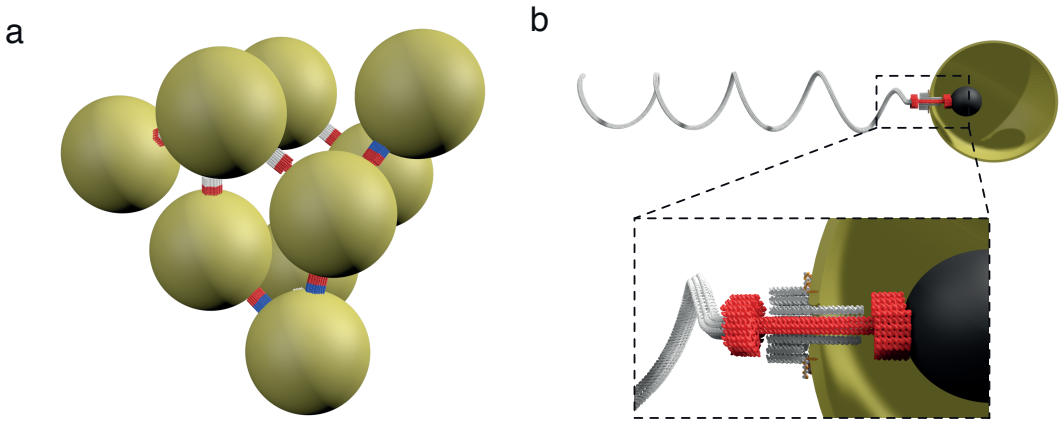

Figure 7.3: Potential Applications in Synthetic Biology. a) Programmed assembly of cell-sized compartments to communicating reaction networks via dimeric DNA channels. b) Synthetic propulsion systems for cell-sized compartments based on a bilayer-embedded rotaxane and driven by magnetic actuation.

been modified to allow translocation of dsDNA [174, 324], biological candidates with sizes large enough to study the transport of proteins are lacking. DNA-based channels can be equipped with transmembrane regions wide enough for such tasks (cf. Figure 7.2a), however, constraints may be imposed by the ability to form a stable toroidal lipid arrangement around the structure, particularly in presence of a transmembrane bias [344]. Careful tuning of the membrane tension may be required to stabilize larger apertures.

Apart from tailoring the channel dimensions, we also aim to amend it with functional features such as selective transport or ligand gating. Selective transport might be achieved by adequate binding sites promoting analyte capture [173]. As we suspect a similar effect to be caused by the scaffold loops of our initial channel structure, a first step might be to replace these loops with extensions of known sequence and to study the sequence dependence of ssDNA capture. For the DNA channel with quadratic cross-section described in Section 4.6, ligand gating of molecular transport may be realized by attaching a flap to the end of the stem region and combining it with an aptamer-based locking mechanism [229] (see Figure 7.2b). An oligonucleotide-gated DNA channel based on strand displacement has been shown by Burns et al. [345]. Ultimatively, gating could be realized by inducing a conformational change – e.g. intentional destabilization of the stem via partial unzipping of duplex regions – that is triggered by the presence of a ligand or a different sensory input such as voltage, light or heat.

Applications in Synthetic Biology. In addition to single molecule sensing, we envision applications for DNA-based channels in synthetic biology such as dimeric DNA channels that pair via controlled stacking interactions [346], allowing programmed assembly of different cell-sized compartments to complex reaction networks and controlling their communication (cf. Figure 7.3a). A particularly ambitious task would be to

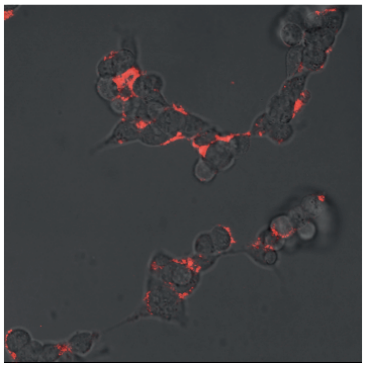

Figure 7.4: Interaction with Cell Membranes. Confocal microscopy images (bright field and fluorescence overlay) of cultured HEK293 cells after incubation with 4 nM of DNA channels overnight. Channels were labeled with one Atto 655 dye per structure.

create synthetic propulsion systems for cell-sized compartments inspired by bacterial flagella (see Figure 7.3b). Such a system may be realized by using the DNA channel as stator of a membrane-embedded rotaxane [347]. An artificial flagellum may be created via tile-based assembly [192] and torque may be transmitted via magnetic actuation. On the long run, synthetic DNA channels may even evolve into complex nano-machines harnessing ion flux to drive membrane transport or rotary motion.

Medical Applications An appealing future application of DNA-based structures is their use *in vivo*, e.g. as antimicrobial agents or cancer therapeutics [229]. DNA-based membrane channels could be modified with receptors for specific membrane proteins (cf. Section 4.1.3) to target cancer cells and trigger cell death by interfering with homeostasis. However, precise tuning of the membrane interaction and further stabilization of the DNA structures may be necessary as preliminary confocal microscopy experiments with HEK293 cells suggest cellular uptake rather than membrane incorporation (see Figure 7.4). For a smaller DNA channel with different hydrophobic modification, a cytotoxic effect to cervical cancer cells has been observed [348].

7.2 Studying Epigenetics with Nanopore Force Spectroscopy

With CpG methylation, we studied the influence of an important epigenetic marker on the free energy landscape of DNA-histone interactions using nanopore force spectroscopy (NFS, cf. Section 5.2). With its high throughput and label-free detection scheme, our solid state NFS platform lends itself to a systematic study of the various known post-translational modifications of the histone proteins and their influence on nucleosome stability. Identifying the impact of such modifications on the free energy landscape for the interaction could help to model their complex interplay and its influence on gene expression. Moreover, experiments may be extended to other epigenetic mechanisms such as the effect of DNA methylation on transcription factor binding or

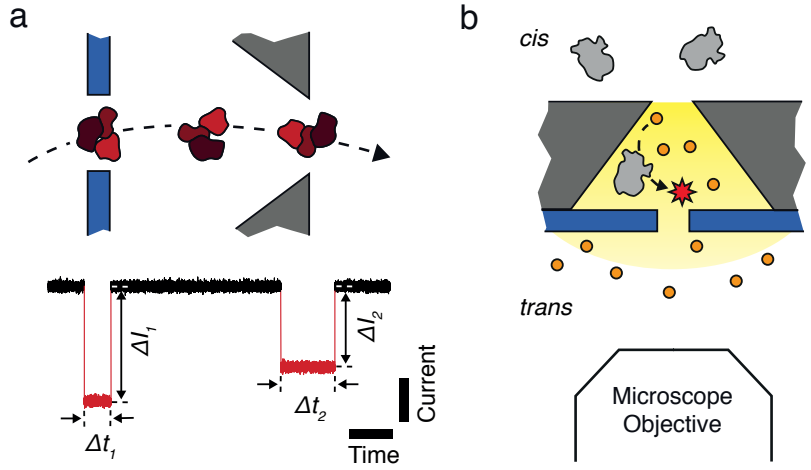

Figure 7.5: The PCP Device as Protein Sensor and Single Molecule Reaction Chamber. a) Studying conformational dynamics of proteins. Upon a protein's subsequent passage of the SiN pore (blue) and the Si pore (gray) of a PCP device (top), we expect pairs of current signals to be detected (bottom). If conformational changes give rise to a different current blockade amplitude ΔI and/or duration Δt, kinetic studies may be performed by correlating the blockade pairs at different bias voltages. b) Optical studies of enzymatic reactions. A single enzyme (gray) is electrophoretically driven into the cavity from the *cis* side, while its substrate (orange) is added on the *trans* side. While the enzyme is trapped inside the cavity, its activity may be monitored via fluorescence microscopy.

interaction with methyl-binding proteins [349], where association rate constants may be obtained via additional recapture experiments (cf. Section 3.3.2).

7.3 The PCP Device as Protein Sensor & Single Molecule Reaction Chamber

The pore-cavity-pore (PCP) device lend itself to measure electrophoretic mobilities of proteins at low analyte concentrations. To reduce unspecific interactions with the cavity surface as observed in protein translocation experiments [350], the surfaces could be coated with organosilanes [50]. As both cavity entry and exit of a single molecule provide a separate current signal, the PCP device may be used for statistical correlation studies, e.g., to detect chemical or physical changes the molecules experience during traversal of the cavity, or to filter out "bad" events from the data recordings. If changes in protein conformation lead to detectable differences in the current blockade amplitude, their kinetics may be probed completely label-free and at sub-millisecond resolution (see Figure 7.5). However, it is yet to be determined whether blockade pairs can be unambiguously assigned for proteins.

Combined with optical readout [80], the PCP device can be turned into a unique tool for electrically controlled loading and manipulation of single molecules into a tailored microenvironment and for the study of biomolecular dynamics and biochemical processes under spatial confinement. Single enzymes may be electrophoretically loaded into its cavity from the *cis* side while the substrate is introduced from the *trans* side.

By careful tuning of pore dimensions, enzymes may be trapped for extended periods of time and their activity may be monitored optically (see Figure 7.5b). As the silicon layer surrounding the cavity is opaque, background fluorescence caused by leakage of substrate to the *cis* side is suppressed. Such experiments could be used to study dynamic disorder in enzymatic reactions without requiring enzyme immobilization [351].

Appendix

A.1 16 Channel MECA Setup

A schematic of the 16 Channel MECA setup presented in Section 2.3.2 is shown in Figure A.1. The MECA chip is inserted into a designated slot of a custom-built aluminum heat exchanger. Below the chip, the heat exchanger features a cylindrical opening to accommodate a magnetic actuator for automated bilayer generation. The chip is contacted and pressed against the heat exchanger by a contact board featuring 16 pogo pins. Moreover, this board contains a PTFE chamber holding the electrolyte solution. It is sealed to the chip with a rubber ring. An aluminum enclosure around the assembly provides electrostatic shielding. For temperature control, the heat exchanger is connected to a thermostatic circulator (F30-C, Julabo GmbH, Germany).

The Triton$^+$ multi-channel amplifier (Tecella LLC., USA) and the EPC 9 single-channel amplifier headstage (Heka GmbH, Germany) are connected to a relay board, which allows to switch individual wells of the MECA chip between amplifiers. The board features 32 high speed low capacitance reed relays (HI05-1A66, StandexMeder GmbH, Germany), which are actuated by a designated controller board[1]. To prevent ground loops, the boards are battery powered and connected to the measurement computer via a custom-built optical isolator circuit. Both boards are encased in aluminum boxes for shielding purposes.

To prevent ground loops, we connect all enclosures in a star-like fashion to the signal ground terminal of the EPC 9 amplifier. Moreover, we turn off the multi-channel amplifier during single channel measurements and ground its power terminals.

A.2 Recapture Experiments

Drift-Diffusion Model for DNA Recapture Experiments For the experiments discussed in Section 3.3.2, we modeled the recapture of dsDNA with a solid state nanopore. Analogous to Gershow et al. [122], we numerically solved the time-dependent drift-diffusion equation in spherical coordinates (cf. Eq. 3.20):

$$\frac{\partial c(r,t)}{\partial t} = \frac{1}{r^2}\frac{\partial}{\partial r} r^2 \left(\frac{\mp \rho \mid \mu I \mid}{2\pi r^2} c(r,t) + D \frac{\partial c(r,t)}{\partial r} \right) \tag{A.1}$$

Here, r is the radial distance to the pore mouth, ρ is the electrolyte resistivity, I is the ionic current across the pore, μ is the electrophoretic mobility of the DNA molecule

[1] Magnetic actuator, Relays board and controller board were kindly provided by Matthias Beckler, Nanion GmbH, München.

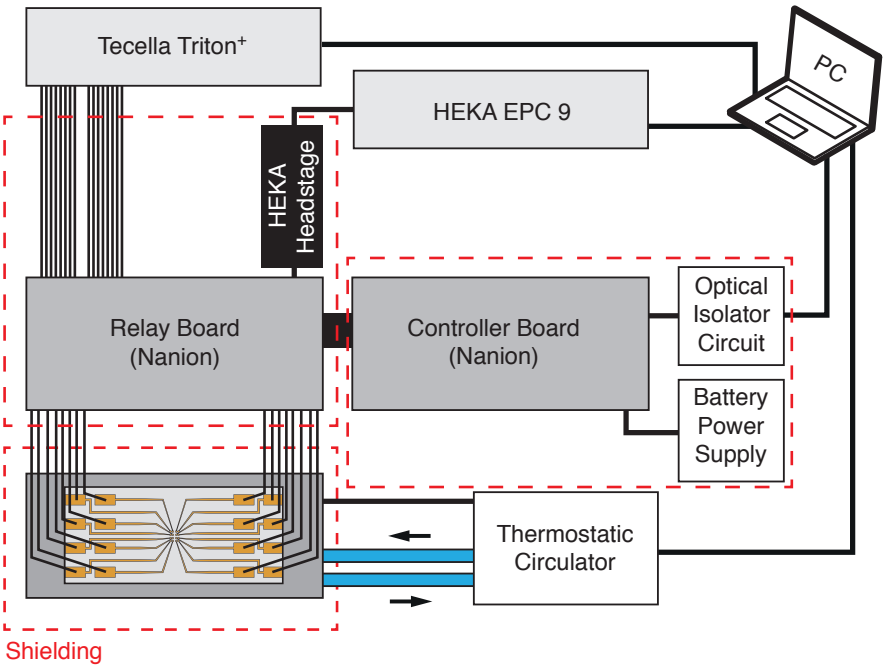

Figure A.1: 16 Channel MECA Setup. Wiring schematic.

and D is its diffusion coefficient. c is the DNA concentration, which here is equivalent to the probability of finding the molecule at a certain position. The negative sign at the drift term accounts for movement away from the pore (for $t \leq t_{delay}$), whereas the positive sign accounts for movement towards it (for $t > t_{delay}$). We solved Eq. A.1 numerically using MATLAB's *pdepe* function with the initial condition

$$c(r, 0) = \frac{\delta(r - r_0)}{2\pi r_0} \tag{A.2}$$

Here, r_0 is the DNA molecule's distance to the pore mouth after its initial translocation. Like Gershow et al. [122], we chose the average end-to-end distance of a Gaussian chain with one fixed end. Moreover, we chose an absorbing boundary condition at a distance r_c to the pore mouth, where recapture occurs with unit probability, and a reflective boundary condition at $r = 5\,\mu m$ to simplify calculations (We tried values of up to $100\,\mu m$ and found no influence). A summary of all used parameters is given in Table A.1.

For r_c, we chose a value that is 5 nm less than r_0. Moreover, we tested values between 0.1 nm and 10 nm and found virtually no impact on the result. For the electrophoretic mobility and diffusion coefficient of DNA, bulk values were used. In Figure A.2, the result of our calculations is illustrated. At $t = 0\,ms$ (the moment at which the voltage is reversed), a narrow population with a peak at 113 nm is observed. Due to diffusion, the population broadens with time and its center moves away from the pore. At the same time, the integrated probability density decreases with increasing time due to an increasing probability of recapture.

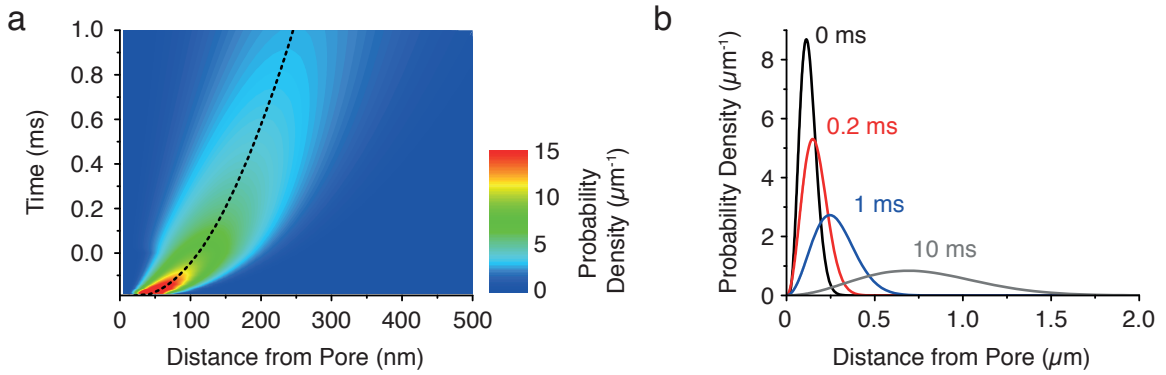

Figure A.2: Drift-Diffusion Model. a) Color-mapped probability density of the DNA molecule after its initial translocation at t = -200 µs. At t = 0 µs, the polarity is switched. Dashed line indicates position of population maximum as a function of time. Parameters in Table A.1 were used for calculation. b) Probability density as a function of pore distance at 0 ms, 0.2 ms, 1 ms and 10 ms. The integrated probability density decreases with time, as the recapture probability increases.

Table A.1: Recapture Simulations. Parameters used for simulating the recapture of 500 bp DNA with a 2.8 nm solid state pore.

μ (cm^2/Vs)	$1.8 \cdot 10^{-4}$	[352]
D (µm^2/s)	11.5	[353]
r_0 (nm)	10	
r_c (nm)	5	
I (nA)	0.86	@ 275 mV
σ (S/m)	4.3	@ 400 mM KCl, 10 mM Tris, 1 mM EDTA, pH 8

A.3 DNA-Based Synthetic Membrane Channels

Data Analysis. All current recordings were analyzed using custom routines implemented in MATLAB. Data recorded using the single channel amplifier were filtered at cut-off frequencies of 2 - 10 kHz using the built-in Bessel filter. For all experiments using the 16 channel amplifier, a cut-off frequency of 3 kHz was set, but as described in Section 2.3.2, the slow frequency response of the amplifier board limited the bandwidth considerably (0.5 - 1.7 kHz). To determine the amplitude of measured current blockades reliably, rising edge and falling edge of all peaks were fitted with single exponentials.

Durations of current blockades were visualized with histograms featuring logarithmically spaced bins [354] and the event total normalized to 1. Such histograms are convenient for exponentially distributed values and allow good separation of multiple exponential components. For a mono-exponential decay, logarithmically binned histograms are fitted with the probability distribution function

$$p_i(t) = \frac{wt}{\tau} e^{\frac{t_0 - t}{\tau_i}}. \tag{A.3}$$

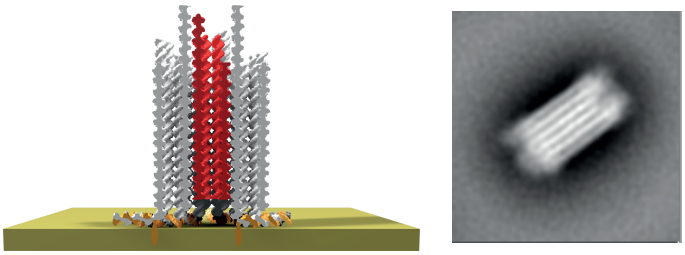

Figure A.3: Control Experiments. A channel mutant without stem constructed for control experiments. Left: Schematic depiction. Right: TEM class average of the structure.

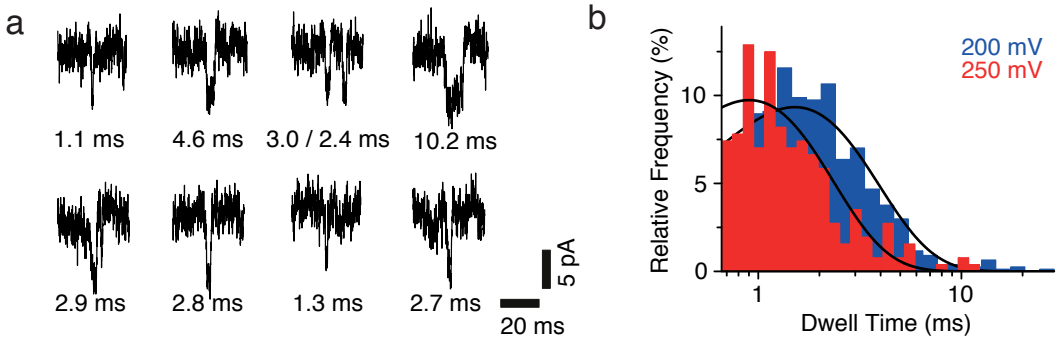

Figure A.4: Voltage Dependence of Hairpin Unzipping Kinetics. a) Examples for hairpin translocation events at 100 mV bias voltage with dwell times in the range of 1 - 10 ms. b) Dwell time histograms for 200 mV (blue, see Figure 4.13) and 250 mV (red) bias voltage. 256 (red) and 777 (blue) events were detected. Solid lines correspond to single-parameter mono-exponential fits. We obtained time constants of 1.5 ± 0.1 ms (200 mV) and 0.9 ± 0.1 ms (250 mV).

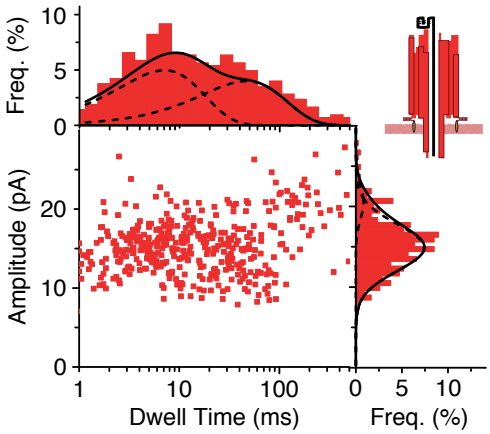

Figure A.5: Long-Lived Population. Scatter Plot of the current amplitude vs. dwell time for forward translocation of Q-T125 (see Figure 4.13), including data from the last part of the measurement. Solid lines correspond to double exponential (top) and double Gaussian (right) fits to the histograms.

Here τ_i is the time constant, w is the logarithmic bin width and t_0 corresponds to the duration of shortest detectable event. The function peaks at $t = \tau_i$ and its amplitude is only dependent on the constant factors w and t_0, leaving the time constant the only fit parameter. For a double-exponential decay, histograms are fitted by

$$p_{double} = ap_1(t) + (1 - a)p_2(t) \tag{A.4}$$

with the event fraction a and time constants τ_1 and τ_2 being the only fit parameters. Unless otherwise noted, all dwell time histograms were fitted using above parameters. In some cases an additional amplitude scaling factor was necessary to account for normalization issues due to "outliers", i.e. events not described by the probability density function.

Control Experiments. Using the same insertion pulse protocol as for the experiments described in Section 4.4.1, we performed experiments with DNA channels lacking a stem. These were prepared and purified in the same way as the complete DNA channels, but with the staples responsible for folding of the protruding six-helix bundle left out (see caDNAno maps in [232]). For these "mutants", we did not observe any incorporation within several hours of observation time. We also performed experiments with cholesterol-labeled anchor strands alone. These also did not lead to the formation of channels in the lipid membranes. At very high concentrations ($> 10\,\mu M$), cholesterol-labeled oligonucleotides destabilized the lipid bilayer, leading to membrane rupture.

Voltage Dependence of Dwell Times for Hairpin Unzipping To study the voltage scaling of blockade dwell times, we performed additional experiments in forward direction at bias voltages of 100 mV and 250 mV. Our results are summarized in Figure A.4. At 100 mV, we observed dwell times in the range of several milliseconds (see Figure A.4a). However, due to a very low event rate at this bias voltage, no quantitative treatment was possible. At 250 mV bias, we detected a total of 256 events, from which we determined a time constant of 0.9 ± 0.1 ms (see Figure A.4b).

Long-Lived Events for Q-T125 Translocation at Long Measurement Times. For prolonged measurement times for the Q-T125 translocation experiment in forward direction (cf. Figure 4.13), a sudden increase in long-lived blockade events was observed. A scatter plot including all Q-T125 measurement data recorded for these events is shown in Figure A.5. In this plot, a second population is clearly visible. It features a higher blockade amplitude (20.5 pA) than the main population and a considerably longer characteristic dwell time (46 ms).

A.4 Nanopore Force Spectroscopy on Nucleosomes

Nucleosome Capture As discussed in Section 5.2.2, nucleosome-associated current blockades feature a multiple shallow current levels preceding the deep blockade level

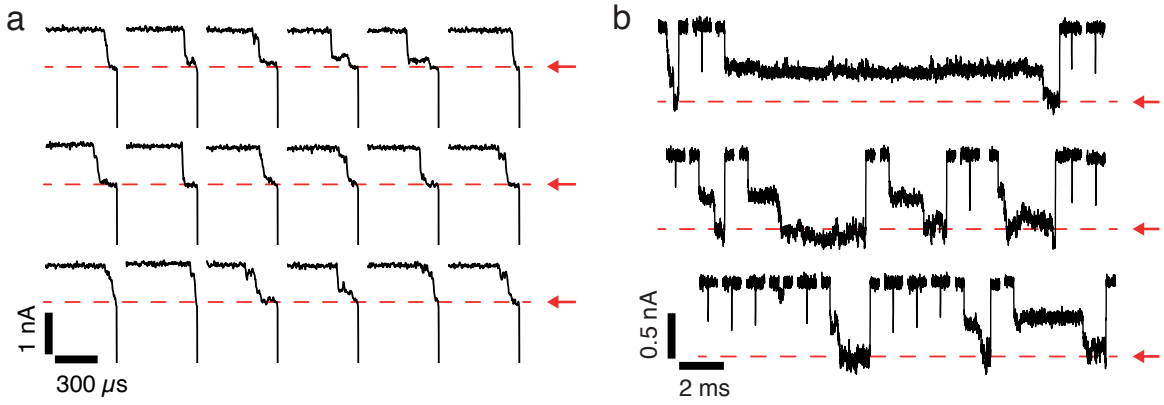

Figure A.6: Nucleosome Capture. a) Representative set of 18 capture traces (red arrows indicate trigger level). Only capture events followed by a detectable opening transition are shown. b) Multilevel-structure of nucleosome-associated current blockades. Events were recorded at 400 mV capture voltage before starting a triggered NFS measurement.

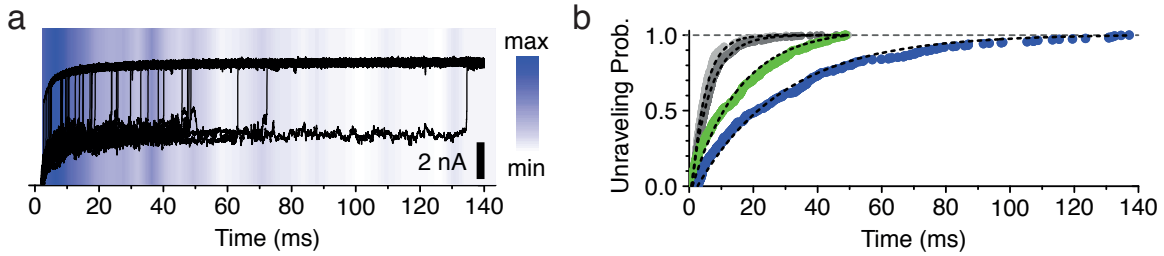

Figure A.7: Triggered Constant Voltage Experiments. a) Current traces at a constant bias voltage of 150 mV, acquired after triggered capture of Widom 601 nucleosomes at a capture voltage of 450 mV (subset of 40 representative traces with an opening transition). Color shading: Distribution of opening transitions for the complete dataset (312 detected transitions). b) Cumulative histograms for experiments at 150 mV (blue), 200 mV (green) and 300 mV bias voltage (gray & light gray). Dashed lines correspond to single exponential fits (single fitting parameter).

associated with threading of the DNA tail into the pore lumen (cf. Figure A.6b). In our NFS experiments, the trigger was set to react to the final (deepest) blockade level only. As intermediate current levels tended to overlap with the final blockade level to a certain degree, the trigger did not always occur at the falling edge of the final level, but was delayed by up to 200 µs in some cases (see Figure A.6a). Choosing trigger levels of either 39 % or 47 % of the open pore level did not affect the transition voltage distribution.

Triggered Constant Voltage Experiments. To confirm the applicability of Eq. 3.25 when transforming ramp data to voltage-dependent dissociation rates in nucleosome unraveling experiments (Section 5.2), we performed additional experiments for the unmethylated Widom 601 sample. As for the ramp experiments, we used a hardware trigger to reduce the measurement voltage upon nucleosome capture. Then, the measurement voltage was kept constant and the elapsed time until detection of the opening transition was recorded. Our results are summarized in Figure A.7 and Figure 5.8.

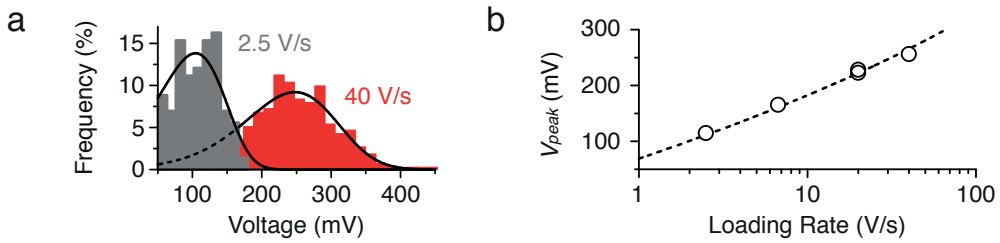

Figure A.8: Modeling Nucleosome Force Spectroscopy Data with Kramers Diffusion Theory. a) Transition voltage distributions for 5S rDNA nucleosomes obtained at 2.5 V/s (gray) and 40 V/s (red). Lines correspond to predictions from the Kramer's diffusion model using Eq. 3.28 and the parameters obtained in Section 5.2.4. b) Loading rate dependence of the most probable transition voltage. Dashed line corresponds to prediction from the Kramer's model (Eq. 3.29, including a scaling parameter).

Kramers Diffusion Theory. In Section 5.2.4, we fitted dissociation rate vs. voltage data with a Kramers diffusion model described in Section 3.4.5. Using the obtained parameter sets, we were able to accurately predict the shapes of unraveling voltage distributions and the loading rate dependence for 5S rDNA (see Figure A.8).

A.5 Time-of-Flight Experiments

Pulse Pair Assignment. For data analysis, we modified an existing peak detection algorithm [355] implemented in MATLAB. In addition to the peak minimum and duration, the interval between the end of each current blockade and the onset of the subsequent blockade is determined for all pulses. The position of the maximum in the TOF distribution (here: 75 ms) – corresponding to the typical TOF – is used to define a "correlation range" for the assignment of peaks. All peak intervals significantly larger than the pre-defined correlation range are then excluded from the analysis to unambiguously assign each pulse to a translocation event through either the first or the second pore. Furthermore, if there are more than two subsequent peaks within the correlation range, all of them are discarded. This allows us to exclude events where two or more molecules translocate the device in an interval comparable to a single molecule's time of flight, rendering a definite assignment to either pore impossible. This criterion becomes important for high event rates. Under our experimental conditions, 94 % of all detected events were successfully correlated.

Dynamic Light Scattering and Laser Doppler Electrophoresis. The diffusion coefficients and electrophoretic mobility of the 6, 10 and 15 kbp dsDNA fragments were independently determined by dynamic light scattering (DLS) and laser Doppler electrophoresis, employing a ZetaSizer Nano Instrument (Malvern Ltd., UK). The measurements were performed with 1 nM DNA concentration at the same buffer conditions as the TOF measurements. For DLS, a scattering angle of 173° was used (backscatter mode) and data analysis was performed using the CONTIN [356] model. As shown

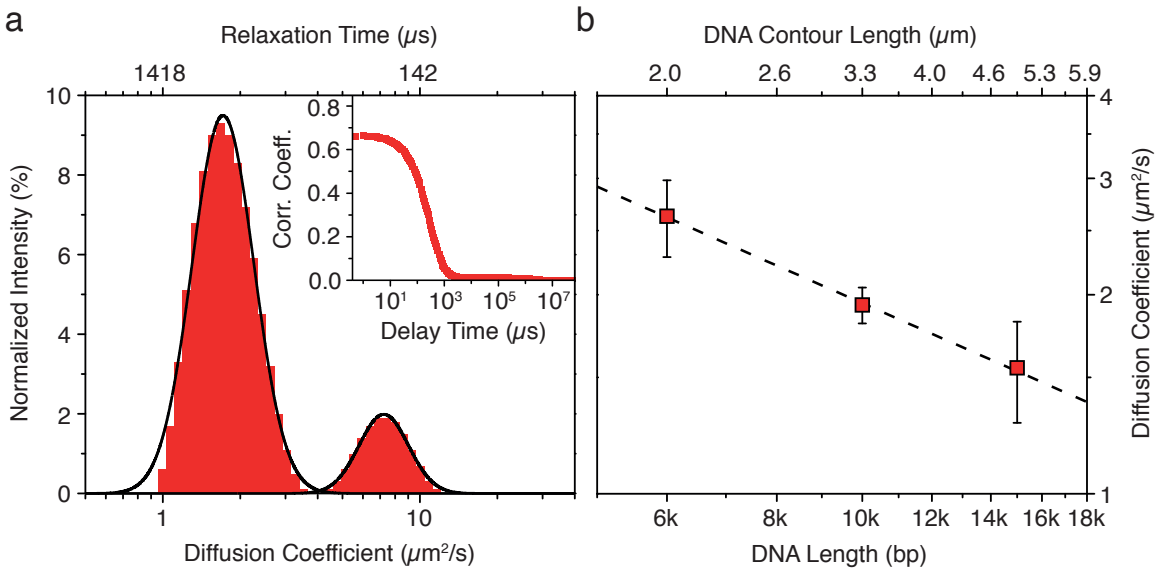

Figure A.9: Dynamic Light Scattering Measurements. a) Diffusion coefficient vs. normalized Intensity for 10 kbp dsDNA fragments. The solid line corresponds to a fit to a bimodal lognormal distribution. Inset: Corresponding correlation function b) Diffusion coefficient vs. DNA length for 6, 10 and 15 kbp fragments. The dashed line corresponds to a power law fit, yielding an exponent $\nu = 0.59 \pm 0.04$.

in Figure A.9, we observe two peaks in the distribution of relaxation times. We attribute the slow peak to translational motion of the molecule, whereas the fast peak is attributed to intramolecular dynamics in combination with translation [357]. The measured diffusion coefficients obey a power law dependence on the length of the molecule $D \sim l_{DNA}^{-\nu}$, resulting in an exponent $\nu = 0.59 \pm 0.04$ as expected for a polymer under good solvent conditions [358] ($\nu \approx 0.588$) and found experimentally for DNA previously [359] ($\nu = 0.57 \pm 0.01$).

Bibliography

[1] Alberts, B. *et al.* *Molecular Biology of the Cell* (Garland Science, 2008), 5th edn.

[2] Kass, R. S. The channelopathies: novel insights into molecular and genetic mechanisms of human disease. *The Journal of Clinical Investigation* **115**, 1986–1989 (2005).

[3] Sakmann, B. & Neher, E. *Single Channel Recording* (Springer, New York, 2009), 2nd edn.

[4] Kasianowicz, J., Brandin, E., Branton, D. & Deamer, D. Characterization of individual polynucleotide molecules using a membrane channel. *Proceedings of the National Academy of Sciences of the United States of America* **93**, 13770–13773 (1996).

[5] Butler, T. Z., Pavlenok, M., Derrington, I. M., Niederweis, M. & Gundlach, J. H. Single-molecule DNA detection with an engineered MspA protein nanopore. *Proceedings of the National Academy of Sciences of the United States of America* **105**, 20647–20652 (2008).

[6] Laszlo, A. H. *et al.* Decoding long nanopore sequencing reads of natural DNA. *Nature Biotechnology* **32**, 829–833 (2014).

[7] Bayley, H. & Cremer, P. S. Stochastic sensors inspired by biology. *Nature* **413**, 226–30 (2001).

[8] Sauer-Budge, A. F., Nyamwanda, J. A., Lubensky, D. K. & Branton, D. Unzipping kinetics of double-stranded DNA in a nanopore. *Physical Review Letters* **90**, 238101 (2003).

[9] Svoboda, K., Schmidt, C. F., Schnapp, B. J. & Block, S. M. Direct observation of kinesin stepping by optical trapping interferometry. *Nature* **365**, 721–727 (1993).

[10] Cui, Y. & Bustamante, C. Pulling a single chromatin fiber reveals the forces that maintain its higher-order structure. *Proceedings of the National Academy of Sciences of the United States of America* **97**, 127–132 (2000).

[11] Rief, M., Gautel, M., Oesterhelt, F., Fernandez, J. M. & Gaub, H. E. Reversible unfolding of individual titin immunoglobulin domains by AFM. *Science* **276**, 1109–1112 (1997).

[12] Woodside, M. T. *et al.* Direct measurement of the full, sequence-dependent folding landscape of a nucleic acid. *Science* **314**, 1001–1004 (2006).

[13] Dekker, C. Solid-state nanopores. *Nature Nanotechnology* **2**, 209–215 (2007).

[14] Matile, S., Jentzsch, A. V., Montenegro, J. & Fin, A. Recent synthetic transport systems. *Chemical Society Reviews* **40**, 2453–2474 (2011).

[15] Joh, N. H. *et al. De novo* design of a transmembrane Zn^{2+}-transporting four-helix bundle. *Science* **346**, 1520–1524 (2014).

[16] Neher, E. & Sakmann, B. Single-channel currents recorded from membrane of denervated frog muscle fibres. *Nature* **260**, 799–802 (1976).

[17] Zhao, Y. *et al.* Patch clamp technique: Review of the current state of the art and potential contributions from nanoengineering. *Proceedings of the Institution of Mechanical Engineers, Part N: Journal of Nanoengineering and Nanosystems* **222**, 1–11 (2008).

[18] Sigworth, F. J. & Neher, E. Single Na^+ channel currents observed in cultured rat muscle cells. *Nature* **287**, 447–449 (1980).

[19] Hamill, O. P., Marty, A., Neher, E., Sakmann, B. & Sigworth, F. J. Improved patch-clamp techniques for high-resolution current recording from cells and cell-free membrane patches. *Pflügers Archiv* **391**, 85–100 (1981).

[20] Dunlop, J., Bowlby, M., Peri, R., Vasilyev, D. & Arias, R. High-throughput electrophysiology: an emerging paradigm for ion-channel screening and physiology. *Nature Reviews Drug Discovery* **7**, 358–368 (2008).

[21] Milenkovic, N. *et al.* A somatosensory circuit for cooling perception in mice. *Nature Neuroscience* **17**, 1560–1566 (2014).

[22] Kralj, J. M., Hochbaum, D. R., Douglass, A. D. & Cohen, A. E. Electrical spiking in *Escherichia coli* probed with a fluorescent voltage-indicating protein. *Science* **333**, 345–348 (2011).

[23] Hochbaum, D. R. *et al.* All-optical electrophysiology in mammalian neurons using engineered microbial rhodopsins. *Nature Methods* **11**, 825–833 (2014).

[24] Magistretri, J., Mantegazza, M., Guatteo, E. & Wanke, E. Action potentials recorded with patch-clamp amplifiers: are they genuine? *Trends in Neurosciences* **19**, 530–534 (1996).

[25] Barnett, M. W. & Larkman, P. M. The action potential. *Practical Neurology* **7**, 192–197 (2007).

[26] Molecular Devices LLC., Sunnyvale, CA, USA. *The Axon Guide*, 3rd edn. (2012).

[27] Lindsay, A. R., Manning, S. D. & Williams, A. J. Monovalent cation conductance in the ryanodine receptor-channel of sheep cardiac muscle sarcoplasmic reticulum. *The Journal of Physiology* **439**, 463–480 (1991).

[28] Tinker, A. & Williams, A. J. Divalent cation conduction in the ryanodine receptor channel of sheep cardiac muscle sarcoplasmic reticulum. *The Journal of General Physiology* **100**, 479–493 (1992).

[29] Bell, J. E. & Miller, C. Effects of phospholipid surface charge on ion conduction in the K^+ channel of sarcoplasmic reticulum. *Biophysical Journal* **45**, 279–287 (1984).

[30] Schindler, H. & Rosenbusch, J. P. Matrix protein from *Escherichia coli* outer membranes forms voltage-controlled channels in lipid bilayers. *Proceedings of the National Academy of Sciences of the United States of America* **75**, 3751–3755 (1978).

[31] Benz, R. Permeation of hydrophilic solutes through mitochondrial outer membranes: review on mitochondrial porins. *Biochimica et Biophysica Acta (BBA) - Reviews on Biomembranes* **1197**, 167–196 (1994).

[32] Song, L. *et al.* Structure of staphylococcal α-hemolysin, a heptameric transmembrane pore. *Science* **274**, 1859–1865 (1996).

[33] Derrington, I. M. *et al.* Nanopore DNA sequencing with MspA. *Proceedings of the National Academy of Sciences of the United States of America* **107**, 16060–16065 (2010).

[34] Mueller, P., Rudin, D. O., Ti Tien, H. & Wescott, W. C. Reconstitution of cell membrane structure *in vitro* and its transformation into an excitable system. *Nature* **194**, 979–980 (1962).

[35] White, S. H. Analysis of the torus surrounding planar lipid bilayer membranes. *Biophysical Journal* **12**, 432 (1972).

[36] Tien, H. T. & Dawidowicz, E. A. Black lipid films in aqueous media: A new type of interfacial phenomenon: Experimental techniques and thickness measurements. *Journal of Colloid and Interface Science* **22**, 438–453 (1966).

[37] Montal, M. & Mueller, P. Formation of bimolecular membranes from lipid monolayers and a study of their electrical properties. *Proceedings of the National Academy of Sciences of the United States of America* **69**, 3561–3566 (1972).

[38] Sondermann, M., George, M., Fertig, N. & Behrends, J. C. High-resolution electrophysiology on a chip: Transient dynamics of alamethicin channel formation. *Biochimica et Biophysica Acta (BBA) - Biomembranes* **1758**, 545–551 (2006).

[39] Holden, M. A., Needham, D. & Bayley, H. Functional bionetworks from nanoliter water droplets. *Journal of the American Chemical Society* **129**, 8650–8655 (2007).

[40] White, S. H. The physical nature of planar bilayer membranes. In Miller, C. (ed.) *Ion Channel Reconstitution*, book section 7, 3–35 (Plenum Press, New York, 1986).

[41] Hanke, W. Incorporation of ion channels by fusion. In Miller, C. (ed.) *Ion Channel Reconstitution*, book section 7, 141–153 (Plenum Press, New York, 1986).

[42] Baaken, G., Sondermann, M., Schlemmer, C., Ruhe, J. & Behrends, J. C. Planar microelectrode-cavity array for high-resolution and parallel electrical recording of membrane ionic currents. *Lab on a Chip* **8**, 938–944 (2008).

[43] del Rio Martinez, J. M., Zaitseva, E., Petersen, S., Baaken, G. & Behrends, J. C. Automated formation of lipid membrane microarrays for ionic single-molecule sensing with protein nanopores. *Small* **11**, 119–125 (2015).

[44] Baaken, G., Ankri, N., Schuler, A.-K., Rühe, J. & Behrends, J. C. Nanopore-based single-molecule mass spectrometry on a lipid membrane microarray. *ACS Nano* **5**, 8080–8088 (2011).

[45] Renner, S., Bessonov, A. & Simmel, F. C. Voltage-controlled insertion of single α-hemolysin and mycobacterium smegmatis nanopores into lipid bilayer membranes. *Applied Physics Letters* **98**, 083701 (2011).

[46] Sakmann, B. & Boheim, G. Alamethicin-induced single channel conductance fluctuations in biological membranes. *Nature* **282**, 336–339 (1979).

[47] Bamberg, E. & Läuger, P. Channel formation kinetics of gramicidin A in lipid bilayer membranes. *The Journal of Membrane Biology* **11**, 177–194 (1973).

[48] Krasilnikov, O. & Sabirov, V., R. Ternovsky. The structure of staphylococcus aureus alpha-toxin-induced ionic channel. *General Physiology and Biophysics* **7**, 467–473 (1988).

[49] Gutsmann, T., Heimburg, T., Keyser, U., Mahendran, K. R. & Winterhalter, M. Protein reconstitution into freestanding planar lipid membranes for electrophysiological characterization. *Nature Protocols* **10**, 188–98 (2014).

[50] Wanunu, M. & Meller, A. Chemically modified solid-state nanopores. *Nano Letters* **7**, 1580–1585 (2007).

[51] Smeets, R. M. M., Keyser, U. F., Dekker, N. H. & Dekker, C. Noise in solid-state nanopores. *Proceedings of the National Academy of Sciences of the United States of America* **105**, 417–421 (2008).

[52] Branton, D. *et al.* The potential and challenges of nanopore sequencing. *Nature Biotechnology* **26**, 1146–1153 (2008).

[53] Benndorf, K. Low noise recording. In Sakmann, B. & Neher, E. (eds.) *Single Channel Recording*, book section 5, 129–145 (Plenum Press, New York, 2009), 2nd edn.

[54] Mayer, M., Kriebel, J. K., Tosteson, M. T. & Whitesides, G. M. Microfabricated teflon membranes for low-noise recordings of ion channels in planar lipid bilayers. *Biophysical Journal* **85**, 2684–2695 (2003).

[55] Rosenstein, J. K., Wanunu, M., Merchant, C. A., Drndic, M. & Shepard, K. L. Integrated nanopore sensing platform with sub-microsecond temporal resolution. *Nature Methods* **9**, 487–492 (2012).

[56] Uram, J. D., Ke, K. & Mayer, M. Noise and bandwidth of current recordings from submicrometer pores and nanopores. *ACS Nano* **2**, 857–872 (2008).

[57] Wonderlin, W. F., Finkel, A. & French, R. J. Optimizing planar lipid bilayer single-channel recordings for high resolution with rapid voltage steps. *Biophysical Journal* **58**, 289–297 (1990).

[58] Pedone, D. *et al.* Fabrication and electrical characterization of a pore–cavity–pore device. *Journal of Physics: Condensed Matter* **22**, 454115 (2010).

[59] Lin, J., Merzlyakov, M., Hristova, K. & Searson, P. C. Impedance spectroscopy of bilayer membranes on single crystal silicon. *Biointerphases* **3**, FA33–FA40 (2008).

[60] Schuster, B., Pum, D., Braha, O., Bayley, H. & Sleytr, U. B. Self-assembled α-hemolysin pores in an S-layer-supported lipid bilayer. *Biochimica et Biophysica Acta (BBA) - Biomembranes* **1370**, 280–288 (1998).

[61] Nyquist, H. Thermal agitation of electric charge in conductors. *Physical Review* **32**, 110–113 (1928).

[62] Sigworth, F. J. Electronic design of the patch clamp. In Sakmann, B. & Neher, E. (eds.) *Single Channel Recording*, book section 4, 95–127 (Plenum Press, New York, 2009), 2nd edn.

[63] Tabard-Cossa, V., Dhruti, T., Matthew, W., Nahid, N. J. & Andre, M. Noise analysis and reduction in solid-state nanopores. *Nanotechnology* **18**, 305505 (2007).

[64] Bezrukov, S. M. & Winterhalter, M. Examining noise sources at the single-molecule level: 1/f noise of an open maltoporin channel. *Physical Review Letters* **85**, 202–205 (2000).

[65] Nekolla, S., Andersen, C. & Benz, R. Noise analysis of ion current through the open and the sugar-induced closed state of the LamB channel of *Escherichia coli* outer membrane: evaluation of the sugar binding kinetics to the channel interior. *Biophysical Journal* **66**, 1388–1397 (1994).

[66] Hooge, F. N. 1/f noise is no surface effect. *Physics Letters A* **29**, 139–140 (1969).

[67] Chen, P. *et al.* Atomic layer deposition to fine-tune the surface properties and diameters of fabricated nanopores. *Nano Letters* **4**, 1333–1337 (2004).

[68] Smeets, R. M. M., Keyser, U. F., Wu, M. Y., Dekker, N. H. & Dekker, C. Nanobubbles in solid-state nanopores. *Physical Review Letters* **97**, 088101 (2006).

[69] Smeets, R. M. M., Dekker, N. H. & Dekker, C. Low-frequency noise in solid-state nanopores. *Nanotechnology* **20**, 095501 (2009).

[70] Bezrukov, S. M. & Kasianowicz, J. J. Current noise reveals protonation kinetics and number of ionizable sites in an open protein ion channel. *Physical Review Letters* **70**, 2352–2355 (1993).

[71] Krause, D. Glasses. In Martienssen, W. & Warlimont, H. (eds.) *Handbook of Condensed Matter and Materials Data*, book section 4, 523–574 (Springer, Berlin, 2005).

[72] Rosenstein, J. K., Ramakrishnan, S., Roseman, J. & Shepard, K. L. Single ion channel recordings with CMOS-anchored lipid membranes. *Nano Letters* **13**, 2682–2686 (2013).

[73] Molecular Devices Technical Support. Axopatch 200B's: cooling is causing a small 100 kHz signal. `http://mdc.custhelp.com/app/answers/detail/a_id/16564/~/axopatch-200bs%3A-cooling-is-causing-a-small-100-khz-signal`. Accessed: August 12, 2014.

[74] Williams, S. A. *et al.* A prostate-specific antigen–activated channel-forming toxin as therapy for prostatic disease. *Journal of the National Cancer Institute* **99**, 376–385 (2007).

[75] Boyden, E. S., Zhang, F., Bamberg, E., Nagel, G. & Deisseroth, K. Millisecond-timescale, genetically targeted optical control of neural activity. *Nature Neuroscience* **8**, 1263–1268 (2005).

[76] Akeson, M., Branton, D., Kasianowicz, J. J., Brandin, E. & Deamer, D. W. Microsecond time-scale discrimination among polycytidylic acid, polyadenylic acid, and polyuridylic acid as homopolymers or as segments within single RNA molecules. *Biophysical Journal* **77**, 3227–3233 (1999).

[77] Howorka, S. & Siwy, Z. Nanopore analytics: sensing of single molecules. *Chemical Society Reviews* **38**, 2360–2384 (2009).

[78] Wanunu, M. *et al.* Rapid electronic detection of probe-specific microRNAs using thin nanopore sensors. *Nature Nanotechnology* **5**, 807–814 (2010).

[79] Plesa, C., Cornelissen, L., Tuijtel, M. W. & Dekker, C. Non-equilibrium folding of individual DNA molecules recaptured up to 1000 times in a solid state nanopore. *Nanotechnology* **24**, 475101 (2013).

[80] Pedone, D., Langecker, M., Abstreiter, G. & Rant, U. A pore-cavity-pore device to trap and investigate single nanoparticles and DNA molecules in a femtoliter compartment: Confined diffusion and narrow escape. *Nano Letters* **11**, 1561–1567 (2011).

[81] Bayley, H. & Martin, C. R. Resistive-pulse sensing - from microbes to molecules. *Chemical Reviews* **100**, 2575–2594 (2000).

[82] Stoddart, D., Heron, A. J., Mikhailova, E., Maglia, G. & Bayley, H. Single-nucleotide discrimination in immobilized DNA oligonucleotides with a biological nanopore. *Proceedings of the National Academy of Sciences of the United States of America* **106**, 7702–7707 (2009).

[83] Larkin, J., Henley, R. Y., Muthukumar, M., Rosenstein, J. & Wanunu, M. High-bandwidth protein analysis using solid-state nanopores. *Biophysical Journal* **106**, 696–704 (2014).

[84] Smeets, R. M. M. *et al.* Salt dependence of ion transport and DNA translocation through solid-state nanopores. *Nano Letters* **6**, 89–95 (2006).

[85] Hille, B. *Ion Channels of Excitable Membranes* (Sinauer Associates, Sunderland, 2001), 3rd edn.

[86] DeBlois, R. W. & Bean, C. P. Counting and sizing of submicron particles by the resistive pulse technique. *Review of Scientific Instruments* **41**, 909–916 (1970).

[87] Kowalczyk, S. W., Grosberg, A. Y., Rabin, Y. & Dekker, C. Modeling the conductance and DNA blockade of solid-state nanopores. *Nanotechnology* **22**, 315101 (2011).

[88] Mirsaidov, U., Comer, J., Dimitrov, V., Aksimentiev, A. & Timp, G. Slowing the translocation of double-stranded DNA using a nanopore smaller than the double helix. *Nanotechnology* **21**, 395501 (2010).

[89] Carson, S., Wilson, J., Aksimentiev, A. & Wanunu, M. Smooth DNA transport through a narrowed pore geometry. *Biophysical Journal* **107**, 2381–2393 (2014).

[90] Faller, M., Niederweis, M. & Schulz, G. E. The structure of a mycobacterial outer-membrane channel. *Science* **303**, 1189–1192 (2004).

[91] Butt, H.-J., Graf, K. & Kappl, M. *Physics and Chemistry of Interfaces* (Wiley-VCH, Weinheim, 2003).

[92] Manrao, E. A. *et al.* Reading DNA at single-nucleotide resolution with a mutant MspA nanopore and phi29 DNA polymerase. *Nature Biotechnology* **30**, 349–353 (2012).

[93] Cherf, G. M. *et al.* Automated forward and reverse ratcheting of DNA in a nanopore at 5-$\AA$ precision. *Nature Biotechnology* **30**, 344–348 (2012).

[94] Chu, J., González-López, M., Cockroft, S. L., Amorin, M. & Ghadiri, M. R. Real-time monitoring of DNA polymerase function and stepwise single-nucleotide DNA strand translocation through a protein nanopore. *Angewandte Chemie International Edition* **49**, 10106–10109 (2010).

[95] Viovy, J.-L. Electrophoresis of DNA and other polyelectrolytes: Physical mechanisms. *Reviews of Modern Physics* **72**, 813–872 (2000).

[96] van Dorp, S., Keyser, U. F., Dekker, N. H., Dekker, C. & Lemay, S. G. Origin of the electrophoretic force on DNA in solid-state nanopores. *Nature Physics* **5**, 347–351 (2009).

[97] Schoch, R. B., Han, J. & Renaud, P. Transport phenomena in nanofluidics. *Reviews of Modern Physics* **80**, 839–883 (2008).

[98] Firnkes, M., Pedone, D., Knezevic, J., Döblinger, M. & Rant, U. Electrically facilitated translocations of proteins through silicon nitride nanopores: Conjoint and competitive action of diffusion, electrophoresis, and electroosmosis. *Nano Letters* **10**, 2162–2167 (2010).

[99] Schellman, J. A. & Stigter, D. Electrical double layer, zeta potential, and electrophoretic charge of double-stranded DNA. *Biopolymers* **16**, 1415–1434 (1977).

[100] Keyser, U. F. *et al.* Direct force measurements on DNA in a solid-state nanopore. *Nature Physics* **2**, 473–477 (2006).

[101] Galla, L. *et al.* Hydrodynamic slip on DNA observed by optical tweezers-controlled translocation experiments with solid-state and lipid-coated nanopores. *Nano Letters* **14**, 4176–4182 (2014).

[102] Luan, B. & Aksimentiev, A. Control and reversal of the electrophoretic force on DNA in a charged nanopore. *Journal of Physics: Condensed Matter* **22**, 454123 (2010).

[103] Gu, L.-Q., Cheley, S. & Bayley, H. Electroosmotic enhancement of the binding of a neutral molecule to a transmembrane pore. *Proceedings of the National Academy of Sciences of the United States of America* **100**, 15498–15503 (2003).

[104] Wong, C. T. A. & Muthukumar, M. Polymer translocation through α-hemolysin pore with tunable polymer-pore electrostatic interaction. *The Journal of Chemical Physics* **133**, 045101 (2010).

[105] Robertson, J. W. F. *et al.* Single-molecule mass spectrometry in solution using a solitary nanopore. *Proceedings of the National Academy of Sciences of the United States of America* **104**, 8207–8211 (2007).

[106] Ying, L. *et al.* Frequency and voltage dependence of the dielectrophoretic trapping of short lengths of DNA and dCTP in a nanopipette. *Biophysical Journal* **86**, 1018–1027 (2004).

[107] Nagashima, G., Levine, E. V., Hoogerheide, D. P., Burns, M. M. & Golovchenko, J. A. Superheating and homogeneous single bubble nucleation in a solid-state nanopore. *Physical Review Letters* **113**, 024506 (2014).

[108] Muthukumar, M. Theory of capture rate in polymer translocation. *The Journal of Chemical Physics* **132**, 195101 (2010).

[109] Grosberg, A. Y. & Rabin, Y. DNA capture into a nanopore: Interplay of diffusion and electrohydrodynamics. *The Journal of Chemical Physics* **133**, 165102 (2010).

[110] Muthukumar, M. *Polymer translocation* (CRC Press, 2011).

[111] He, Y. *et al.* Mechanism of how salt-gradient-induced charges affect the translocation of DNA molecules through a nanopore. *Biophysical Journal* **105**, 776–782 (2013).

[112] Rubinstein, M. & Colby, R. H. *Polymer Physics* (Oxford University Press, Oxford and New York, 2003).

[113] Chen, P. *et al.* Probing single DNA molecule transport using fabricated nanopores. *Nano Letters* **4**, 2293–2298 (2004).

[114] Kong, C. Y. & Muthukumar, M. Polymer translocation through a nanopore. II. excluded volume effect. *The Journal of Chemical Physics* **120**, 3460–3466 (2004).

[115] Kumar, R. & Muthukumar, M. Origin of translocation barriers for polyelectrolyte chains. *The Journal of Chemical Physics* **131**, 194903 (2009).

[116] Wanunu, M., Morrison, W., Rabin, Y., Grosberg, A. Y. & Meller, A. Electrostatic focusing of unlabelled DNA into nanoscale pores using a salt gradient. *Nature Nanotechnology* **5**, 160–165 (2010).

[117] Henrickson, S. E., Misakian, M., Robertson, B. & Kasianowicz, J. J. Driven DNA transport into an asymmetric nanometer-scale pore. *Physical Review Letters* **85**, 3057–3060 (2000).

[118] Ling, D. Y. & Ling, X. S. On the distribution of DNA translocation times in solid-state nanopores: an analysis using Schrödinger's first-passage-time theory. *Journal of Physics: Condensed Matter* **25**, 375102 (2013).

[119] Plesa, C., van Loo, N., Ketterer, P., Dietz, H. & Dekker, C. Velocity of DNA during translocation through a solid-state nanopore. *Nano Letters* **15**, 732–737 (2014).

[120] Renner, S., Geltinger, S. & Simmel, F. C. Nanopore translocation and force spectroscopy experiments in microemulsion droplets. *Small* **6**, 190–194 (2010).

[121] Mathé, J., Visram, H., Viasnoff, V., Rabin, Y. & Meller, A. Nanopore unzipping of individual DNA hairpin molecules. *Biophysical Journal* **87**, 3205–3212 (2004).

[122] Gershow, M. & Golovchenko, J. A. Recapturing and trapping single molecules with a solid-state nanopore. *Nature Nanotechnology* **2**, 775–779 (2007).

[123] Golowasch, J. *et al.* Membrane capacitance measurements revisited: Dependence of capacitance value on measurement method in nonisopotential neurons. *Journal of Neurophysiology* **102**, 2161–2175 (2009).

[124] Kester, W. A. *Data conversion handbook* (Newnes, 2005).

[125] Ivankin, A., Carson, S., Kinney, S. R. M. & Wanunu, M. Fast, label-free force spectroscopy of histone-DNA interactions in individual nucleosomes using nanopores. *Journal of the American Chemical Society* **135**, 15350–15352 (2013).

[126] Greenleaf, W. J., Woodside, M. T., Abbondanzieri, E. A. & Block, S. M. Passive all-optical force clamp for high-resolution laser trapping. *Physical Review Letters* **95**, 208102 (2005).

[127] Neupane, K., Yu, H., Foster, D. A. N., Wang, F. & Woodside, M. T. Single-molecule force spectroscopy of the add adenine riboswitch relates folding to regulatory mechanism. *Nucleic Acids Research* **39**, 7677–7687 (2011).

[128] Abels, J. A., Moreno-Herrero, F., van der Heijden, T., Dekker, C. & Dekker, N. H. Single-molecule measurements of the persistence length of double-stranded RNA. *Biophysical Journal* **88**, 2737–2744 (2005).

[129] Florin, E. L., Moy, V. T. & Gaub, H. E. Adhesion forces between individual ligand-receptor pairs. *Science* **264**, 415–417 (1994).

[130] Schnitzer, M. J. & Block, S. M. Kinesin hydrolyses one ATP per 8-nm step. *Nature* **388**, 386–390 (1997).

[131] Abbondanzieri, E. A., Greenleaf, W. J., Shaevitz, J. W., Landick, R. & Block, S. M. Direct observation of base-pair stepping by RNA polymerase. *Nature* **438**, 460–465 (2005).

[132] Kellermayer, M. S. Z., Smith, S. B., Granzier, H. L. & Bustamante, C. Folding-unfolding transitions in single titin molecules characterized with laser tweezers. *Science* **276**, 1112–1116 (1997).

[133] Gosse, C. & Croquette, V. Magnetic tweezers: micromanipulation and force measurement at the molecular level. *Biophysical Journal* **82**, 3314–3329 (2002).

[134] Nakane, J., Wiggin, M. & Marziali, A. A nanosensor for transmembrane capture and identification of single nucleic acid molecules. *Biophysical Journal* **87**, 615–621 (2004).

[135] Tabard-Cossa, V. *et al.* Single-molecule bonds characterized by solid-state nanopore force spectroscopy. *ACS Nano* **3**, 3009–3014 (2009).

[136] Strunz, T., Oroszlan, K., Schäfer, R. & Güntherodt, H.-J. Dynamic force spectroscopy of single DNA molecules. *Proceedings of the National Academy of Sciences of the United States of America* **96**, 11277–11282 (1999).

[137] Merkel, R., Nassoy, P., Leung, A., Ritchie, K. & Evans, E. Energy landscapes of receptor-ligand bonds explored with dynamic force spectroscopy. *Nature* **397**, 50–53 (1999).

[138] Arnaut, V., Langecker, M. & Simmel, F. C. Nanopore force spectroscopy of aptamer–ligand complexes. *Biophysical Journal* **105**, 1199–1207 (2013).

[139] Hornblower, B. *et al.* Single-molecule analysis of DNA-protein complexes using nanopores. *Nature Methods* **4**, 315–317 (2007).

[140] Tropini, C. & Marziali, A. Multi-nanopore force spectroscopy for DNA analysis. *Biophysical Journal* **92**, 1632–1637 (2007).

[141] Schink, S. *et al.* Quantitative analysis of the nanopore translocation dynamics of simple structured polynucleotides. *Biophysical Journal* **102**, 85–95 (2012).

[142] Anderson, B. N. *et al.* Probing solid-state nanopores with light for the detection of unlabeled analytes. *ACS Nano* **8**, 11836–11845 (2014).

[143] Ivankin, A. *et al.* Label-free optical detection of biomolecular translocation through nanopore arrays. *ACS Nano* **8**, 10774–10781 (2014).

[144] Evans, E. & Ritchie, K. Dynamic strength of molecular adhesion bonds. *Biophysical Journal* **72**, 1541–1555 (1997).

[145] Zhang, Y. & Dudko, O. K. A transformation for the mechanical fingerprints of complex biomolecular interactions. *Proceedings of the National Academy of Sciences of the United States of America* **110**, 16432–16437 (2013).

[146] Dudko, O. K., Hummer, G. & Szabo, A. Theory, analysis, and interpretation of single-molecule force spectroscopy experiments. *Proceedings of the National Academy of Sciences of the United States of America* **105**, 15755–15760 (2008).

[147] Ebner, A. *et al.* Probing the energy landscape of protein-binding reactions by dynamic force spectroscopy. In Hinterdorfer, P. & Oijen, A. (eds.) *Handbook of Single-Molecule Biophysics*, book section 15, 407–447 (Springer, New York, 2009).

[148] Dudko, O. K., Hummer, G. & Szabo, A. Intrinsic rates and activation free energies from single-molecule pulling experiments. *Physical Review Letters* **96**, 108101 (2006).

[149] Dudko, O. K., Filippov, A. E., Klafter, J. & Urbakh, M. Beyond the conventional description of dynamic force spectroscopy of adhesion bonds. *Proceedings of the National Academy of Sciences of the United States of America* **100**, 11378–11381 (2003).

[150] Hummer, G. & Szabo, A. Kinetics from nonequilibrium single-molecule pulling experiments. *Biophysical Journal* **85**, 5–15 (2003).

[151] Bell, G. I. Models for specific adhesion of cells to cells. *Science* **200**, 618–627 (1978).

[152] Szabo, A., Schulten, K. & Schulten, Z. First passage time approach to diffusion controlled reactions. *The Journal of Chemical Physics* **72**, 4350–4357 (1980).

[153] Dudko, O. K., Mathé, J., Szabo, A., Meller, A. & Hummer, G. Extracting kinetics from single-molecule force spectroscopy: Nanopore unzipping of DNA hairpins. *Biophysical Journal* **92**, 4188–4195 (2007).

[154] Schlierf, M. & Rief, M. Single-molecule unfolding force distributions reveal a funnel-shaped energy landscape. *Biophysical Journal* **90**, L33–L35 (2006).

[155] Neuman, K. C. & Nagy, A. Single-molecule force spectroscopy: optical tweezers, magnetic tweezers and atomic force microscopy. *Nature Methods* **5**, 491–505 (2008).

[156] Manrao, E. A., Derrington, I. M., Pavlenok, M., Niederweis, M. & Gundlach, J. H. Nucleotide discrimination with DNA immobilized in the MspA nanopore. *PLoS ONE* **6**, e25723 (2011).

[157] Wei, R., Gatterdam, V., Wieneke, R., Tampe, R. & Rant, U. Stochastic sensing of proteins with receptor-modified solid-state nanopores. *Nature Nanotechnology* **7**, 257–263 (2012).

[158] Howorka, S., Cheley, S. & Bayley, H. Sequence-specific detection of individual DNA strands using engineered nanopores. *Nature Biotechnology* **19**, 636–639 (2001).

[159] Schmidt, D., Jiang, Q.-X. & MacKinnon, R. Phospholipids and the origin of cationic gating charges in voltage sensors. *Nature* **444**, 775–779 (2006).

[160] Long, S. B., Campbell, E. B. & MacKinnon, R. Voltage sensor of Kv1.2: structural basis of electromechanical coupling. *Science* **309**, 903–908 (2005).

[161] Tang, L. *et al.* Structural basis for Ca^{2+} selectivity of a voltage-gated calcium channel. *Nature* **505**, 56–61 (2013).

[162] Booth, M. J., Schild, V. R., Downs, F. G. & Bayley, H. Functional aqueous droplet networks. *Molecular bioSystems* **13**, 1658–1691 (2017).

[163] Buddingh, B. C. & van Hest, J. C. M. Artificial cells: Synthetic compartments with life-like functionality and adaptivity. *Accounts of Chemical Research* **50**, 769–777 (2017).

[164] Sakai, N., Mareda, J. & Matile, S. Ion channels and pores, made from scratch. *Molecular bioSystems* **3**, 658–666 (2007).

[165] Fyles, T. M., Loock, D. & Zhou, X. A voltage-gated ion channel based on a bis-macrocyclic bolaamphiphile. *Journal of the American Chemical Society* **120**, 2997–3003 (1998).

[166] Tanaka, Y., Kobuke, Y. & Sokabe, M. A non-peptidic ion channel with K^+ selectivity. *Angewandte Chemie International Edition* **34**, 693–694 (1995).

[167] Jeon, Y. J. *et al.* Artificial ion channel formed by cucurbit[n]uril derivatives with a carbonyl group fringed portal reminiscent of the selectivity filter of K^+ channels. *Journal of the American Chemical Society* **126**, 15944–15945 (2004).

[168] Gräslund, S. *et al.* Protein production and purification. *Nature Methods* **5**, 135–146 (2008).

[169] Patel, S. C. & Hecht, M. H. Directed evolution of the peroxidase activity of a *de novo*-designed protein. *Protein Engineering Design and Selection* **25**, 445–452 (2012).

[170] Huang, P.-S., Boyken, S. E. & Baker, D. The coming of age of *de novo* protein design. *Nature* **537**, 320–327 (2016).

[171] Pace, C. N., Scholtz, J. M. & Grimsley, G. R. Forces stabilizing proteins. *FEBS letters* **588**, 2177–2184 (2014).

[172] Bayley, H. & Jayasinghe, L. Functional engineered channels and pores (review). *Molecular Membrane Biology* **21**, 209–220 (2004).

[173] Soskine, M. *et al.* An engineered ClyA nanopore detects folded target proteins by selective external association and pore entry. *Nano Letters* **12**, 4895–4900 (2012).

[174] Wendell, D. *et al.* Translocation of double-stranded DNA through membrane-adapted phi29 motor protein nanopores. *Nature Nanotechnology* **4**, 765–772 (2009).

[175] Hong, F., Zhang, F., Liu, Y. & Yan, H. DNA origami: Scaffolds for creating higher order structures. *Chemical Reviews* **117**, 12584–12640 (2017).

[176] Langecker, M. *et al.* Synthetic lipid membrane channels formed by designed DNA nanostructures. *Science* **338**, 932–936 (2012).

[177] Avery, O. T., Macleod, C. M. & McCarty, M. Studies on the chemical nature of the substance inducing transformation of pneumococcal types: Induction of transformation by a desoxyribonucleic acid fraction isolated from pneumococcus type III. *The Journal of experimental medicine* **79**, 137–158 (1944).

[178] Dahm, R. Friedrich Miescher and the discovery of DNA. *Developmental Biology* **278**, 274–288 (2005).

[179] Seeman, N. C. An overview of structural DNA nanotechnology. *Molecular Biotechnology* **37**, 246–257 (2007).

[180] Zadeh, J. N. *et al.* NUPACK: analysis and design of nucleic acid systems. *Journal of Computational Chemistry* **32**, 170–173 (2010).

[181] Zuker, M. Mfold web server for nucleic acid folding and hybridization prediction. *Nucleic Acids Research* **31**, 3406–3415 (2003).

[182] Fox, K. R. & Brown, T. (eds.) *DNA Conjugates and Sensors* (RSC Biomolecular Sciences, 2012).

[183] Sinden, R. R. *DNA: Structure and function* (Academic Press, 1994).

[184] Watson, J. D. & Crick, F. H. Molecular structure of nucleic acids; a structure for deoxyribose nucleic acid. *Nature* **171**, 737–738 (1953).

[185] Yakovchuk, P., Protozanova, E. & Frank-Kamenetskii, M. D. Base-stacking and base-pairing contributions into thermal stability of the DNA double helix. *Nucleic Acids Research* **34**, 564–574 (2006).

[186] Dervan, P. B. Design of sequence-specific DNA-binding molecules. *Science* **232**, 464–471 (1986).

[187] Seeman, N. C. Nucleic acid junctions and lattices. *Journal of theoretical biology* **99**, 237–247 (1982).

[188] Lilley, D. M. Structures of helical junctions in nucleic acids. *Quarterly Reviews of Biophysics* **33**, 109–159 (2000).

[189] Chen, J. H. & Seeman, N. C. Synthesis from DNA of a molecule with the connectivity of a cube. *Nature* **350**, 631–633 (1991).

[190] Fu, T. J. & Seeman, N. C. DNA double-crossover molecules. *Biochemistry* **32**, 3211–3220 (1993).

[191] Rothemund, P. W. K. Folding DNA to create nanoscale shapes and patterns. *Nature* **440**, 297–302 (2006).

[192] Ke, Y., Ong, L. L., Shih, W. M. & Yin, P. Three-dimensional structures self-assembled from DNA bricks. *Science* **338**, 1177–1183 (2012).

[193] Douglas, S. M. *et al.* Self-assembly of DNA into nanoscale three-dimensional shapes. *Nature* **459**, 414–418 (2009).

[194] Dietz, H., Douglas, S. M. & Shih, W. M. Folding DNA into twisted and curved nanoscale shapes. *Science* **325**, 725–730 (2009).

[195] Douglas, S. M. *et al.* Rapid prototyping of 3D DNA-origami shapes with caDNAno. *Nucleic Acids Research* **37**, 5001–5006 (2009).

[196] Kim, D.-N., Kilchherr, F., Dietz, H. & Bathe, M. Quantitative prediction of 3D solution shape and flexibility of nucleic acid nanostructures. *Nucleic Acids Research* **40**, 2862–2868 (2011).

[197] Castro, C. E. *et al.* A primer to scaffolded DNA origami. *Nature Methods* **8**, 221–229 (2011).

[198] Praetorius, F. *et al.* Biotechnological mass production of DNA origami. *Nature* **552**, 84–87 (2017).

[199] Wang, R., Kuzuya, A., Liu, W. & Seeman, N. C. Blunt-ended DNA stacking interactions in a 3-helix motif. *Chemical Communications* **46**, 4905–4907 (2010).

[200] Sobczak, J.-P. J., Martin, T. G., Gerling, T. & Dietz, H. Rapid folding of DNA into nanoscale shapes at constant temperature. *Science* **338**, 1458–1461 (2012).

[201] Duckett, D. R., Murchie, A. I. & Lilley, D. M. The role of metal ions in the conformation of the four-way DNA junction. *The EMBO journal* **9**, 583–590 (1990).

[202] Martin, T. G., Dietz, H. & Martin, T. G. Magnesium-free self-assembly of multi-layer DNA objects. *Nature Communications* **3**, 1103 (2012).

[203] Langecker, M., Arnaut, V., List, J. & Simmel, F. C. DNA nanostructures interacting with lipid bilayer membranes. *Accounts of Chemical Research* **47**, 1807–1815 (2014).

[204] Felgner, P. L. *et al.* Lipofection: a highly efficient, lipid-mediated DNA-transfection procedure. *Proceedings of the National Academy of Sciences of the United States of America* **84**, 7413–7 (1987).

[205] Pozharski, E. & MacDonald, R. C. Thermodynamics of cationic lipid-DNA complex formation as studied by isothermal titration calorimetry. *Biophysical Journal* **83**, 556–565 (2002).

[206] Gromelski, S. & Brezesinski, G. DNA condensation and interaction with zwitterionic phospholipids mediated by divalent cations. *Langmuir* **22**, 6293–6301 (2006).

[207] McManus, J. J., Rädler, J. O. & Dawson, K. A. Does calcium turn a zwitterionic lipid cationic? *Journal of Physical Chemistry B* **107**, 9869–9875 (2003).

[208] Ainalem, M. L. *et al.* DNA binding to zwitterionic model membranes. *Langmuir* **26**, 4965–4976 (2010).

[209] Malghani, M. S. & Yang, J. Stable binding of DNA to zwitterionic lipid bilayers in aqueous solutions. *Journal of Physical Chemistry B* **102**, 8930–8933 (1998).

[210] Khalid, S., Bond, P. J., Holyoake, J., Hawtin, R. W. & Sansom, M. S. P. DNA and lipid bilayers: self-assembly and insertion. *Journal of the Royal Society Interface* **5**, S241–S250 (2008).

[211] Kato, A. *et al.* Phase separation on a phospholipid membrane inducing a characteristic localization of DNA accompanied by its structural transition. *Journal of Physical Chemistry Letters* **1**, 3391–3395 (2010).

[212] Chan, Y. H. M., van Lengerich, B. & Boxer, S. G. Effects of linker sequences on vesicle fusion mediated by lipid-anchored DNA oligonucleotides. *Proceedings of the National Academy of Sciences of the United States of America* **106**, 979–984 (2009).

[213] Stengel, G., Simonsson, L., Campbell, R. A. & Höök, F. Determinants for membrane fusion induced by cholesterol-modified DNA zippers. *Journal of Physical Chemistry B* **112**, 8264–8274 (2008).

[214] Beales, P. A., Nam, J. & Vanderlick, T. K. Specific adhesion between DNA-functionalized "Janus" vesicles: size-limited clusters. *Soft Matter* **7**, 1747–1755 (2011).

[215] Rode, A. B., Endoh, T., Tateishi-Karimata, H., Takahashi, S. & Sugimoto, N. Real-time monitoring of DNA hybridization kinetics on living cell surfaces. *Chemical Communications* **49**, 8444–8446 (2013).

[216] Selden, N. S. *et al.* Chemically programmed cell adhesion with membrane-anchored oligonucleotides. *Journal of the American Chemical Society* **134**, 765–768 (2012).

[217] Dave, N. & Liu, J. W. Programmable assembly of DNA-functionalized liposomes by DNA. *ACS Nano* **5**, 1304–1312 (2011).

[218] Pfeiffer, I. & Höök, F. Bivalent cholesterol-based coupling of oligonucletides to lipid membrane assemblies. *Journal of the American Chemical Society* **126**, 10224–10225 (2004).

[219] Czogalla, A. *et al.* Switchable domain partitioning and diffusion of DNA origami rods on membranes. *Faraday Discussions* **161**, 31–43 (2013).

[220] Bunge, A. *et al.* Lipid membranes carrying lipophilic cholesterol-based oligonucleotides – characterization and application on layer-by-layer coated particles. *Journal of Physical Chemistry B* **113**, 16425–16434 (2009).

[221] Beales, P. A. & Vanderlick, T. K. Partitioning of membrane-anchored DNA between coexisting lipid phases. *Journal of Physical Chemistry B* **113**, 13678–13686 (2009).

[222] Kurz, A. *et al.* Lipid-anchored oligonucleotides for stable double-helix formation in distinct membrane domains. *Angewandte Chemie-International Edition* **45**, 4440–4444 (2006).

[223] Rodriguez-Pulido, A. *et al.* Light-triggered sequence-specific cargo release from DNA block copolymer-lipid vesicles. *Angewandte Chemie-International Edition* **52**, 1008–1012 (2013).

[224] Börjesson, K., Lundberg, E. P., Woller, J. G., Nordén, B. & Albinsson, B. Soft-surface DNA nanotechnology: DNA constructs anchored and aligned to lipid membrane. *Angewandte Chemie-International Edition* **50**, 8312–8315 (2011).

[225] Börjesson, K. *et al.* Functionalized nanostructures: Redox-active porphyrin anchors for supramolecular DNA assemblies. *ACS Nano* **4**, 5037–5046 (2010).

[226] Gut, I. G. & Beck, S. A procedure for selective DNA alkylation and detection by mass-spectrometry. *Nucleic Acids Research* **23**, 1367–1373 (1995).

[227] Tang, Z. W. *et al.* Selection of aptamers for molecular recognition and characterization of cancer cells. *Analytical Chemistry* **79**, 4900–4907 (2007).

[228] Huang, Y. F. *et al.* Molecular assembly of an aptamer-drug conjugate for targeted drug delivery to tumor cells. *Chembiochem* **10**, 862–868 (2009).

[229] Douglas, S. M., Bachelet, I. & Church, G. M. A logic-gated nanorobot for targeted transport of molecular payloads. *Science* **335**, 831–834 (2012).

[230] Koyfman, A. Y., Braun, G. B. & Reich, N. O. Cell-targeted self-assembled DNA nanostructures. *Journal of the American Chemical Society* **131**, 14237–14239 (2009).

[231] Hsiao, S. C. *et al.* Direct cell surface modification with DNA for the capture of primary cells and the investigation of myotube formation on defined patterns. *Langmuir* **25**, 6985–6991 (2009).

[232] Langecker, M. *et al.* Synthetic lipid membrane channels formed by designed DNA nanostructures – Supplement. *Science* **338**, 932–936 (2012).

[233] Göpfrich, K. *et al.* Large-conductance transmembrane porin made from DNA origami. *ACS nano* **10**, 8207–8214 (2016).

[234] McIntosh, T. J. & Simon, S. A. Roles of bilayer material properties in function and distribution of membrane proteins. *Annual Review of Biophysics and Biomolecular Structure* **35**, 177–198 (2006).

[235] Marrink, S. J., de Vries, A. H. & Tieleman, D. P. Lipids on the move: simulations of membrane pores, domains, stalks and curves. *Biochimica et Biophysica Acta* **1788**, 149–168 (2008).

[236] Papahadjopoulos, D., Jacobson, K., Nir, S. & Isac, T. Phase transitions in phospholipid vesicles. Fluorescence polarization and permeability measurements concerning the effect of temperature and cholesterol. *Biochimica et Biophysica Acta* **311**, 330–348 (1973).

[237] Blicher, A., Wodzinska, K., Fidorra, M., Winterhalter, M. & Heimburg, T. The temperature dependence of lipid membrane permeability, its quantized nature, and the influence of anesthetics. *Biophysical Journal* **96**, 4581–4591 (2009).

[238] Jain, M. K. & Zakim, D. The spontaneous incorporation of proteins into preformed bilayers. *Biochimica et Biophysica Acta* **906**, 33–68 (1987).

[239] Danelon, C., Nestorovich, E. M., Winterhalter, M., Ceccarelli, M. & Bezrukov, S. M. Interaction of zwitterionic penicillins with the OmpF channel facilitates their translocation. *Biophysical Journal* **90**, 1617–1627 (2005).

[240] Wei, R., Martin, T. G., Rant, U. & Dietz, H. DNA origami gatekeepers for solid-state nanopores. *Angewandte Chemie International Edition* **51**, 4864–4867 (2012).

[241] Yoo, J. & Aksimentiev, A. Molecular dynamics of membrane-spanning DNA channels: Conductance mechanism, electro-osmotic transport, and mechanical gating. *Journal of Physical Chemistry Letters* **6**, 4680–4687 (2015).

[242] Arnaut, V. *Characterization and Application of Membrane Spanning Synthetic and Biological Nanopores*. Phd thesis, Technische Universität München (2017).

[243] Burge, S., Parkinson, G. N., Hazel, P., Todd, A. K. & Neidle, S. Quadruplex DNA: sequence, topology and structure. *Nucleic Acids Research* **34**, 5402–5415 (2006).

[244] Pratt, K. W., Koch, W., Wu, Y. & Berezansky, P. Molality-based primary standards of electrolytic conductivity. *Pure Applied Chemistry* **73**, 1783–1793 (2001).

[245] Göpfrich, K. *et al.* Ion channels made from a single membrane-spanning DNA duplex. *Nano Letters* **16**, 4665–4669 (2016).

[246] Göpfrich, K. *et al.* DNA-tile structures induce ionic currents through lipid membranes. *Nano Letters* **15**, 3134–3138 (2015).

[247] Burns, J. R., Stulz, E. & Howorka, S. Self-assembled DNA nanopores that span lipid bilayers. *Nano Letters* **13**, 2351–2356 (2013).

[248] Burns, J. R. *et al.* Lipid-bilayer-spanning DNA nanopores with a bifunctional porphyrin anchor. *Angewandte Chemie International Edition* **52**, 12069–12072 (2013).

[249] Krishnan, S. *et al.* Molecular transport through large-diameter DNA nanopores. *Nature Communications* **7**, 12787 (2016).

[250] Bell, N. A. W. *et al.* DNA origami nanopores. *Nano Letters* **12**, 512–517 (2012).

[251] Li, J. *et al.* Ion-beam sculpting at nanometre length scales. *Nature* **412**, 166–169 (2001).

[252] Sexton, L. T. *et al.* Resistive-pulse studies of proteins and protein/antibody complexes using a conical nanotube sensor. *Journal of the American Chemical Society* **129**, 13144–13152 (2007).

[253] Fologea, D., Ledden, B., McNabb, D. S. & Li, J. Electrical characterization of protein molecules by a solid-state nanopore. *Applied Physics Letters* **91**, 539011–539013 (2007).

[254] Han, A. *et al.* Label-free detection of single protein molecules and protein-protein interactions using synthetic nanopores. *Analytical Chemistry* **80**, 4651–4658 (2008).

[255] Han, A. *et al.* Sensing protein molecules using nanofabricated pores. *Applied Physics Letters* **88**, 093901 (2006).

[256] Oukhaled, A. *et al.* Dynamics of completely unfolded and native proteins through solid-state nanopores as a function of electric driving force. *ACS Nano* **5**, 3628–3638 (2011).

[257] Plesa, C. *et al.* Fast translocation of proteins through solid state nanopores. *Nano Letters* **13**, 658–663 (2013).

[258] Siwy, Z. *et al.* Protein biosensors based on biofunctionalized conical gold nanotubes. *Journal of the American Chemical Society* **127**, 5000–5001 (2005).

[259] Talaga, D. S. & Li, J. Single-molecule protein unfolding in solid state nanopores. *Journal of the American Chemical Society* **131**, 9287–9297 (2009).

[260] Dorvel, B. *et al.* Analyzing the forces binding a restriction endonuclease to DNA using a synthetic nanopore. *Nucleic Acids Research* **37**, 4170–4179 (2009).

[261] Kowalczyk, S. W., Hall, A. R. & Dekker, C. Detection of local protein structures along DNA using solid-state nanopores. *Nano Letters* **10**, 324–328 (2009).

[262] Smeets, R. M. M., Kowalczyk, S. W., Hall, A. R., Dekker, N. H. & Dekker, C. Translocation of RecA-coated double-stranded DNA through solid-state nanopores. *Nano Letters* **9**, 3089–3095 (2009).

[263] Spiering, A., Getfert, S., Sischka, A., Reimann, P. & Anselmetti, D. Nanopore translocation dynamics of a single DNA-bound protein. *Nano Letters* **11**, 2978–2982 (2011).

[264] Zhao, Q. *et al.* Detecting SNPs using a synthetic nanopore. *Nano Letters* **7**, 1680–1685 (2007).

[265] Ivanov, A. P. *et al.* DNA tunneling detector embedded in a nanopore. *Nano Letters* **11**, 279–285 (2010).

[266] Xie, P., Xiong, Q., Fang, Y., Qing, Q. & Lieber, C. M. Local electrical potential detection of DNA by nanowire-nanopore sensors. *Nature Nanotechnology* **7**, 119–125 (2012).

[267] Tsutsui, M., Taniguchi, M., Yokota, K. & Kawai, T. Identifying single nucleotides by tunnelling current. *Nature Nanotechnology* **5**, 286–290 (2010).

[268] Yusko, E. C. *et al.* Controlling protein translocation through nanopores with bio-inspired fluid walls. *Nature Nanotechnology* **6**, 253–260 (2011).

[269] Hall, A. R. *et al.* Hybrid pore formation by directed insertion of α-haemolysin into solid-state nanopores. *Nature Nanotechnology* **5**, 874–877 (2010).

[270] Chang, H. *et al.* Fabrication and characterization of solid-state nanopores using a field emission scanning electron microscope. *Applied Physics Letters* **88**, 103109 – 103109–3 (2006).

[271] Park, S. R., Peng, H. B. & Ling, X. S. Fabrication of nanopores in silicon chips using feedback chemical etching. *Small* **3**, 116–119 (2007).

[272] Stein, D. M., McMullan, C. J., Li, J. L. & Golovchenko, J. A. Feedback-controlled ion beam sculpting apparatus. *Review of Scientific Instruments* **75**, 900–905 (2004).

[273] Storm, A. J., Chen, J. H., Ling, X. S., Zandbergen, H. W. & Dekker, C. Fabrication of solid-state nanopores with single-nanometre precision. *Nature Materials* **2**, 537–540 (2003).

[274] Vlassiouk, I., Apel, P. Y., Dmitriev, S. N., Healy, K. & Siwy, Z. S. Versatile ultrathin nanoporous silicon nitride membranes. *Proceedings of the National Academy of Sciences of the United States of America* **106**, 21039–21044 (2009).

[275] Wei, R., Pedone, D., Zürner, A., Döblinger, M. & Rant, U. Fabrication of metallized nanopores in silicon nitride membranes for single-molecule sensing. *Small* **6**, 1406–1414 (2010).

[276] Apel, P. Y., Korchev, Y. E., Siwy, Z., Spohr, R. & Yoshida, M. Diode-like single-ion track membrane prepared by electro-stopping. *Nuclear Instruments and Methods in Physics Research Section B: Beam Interactions with Materials and Atoms* **184**, 337–346 (2001).

[277] Shim, J. H. *et al.* Glass nanopore-based ion-selective electrodes. *Analytical Chemistry* **79**, 3568–3574 (2007).

[278] Steinbock, L. J., Stober, G. & Keyser, U. F. Sensing DNA-coatings of microparticles using micropipettes. *Biosensors & Bioelectronics* **24**, 2423–2427 (2009).

[279] Merchant, C. A. *et al.* DNA translocation through graphene nanopores. *Nano Letters* **10**, 2915–2921 (2010).

[280] Schneider, G. F. *et al.* DNA translocation through graphene nanopores. *Nano Letters* **10**, 3163–3167 (2010).

[281] Garaj, S. *et al.* Graphene as a subnanometre trans-electrode membrane. *Nature* **467**, 190–193 (2010).

[282] Larkin, J. *et al.* Slow DNA transport through nanopores in hafnium oxide membranes. *ACS Nano* **7**, 10121–10128 (2013).

[283] Venkatesan, B. M. *et al.* Highly sensitive, mechanically stable nanopore sensors for DNA analysis. *Advanced Materials* **21**, 2771–2776 (2009).

[284] Kim, M. J., McNally, B., Murata, K. & Meller, A. Characteristics of solid-state nanometre pores fabricated using a transmission electron microscope. *Nanotechnology* **18**, 205302 (2007).

[285] Seidel, H., Csepregi, L., Heuberger, A. & Baumgärtel, H. Anisotropic etching of crystalline silicon in alkaline solutions: I. Orientation dependence and behavior of passivation layers. *Journal of The Electrochemical Society* **137**, 3612–3626 (1990).

[286] Luger, K., Mader, A. W., Richmond, R. K., Sargent, D. F. & Richmond, T. J. Crystal structure of the nucleosome core particle at 2.8 $\mathring{A}$ resolution. *Nature* **389**, 251–260 (1997).

[287] Rohs, R. *et al.* The role of DNA shape in protein-DNA recognition. *Nature* **461**, 1248–1253 (2009).

[288] Olson, W. K., Gorin, A. A., Lu, X.-J., Hock, L. M. & Zhurkin, V. B. DNA sequence-dependent deformability deduced from protein–DNA crystal complexes. *Proceedings of the National Academy of Sciences of the United States of America* **95**, 11163–11168 (1998).

[289] Widlund, H. R. *et al.* Identification and characterization of genomic nucleosome-positioning sequences. *Journal of Molecular Biology* **267**, 807–817 (1997).

[290] Lowary, P. T. & Widom, J. Nucleosome packaging and nucleosome positioning of genomic DNA. *Proceedings of the National Academy of Sciences of the United States of America* **94**, 1183–1188 (1997).

[291] Lowary, P. T. & Widom, J. New DNA sequence rules for high affinity binding to histone octamer and sequence-directed nucleosome positioning. *Journal of Molecular Biology* **276**, 19–42 (1998).

[292] Tuerk, C. & Gold, L. Systematic evolution of ligands by exponential enrichment: RNA ligands to bacteriophage T4 DNA polymerase. *Science* **249**, 505–510 (1990).

[293] Ellington, A. D. & Szostak, J. W. *In vitro* selection of RNA molecules that bind specific ligands. *Nature* **346**, 818–822 (1990).

[294] Workman, J. L. & Kingston, R. E. Alteration of nucleosome structure as a mechanism of transcriptional regulation. *Annual Review of Biochemistry* **67**, 545–579 (1998).

[295] Jin, J. *et al.* Synergistic action of RNA polymerases in overcoming the nucleosomal barrier. *Nature Structural & Molecular Biology* **17**, 745–752 (2010).

[296] Studitsky, V. M., Kassavetis, G. A., Geiduschek, E. P. & Felsenfeld, G. Mechanism of transcription through the nucleosome by eukaryotic RNA polymerase. *Science* **278**, 1960–1963 (1997).

[297] Möbius, W., Osberg, B., Tsankov, A. M., Rando, O. J. & Gerland, U. Toward a unified physical model of nucleosome patterns flanking transcription start sites. *Proceedings of the National Academy of Sciences of the United States of America* **110**, 5719–5724 (2013).

[298] Möbius, W. & Gerland, U. Quantitative test of the barrier nucleosome model for statistical positioning of nucleosomes up- and downstream of transcription start sites. *PLoS Computational Biology* **6**, e1000891 (2010).

[299] Mavrich, T. N. *et al.* A barrier nucleosome model for statistical positioning of nucleosomes throughout the yeast genome. *Genome Research* **18**, 1073–1083 (2008).

[300] Zhang, Y. *et al.* Intrinsic histone-DNA interactions are not the major determinant of nucleosome positions *in vivo*. *Nature Structural & Molecular Biology* **16**, 847–852 (2009).

[301] Segal, E. *et al.* A genomic code for nucleosome positioning. *Nature* **442**, 772–778 (2006).

[302] Kaplan, N. *et al.* The DNA-encoded nucleosome organization of a eukaryotic genome. *Nature* **458**, 362–366 (2009).

[303] Li, G., Levitus, M., Bustamante, C. & Widom, J. Rapid spontaneous accessibility of nucleosomal DNA. *Nature Structural & Molecular Biology* **12**, 46–53 (2005).

[304] Narlikar, G. J., Sundaramoorthy, R. & Owen-Hughes, T. Mechanisms and functions of ATP-dependent chromatin-remodeling enzymes. *Cell* **154**, 490–503 (2013).

[305] Bowman, G. D. Mechanisms of ATP-dependent nucleosome sliding. *Current opinion in Structural Biology* **20**, 73–81 (2010).

[306] Grewal, S. I. S. & Moazed, D. Heterochromatin and epigenetic control of gene expression. *Science* **301**, 798–802 (2003).

[307] Kondo, Y., Shen, L. & Issa, J.-P. J. Critical role of histone methylation in tumor suppressor gene silencing in colorectal cancer. *Molecular and Cellular Biology* **23**, 206–215 (2003).

[308] Wolffe, A. P. & Matzke, M. A. Epigenetics: Regulation through repression. *Science* **286**, 481–486 (1999).

[309] Collings, C., Waddell, P. & Anderson, J. Effects of DNA methylation on nucleosome stability. *Nucleic Acids Research* **41**, 2918–2931 (2013).

[310] Gansen, A. *et al.* Nucleosome disassembly intermediates characterized by single-molecule FRET. *Proceedings of the National Academy of Sciences of the United States of America* **106**, 15308–15313 (2009).

[311] Brower-Toland, B. D. *et al.* Mechanical disruption of individual nucleosomes reveals a reversible multistage release of DNA. *Proceedings of the National Academy of Sciences of the United States of America* **99**, 1960–1965 (2002).

[312] Gemmen, G. J. *et al.* Forced unraveling of nucleosomes assembled on heterogeneous DNA using core, histones, NAP-1, and ACF. *Journal of Molecular Biology* **351**, 89–99 (2005).

[313] Hall, M. A. *et al.* High-resolution dynamic mapping of histone-DNA interactions in a nucleosome. *Nature Structural & Molecular Biology* **16**, 124–129 (2009).

[314] Leuba, S. H., Karymov, M. A., Liu, Y., Lindsay, S. M. & Zlatanova, J. Mechanically stretching single chromatin fibers. *Gene Therapy and Molecular Biology* **4**, 209–301 (1999).

[315] Wang, H. *et al.* Using atomic force microscopy to study nucleosome remodeling on individual nucleosomal arrays *in situ*. *Biophysical Journal* **87**, 1964–1971 (2004).

[316] Choy, J. S. *et al.* DNA methylation increases nucleosome compaction and rigidity. *Journal of the American Chemical Society* **132**, 1782–1783 (2010).

[317] Lee, J. Y. & Lee, T.-H. Effects of DNA methylation on the structure of nucleosomes. *Journal of the American Chemical Society* **134**, 173–175 (2011).

[318] Jimenez-Useche, I. *et al.* DNA methylation regulated nucleosome dynamics. *Scientific Reports* **3**, 2121 (2013).

[319] Jimenez-Useche, I. & Yuan, C. The effect of DNA CpG methylation on the dynamic conformation of a nucleosome. *Biophysical Journal* **103**, 2502–2512 (2012).

[320] Mihardja, S., Spakowitz, A. J., Zhang, Y. & Bustamante, C. Effect of force on mononucleosomal dynamics. *Proceedings of the National Academy of Sciences of the United States of America* **103**, 15871–15876 (2006).

[321] Dobrovolskaia, I. V. & Arya, G. Dynamics of forced nucleosome unraveling and role of nonuniform histone-DNA interactions. *Biophysical Journal* **103**, 989–998 (2012).

[322] Shundrovsky, A., Smith, C. L., Lis, J. T., Peterson, C. L. & Wang, M. D. Probing SWI/SNF remodeling of the nucleosome by unzipping single DNA molecules. *Nature Structural & Molecular Biology* **13**, 549–554 (2006).

[323] Renner, S., Bessonov, A., Gerland, U. & Simmel, F. C. Sequence-dependent unfolding kinetics of DNA hairpins studied by nanopore force spectroscopy. *Journal of Physics: Condensed Matter* **22**, 454119 (2010).

[324] Franceschini, L., Soskine, M., Biesemans, A. & Maglia, G. A nanopore machine promotes the vectorial transport of DNA across membranes. *Nature Communications* **4**, 2415 (2013).

[325] Carlsen, A. T., Zahid, O. K., Ruzicka, J. A., Taylor, E. W. & Hall, A. R. Selective detection and quantification of modified DNA with solid-state nanopores. *Nano Letters* **14**, 5488–5492 (2014).

[326] Raillon, C., Granjon, P., Graf, M. & Radenovic, A. Detection of RNAP-DNA complexes using solid state nanopores. In *IEEE Engineering in Medicine and Biology Society, Annual International Conference*, 4106–4109 (2013).

[327] Langecker, M. *et al.* Nanopores suggest a negligible influence of CpG methylation on nucleosome packaging and stability. *Nano Letters* **15**, 783–790 (2015).

[328] Dick, D. A. The distribution of sodium, potassium and chloride in the nucleus and cytoplasm of bufo bufo oocytes measured by electron microprobe analysis. *The Journal of Physiology* **284**, 37–53 (1978).

[329] Thåström, A., Bingham, L. M. & Widom, J. Nucleosomal locations of dominant DNA sequence motifs for histone–dna interactions and nucleosome positioning. *Journal of Molecular Biology* **338**, 695–709 (2004).

[330] Cui, F. & Zhurkin, V. B. Structure-based analysis of DNA sequence patterns guiding nucleosome positioning *in vitro*. *Journal of Biomolecular Structure and Dynamics* **27**, 821–841 (2010).

[331] Ioshikhes, I., Bolshoy, A., Derenshteyn, K., Borodovsky, M. & Trifonov, E. N. Nucleosome DNA sequence pattern revealed by multiple alignment of experimentally mapped sequences. *Journal of Molecular Biology* **262**, 129–139 (1996).

[332] Sivolob, A. V. & Khrapunov, S. N. Translational positioning of nucleosomes on DNA: The role of sequence-dependent isotropic DNA bending stiffness. *Journal of Molecular Biology* **247**, 918–931 (1995).

[333] Pérez, A. *et al.* Impact of methylation on the physical properties of DNA. *Biophysical Journal* **102**, 2140–2148 (2012).

[334] Langecker, M., Pedone, D., Simmel, F. C. & Rant, U. Electrophoretic time-of-flight measurements of single DNA molecules with two stacked nanopores. *Nano Letters* **11**, 5002–5007 (2011).

[335] Li, J. L., Gershow, M., Stein, D., Brandin, E. & Golovchenko, J. A. DNA molecules and configurations in a solid-state nanopore microscope. *Nature Materials* **2**, 611–615 (2003).

[336] Trepagnier, E. H., Radenovic, A., Sivak, D., Geissler, P. & Liphardt, J. Controlling DNA capture and propagation through artificial nanopores. *Nano Letters* **7**, 2824–2830 (2007).

[337] Madampage, C. A., Andrievskaia, O. & Lee, J. S. Nanopore detection of antibody prion interactions. *Analytical Biochemistry* **396**, 36–41 (2010).

[338] Foley, J. P. & Dorsey, J. G. A review of the exponentially modified gaussian (EMG) function - evaluation and subsequent calculation of universal data. *Journal of Chromatographic Science* **22**, 40–46 (1984).

[339] Hoagland, D., Arvanitidou, E. & Welch, C. Capillary electrophoresis measurements of the free solution mobility for several model polyelectrolyte systems. *Macromolecules* **32**, 6180–6190 (1999).

[340] Ohshima, H. A simple expression for henry's function for the retardation effect in electrophoresis of spherical colloidal particles. *Journal of Colloid and Interface Science* **168**, 269–271 (1994).

[341] Lubensky, D. K. & Nelson, D. R. Driven polymer translocation through a narrow pore. *Biophysical Journal* **77**, 1824–1838 (1999).

[342] Greenwood, P. E. & Nikulin, M. S. *A guide to chi-squared testing* (Wiley-Interscience, New York, 1996).

[343] Maglia, G., Restrepo, M. R. & Mikhailova, E. Enhanced translocation of single DNA molecules through α-hemolysin nanopores by manipulation of internal charge. *Proceedings of the National Academy of Sciences of the United States of America* **105**, 19720–19725 (2008).

[344] Akimov, S. A. *et al.* Pore formation in lipid membrane II: Energy landscape under external stress. *Scientific Reports* **7**, 12509 (2017).

[345] Burns, J. R., Seifert, A., Fertig, N. & Howorka, S. A biomimetic DNA-based channel for the ligand-controlled transport of charged molecular cargo across a biological membrane. *Nature Nanotechnology* **11**, 152–156 (2016).

[346] Gerling, T., Wagenbauer, K. F., Neuner, A. M. & Dietz, H. Dynamic DNA devices and assemblies formed by shape-complementary, non–basepairing 3D components. *Science* **347**, 1446–1452 (2015).

[347] List, J., Falgenhauer, E., Kopperger, E., Pardatscher, G. & Simmel, F. C. Long-range movement of large mechanically interlocked DNA nanostructures. *Nature Communications* **7**, 12414 (2016).

[348] Burns, J. R., Al-Juffali, N., Janes, S. M. & Howorka, S. Membrane-spanning DNA nanopores with cytotoxic effect. *Angewandte Chemie International Edition* **53**, 12466–12470 (2014).

[349] Gibney, E. R. & Nolan, C. M. Epigenetics and gene expression. *Heredity* **105**, 4–13 (2010).

[350] Niedzwiecki, D. J., Grazul, J. & Movileanu, L. Single-molecule observation of protein adsorption onto an inorganic surface. *Journal of the American Chemical Society* **132**, 10816–10822 (2010).

[351] Terentyeva, T. G. *et al.* Dynamic disorder in single-enzyme experiments: Facts and artifacts. *ACS Nano* **6**, 346–354 (2012).

[352] Fischer, S., Naji, A. & Netz, R. R. Salt-induced counterion-mobility anomaly in polyelectrolyte electrophoresis. *Physical Review Letters* **101**, 176103 (2008).

[353] Petrov, E. P., Ohrt, T., Winkler, R. G. & Schwille, P. Diffusion and segmental dynamics of double-stranded DNA. *Physical Review Letters* **97**, 258101 (2006).

[354] Sigworth, F. J. & Sine, S. M. Data transformations for improved display and fitting of single-channel dwell time histograms. *Biophysical Journal* **52**, 1047–1054 (1987).

[355] Pedone, D., Firnkes, M. & Rant, U. Data analysis of translocation events in nanopore experiments. *Analytical Chemistry* **81**, 9689–9694 (2009).

[356] Provencher, S. CONTIN: A general purpose constrained regularization program for inverting noisy linear algebraic and integral equations. *Computer Physics Communications* **27**, 229–242 (1982).

[357] Sorlie, S. S. & Pecora, R. A dynamic light scattering study of four DNA restriction fragments. *Macromolecules* **23**, 487–497 (1990).

[358] Doi, M. & Edwards, S. F. *The Theory of Polymer Dynamics* (Oxford University Press, Oxford, 1988).

[359] Robertson, R. M., Laib, S. & Smith, D. E. Diffusion of isolated DNA molecules: Dependence on length and topology. *Proceedings of the National Academy of Sciences of the United States of America* **103**, 7310–7314 (2006).

Acknowledgments

I would like to express my deep gratitude to Prof. Friedrich Simmel. Thank you for all the freedom you gave me in planning and conducting research projects and for your great support. Thank you so much for your patience, without it this work would certainly not have been possible.

I would also like to thank Prof. Meni Wanunu. Thank you for the warm welcome in Boston and for all your support.

Moreover, I would like to thank Deutsche Forschungsgemeinschaft (DFG) for funding my research.

My very special thanks go to all colleagues I had the chance to team up with, Vera Arnaut, Andrey Ivankin, and Daniel Pedone. Without you, this time would have been half as enjoyable and half as productive.

I would also like to extend my thanks to all members of the Simmel, Dietz and Wanunu labs for providing such a great working atmosphere and for all their support and friendship. Special thanks go to Thomas Martin, Korbinian Kapsner, Jonathan List, Enzo Kopperger, Daniela Ziegler, Helene Budjarek, Erika Bischofs and Susanne Kinzel.

More thanks go to all collaboration partners, Prof. Hendrik Dietz, Prof. Michael Mayer, Ulrich Rant, Spencer Carson and Shannon Kinney. Thanks also go to Niels Fertig, Matthias Beckler and Timo Stengel from Nanion and to Markus Döblinger for their support.

At last, I want to thank my wife Sandra, my family and friends for all their support.